

Lithium Niobate Resonators and Filters

Toward Reconfigurable Filter Banks

Submitted in partial fulfillment of the requirements for
the degree of
Doctor of Philosophy
in
Electrical and Computer Engineering

Sean Yen

B.S., Electrical and Computer Engineering, Cornell University

M.S., Electrical and Computer Engineering, Carnegie Mellon University

Carnegie Mellon University

Pittsburgh, PA

June, 2016

© Sean Yen 2016

All rights reserved

Acknowledgments

I thank my thesis advisors, Professors Gary K. Fedder and Tamal Mukherjee. It astounds and humbles me that they were able to make the time meet with me nearly every week, despite their busy schedules, in order to guide my research and career. They demonstrate creativity, integrity, and a sense of humor that inspire and motivate me.

My thesis committee, comprising my thesis advisors, and Professors Gianluca Piazza and Songbin Gong, have given great guidance for this work. I am grateful for their suggestions and support.

The devices were fabricated by Abhay Kochhar, Gabriel Vidal-Álvarez, and Lisha Shi over various fabrication runs – I thank them for their efforts to provide me with samples. I would also like to thank Suresh Santhanam and the cleanroom staff for supporting the fabrication. At the layout stage, I thank Enes Calayir and Mohamed Mahmoud for the help with SKILL scripts, which saved me from countless hours of drawing rectangles.

I enjoyed working in the MEMS Lab because of the professionalism, wisdom, and friendship of my fellow Ph.D. students. Kristen L. Dorsey and Ashwati Krishnan in particular were (and are) great mentors. I am glad for my former and present labmates including Peter Gilgunn, Dylan Fang, Nathan Lazarus, Congzhong Guo, Lionel Wong, Erdinc Tatar, Jinglin Xu, Xiao Chuan Ong, Megha Sunny, Mats Forssell, Mary Beth Galanko, and Metin Gokhan Guney. Outside the office, I thank my friends Mohamed Omar Darwish and Clay Long for the exciting games of squash.

My family has always been there for me, and for that I am thankful. My parents have supported a world-class education for me and my sister. My sister demonstrates sincerity in everything she endeavors. The selflessness, grit, and mindfulness of my family motivate me to become a better person.

I am grateful for the financial support. The Benjamin Lamme Westinghouse Graduate Fellowship supported my first year as a graduate student at Carnegie Mellon University. The C2S2 Focus Center, one of six research centers funded under the Focus Center Research Program, a Semiconductor Research Corporation entity, supported the research I performed during the first 15 months of my Ph.D. career. The Defense Advanced Research Projects Agency RF-FPGA program provided funding support for this project under award HR0111210004. The National Science Foundation has provided partial support of this work as part of the Cyber-enabled Discovery and Innovation (CDI) program under grant CNS0941497.

Abstract

Reconfigurable filter banks are an enabling technology for wireless communications. Spectrum scarcity motivates radios that can adjust to new wireless standards and block interferers. These can be achieved by programming a reconfigurable filter bank. However, state-of-the-art reconfigurable filter banks do not simultaneously meet performance and size requirements needed for handheld applications. To that end, this work focuses on designing filters as building blocks for filter banks using lithium niobate laterally-vibrating microresonators (“LN microresonators”).

LN microresonators show promise by virtue of their small size, low loss, ability to instantiate devices of multiple frequencies on the same die, and high coupling coefficient K_t^2 (leading to wide filter bandwidths or tuning range). This work focuses on techniques to incorporate these qualities into filters suitable for use in filter banks.

A low-loss bandpass filter is designed to exploit the high K_t^2 provided by the LN. Because of the high resonator quality factor Q , the measured filter demonstrates an insertion loss less than 3 dB, comparable to the state-of-the-art. However, resonator spurious modes (“spurs”) outside resonance compromise the rejection in the filter stopband such that the out-of-band rejection is about 6 dB worse than what it would be without the presence of spurs. This motivates an investigation of spurs due to misalignment and underetch.

A tunable absorptive notch filter is designed and fabricated as a platform to demonstrate tuning. The tuning range is about 6% of the K_t^2 of the resonators; a method is proposed to extend the tuning range by stepping the impedance of the circuit surrounding the resonators. In measurement, the tuning range is found to be discontinuous because of fluctuations due to modal coupling in the resonators near the resonance. This motivates the need for resonators that have a smooth response free of fluctuations.

This work presents two views of the fluctuations. First, the effects of connecting parallel resonators are considered, namely mechanical and electrical coupling of adjacent resonators. Second, the spurious modes in individual resonators are explained using models in one, two, and three dimensions. Studies endeavoring to mitigate the spurs due to the 1D and 3D effects are performed.

Contents

List of Tables	ix
List of Figures	xi
1 Introduction	1
1.1 Background and motivation	1
1.1.1 Reconfigurable filter banks: terminology	1
1.1.2 State-of-the-art reconfigurable filter banks for software-defined radio	2
1.1.3 Lithium niobate microresonators	6
1.2 Thesis statement	10
1.3 Thesis organization and contributions	10
2 Adapting existing resonator filters to high K_r^2	15
2.1 Introduction	15
2.2 Filter design	16
2.2.1 Intuitive understanding of ladder filters	16
2.2.2 Low- K_r^2 design: ladder filters as cascaded L-sections	18
2.2.3 Calculating the image impedance	21
2.2.4 Improved design of ladder filters with matched image impedance	23

CONTENTS

2.2.5	Coupled filter bandwidth improves with image impedance guidance	25
2.3	Filter design to mitigate uncertainty in $K_{t,p}^2$	25
2.4	Fabrication and measurement	31
2.5	Matching simulation and measurement	33
2.5.1	Standalone resonators and capacitor	34
2.5.2	Adding parasitic capacitance	37
2.5.2.1	Extraction of C_{1p} , C_{2p} , and C_{12} embedding capacitances	38
2.5.2.2	Estimating and including C_{pp} in filter simulation	42
2.5.3	Filter simulation constructed with measured resonator and capacitor data (not models)	44
2.6	Discussion and conclusions	45
3	Varactor tuning of filters	47
3.1	Introduction	47
3.2	Tuning single resonators and bandpass filter example	48
3.2.1	Parasitic capacitance of varactors	54
3.3	Absorptive notch filter design	59
3.4	Fabrication and measurement of a fixed absorptive notch filter	66
3.5	Tuning the absorptive notch filter	68
3.6	Fabrication and measurement of a tunable absorptive notch filter	70
3.7	Discussion on discontinuous tuning range	72
3.8	Proposed method to extend the tuning range	74
3.9	Conclusions	76
4	Fluctuations from modal coupling in arrayed resonators	79
4.1	Introduction	79

4.2	Why arrayed resonators?	81
4.3	Mechanical coupling of parallel identical resonators	82
4.3.1	COMSOL simulation of mechanical coupling	84
4.4	Electrical coupling of parallel mismatched resonators	88
4.5	Proposed method to align the response of arrayed resonators	91
4.5.1	Remark on Q and split varactor tuning	92
4.5.2	Practical considerations	92
5	Resonator spur mitigation	99
5.1	Introduction	99
5.2	Origins of spurs in standalone resonators	101
5.2.1	Misalignment and under/overetch (1D)	101
5.2.2	Non-S0 modes of vibration (2D)	106
5.2.3	Transverse modes (3D)	107
5.3	Scaling laws and tradeoffs	114
5.4	Further details on mitigating spurs due to misalignment and under- and overetch	115
5.4.1	Simulation of sensitivity to misalignment and underetch	115
5.5	Transverse mode suppression techniques	118
5.5.1	Simulation setup	118
6	Conclusion	121
6.1	Future prospects	123
6.1.1	Increasing resonator f_s, C_0, K_t^2 , and Q	123
6.1.2	More resonator routing layers	124
6.1.3	Investigation of undercut LN film effects	126
6.1.4	Switching networks	127

CONTENTS

6.1.5	Integration with CMOS	129
6.1.6	Optimization for reconfiguration control	130
References		131
A Definitions and models		137
A.1	Acronyms and abbreviations	137
A.2	Resonator geometry parameters	138
A.3	Modified Butterworth-Van-Dyke (MBVD) model	139
A.4	K_t^2 vs. k_t^2	145
B RF measurement		147
B.1	RF Probe Station setup	147
B.2	Network analyzer setup	147
B.3	Deembedding procedures	148
C COMSOL FEA simulation setups		151
C.1	2D simulation	151
C.2	3D simulation with misalignment and underetch	162
D Additional measurements		187
D.1	Ladder filter measurements	187
D.2	Resonator measurements	188
E Layout directory		189
E.1	LN/SiO ₂ run, 2014	189
E.2	LN run, 2015	189

List of Tables

1.1	Summary of the state-of-the-art for reconfigurable filter banks	5
2.1	MBVD model parameters for the series and shunt resonators obtained by fitting to COMSOL 3D simulation	30
2.2	MBVD model parameters for the series and shunt resonators obtained by fitting to measurement	34
3.1	Parameters for MBVD models fitted to measurement of the two resonators used in the tunable absorptive notch filter	63
5.1	Comparison of measurement, 2D simulation, and theory for misalignment and un- deretch	113

This page intentionally left blank

List of Figures

1.1	Filter bank concept	2
1.2	Teardown of the Apple iPhone 6s showing multiple frontend chains in a modern cellular phone	3
1.3	Architecture of the Ettus B200mini software-defined radio transceiver showing the single receiver chain and lack of RF filtering	4
1.4	Flowchart illustrating the rationale leading to the choice of lithium niobate microresonators	7
1.5	Resonator cross section, model, symbol, and SEM	8
1.6	Resonator MBVD model admittance frequency response marked with issues addressed in this thesis	9
2.1	Ladder filter topologies used in this work	17
2.2	Typical transmission frequency responses ($ S_{21} $) for coupled and full ladder filters .	17
2.3	Analyzing a full ladder filter as cascaded L-sections	19
2.4	Schematic of a full ladder filter composed of four cascaded L-sections	20
2.5	Simulated S-parameters for the full ladder filter composed of four cascaded L-sections in aluminum nitride	20
2.6	Simulated S-parameters for the full ladder filter composed of four cascaded L-sections in LN showing the problem of “shoulders”	21

LIST OF FIGURES

2.7	Infinite ladder filter schematic for calculating image impedance.	22
2.8	Schematic for full-ladder filter generated by cascading four L-sections with alternating direction	24
2.9	Simulated S-parameters for a full ladder filter with improved matching	24
2.10	Comparing insertion loss and return loss for traditional and modified coupled filter designs	25
2.11	Schematic for 1-T full ladder filter as fabricated, including a laser-trimmable capacitor to mitigate uncertainty in K_t^2	26
2.12	Effect of reduced $K_{t,p}^2$ upon the passband of a full ladder filter consisting of one T-section	27
2.13	Suite of S-parameters of trimmable full ladder filter consisting of one T-section with a trimmable capacitor C_p in parallel with the shunt branch.	28
2.14	Minimal effect of reduced $K_{t,s}^2$ upon the passband of a full ladder filter consisting of one T-section	29
2.15	Admittance magnitude and phase from COMSOL FEA simulation of series and shunt resonators, with fitted MBVD models	30
2.16	Simulated S-parameters of a full-ladder filter consisting of one T-section with shunt trimmer capacitor, simulated with MBVD and COMSOL-simulated resonators and an ideal capacitor	31
2.17	Microscope image of the 1-T full ladder filter as fabricated, including a laser-trimmable capacitor to mitigate uncertainty in K_t^2	32
2.18	Measured S-parameters for a 1-T ladder filter with trimmable capacitor intact, without deembedding	33
2.19	Close-up of passband of measured $ S_{21} $ for a 1-T ladder filter with trimmable capacitor intact, without deembedding	33

LIST OF FIGURES

2.20	Measured admittance plots for standalone series and shunt resonators, with pad-to-pad feedthrough deembedded, along with fitted MBVD models	35
2.21	Images of the standalone series and shunt resonators corresponding to those used in the fabricated ladder filter	36
2.22	Admittance of standalone capacitor with staggered 1.5 μm /4.5 μm spaced fingers .	37
2.23	Image of the fabricated standalone capacitor corresponding to the capacitor in the ladder filter	37
2.24	S-parameters for ladder filter, after fitting MBVD parameters to the standalone resonators, compared to measured filter S-parameters	38
2.25	Schematic for 1-T full ladder as fabricated, with parasitic capacitances added . . .	38
2.26	Microscope image of open deembedding structure for 1-T full ladder filter	39
2.27	Measured admittance plots for the feedthrough element of the Π network of the open deembedding structure for the 1-T full ladder filter	40
2.28	Measured admittance plots for the shunt element at port 1 of the Π network of the open deembedding structure for the 1-T full ladder filter	40
2.29	Measured admittance plots for the shunt element at port 2 of the Π network of the open deembedding structure for the 1-T full ladder filter	41
2.30	S-parameters for ladder filter, after fitting MBVD parameters to the standalone resonators and with parasitic capacitances due to the embedding structure added, compared to measured filter S-parameters (no deembedding)	41
2.31	Microscope image of 1-T filter, labeled with gaps corresponding to parasitic capacitance C_{pp} to ground	42

LIST OF FIGURES

2.32	S-parameters for ladder filter, after fitting MBVD parameters to the standalone resonators and with parasitic capacitances due to the embedding structure added, and the parasitic capacitance estimate of middle nodes to ground, compared to measured filter S-parameters (no deembedding)	43
2.33	Constructing S-parameter response by inserting measurements of standalone resonators and capacitors into circuit simulation, along with the parasitic capacitances of the embedding routing and the middle node to ground.	44
2.34	Comparison of simulating 1-T full ladder filter S-parameters, using MBVD and ideal capacitor models vs. using measurements from the standalone devices, both with ideal parasitic capacitances included.	45
3.1	Schematic of MBVD model of resonator	49
3.2	Series capacitor tuning of a single resonator, admittance magnitude and phase . . .	50
3.3	Parallel capacitor tuning of a single resonator, admittance magnitude and phase . .	51
3.4	Schematic of tunable full ladder filter with varactor tuning	51
3.5	Tunable ladder filter simulations for varactor corner configurations	52
3.6	Simulated fractional bandwidth vs. center frequency plot for tunable full ladder filter	54
3.7	Simulated fractional bandwidth vs. center frequency plot for two tunable full ladder filters in an array	55
3.8	Model of parasitic capacitance of varactors	55
3.9	Model including parasitic capacitance for a tunable bandpass ladder filter	56
3.10	Simulation of 1T ladder filter showing the effect of parasitic shunt capacitance . . .	57
3.11	Simulation of 1T ladder at various values of parasitic shunt capacitance	58
3.12	Simulation of 1T ladder filter with compensation of parasitic shunt capacitance by frequency-shifting the shunt resonator	59
3.13	Absorptive notch filter topology with generic coupling and transmission line	60

LIST OF FIGURES

3.14	Microscope images of the resonators used in the absorptive notch filter	61
3.15	Admittance magnitude and phase, measured and MBVD fitted model, for “Resonator 1” used in the tunable absorptive notch filter	62
3.16	Admittance magnitude and phase, measured and MBVD fitted model, for “Resonator 2” used in the tunable absorptive notch filter	62
3.17	Absorptive notch filter topology with lumped elements for coupling and transmission line	64
3.18	Simulated S-parameters of an ideal absorptive notch filter using matched MBVD models	65
3.19	Effect of resonator Q on absorptive notch filter bandwidth	65
3.20	Photograph and schematic of absorptive notch filter without tuning	67
3.21	Measured S-parameters of an absorptive notch filter and fitted model	67
3.22	Absorptive notch filter topology with tuning, with lumped elements for coupling and transmission line	68
3.23	Simulated S-parameters of an ideal tunable absorptive notch filter with varactor tuning	69
3.24	Tuning range of absorptive notch filter as a function of resonator K_r^2 at a 20 dB notch depth specification	70
3.25	Absorptive notch filter topology with tuning, as implemented with fine-tunable shunt capacitors in the transmission line and inverter sections	71
3.26	Photograph of the tunable absorptive notch filter as implemented	71
3.27	Measured S-parameters of tunable absorptive notch filter with varactor tuning	72
3.28	Simulated $ S_{21} $ of an absorptive notch filter using relatively clean resonator measurements	73
3.29	Proposed topology to offload impedance match burden to the remainder of the circuit	75

LIST OF FIGURES

3.30	Simulated $ S_{21} $ of tunable absorptive notch filter with proposed stepped impedance tuning	75
4.1	Simulated tuning of the measured resonator response using an ideal varactor, showing impact of spurs	80
4.2	Microscope image of a resonator with LN undercut marked	82
4.3	COMSOL 3D geometry setup for two resonators with isolated pits, with anchored PML regions highlighted	83
4.4	COMSOL 3D geometry setup for two resonators with shared pit, with anchored PML regions highlighted	84
4.5	COMSOL simulations of mechanical coupling comparing two resonators with isolated pits to two with a shared etch pit	85
4.6	COMSOL 3D geometry setup for isolated-pit resonators (just one resonator shown) with 12 and 15 μm long anchors	86
4.7	COMSOL simulations of isolated pit resonator devices with fixed boundary condition comparing two anchor lengths	87
4.8	COMSOL simulations of mechanical coupling comparing two resonators with isolated pits vs. a shared etch pit at several spacings with anchor length 15 μm	87
4.9	Close-up view of the measured admittance near resonance for “Resonator 1” used in the absorptive notch filter	89
4.10	Schematic of arrayed resonator with four parallel MBVD models with possibly different frequencies	89
4.11	Comparison of measurement vs. simulation with four MBVD models with mismatched frequency	90
4.12	Schematic of arrayed resonator with varactor tuning of individual resonators	91

LIST OF FIGURES

4.13	Demonstration of frequency alignment using varactors tuning each individual resonator within the arrayed resonator	92
4.14	Demonstration of frequency alignment using varactors tuning each individual resonator within the arrayed resonator, with high Q	93
4.15	Model including parasitic capacitance for a tunable absorptive notch filter	95
4.16	Simulated S-parameters for the absorptive notch filter with varying shunt parasitic capacitance	95
4.17	Simulated S-parameters demonstrating improvement to the notch depth against parasitic capacitance	96
4.18	Simulated S-parameters demonstrating improvement to the passband against parasitic capacitance by lowering the outer line capacitance	97
5.1	Quantifying spurs by their peaks in $ Y $	100
5.2	Quantifying spurs by their peaks in filter $ S_{21} $	101
5.3	Illustration of nominal, underetched, and misaligned resonators	102
5.4	2D COMSOL FEA simulations for under/overetch and misalignment	103
5.5	Visualization of mode shapes for underetch using 2D COMSOL simulation	104
5.6	Visualization of mode shapes for misalignment using 2D COMSOL simulation	105
5.7	Visualization of flexural mode in COMSOL 2D simulation	107
5.8	Visualization of third-order transverse S_0 mode in COMSOL 3D simulation	109
5.9	Microscope image ($50\times$ magnification) of standalone shunt resonator, with $6.551\ \mu\text{m}$ pitch, with measured dimensions labeled	110
5.10	Spurs labeled in admittance of the standalone shunt resonator, with close-up view of rolloff	111

LIST OF FIGURES

5.11	2D COMSOL simulation vs. measurement for resonator, explaining the K_t^2 reduction, the frequency shift, and spurs outside resonance due to misalignment and underetch	112
5.12	Zoomed-in view of 2D COMSOL simulation vs. measurement for the resonator, focusing on flexural modes	112
5.13	Zoomed-in view of 3D COMSOL simulation vs. measurement for the resonator, with spurious modes labeled	114
5.14	Simulated spur magnitude as a function of misalignment and underetch amounts . .	116
5.15	Simulated effect of misalignment spurs upon filter out-of-band rejection in the region of the first undertone	116
5.16	Admittance of resonator with high Q simulated in COMSOL 3D FEA, to be used for the study of misalignment and underetch	118
5.17	Labeled layout of resonator with stubs for transverse spur suppression	119
5.18	COMSOL 3D simulation showing suppression of the third order transverse mode with increased stub coverage.	120
6.1	COMSOL geometry for single resonator placed in widened pit	126
6.2	COMSOL 3D simulations of a single resonator with varying pit widths, with PML and Fixed Constraints	127
6.3	Potential “intrinsic” switching topology to turn resonance on and off	129
A.1	Image of resonator annotated with geometry parameters	138
A.2	Modified Butterworth-Van-Dyke model schematic and frequency response	139
A.3	Example of trading off Q and R_s in the MBVD model	142
B.1	Model of embedding network assumed during open deembedding	148
B.2	Schematic to isolate embedding network assumed during open deembedding	149

LIST OF FIGURES

D.1 Measurements of ladder filter S-parameters, no deembedding, from the four samples in the 2015 LN fabrication run 187

D.2 Measurements of ladder filter S-parameters (zoomed in to passband region), no deembedding, from the four samples in the 2015 LN fabrication run 188

D.3 Measurements of shunt resonator admittance, no deembedding, from three of the samples in the 2015 LN fabrication run 188

This page intentionally left blank

Chapter 1

Introduction

1.1 Background and motivation

Reconfigurable filters or filter banks are an enabling technology for wireless communications. As communications have moved to the wireless domain, the spectrum has become increasingly scarce [1]. Radio designers are overcoming spectrum scarcity by designing new standards and by using methods to block interferers. These capabilities can be achieved by programming a reconfigurable filter bank to optimize the overall radio performance. Several applications and technologies are reviewed in [2].

This section introduces a definition for reconfigurable filter banks, surveys the state-of-the-art, and identifies an approach that will advance the state-of-the-art.

1.1.1 Reconfigurable filter banks: terminology

A reconfigurable filter bank consists of a network of individually tunable filters, which combine to provide filtering capability across the spectrum (Figure 1.1). The filters are connected within a reconfiguration network, such as a switch network. Switching between filters provides coarse

1. INTRODUCTION

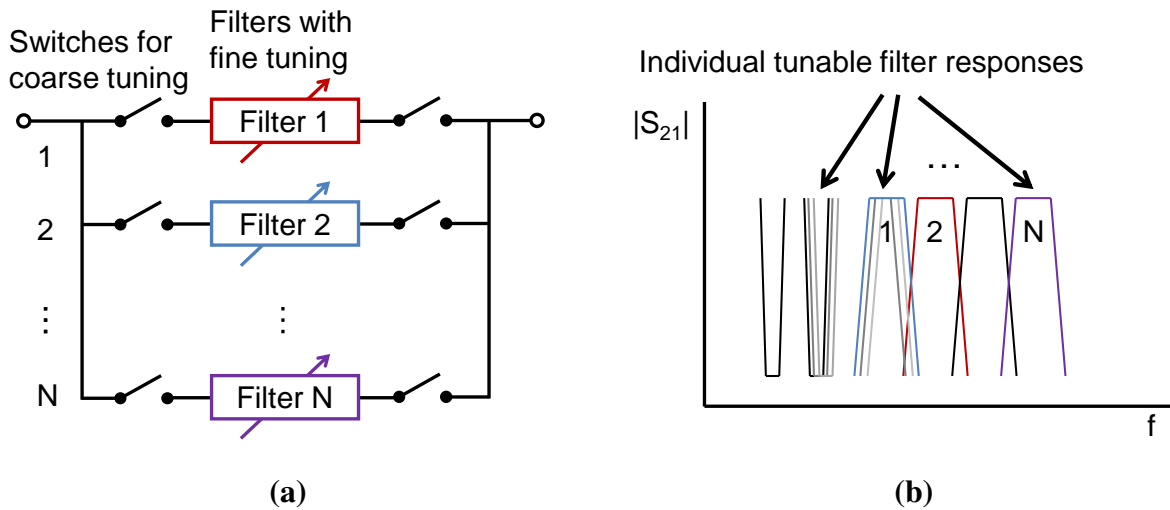


Figure 1.1: Conceptual (a) schematic and (b) transmission frequency response of a reconfigurable filter bank, with individually tunable filters of different types and different frequencies connected using a switch network.

tuning, while the tuning within each filter provides fine tuning.

This is a “bank” of filters because there are various filters from which to select frequency responses. The filter bank is “reconfigurable” to the extent of the ability to program the frequency response during in-field usage. The extent of reconfiguration varies among the state-of-the-art; this work supports a level of tuning where each filter in the bank is tunable, and where it is possible to use a switching network to select which filter through which to pass the signal.

1.1.2 State-of-the-art reconfigurable filter banks for software-defined radio

Modern handheld radios (cellular phones) are facing pressure (because of spectrum scarcity) to provide versatile RF functionality, such as being able to operate on multiple bands. Contemporary receiver chains have tuning ability for gain and linearity, but not for frequency. As a result, modern mobile terminals address the demand for multi-band radio with multiple *receiver chains* arrayed in parallel, at the expense of area and complexity. With this paradigm, adding more frequency bands adds more receivers (not only filters), which takes up more area (and power) than if only filters

1.1 Background and motivation

were added in a filter bank. For example, a contemporary phone, the Apple iPhone 6s, contains at least four power amplifier (PA) modules to provide coverage for the multiple bands. This is illustrated in the teardown shown in Figure 1.2, showing the area taken up by the multiple chips.

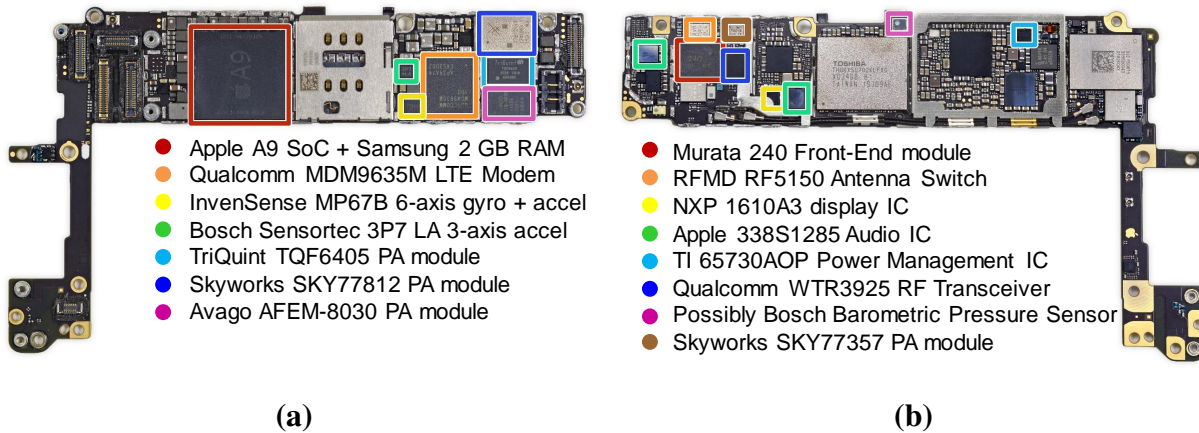


Figure 1.2: Circuit board from a teardown of the Apple iPhone 6s showing multiple frontend chains in a modern cellular phone; (a) front side, (b) back side. Image from [3] with labels added.

A promising way to minimize the number of receiver chains is with *software-defined radio*. Software-defined radio is a state-of-the-art radio frontend consisting of a software stage following a minimal RF hardware stage. The innovation of software-defined radio is that it can communicate on a wide range of frequencies with a single receiver chain. For example, one can purchase an entire radio transceiver with frequency range 70 MHz to 6 GHz [4] with the size of a business card (this is considered a small size for a prototyping-oriented product). The RF hardware is said to be “minimal” because there is no RF filter for the receiver; the local oscillator mixes down the wideband incoming signal to the baseband where the filtering is performed. This is illustrated in Figure 1.3, which shows the architecture of the radio in [4], which has a single (one each for I and Q components) receiver chain and lack of RF filtering. This lack of RF hardware, in addition to the single receiver chain, is what confers compact size to software-defined radio.

A limitation of the wideband (no RF filter) approach of software-defined radio is susceptibility

1. INTRODUCTION

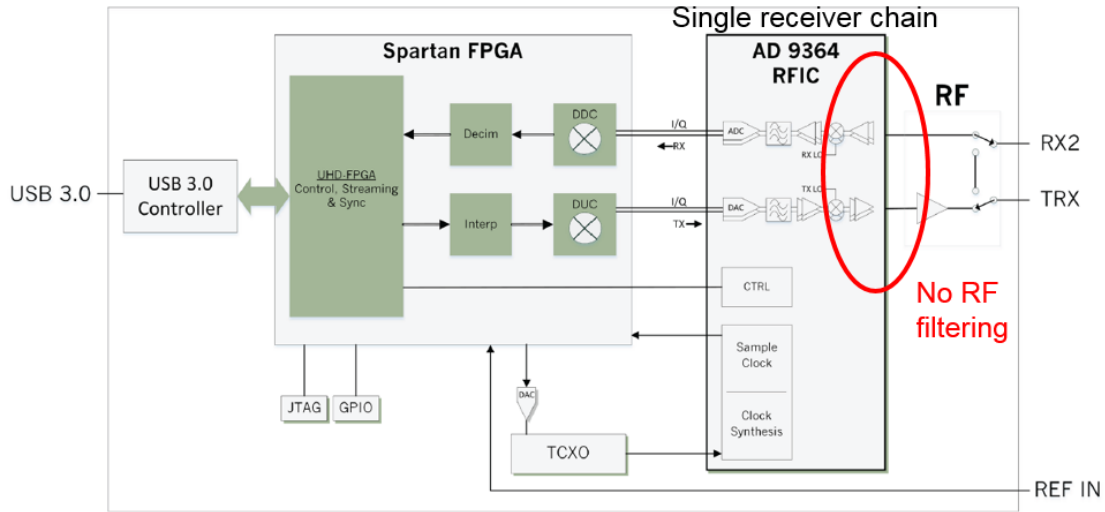


Figure 1.3: Architecture of the Ettus B200mini software-defined radio transceiver showing the single receiver chain and lack of RF filtering. Image from [4] with highlights added.

to interference [2], where signals in adjacent bands might saturate the mixers and amplifiers, and thereby interfere with the desired signal. Adding a *fixed* (non-tunable, non-reconfigurable) RF filter in front of the local oscillator mixer would clean up the interference, but the frequency agility would disappear.

Adding a reconfigurable filter bank in front of the local oscillator mixer in the software-defined radio would enable both the mitigation of interference and the ability to tune to different frequencies. The cost of providing the reconfigurable frequency selectivity with a reconfigurable bank is size and insertion loss penalties, both of which are typically greater in filter banks than in fixed filters. A single tunable filter is typically larger or more complex and has higher insertion loss than a single fixed filter because of the addition of a tuning mechanism. An array of filters is larger than a single filter, both because of the additional size of the switching network (which also adds insertion loss) and because of the multiple filters (multiplying the size of an individual filter by the number of filters).

Table 1.1 summarizes the state-of-the-art in terms of their size and integration, insertion loss,

1.1 Background and motivation

Table 1.1: Summary of the state-of-the-art for reconfigurable filter banks.

	Size, integration	Filter insertion loss	Frequency tuning or reconfiguration capability
Lumped-element switchable filter bank [5]	cm × cm size; assembled in machined enclosure	5-10 dB including switches	Switching between 2-7 channels; cannot tune individual filter frequency response
Bulk acoustic wave resonator filter switched filter bank [6]	mm × mm size; one frequency per die; integration by flip-chip bonding	1.5 dB filter only, < 3 dB with switches	Switching between 2 channels; no frequency tuning of individual filters (if implemented, would be limited by 1.2-1.5% fractional bandwidth).
Intrinsically-switched filter bank using microstrip [7]	10 cm × 10 cm size; microstrips fabricated on PCB with tuning/switching varactors soldered on	< 5 dB including intrinsic switching	Switchable between 3 channel filters, each filter tunable by about 50%
Intrinsically-switched bandstop filters using cavity resonators [8]	cm × cm; cavity resonators integrated into substrate; tuning by piezoelectric or MEMS actuators soldered on	(Bandstop filter) about 2 dB passband insertion loss including intrinsic switching	Two versions: 4-6 GHz and 6.3-11.4 GHz tuning ranges; each switchable between bandstop and all-pass configurations
This work	< mm × mm filters; multiple frequencies on single die, integration to be achieved by flip-chip or wire bonding	Fixed bandpass: measured 2.7 dB, < 1 dB possible with fabrication improvement. Tunable notch filter: 2-5 dB passband depending on match quality; < 2 dB possible.	Bandpass: demonstrated non-tunable configuration; tuning can be done similar to [9] with limits defined by the ≈ 17% possible bandwidth. Notch: 0.8% theoretical, 1.4% demonstrated. Switching between filters to be demonstrated in future work.

and frequency reconfiguration capability. Size is minimized in this work by focusing on using a technology that provides small filters that can be arrayed on a single substrate. In contrast,

1. INTRODUCTION

the state-of-the-art reconfigurable filters or filter banks tend to use technologies such as striplines [7], evanescent cavities [8], or lumped elements [5], which occupy a relatively large area (filter dimensions measured in centimeters) in the GHz frequency range. Insertion loss including the reconfiguration mechanism is typically in the range of 5 to 10 dB for these types of filters. The level of reconfiguration ranges from switched fixed filters [5, 7] to switched tunable filters [8]. There has been an attempt to miniaturize using bulk acoustic wave resonator filters [6], which resulted in a bank insertion loss of about 3 dB in a package, with each filter 1.5×0.75 mm in size. However, each filter in the bank had to be fabricated on a different substrate (because the bulk acoustic wave resonator frequency depends on the material thickness). This is not an optimal solution for scaling to many filters in a bank; it would be more elegant to be able to include all the frequencies on the same filter chip. The capability to synthesize multiple frequencies on the same substrate can be attained using the laterally vibrating microresonator technology, which is what is used in this work and which will be discussed in the next subsection. With the size of the resonators established to be small, the goals of this work include achieving filter insertion loss that is competitive with the state-of-the-art, and maximizing the filter tuning range.

1.1.3 Lithium niobate microresonators

To meet size, frequency tuning range, and insertion loss requirements, filters banks may use lithium niobate microresonators as a building block. Figure 1.4 illustrates the thought process leading to the choice of LN microresonators.

Microresonators are a type of acoustic resonator; compared to electromagnetic resonators, acoustic resonators are a few orders of magnitude smaller in size because the acoustic velocity is lower than electromagnetic velocity. Compared to lumped-element (LC tank) resonators, acoustic resonators can achieve higher Q factors, meaning lower insertion loss. Compared to SAW and FBAR resonators, laterally vibrating (or contour-mode) microresonators promise superior figure-

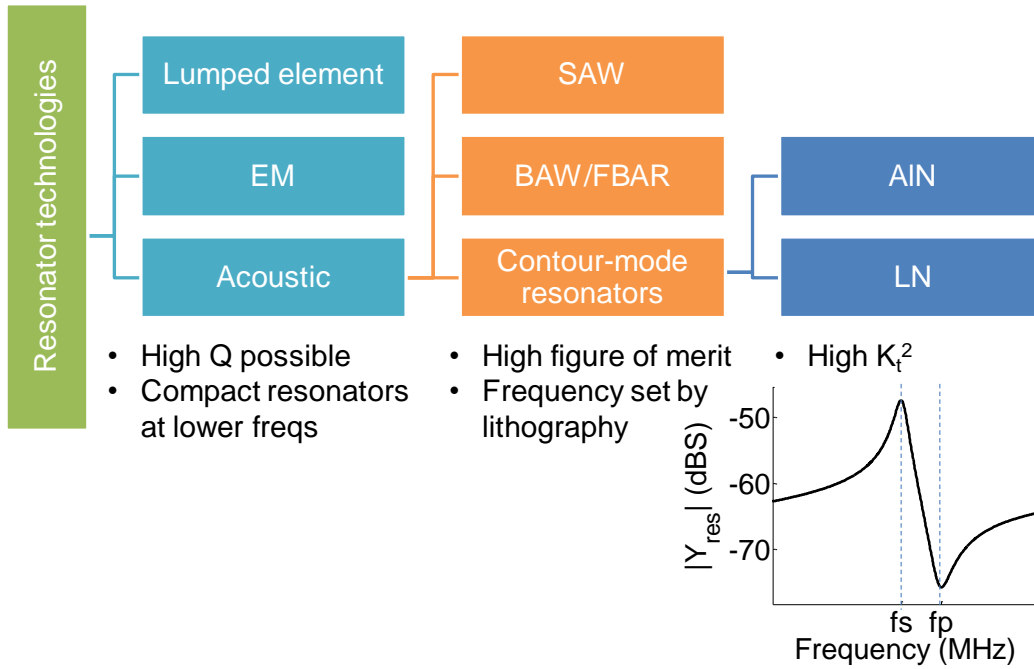


Figure 1.4: Flowchart illustrating why LN addresses the size, insertion loss, and tuning range (embodied by K_t^2) design directions. The K_t^2 quantifies the frequency difference between the resonance and antiresonance, which correspond to the available tuning range for the filters built using the resonators.

of-merit (leading to better insertion loss and tuning range) and the ability to lay out devices at different frequencies on the same substrate (which confers a compact way to make arrays of filters at a broad range of frequencies). The choice of LN as a piezoelectric material promises higher tuning ranges (by way of a higher K_t^2 , which quantifies the separation between resonance and antiresonance, corresponding to the rate of impedance rolloff, dictating tuning range) than other materials, such as aluminum nitride. The cross-section, 3D model, symbol, and SEM of a LN microresonator are shown in Figure 1.5.

The resonators used in the filters discussed here are laterally vibrating piezoelectric microresonators [10], whose width is dictated by the acoustic wavelength. As shown in the cross section and SEM of Figure 1.5, interdigitated electrodes with half-acoustic-wavelength pitch are arrayed in the width direction (“width” and “length” are labeled in the 3D model). The electrodes apply a

1. INTRODUCTION

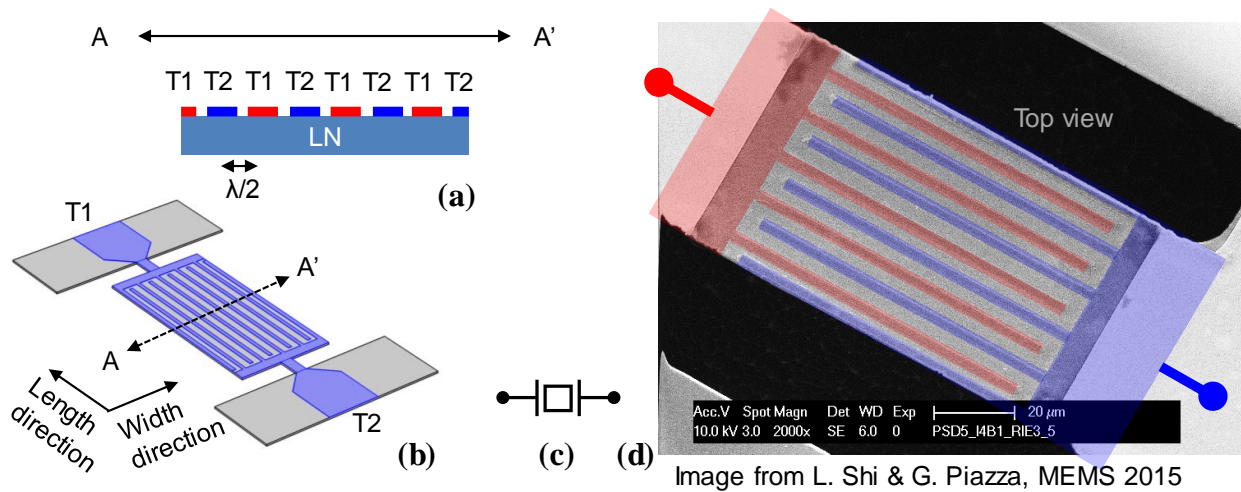


Figure 1.5: Resonator (a) cross-section along width direction, (b) 3-D model, (c) symbol, and (d) SEM of a resonator device, top view, with terminals marked with color overlay (SEM from [10], showing a device with odd number of fingers; both odd and even fingered devices are used in this work).

periodic (in the width direction) electric field through a suspended plate of LN (the piezoelectric material). The piezoelectric effect causes the LN to expand or contract within the material plane, again in a spatially periodic manner. This periodicity gives the resonator its frequency selection.

Figure 1.6 shows a typical frequency response of a LN microresonator; it is customary to report the electrical admittance (Y_{11}) as a function of frequency. The frequency at which the electrode pitch is half the acoustic wavelength becomes the resonant frequency (where the admittance measured at the electrodes is maximum). The frequency at which the admittance magnitude is minimum is the antiresonance frequency.

Because the acoustic velocity is several orders of magnitude less than that of electromagnetic waves, the size of an acoustic resonator is commensurately smaller than that of the equivalent electromagnetic version at a given frequency. This is particularly beneficial around the frequencies commonly used for wireless communications; for example, the wavelength corresponding to the 2.4 GHz ISM band is about 2.5 μm in the acoustic domain. At this frequency, resonators would

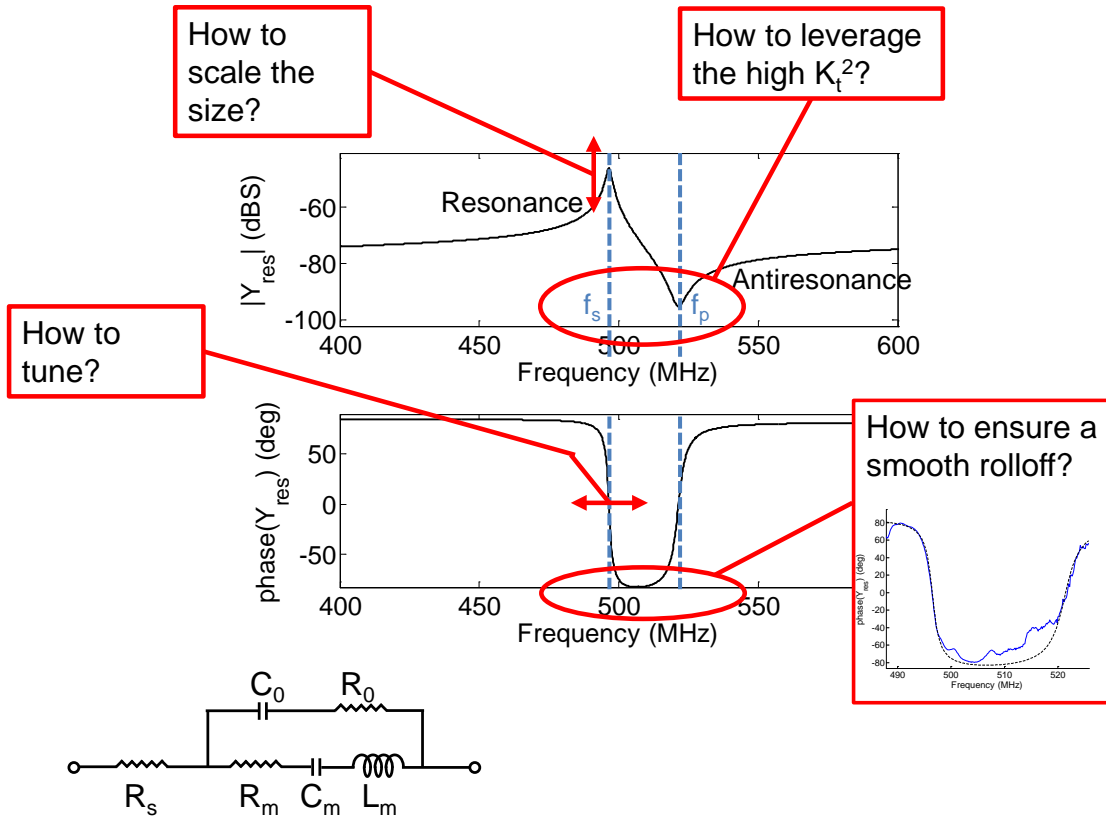


Figure 1.6: Modified Butterworth-Van-Dyke (MBVD) model of the resonator, with its admittance frequency response, magnitude and phase, annotated with the issues addressed in this thesis. Leveraging the high K_t^2 is addressed in Chapter 2; tuning is addressed in Chapter 3; sizing (leading to mismatched resonances) is addressed in Chapter 4; spurs are addressed in Chapter 5. Information about the MBVD model can be found in Appendix A.

each be about $70 \mu\text{m} \times 120 \mu\text{m}$ in size to achieve a 50Ω impedance match. This thesis is an exploratory work, and therefore uses a frequency of 500 MHz (acoustic wavelength $12 \mu\text{m}$) in order to have reasonably reliable fabrication results from the university cleanroom (namely to relax requirements for the lift-off step for fabricating the interdigitated electrodes, whose minimum width scales inversely with frequency). It is possible to adapt the results of this thesis to higher frequencies, provided scaling of the LN film thickness to avoid interfering modes due to dispersion (Chapter 5), and mitigation of parasitic capacitance.

1. INTRODUCTION

1.2 Thesis statement

This work aims to augment the knowledge on the design of tunable filters using LN microresonators. The goal is the demonstration of a low-loss, high bandwidth filter, and a tunable notch filter, both on the LN platform.

The approach is to create filters that test the various challenges of using LN microresonators. Observations from these filters feed back into hypotheses and further experiments to iteratively improve the ability to design the resonators and filters. Ladder bandpass filters in LN serve as a platform for developments improving the bandwidth, insertion loss, selectivity, and ripple metrics. A tunable notch filter using LN microresonators and off-chip components serves as a platform to demonstrate tuning and motivate resonator-level developments to improve the smoothness of the tuning range. Information gleaned from these filters highlights issues from resonator-level “spurs” that negatively impact the filter frequency responses. Two origins are hypothesized for the spurs: spurs due to coupling (mechanical or electrical) between resonators routed in parallel, and spurs due to standing-wave modes at the level of individual resonators. Experiments to isolate and mitigate these spurs are carried out in simulation.

1.3 Thesis organization and contributions

Figure 1.6 annotates features of the resonator response that loosely correspond to the issues addressed in this thesis. This thesis is organized by these issues.

Chapter 2 considers how to leverage the high electromechanical coupling coefficient K_t^2 of lithium niobate for maximal bandwidth. The K_t^2 quantifies the frequency difference between the resonance (f_s) and antiresonance (f_p); the higher the K_t^2 , the farther apart are the two frequencies. The K_t^2 sets the filter bandwidth and tuning range for filter topologies in which the rolloff between passband and stopband corresponds to the transition between resonance and antiresonance.

1.3 Thesis organization and contributions

Lithium niobate has a far higher K_t^2 (about 10-40%) than other piezoelectric materials, such as aluminum nitride (AlN, K_t^2 about 1-5%), and therefore promises higher bandwidths and tuning ranges. However, when filter designs from the AlN literature are directly implemented in LN, imperfections appear in the filter response, such as poor ripple performance and sub-optimal relation between K_t^2 and bandwidth. The key to optimizing the ripple and bandwidth turns out to be the impedance matching within the filter. This chapter presents a modification to the ladder circuit to achieve internal impedance matching, improving the theoretical bandwidth in the case of a coupled ladder filter by 40 percent without changing the resonator K_t^2 . The measured results of the chapter serve as motivation for the later chapter regarding resonator spurs.

The contributions in this chapter are: the identification of the flaws of using low- K_t^2 filter designs with high- K_t^2 resonators, carrying out the filter design using LN laterally vibrating microresonators, and a method to mitigate uncertainty in resonator K_t^2 for the initial filter fabrication.

Chapter 3 examines the K_t^2 from a tuning perspective. Although the K_t^2 is high, the antiresonance still limits the bandwidth and tuning range. The tuning of a ladder bandpass filter is reviewed, with a contribution being a discussion on the parasitic capacitance and how to mitigate them. For experimental demonstration, a notch filter serves as a vehicle to show the limit imposed by K_t^2 upon tuning range. In addition, measured results shown two sources of imperfection: parasitic elements and resonator spurs. The parasitic elements compromised the filter performance in a way that could not be neglected; the parasitics due to bondpads are analyzed and mitigation methods proposed. The spurs (which compromised the continuity of tuning) are a much more complicated issue and are discussed in the subsequent chapters. This chapter ends with a proposed solution to this limit, offloading the tuning burden from the resonator to the surrounding components of the filter.

The contributions in this chapter are: the equations for varactor tuning of the resonators, an analysis and mitigation of parasitic capacitance due to bondpads to the varactors for the bandpass

1. INTRODUCTION

filter, the implementation of a notch filter (in fixed and tunable renditions) using LN microresonators, identification of tuning range limits, and a proposed method to extend the tuning range by offloading the tuning to the surrounding circuit.

Chapter 4 discusses one possible source of fluctuations near the resonance that show up when scaling the size by wiring several resonators wired in parallel into arrayed resonators. Wiring resonators in parallel is a method to lower the characteristic filter impedance to typical RF levels. However, simulation reveals that small mismatches between (even ideal) constituent resonators can lead to fluctuations in the total resonance of the arrayed resonators. This chapter presents two possible mechanisms leading to the fluctuations: mechanical coupling of electrically identical resonators, and electrical coupling of mechanically isolated (but electrically different) resonators. For the latter, this chapter includes a proposed method to fix the resultant fluctuations by dividing the tuning capacitor into smaller tunable capacitors that address each resonator individually. The practical limitations to this proposed method are discussed.

The contributions in this chapter are: carrying out the analysis of the mechanical coupling between resonators sharing an etch pit, and proposing a method to align electrically mismatched resonators in parallel along with an analysis of scaling and mitigation methods for parasitic capacitance due to bondpads.

Chapter 5 focuses on the resonator-level origins and mitigation of spurs. Existing work in LN has targeted a figure-of-merit ($K_t^2 Q$ product) that focuses on the resonance and antiresonance, or focused on eliminating spurs in specific regions inside or outside the resonance, but not a comprehensive view of spurs. In this chapter, the impact of spurs is quantified and a model to explain the spurs is presented, including a description of scaling laws and tradeoffs. Several techniques to mitigate the spurs are considered.

The contributions in this chapter are: the aggregation of various theories on spurs to identify the spurs in a given measurement, analysis of mismatch and under/overetch and their impact upon

1.3 Thesis organization and contributions

K_l^2 and spurs outside resonance, and carrying out an exploration in simulation on using “stubs” of varying lengths to mitigate transverse mode spurs in single-routing-layer lateral LN microresonators.

This thesis presumes that the reader is familiar with background knowledge about microresonators and the Modified Butterworth-Van-Dyke model. This background information is provided for reference in the Appendix. Appendix A.2 illustrates the resonator, with labels for geometry parameters, and Appendix A.3 contains a summary of the MBVD model.

This page intentionally left blank

Chapter 2

Adapting existing resonator filters to high

K_t^2

2.1 Introduction

This chapter introduces the ladder and coupled filter topologies used as bandpass filters in this thesis. The sizing guidelines from image impedance filter design are validated in order to take advantage of the high K_t^2 of the LN resonators. Observations on the measured results motivate the subsequent chapters in this thesis.

The ladder filter topology is one of the simplest filter topologies using piezoelectric resonators because the resonators are directly coupled to each other with no external components. The simplicity, with uniform sizing and frequency ratios for the resonators, makes the ladder topology attractive to implement. However, when K_t^2 resonators are directly inserted into existing ladder topologies (originally developed for low K_t^2 resonators, such as in [11] and [12]), the *filter* performance can fail to scale with the increased *resonator* performance.

In particular, when increasing the K_t^2 of resonators in narrowband filter designs, the passband

2. ADAPTING EXISTING RESONATOR FILTERS TO HIGH K_T^2

ripple amplitude can exceed 3 dB, forming “shoulders” outside the intended passband. This leads not only to poor rolloff and shape factor, and sub-maximal bandwidth (especially for coupled ladder filters).

These “shoulders” are caused by internal impedance mismatch. Image impedance filter design principles (developed about 50 years ago [13]) inform sizing modifications that improve the internal impedance match. These sizing modifications coincide with the sizing found in some of the existing literature using Surface Acoustic Wave (SAW) resonators by Ikata et al. [14] and Komatsu et al. [9] as well as by Kadota et al. in SH0 mode resonators [15]. In this chapter, the design guidelines are applied to filters using lithium niobate extensional-mode Lamb-wave microresonators (as opposed to SAW resonators) with the goal of creating a low-insertion-loss wideband filter that could be used in a filter bank.

This chapter begins with a review of the ladder filter designs. A calculation of the image impedance of the segments of the ladder filter leads to an improvement to the guidelines on how to cascade filter sections. This filter was fabricated and measured. This chapter ends with a discussion about experimental results from the fabricated filters, motivating the work on spurs subsequent chapters.

2.2 Filter design

This section reviews the design of ladder filters and applies the idea of image impedance to create design guidelines.

2.2.1 Intuitive understanding of ladder filters

A ladder filter consists of alternating series and shunt elements between two ports, as shown in Figure 2.1. In this work, the series elements are always resonators to form a bandpass charac-

teristic. The series resonance defines the passband (by forming “transmission poles”), while the antiresonance defines the notch terminating the right skirt (a “transmission zero”).

In this work, there are two options for the shunt elements of the ladder filter: a shunt capacitor or a shunt resonator to form a “coupled filter” or “full ladder filter”, respectively.

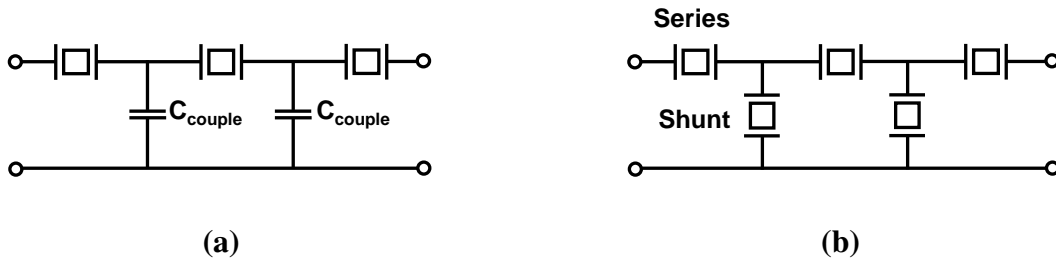


Figure 2.1: Ladder filter topologies used in this work. The shunt elements can be coupling capacitors or shunt resonators to form (a) “coupled filters” or (b) “full ladder filters”, respectively.

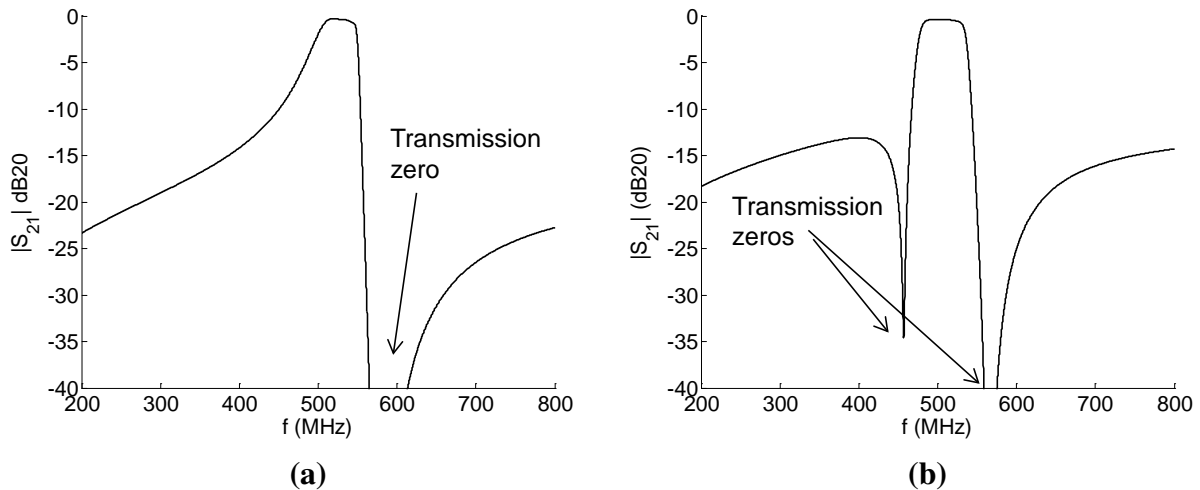


Figure 2.2: Typical transmission frequency responses ($|S_{21}|$) for (a) coupled and (b) full ladder filters

In the coupled filter, the shunt capacitors determine the coupling strength between the series resonators, which determines the bandwidth (among other metrics), leaving a shallow rolloff at the left skirt and a steep rolloff at the right skirt, as illustrated in Figure 2.2a

2. ADAPTING EXISTING RESONATOR FILTERS TO HIGH K_T^2

In the full ladder filter, the shunt resonators are set so that their antiresonance aligns with the series resonance of the series resonators in order to define the passband. Reversing the formula for K_T^2 in Equation (A.5), this means that the shunt resonator resonance should be

$$f_{s,p} = f_{s,s} \frac{1}{\sqrt{1 + \frac{8}{\pi^2} K_T^2}}, \quad (2.1)$$

where $f_{s,s}$ is the resonance of the series resonators and K_T^2 is the K_T^2 of the shunt resonators, which may be different from that of the series resonators. The (series) resonance of the shunt resonators creates a transmission zero to the left skirt, as shown in Figure 2.2b. Thus, with the two transmission zeros, the full ladder filter has steep skirts for both the upper and lower rolloffs.

The bandwidth of the filter is set by the K_T^2 of the resonators being used [16]. Intuitively: the bandwidth is limited by the transmission zeros, and the transmission zeros are defined by the separation between the resonance and antiresonance of the resonators, which is characterized by the resonator K_T^2 .

2.2.2 Low- K_T^2 design: ladder filters as cascaded L-sections

In a low- K_T^2 regime, a simple way to analyze the ladder topology is to break the ladder into identical L-shaped segments, calculate the ABCD parameters for a segment, then cascade the segments together to achieve the desired filter order, which determines the out-of-band rejection (OBR). The design approach and equations for the full ladder filter can be found in various papers [12, 17]¹; this chapter presents only the salient results.

Figure 2.3 shows the partitioning of a full ladder into L-sections. Let Z_s be the impedance of the series resonator and Y_p be the admittance of the shunt resonator (if there is no shunt resonator

¹In [12], K_T^2 is written as “ K^2 ”, while in [17], K_T^2 is written as “ k_t^2 ”. Appendix A.4 presents the conventions on K_T^2 used in this thesis.

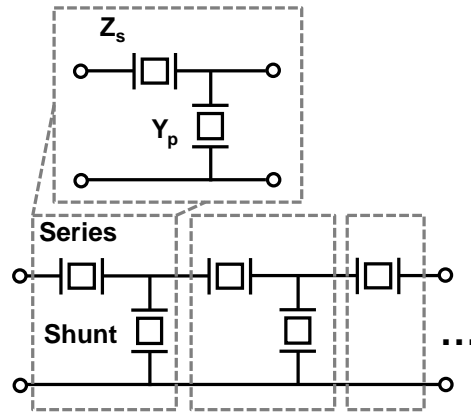


Figure 2.3: Analyzing a full ladder filter as cascaded L-sections. In the case of the rightmost section as shown, there is no shunt element, meaning that Y_p is set to zero when formulating the ABCD parameters for that particular section.

in the rightmost section, then $Y_p = 0$). The ABCD parameters for a single section are given by

$$\begin{bmatrix} A & B \\ C & D \end{bmatrix} = \begin{bmatrix} 1 + Y_p Z_s & Z_s \\ Y_p & 1 \end{bmatrix}. \quad (2.2)$$

Cascading the L-sections is represented by performing matrix multiplication on the ABCD parameters of the cascaded sections. Conversion from the ABCD parameters to S-parameters requires a characteristic impedance, which is given by the reactance of the geometric mean of the static capacitances,

$$R_{term} = \frac{1}{2\pi f_c \sqrt{C_{0s} C_{0p}}}. \quad (2.3)$$

C_{0s} and C_{0p} are the static capacitances of the series and shunt resonators, respectively, and f_c is the center frequency of the filter, which, by design, is equal to the resonance of the series resonators and to the antiresonance of the shunt resonators. As an example, a full ladder filter with four L-sections is simulated. The schematic is shown in Figure 2.4.

2. ADAPTING EXISTING RESONATOR FILTERS TO HIGH K_T^2

The simulated S-parameters are shown in Figure 2.5 when using $K_T^2 = 0.03$ (a good value for aluminum nitride resonators, for instance) and in Figure 2.6 when using $K_T^2 = 0.30$ for LN microresonators.

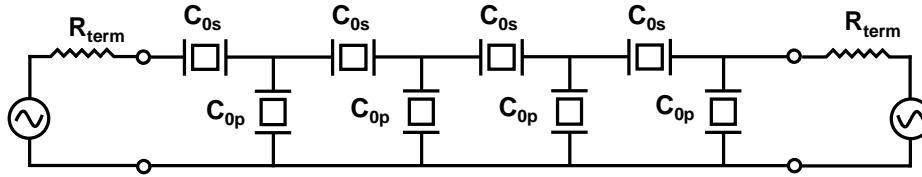


Figure 2.4: Schematic of a full ladder filter composed of four cascaded L-sections. The simulation uses $C_{0s} = 95$ fF and $C_{0p} = 165$ fF, which are typical values for a typical size of LN microresonators at the time of this publication. The termination is about 2500Ω . Q of the resonators is set at 1000 for all resonators, and $R_s = R_0 = 0$ in the MBVD model.

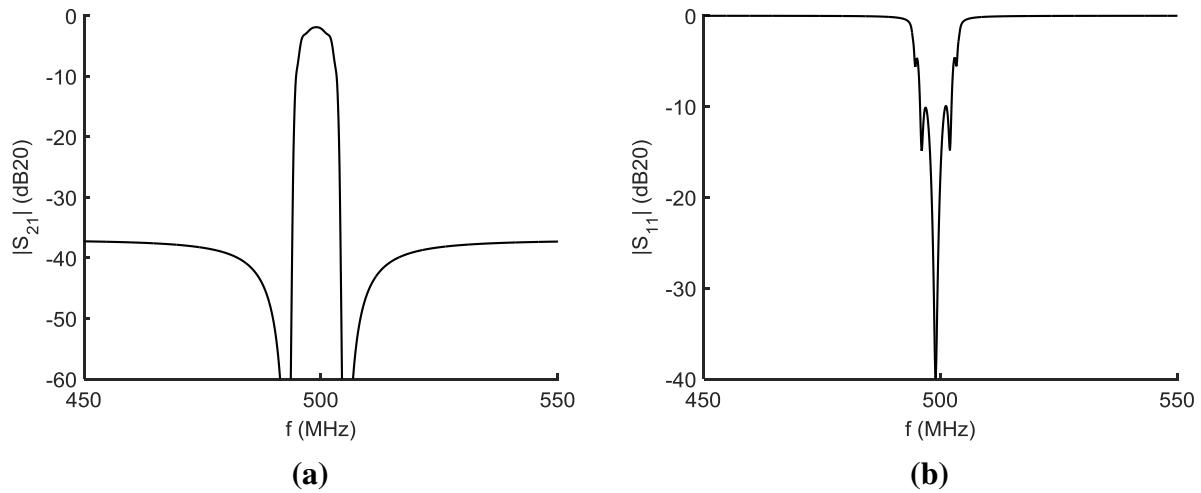


Figure 2.5: Simulated (a) $|S_{21}|$ and (b) $|S_{11}|$ for the full ladder filter composed of four cascaded L-sections in aluminum nitride ($K_T^2 = 0.03$). The narrow bandwidth hides the problem of “shoulders” seen when using high- K_T^2 resonators.

In both cases, the simulation uses $C_{0s} = 95$ fF and $C_{0p} = 165$ fF, which are typical values for a typical size of LN microresonators (about $60 \mu\text{m} \times 120 \mu\text{m}$ and 500 MHz operating frequency) at

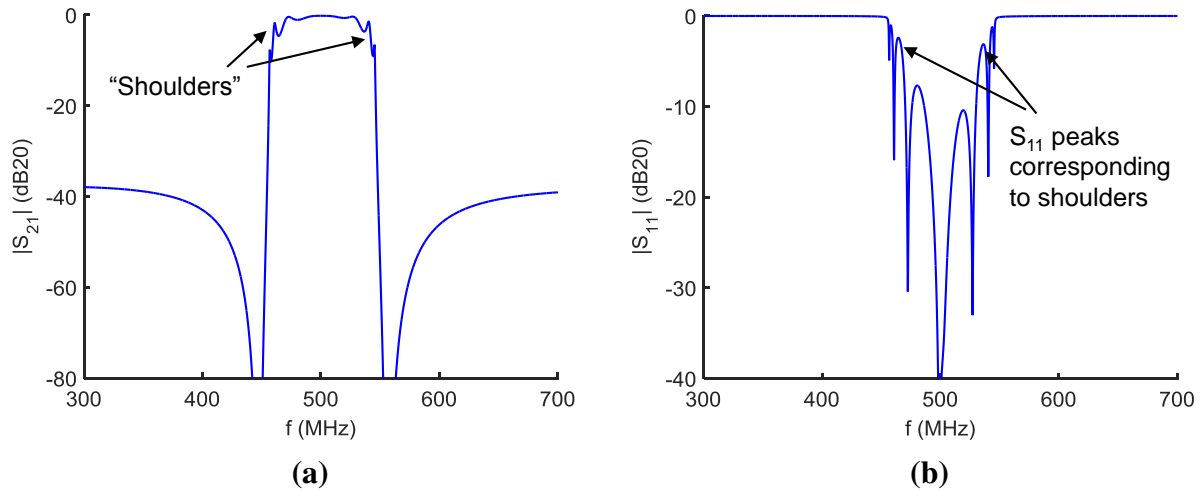


Figure 2.6: Simulated (a) $|S_{21}|$ and (b) $|S_{11}|$ for the full ladder filter composed of four cascaded L-sections in LN (K_t^2 assumed to be 0.30), with the “shoulders” marked. Note the wider frequency scale compared to the low- K_t^2 case in Figure 2.5.

the time of this publication. The termination, using Equation (2.3), is about 2500Ω . The Q of the resonators is set at 1000 for all resonators, and $R_s = R_0 = 0$ in the MBVD model.

The low $K_t^2 = 0.03$ causes a narrow bandwidth (about 2.5 percent). Because the filter poles are squeezed in such a tight bandwidth, the shape of the passband rolls off monotonically. However, for higher values of K_t^2 , imperfections appear. As indicated in Figure 2.6, “shoulders” appear to the sides of the passband. These shoulders are deeper than 3 dB (in $|S_{21}|$), and thus cannot be counted as part of the passband.

Note that the same effect persists even when the rightmost resonator in Figure 2.4 is removed such that the filter is symmetric. The results still exhibit the same “shoulders” seen in Figure 2.6, so symmetry in the schematic does not solve the problem.

2.2.3 Calculating the image impedance

The “shoulders” correspond to peaks in $|S_{11}|$. Because $|S_{11}|$ indicates the quality of impedance match, it is suspected that the “shoulders” indicate a poor match.

2. ADAPTING EXISTING RESONATOR FILTERS TO HIGH K_T^2

An optimal way to generate a good match would be to follow polynomial filter design principles to set the sizing, coupling, and frequency of the resonators in the filter to form responses such as the Butterworth filter response [13]. Typical polynomial filters require coupling structures between resonators and distinct sizing and frequency for each resonator in a given filter design. This is impractical to realize at this stage in the development of LN because of limited precision for the frequency definition and sizing contrasts, as well as a lack of low-loss coupling structures. Instead, this work uses the older **image impedance** approach to analyzing and designing filters, which can guide the design of simple ladder topologies.

The image impedance is the impedance looking into an infinite ladder; this is noted as Z_T in Figure 2.7. Of note, the direction of every other L-section has been flipped mirror-image to form this ladder. In this sense, the ladder can be viewed as a cascade of T-sections (each of which comprises two L-sections).

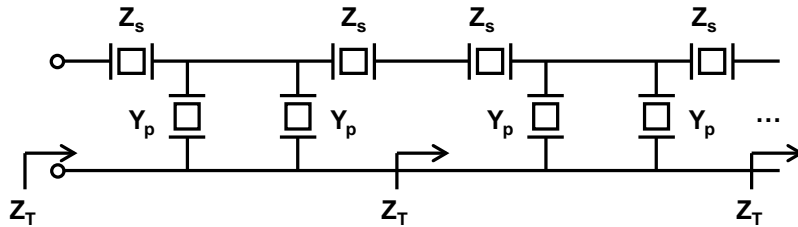


Figure 2.7: Schematic of infinite ladder for calculating the image impedance, noted here as Z_T .

The image impedance Z_T can be solved to be

$$Z_T = \sqrt{Z_s \left(Z_s + \frac{1}{Y_p} \right)}. \quad (2.4)$$

The impedance and admittance of the resonators can be written as [18]:

$$Z_s = \frac{1}{j2\pi f C_{0s}} \frac{f_{s,s}^2 - f^2}{f_{p,s}^2 - f^2} \quad (2.5)$$

and

$$Y_p = j2\pi f C_{0p} \frac{f_{p,p}^2 - f^2}{f_{s,p}^2 - f^2} \quad (2.6)$$

where C_{0s} and C_{0p} are the static capacitances of the series and shunt resonators, respectively; $f_{s,s}$ and $f_{p,s}$ are the resonance and antiresonance frequencies of the series resonator; and $f_{s,p}$ and $f_{p,p}$ are the resonance and antiresonance frequencies of the shunt resonator. If $f_{s,s} = f_{p,p}$ (aligning the resonance of the series resonators with the antiresonance of the shunt resonators), then, at resonance,

$$Z_T(f = f_{s,s}) = \sqrt{\frac{1}{(j2\pi f_{s,s})^2 C_{0s} C_{0p}} \left(\frac{f_{s,p}^2 - f_{s,s}^2}{f_{p,s}^2 - f_{s,s}^2} \right)} \approx \frac{1}{j2\pi f_{s,s}} \frac{1}{\sqrt{C_{0s} C_{0p}}}, \quad (2.7)$$

which agrees with the termination impedance in Equation (2.3). The approximation is because the center frequency $f_{s,s}$ is assumed to approach the arithmetic mean between $f_{s,p}$ and $f_{p,s}$.

2.2.4 Improved design of ladder filters with matched image impedance

By cascading the L-sections facing in alternating directions (as in Figure 2.7), instead of the simple cascade (Figure 2.4), better internal impedance matching can be achieved because each segment will see its own image impedance.

The topology can be represented by the schematic in Figure 2.8, which simplifies the parallel and series impedance combinations.

The filter performance can be computed using the sizing of the L-sections from Figure 2.4, such that the Z_s represents series resonators with size $C_{0s} = 95$ fF and Y_p represents shunt resonators with size $C_{0p} = 165$ fF. The results are plotted in Figure 2.9 alongside the results from the original

2. ADAPTING EXISTING RESONATOR FILTERS TO HIGH K_T^2

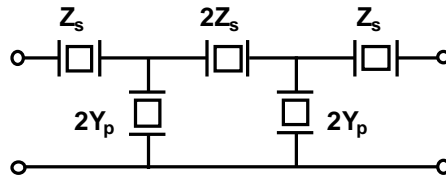


Figure 2.8: Schematic for full-ladder filter generated by cascading four L-sections with alternating direction. Note the sizing ratios of the resonators, which follow the T/π pattern from analyzing the image impedance.

ladder filter from Figure 2.6.

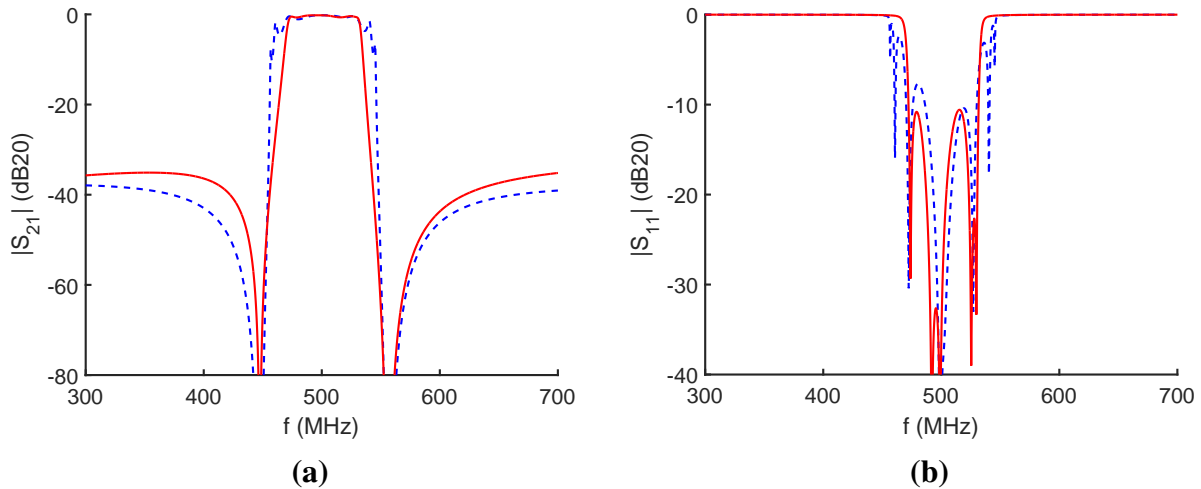


Figure 2.9: Simulated (a) $|S_{21}|$ and (b) $|S_{11}|$ for a full ladder filter with improved matching (red solid) as compared to the original filter (blue dash). The resonator model parameters are identical for the two cases.

The response is noticeably free of the “shoulders” plaguing the original design. This results in a monotonic rolloff. A way to quantify this is the Shape Factor specification, which is the ratio of the 20 dB bandwidth to the 3 dB bandwidth. The fractional 3 dB bandwidth in the original is 13.5%; in the improved version it is 12.4%. The 20 dB (fractional) bandwidth is 18.1% in the original and 14.9% in the improved. The shape factors are 1.34 and 1.20, respectively, with a lower the shape factor meaning a sharper filter.

2.2.5 Coupled filter bandwidth improves with image impedance guidance

The above findings also apply to the coupled filters. Figure 2.10 shows the comparison between a coupled filter before (as used in [11]) and after applying the insight from image impedance design. In this case, there is a bandwidth improvement as a result of getting rid of the shoulder. In the original case, the fractional bandwidth (FBW) is 2.5% (for resonator $K_t^2 = 11.5\%$), whereas in the improved case the FBW is 3.6% (for the same resonator K_t^2). This is a 40% increase in the FBW.

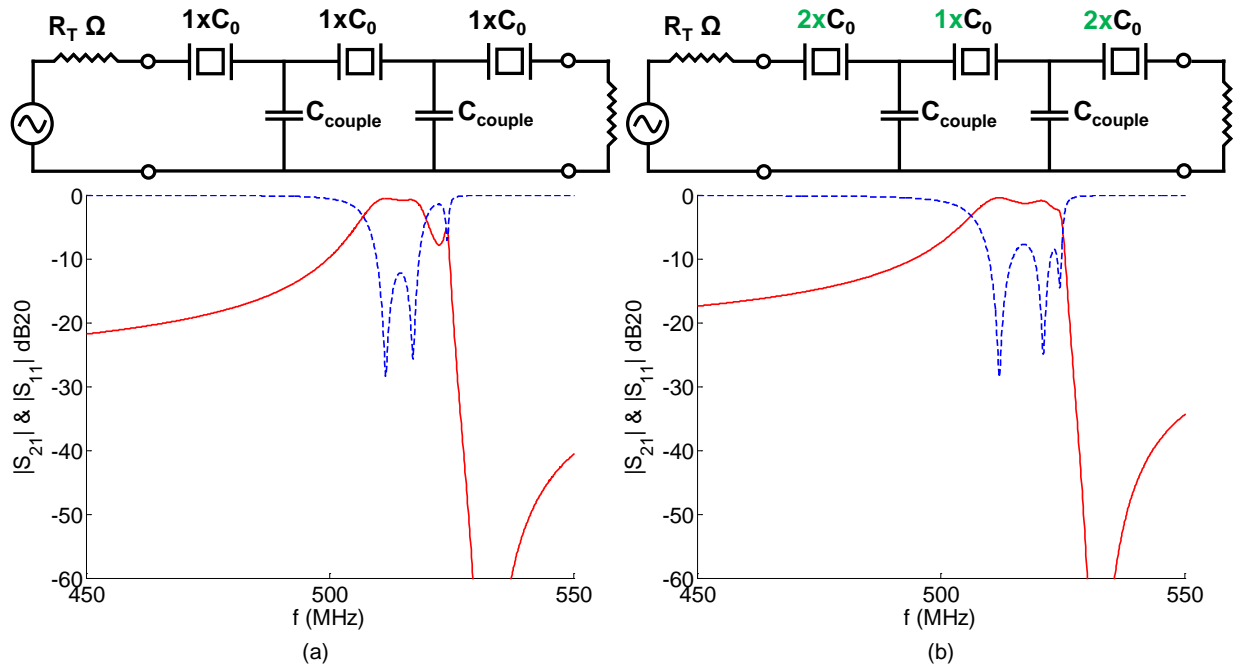


Figure 2.10: (a) Schematic, simulated $|S_{21}|$ (solid), and simulated $|S_{11}|$ (dashed) for traditional coupled filter design. (b) Schematic, simulated $|S_{21}|$ (solid), and simulated $|S_{11}|$ (dashed) for modified coupled filter design, showing improved distribution of poles.

2.3 Filter design to mitigate uncertainty in $K_{t,p}^2$

This section presents the filter design used for the first LN microresonator filters that achieve reasonably low-loss (less than 5 dB insertion loss) passband performance. The filter as laid-out is a

2. ADAPTING EXISTING RESONATOR FILTERS TO HIGH K_T^2

single T-section (or two abutted L-sections); the schematic is shown in Figure 2.11. A modification that is immediately noticeable is the capacitor C_p .

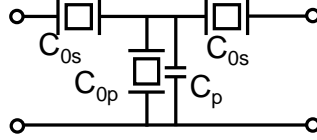


Figure 2.11: Schematic for 1-T full ladder filter as fabricated, including a laser-trimmable capacitor C_p to mitigate uncertainty in K_t^2 .

The motivation for the capacitor C_p is to mitigate uncertainties in the K_t^2 of the shunt resonator: *without* C_p , which is adjustable via laser trimming, the filter is susceptible to variations in $K_{t,p}^2$, the K_t^2 of the shunt resonator, because the shunt antiresonance can move around uncontrollably. Figure 2.12 shows the response of a filter *without* C_p , designed to the $K_{t,p}^2$ predicted by simulation. The filter performs admirably when the $K_{t,p}^2$ is as predicted (dashed trace), but starts to sag in the passband as the $K_{t,p}^2$ is reduced (solid trace). This is because the antiresonance $f_{p,p}$ is no longer aligned with the series resonance of the series resonators ($f_{s,s}$). Note that this sagging cannot be eliminated by adjustments to R_{term} .

To hedge against reductions in $K_{t,p}^2$, the filter is designed *presuming* a reduced $K_{t,p}^2$ (that is, increasing $f_{s,p}$ in Equation (2.1) using the reduced $K_{t,p}^2$), and using a trimmable capacitor (C_p) in parallel with the shunt resonator to enable final adjustment of the effective $K_{t,p}^2$ (equaling $K_{t,p}^2 \frac{C_{0p}}{C_{0p} + C_p}$) to match the presumed value of $K_{t,p}^2$. The mechanism is that the capacitor trims the frequency of antiresonance of the shunt resonator. With the shunt capacitor, the shunt resonator antiresonance frequency decreases (and the effective K_t^2 of the C_p in parallel with the shunt resonator decreases). The antiresonance of the shunt combination ($f_{p,p,eff}$) occurs approximately at

$$f_{p,p,eff} \approx f_{s,p} \sqrt{1 + \frac{8}{\pi^2} K_{t,p}^2 \frac{C_{0p}}{C_{0p} + C_p}} \quad (2.8)$$

2.3 Filter design to mitigate uncertainty in $K_{t,p}^2$

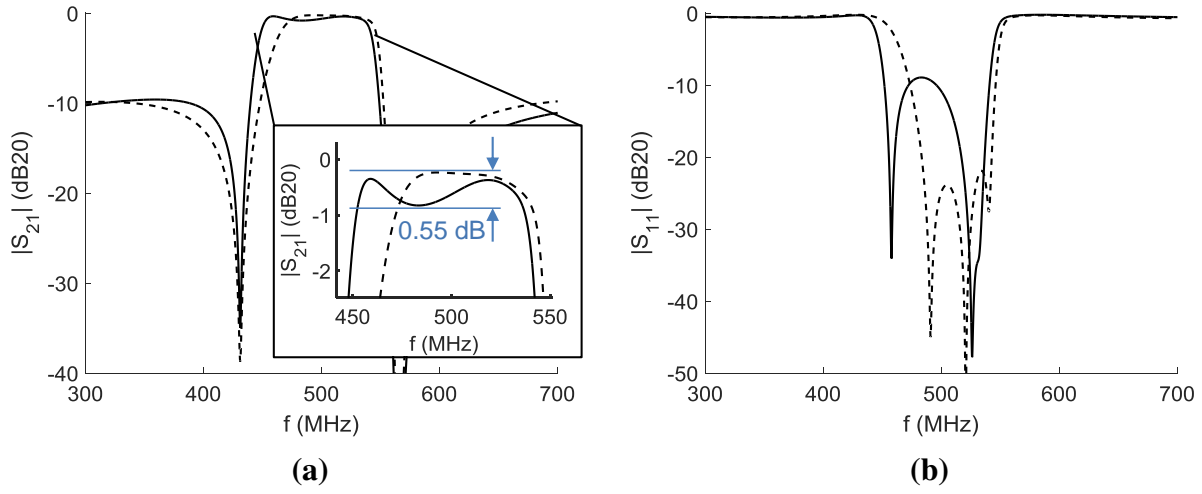


Figure 2.12: Effect of reduced $K_{t,p}^2$ upon the passband of a full ladder filter consisting of one T-section without a trimming capacitor. In both traces, the filter is designed for $K_{t,p}^2 = 0.3975$, the value predicted by COMSOL simulation. In the dashed trace, $K_{t,p}^2 = 0.3975$ as predicted, while in the solid trace, $K_{t,p}^2 = 0.24$, leading to sagging in the passband. The sagging cannot be eliminated by simple adjustments to R_{term} .

where $f_{s,p}$ is the series resonance of the shunt resonator, $K_{t,p}^2$ is the K_t^2 of the shunt resonator, and C_{0p} is the C_0 of the shunt resonator. The simulated frequency responses for the corners of $K_{t,p}^2$ and C_p are shown in Figure 2.13.

In Figure 2.13, the shunt resonator is designed so that if the maximum expected $K_{t,p}^2 = 0.3975$, its effective antiresonance (with C_p), $f_{p,p,eff}$, is aligned with the series resonance of the series resonators, or the center frequency of the filter (Figure 2.13, solid black trace, with shunt resonator $f_{s,p} = 460$ MHz). (It is presumed that the inaccuracy in $K_{t,p}^2$ will only yield actual $K_{t,p}^2$ less than the $K_{t,p}^2$ predicted by simulation). If the manufactured $K_{t,p}^2$ is less than simulated (as low as 0.243 for this particular capacitor design), then $f_{p,p,eff}$ will be less than the center frequency, and the passband will start to sag in the middle (Figure 2.13, dot-dashed trace). To move the shunt antiresonance back to the center frequency, the capacitor can be trimmed (using a laser) to reduce its capacitance, which will allow the shunt antiresonance to increase back into alignment (Figure 2.13, dashed trace). The gray trace is for comparison with the filter designed to $K_{t,p}^2 = 0.3975$ without

2. ADAPTING EXISTING RESONATOR FILTERS TO HIGH K_T^2

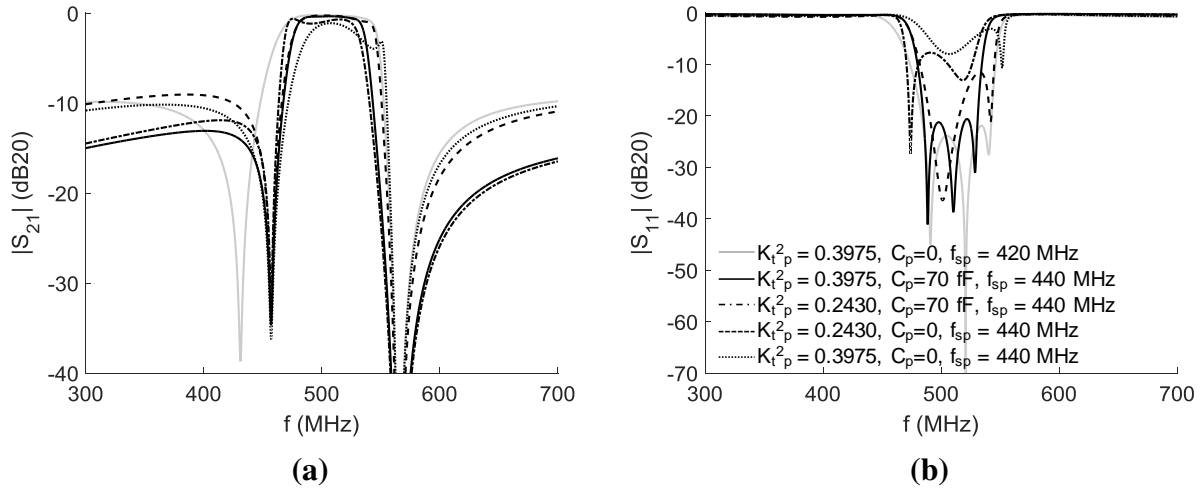


Figure 2.13: Suite of S-parameters of trimmable full ladder filter consisting of one T-section with a trimmable capacitor C_p in parallel with the shunt branch. **Gray:** “naïve” design to maximal $K_{t,p}^2$ ($f_{s,p} = 440$ MHz), without any C_p . **Black traces:** designed to a reduced value of $K_{t,p}^2 = 0.243$ ($f_{s,p} = 460$ MHz). **Solid:** a best-case scenario where $K_{t,p}^2$ is actually as high as predicted, and the capacitor throttles it so the effective $K_{t,p}^2$ is still 0.243 (thus aligning the antiresonance to the filter center frequency). **Dot-dash:** intermediate case where $K_{t,p}^2$ is minimal (0.243) and the capacitor is untrimmed, thus throwing off the alignment with the center frequency. **Dash:** a best-case scenario where $K_{t,p}^2$ is small (0.243) and the capacitor has been trimmed so that the filter behaves exactly as-designed for the $K_{t,p}^2$. **Dot:** a case illustrating what would happen if the filter is designed to $K_{t,p}^2 = 0.243$, but actually has $K_{t,p}^2 = 0.3975$, without a C_p to throttle the effective $K_{t,p}^2$; in this case, the antiresonance is again misaligned, causing ripple.

using C_p (so $f_{s,p} = 440$ MHz), showing a wider bandwidth but no protection against uncertainty in $K_{t,p}^2$. Thus, this technique of using a trimmable capacitor is useful when the $K_{t,p}^2$ is not well-known (such as in initial fabrication runs), but comes at the cost of reduced bandwidth.

There is no capacitor to trim the *series* resonator because the passband of the full ladder topology is not sensitive to minor variations in $K_{t,s}^2$. This is illustrated in Figure 2.14. The primary effect is to move the right skirt without major detriment to the ripple (which can be fine-tuned by minor adjustments to R_{term}). This lack of sensitivity is because varying $K_{t,s}^2$ varies the antiresonance of the series resonator, which does not primarily affect the passband.

2.3 Filter design to mitigate uncertainty in $K_{t,p}^2$

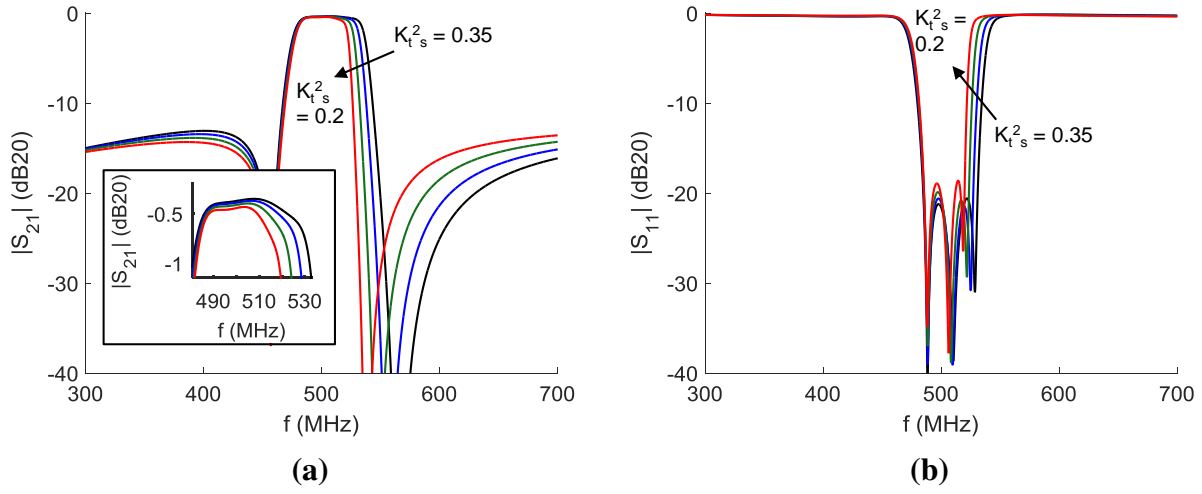


Figure 2.14: Minimal effect of reduced $K_{t,s}^2$ upon the passband of a full ladder filter consisting of one T-section and a trimming capacitor, (a) $|S_{21}|$, (b) $|S_{11}|$. The $K_{t,s}^2$ (of the series resonators) is varied in steps of 0.05 from 0.35 to 0.20. The primary effect is to move the right skirt of the filter. The ripple can be adjusted by minor changes to R_{term} . The inset in (a) shows a close-up view of the passband showing minimal change in ripple as the $K_{t,s}^2$ is changing.

To verify the design before fabricating the filters, the resonators being used are simulated in COMSOL Multiphysics finite-element analysis software in 3D (with clamped boundary conditions, as noted in Appendix C) and the simulated resonator admittance responses are inserted into the circuit simulation. The resonator MBVD model parameters are extracted from the simulation and used them in the filter simulation as well (the extraction procedure and code are included in Appendix A.3). These are shown in Figure 2.15, with the fitted MBVD parameters listed in Table 2.1. The shunt resonator antiresonance frequency overshoots the series resonator resonance; this is what the shunt capacitor $C_p = 140$ fF corrects for by means of Equation (2.8).

The simulated filter response, using both simulated and fitted-MBVD resonators, is shown in Figure 2.16. The shunt capacitor in both simulations is $C_p = 140$ fF to reduce the effective $K_{t,p}^2$ from 0.3975 (native resonator) to 0.243 (resonator in parallel with C_p). The predicted insertion loss is low, at about 0.35 dB, because of the high $Q = 1000$ from COMSOL. There is very little ripple in the design of the filter (less than 0.5 dB in the MBVD trace, somewhat more in the COMSOL

2. ADAPTING EXISTING RESONATOR FILTERS TO HIGH K_T^2

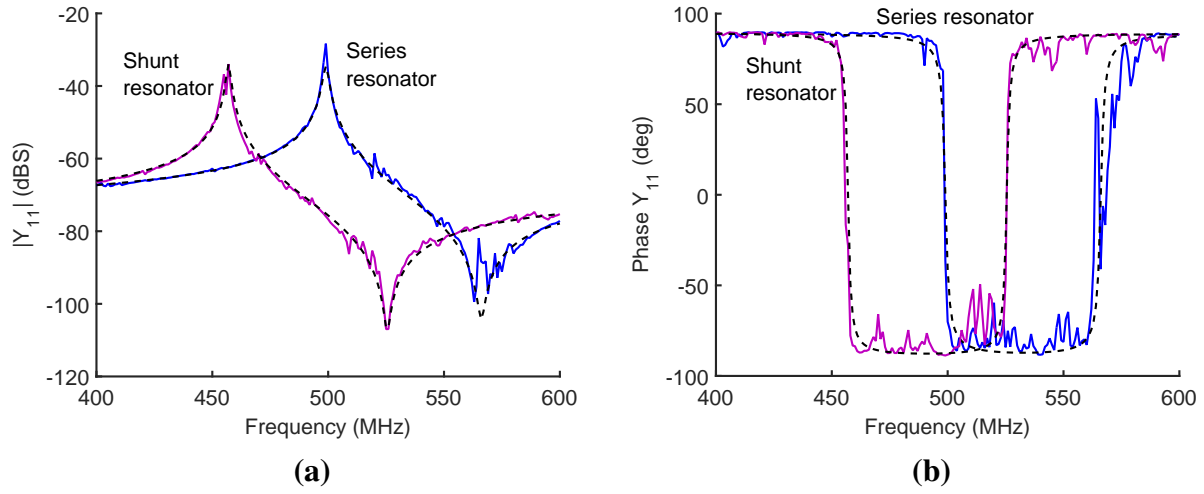


Figure 2.15: Admittance magnitude and phase from COMSOL FEA 3D simulation of series (blue, higher frequency) and shunt resonators (magenta, lower frequency), along with fitted MBVD models (dashed black), used in the filter. The series resonator is the higher-frequency response, while the shunt is the lower-frequency response. The shunt antiresonance is not aligned to the series resonance; this is to be corrected by a shunt capacitor in the full ladder filter.

Table 2.1: MBVD model parameters for the series and shunt resonators obtained by fitting to COMSOL 3D simulation. In the filter as implemented, two of the shunt resonators are used in parallel, so the total C_{0p} is $2 \times 82.6 \text{ fF} = 165.2 \text{ fF}$

	Series	Shunt
f_s (MHz)	500	457
C_0 (fF)	95	82.6
K_t^2 (%)	35	39.75
Q	500	500
R_s (Ω)	24	30
R_0 (Ω)	30	30

trace due to spurs in the resonator response). The predicted fractional bandwidth is 12.5%, and the predicted 20 dB bandwidth is 17.6%, thus forming a predicted 20 dB shape factor of 1.413. The predicted out-of-band rejection is about 13 dB at worst.

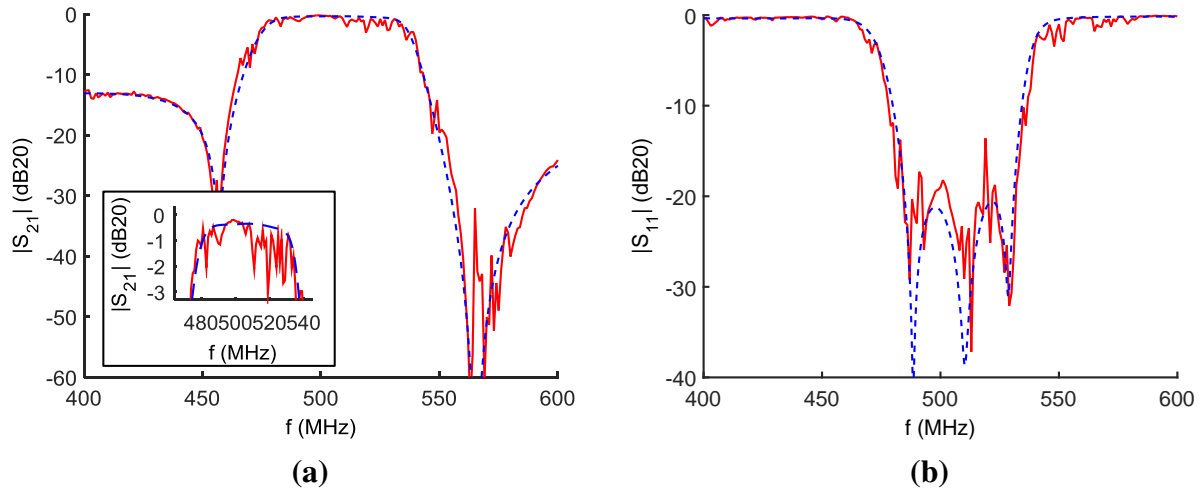


Figure 2.16: Simulated S-parameters of a full-ladder filter consisting of one T-section with shunt trimmer capacitor, simulated with MBVD (blue dash) and COMSOL-simulated (red solid) resonators, and an ideal shunt capacitor. The capacitor $C_p = 140$ fF, and the MBVD parameters are in Table 2.1. The inset in (a) shows some ripple due to spurs in the resonators, but the passband as designed is smooth.

2.4 Fabrication and measurement

The filters were fabricated in LN and measured. The resonators are oriented at 60 degrees to the $+z$ axis on an x -cut LN film nominally $1 \mu\text{m}$ thick. The electrodes, made of Al, are 100 nm thick. The LN was bonded to the sacrificial material, SiO_2 , which sits atop a handle wafer of high-resistivity Si. The fabrication process is described in more detail in Chapter 3 of the Ph.D. dissertation [19] by L. Shi, who developed the fabrication process for the samples presented in this section. The microscope image of the filter is shown in Figure 2.17.

The resonators are spaced such that their etch pits do not coincide; this reduces the likelihood of mechanical coupling between neighboring devices, which may cause splitting of the resonator peaks (as seen in simulation in Chapter 4).

The design of the capacitors contrasts with the design of the resonators. The capacitor should not have any resonances, so its fingers are staggered (at 1.5 and 4.5 μm gaps) and oriented per-

2. ADAPTING EXISTING RESONATOR FILTERS TO HIGH K_T^2

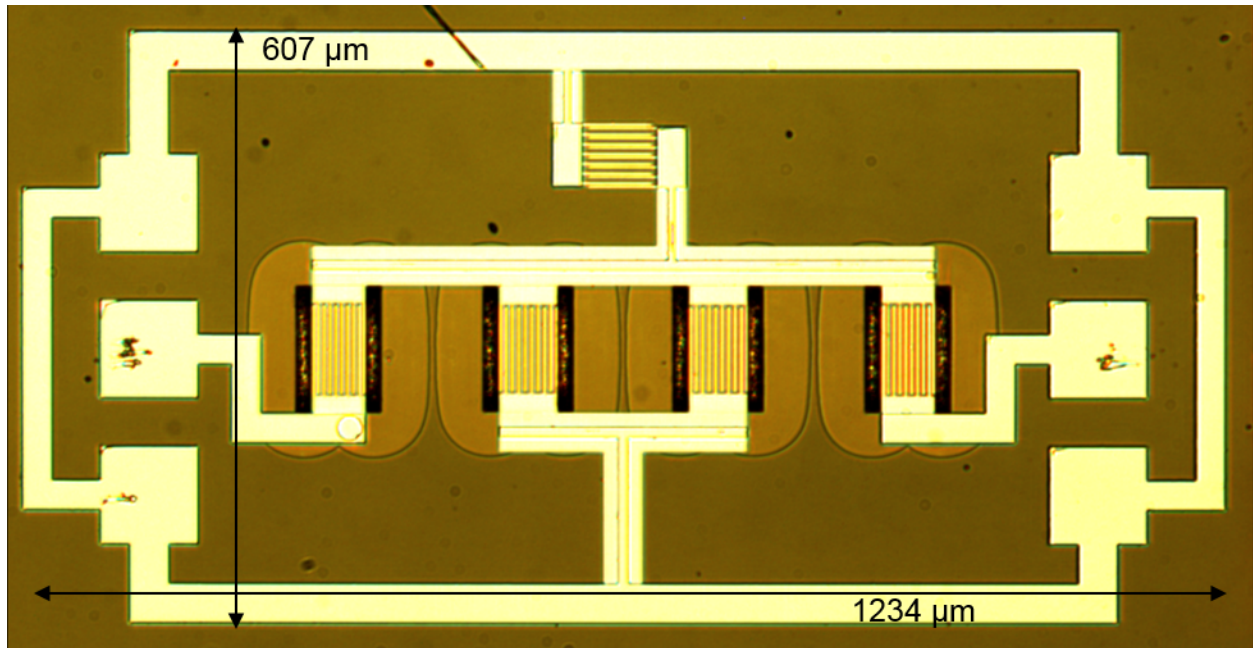


Figure 2.17: Microscope image of the 1-T full ladder filter as fabricated, including a laser-trimmable capacitor C_p (staggered interdigitated electrodes near the top of the layout) to mitigate uncertainty in K_t^2 .

pendicular to the resonators to minimize electromechanical coupling. The staggered spacing also facilitates laser-cutting only one pair of fingers at a time, which allows small steps in increasing the shunt $K_{t,p}^2$.

The measured S-parameters of the filter, without deembedding, are shown in Figure 2.18. The frequency of the filter is at 474 MHz instead of the designed 500 MHz because of underetch (discussed in Chapter 5 by Equation (5.1)). The insertion loss in the middle of the passband is about 2.7 dB (a close-up view of the passband is shown in Figure 2.19). The ripple is due to fluctuations in the resonator responses, to be discussed in the next section. The fractional bandwidth is about 9.1 percent, which is lower than the predicted 12.5% because of the reduced K_t^2 of the series resonator as illustrated in Figure 2.14. The 20 dB shape factor is about 1.5. The out-of-band rejection exceeds 10 dB excluding spurious passbands (with the spurious passbands, the OBR is about 5.5 dB).

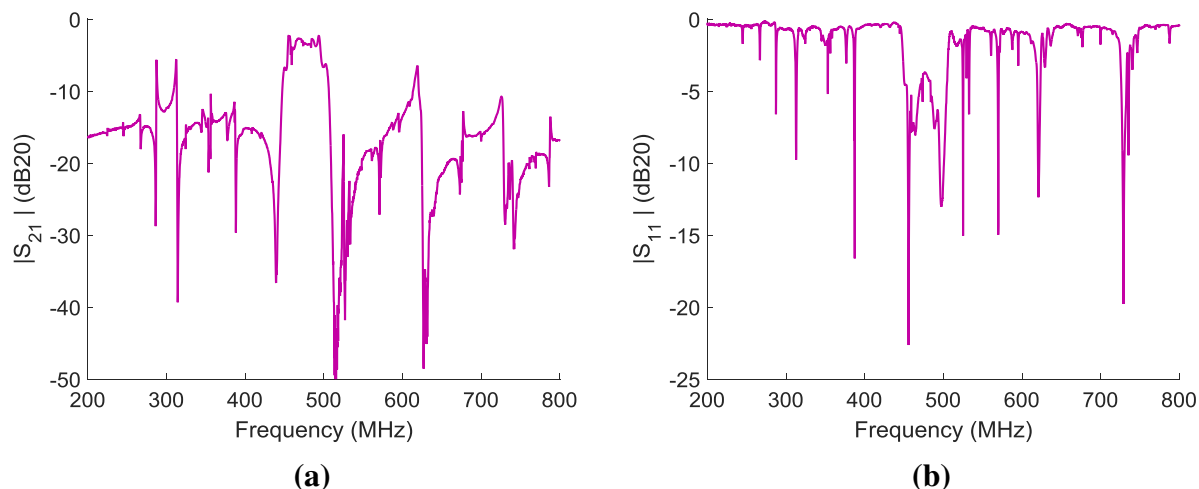


Figure 2.18: Measured S-parameters for a 1-T ladder filter with trimmable capacitor intact, and no deembedding. The frequency of the filter is at 474 MHz instead of the designed 500 MHz. The insertion loss in the middle of the passband is about 2.7 dB. The fractional bandwidth is about 9.1 percent. The out-of-band rejection is at least 5.5 dB, but would be greater than 10 dB if it were not for the spurious passbands.

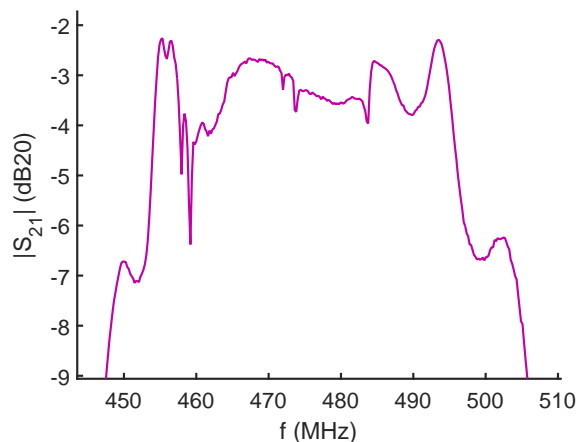


Figure 2.19: Close-up of passband of measured $|S_{21}|$ for a 1-T ladder filter with trimmable capacitor intact, and no deembedding. The whole frequency sweep is shown in Figure 2.18.

2.5 Matching simulation and measurement

To explain the filter performance, progressively detailed models are fitted to the measurement to get a progressively accurate match.

2. ADAPTING EXISTING RESONATOR FILTERS TO HIGH K_T^2

2.5.1 Standalone resonators and capacitor

The measured performance of the components of the filter can provide model parameters to feed into the filter equations. There are standalone resonators and capacitors on the same die as the filter. The shunt resonator and capacitor were located about a millimeter away from their corresponding components in the filter, and the standalone series resonator was about 3.5 mm away. (There had been closer standalone series resonators in the layout, but they had been damaged and were unmeasurable).

The measured admittances for the standalone resonators are shown in Figure 2.20 for the shunt resonator, along with the fitted MBVD models. The fitted MBVD parameters are shown in Table 2.2. The measurements are done using two probes (configured as a two-port), so the through admittance between the pads is deembedded. For the series resonator, the series resonance $f_{s,s} = 478.5$ MHz and the antiresonance $f_{p,s} \approx 516$ MHz (the approximation is because of a spur in the middle of the antiresonance). For the shunt resonator, the series resonance $f_{s,p} = 440.7$ MHz and the antiresonance $f_{p,p} = 490.7$ MHz. The images of the standalone resonators are shown in Figure 2.21.

Table 2.2: MBVD model parameters for the series and shunt resonators obtained by fitting to measurement, which is plotted in Figure 2.20. In the filter as implemented, two of the shunt resonators are used in parallel, so the total C_{0p} is 2×96.5 fF = 193 fF

	Series	Shunt
f_s (MHz)	478.28	440.70
C_0 (fF)	108.9	96.5
K_t^2 (%)	20.5	28.9
Q	1000	1000
R_s (Ω)	55.6	49.7
R_0 (Ω)	197	260

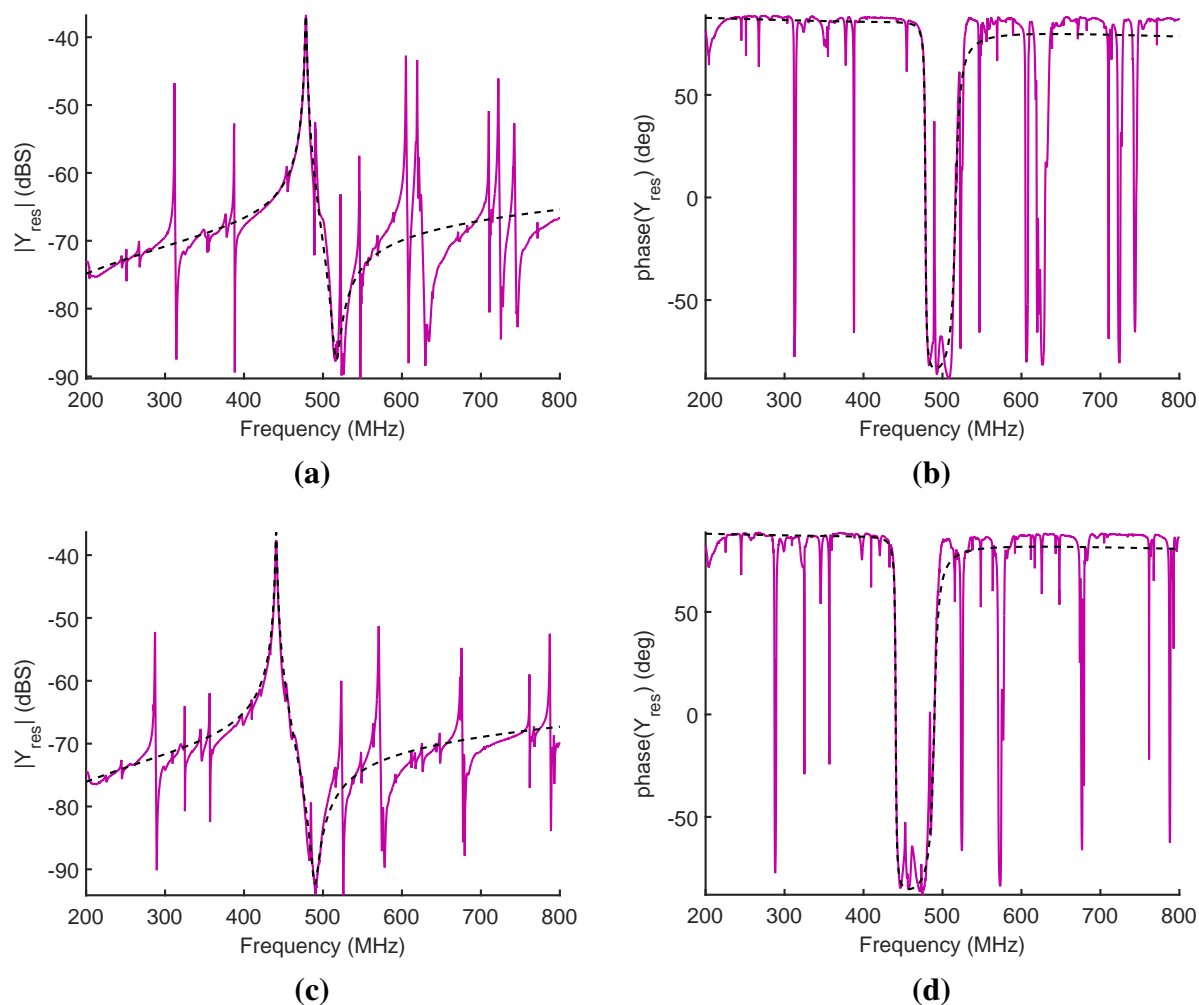


Figure 2.20: Measured admittance plots for standalone (a)-(b) series and (c)-(d) shunt resonators, with pad-to-pad feedthrough deembedded. The fitted MBVD models are plotted in dashed black; the parameters are in Table 2.2. For the series resonator, the series resonance $f_{s,s} = 478.5$ MHz and the antiresonance $f_{p,s} \approx 516$ MHz (the approximation being due to the spur in the middle of the antiresonance). For the shunt resonator, the series resonance $f_{s,p} = 440.7$ MHz and the antiresonance $f_{p,p} = 490.7$ MHz.

The capacitor measurements (also with pad through-admittance deembedded) are shown in Figure 2.22, plotted on a log scale in the x axis. The magnitude increases linearly (as one would expect from $Y_{cap} = j\omega C$ behavior). The phase is relatively flat, with a value of approximately 83 degrees. Compared to the ideal phase of 90 degrees, this corresponds to a series resistance of

2. ADAPTING EXISTING RESONATOR FILTERS TO HIGH K_T^2

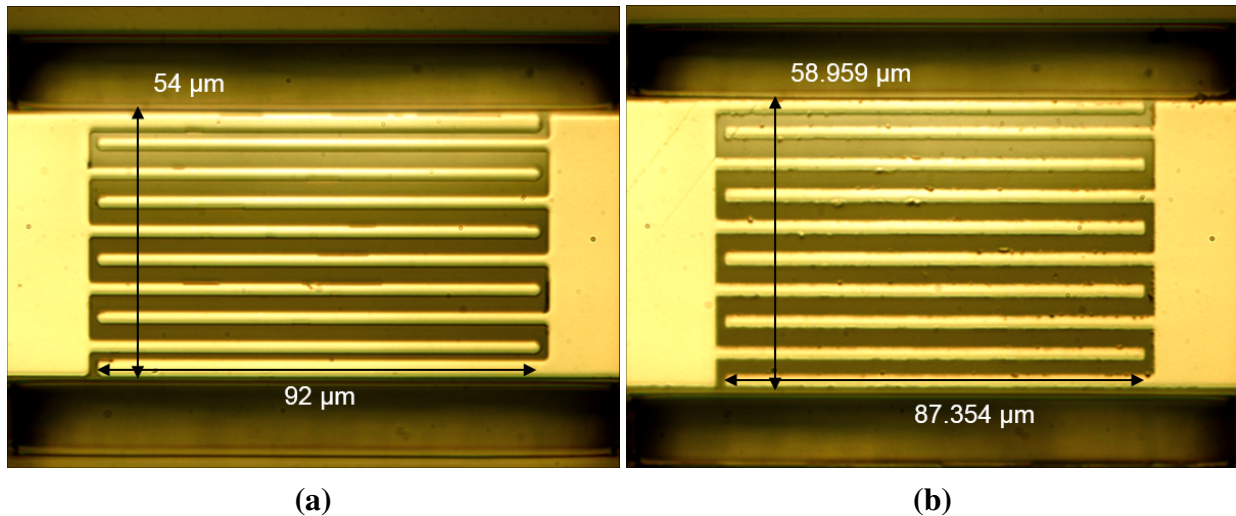


Figure 2.21: Microscope images ($50\times$ magnification) of the standalone (a) series and (b) shunt resonators corresponding to those used in the fabricated ladder filter. The shunt resonator is larger than the series resonator because of the wider electrode pitch ($6\ \mu\text{m}$ for the series; $6.551\ \mu\text{m}$ for the shunt), which defines a lower resonance frequency. The reflector finger designs are different by design in order to avoid a spur in the antiresonance of the shunt resonator; the fingers on the series resonator are $2\ \mu\text{m}$ wide for the inside fingers and $3\ \mu\text{m}$ wide for the outside fingers, while for the shunt resonator all fingers are $2.18\ \mu\text{m}$ wide.

approximately $250\ \Omega$ (whereas the reactance due to the capacitance is approximately $2100\ \Omega$). At the approximate band center of $475\ \text{MHz}$, the extracted capacitance is about $C = \frac{Y_{cap}}{j\omega} = 160\ \text{fF}$.

A microscope image of the standalone capacitor is shown in Figure 2.23. None of the interdigitated fingers have been laser trimmed in this photograph.

A filter simulation using the MBVD model and extracted capacitance is shown in Figure 2.24. The simulation defines the frequency-location of the transmission zeros fairly well (the “notches” – transmission zeros – in the $|S_{21}|$ plot are well matched), and the out-of-band rejection appears to match the measurement where the measurement is smooth. The passband, however, is quite inaccurately modeled; the simulation is too optimistic in computing the insertion loss (*i.e.*, the $|S_{21}|$ is too high and the $|S_{11}|$ too low in the passband). This indicates that the impedance matching is not as good in measurement as in the model, which could be caused by parasitic capacitance that has not been included in this model.

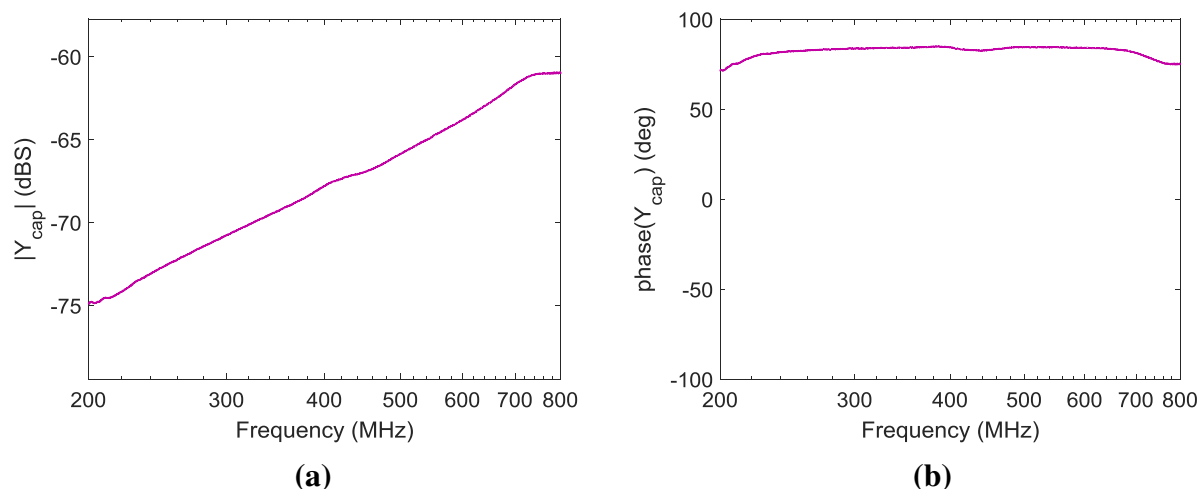


Figure 2.22: Admittance of standalone capacitor with staggered $1.5 \mu\text{m}/4.5 \mu\text{m}$ spaced fingers. Note the log x -axis. The extracted capacitance at 475 MHz is about 160 fF.

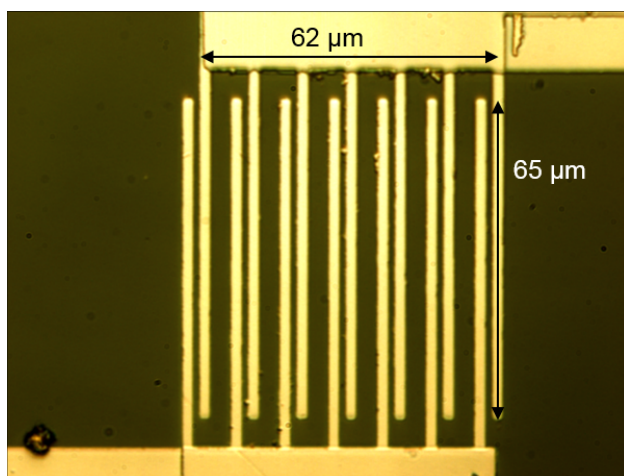


Figure 2.23: Microscope image (50 \times magnification) of the standalone capacitor used in the 1-T filter. The admittance plots for this device are shown in Figure 2.22. The gaps between the fingers are $1.5 \mu\text{m}$ and $4.5 \mu\text{m}$, while each finger is $2 \mu\text{m}$ wide and $71 \mu\text{m}$ long with $65 \mu\text{m}$ overlap.

2.5.2 Adding parasitic capacitance

This discrepancy in the passband can be addressed by adding more components, namely modeling the role of parasitic capacitance. A schematic with the parasitic capacitance is shown in Figure 2.25. There are two shunt elements at the input and output, one shunt element in the middle

2. ADAPTING EXISTING RESONATOR FILTERS TO HIGH K_T^2

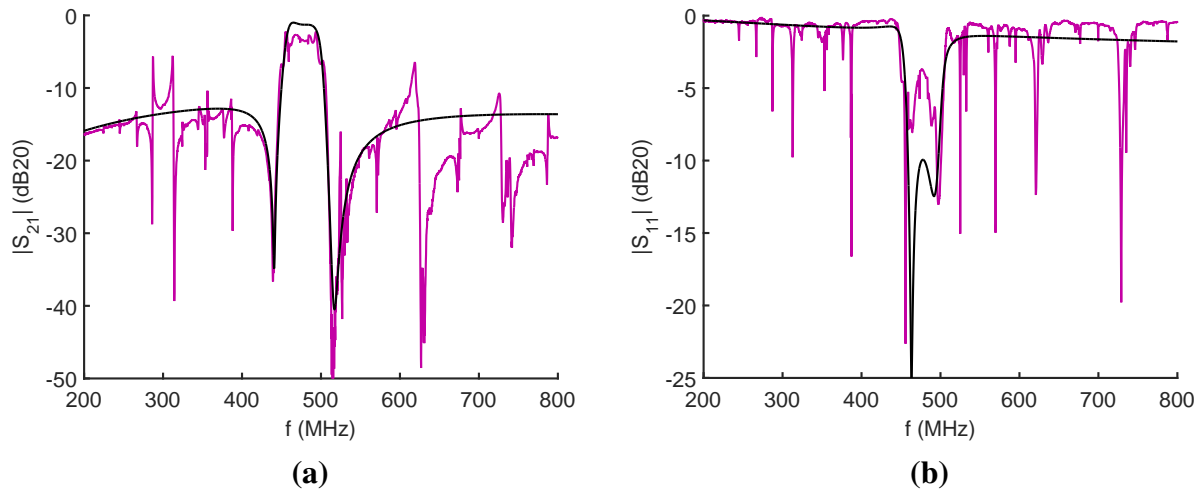


Figure 2.24: Comparison of measured (magenta) and simulated (black) S-parameters. The simulated response takes the fitted MBVD parameters (Table 2.2) and the extracted C_p of 160 fF.

node, and a feedthrough element.

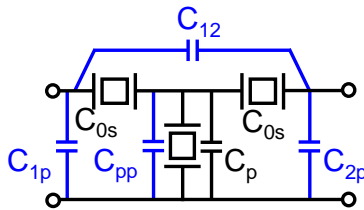


Figure 2.25: Schematic for 1-T full ladder as fabricated, with parasitic capacitances added.

2.5.2.1 Extraction of C_{1p} , C_{2p} , and C_{12} embedding capacitances

The models of C_{1p} , C_{2p} , and C_{12} can be extracted from the deembedding structure placed next to the filter. The structure is an “open”, which can be modeled as a Π -network of C_{1p} , C_{2p} , and C_{12} . The filter deembedding structure is shown in a microscope image in Figure 2.26.

The T-shaped ground trace in the middle of the structure is included in order to include its effect on feedthrough capacitance C_{12} . (The structure is somewhat liberal in the signal lines on the

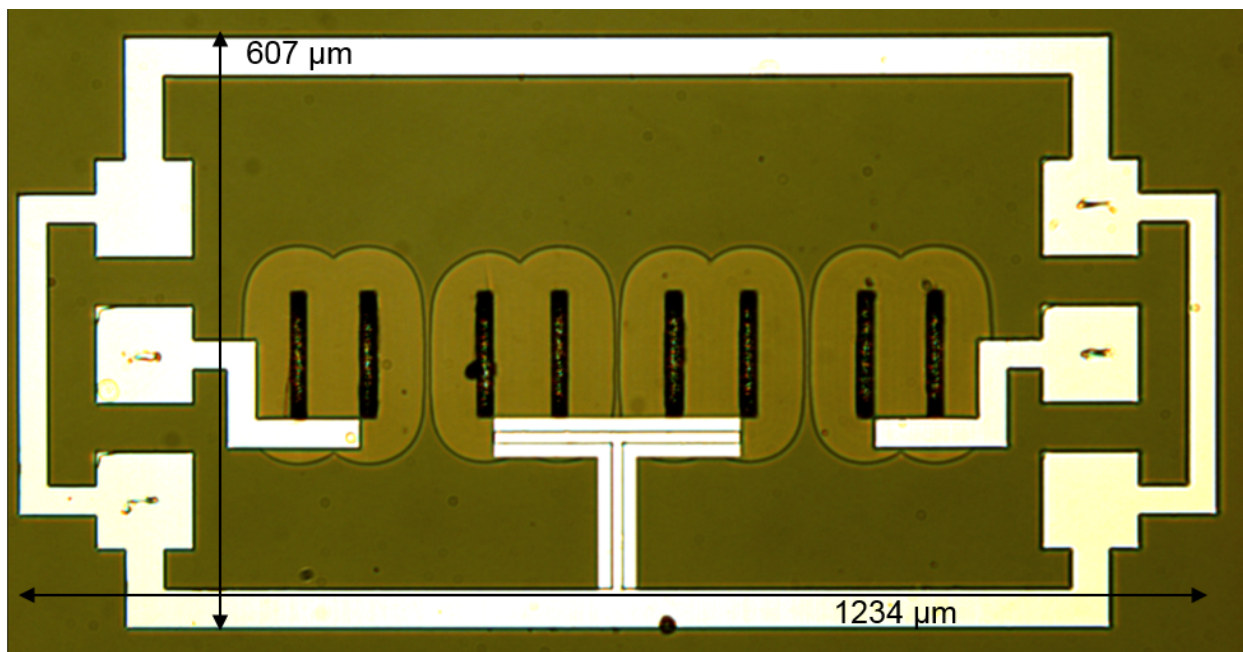


Figure 2.26: Microscope image of open deembedding structure for 1-T full ladder filter.

right and left extend to abut the resonator; that segment increases the capacitance estimate slightly). Also, without the interdigitated electrodes obscuring the view, the de-embedding structure shows that the resonators released cleanly during fabrication.

The capacitance can be extracted from the admittances of the Π network. These are plotted in Figure 2.27, Figure 2.28, and Figure 2.29, for Y_{C12} , Y_{p1} , and Y_{p2} , respectively, on a log-frequency scale.

It is clear that there is very little feedthrough between the two ports; the magnitude of Y_{C12} is several times less than the magnitude of the resonators at antiresonance. (This is consistent with the excellent deep notches in the measured filter $|S_{21}|$, Figure 2.18). Thus, $C_{12} = 0$ in the model. Y_{p1} and Y_{p2} behave as capacitors from the signal terminal to ground for each port, as seen from the approximately straight-line magnitude response and 90 degree constant phase. The capacitances can be extracted at the operating frequency (approximately 475 MHz) as $C_{p1} = \frac{Y_{p1}}{j\omega} = 32$ fF and $C_{p2} = \frac{Y_{p2}}{j\omega} = 33$ fF.

2. ADAPTING EXISTING RESONATOR FILTERS TO HIGH K_T^2

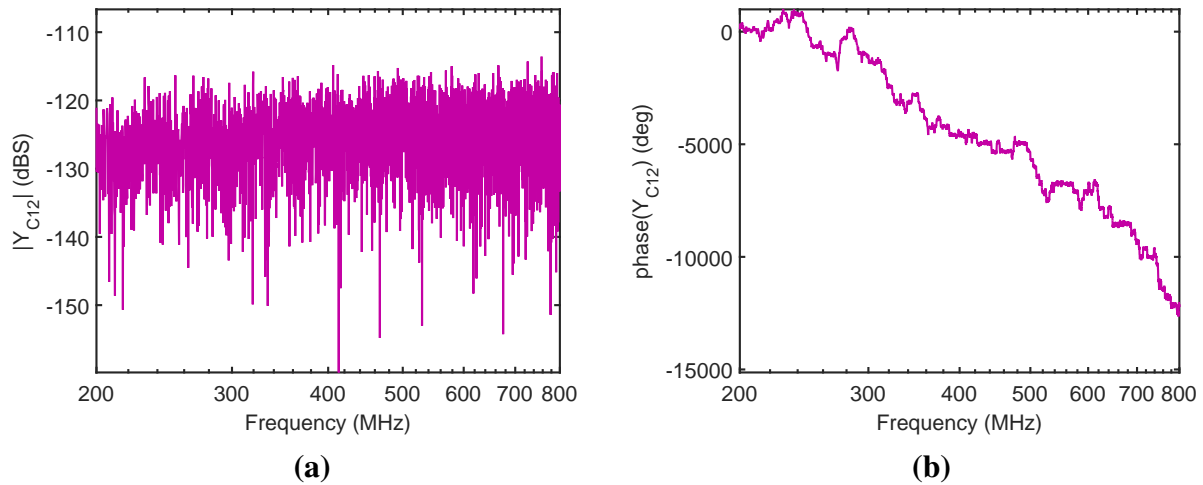


Figure 2.27: Measured admittance plots for the feedthrough element Y_{C12} of the Π network from Figure 2.25, (a) admittance magnitude, (b) admittance phase.

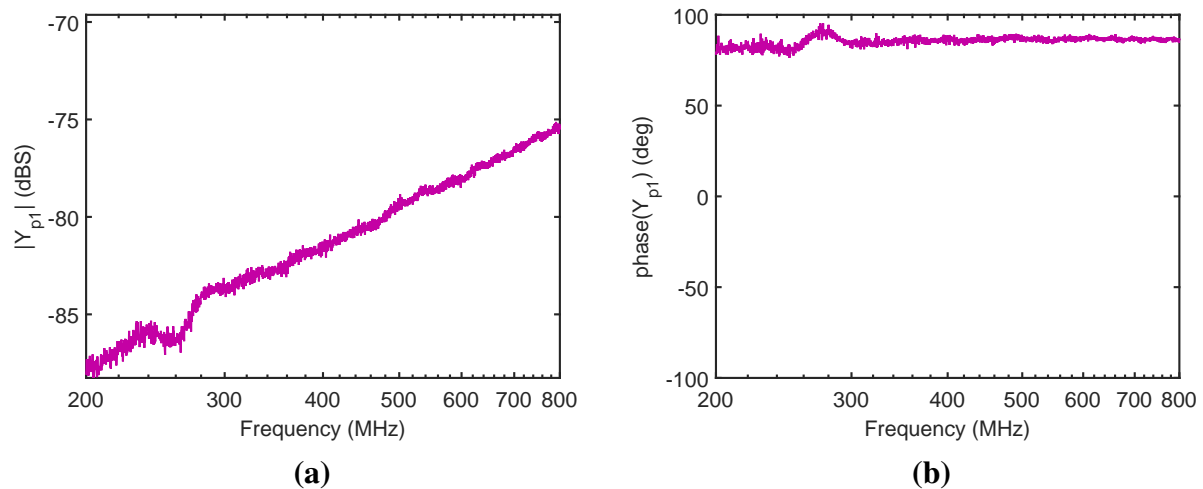


Figure 2.28: Measured admittance plots for the shunt element Y_{p1} of the Π network from Figure 2.25, (a) admittance magnitude, (b) admittance phase.

Comparing the simulated and measured responses (setting $C_{pp} = 0$) shows the effect of the embedding parasitics. This is plotted in Figure 2.30. The simulation is now a lot closer to measurement (compared to Figure 2.24, which does not include parasitic capacitances at all). There is still some discrepancy, which can be addressed by estimating and including C_{pp} in the filter simulation.

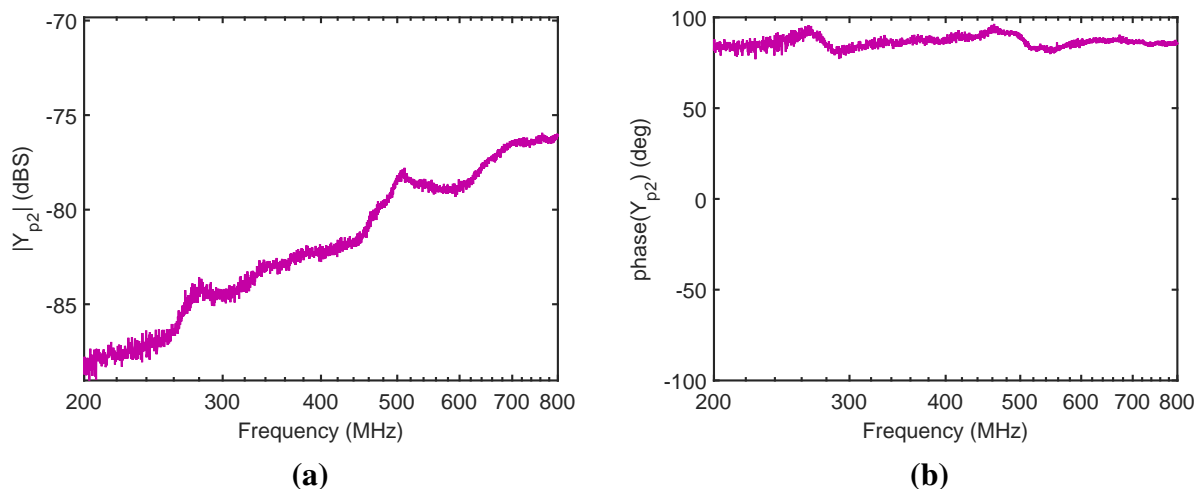


Figure 2.29: Measured admittance plots for the shunt element Y_{p2} of the Π network from Figure 2.25, (a) admittance magnitude, (b) admittance phase.

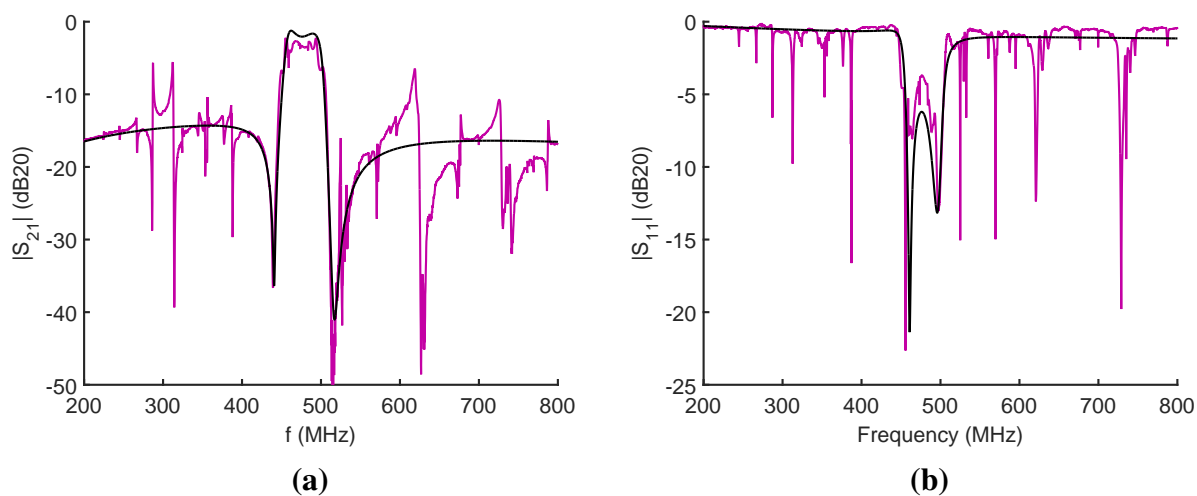


Figure 2.30: Comparison of measured (magenta) and simulated (black) S-parameters with embedding parasitic capacitance added. The simulated response corresponds to the schematic in Figure 2.25 and takes the fitted MBVD parameters (Table 2.2) and the extracted $C_p = 160$ fF, $C_{p1} = 32$ fF, $C_{p2} = 33$ fF, and $C_{12} = 0$. $C_{pp} = 0$ here; the purpose of this comparison is to illustrate how much closer the simulation vs. measurement becomes when including the embedding parasitics.

2. ADAPTING EXISTING RESONATOR FILTERS TO HIGH K_T^2

2.5.2.2 Estimating and including C_{pp} in filter simulation

The value of C_{pp} can be estimated from a 2D simulation in COMSOL Multiphysics (with all materials included) to estimate the capacitance between routing traces at various gaps. The gaps are labeled on the filter microscope image in Figure 2.31. $G_1 = 118 \mu\text{m}$, $G_2 = 180 \mu\text{m}$, and $G_3 = 61.5 \mu\text{m}$. The lengths of overlap (neglecting fringing fields) are approximately $6 \mu\text{m}$, $247 \mu\text{m}$, and $61.5 \mu\text{m}$, respectively. The 2D simulation estimates the capacitances to be approximately 0.3 fF, 12.6 fF, and 2.0 fF, respectively; these add in parallel to form the total capacitance of half the filter as 14.9 fF. This value is doubled for the whole filter to get $C_{pp} = 29.8 \text{ fF}$.

This value is likely an underestimate because of the neglected fringing, not to mention that the actual material permittivity is possibly higher than in the COMSOL material model – for example, the capacitance in Table 2.1 (COMSOL simulated resonator MBVD parameters) is about 15% lower than the capacitance in Table 2.2 (measured resonator MBVD parameters).

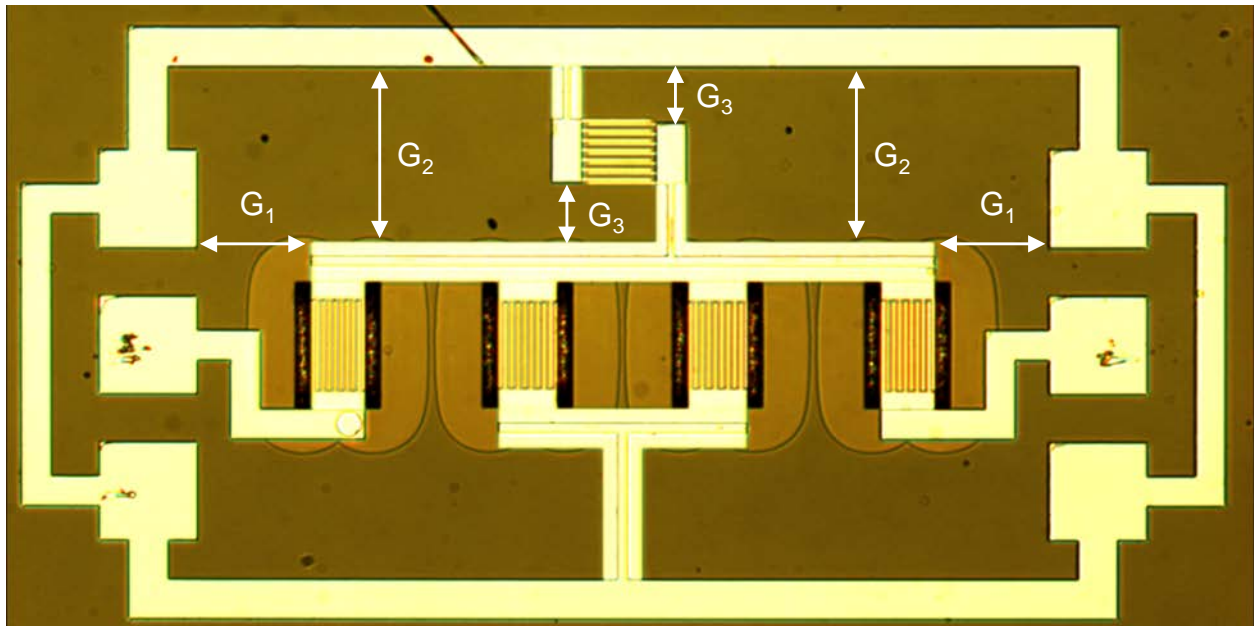


Figure 2.31: Microscope image of 1-T filter, labeled with gaps corresponding to parasitic capacitance C_{pp} to ground. $G_1 = 118 \mu\text{m}$, $G_2 = 180 \mu\text{m}$, and $G_3 = 61.5 \mu\text{m}$. The lengths of overlap are approximately $6 \mu\text{m}$, $247 \mu\text{m}$, and $61.5 \mu\text{m}$, respectively.

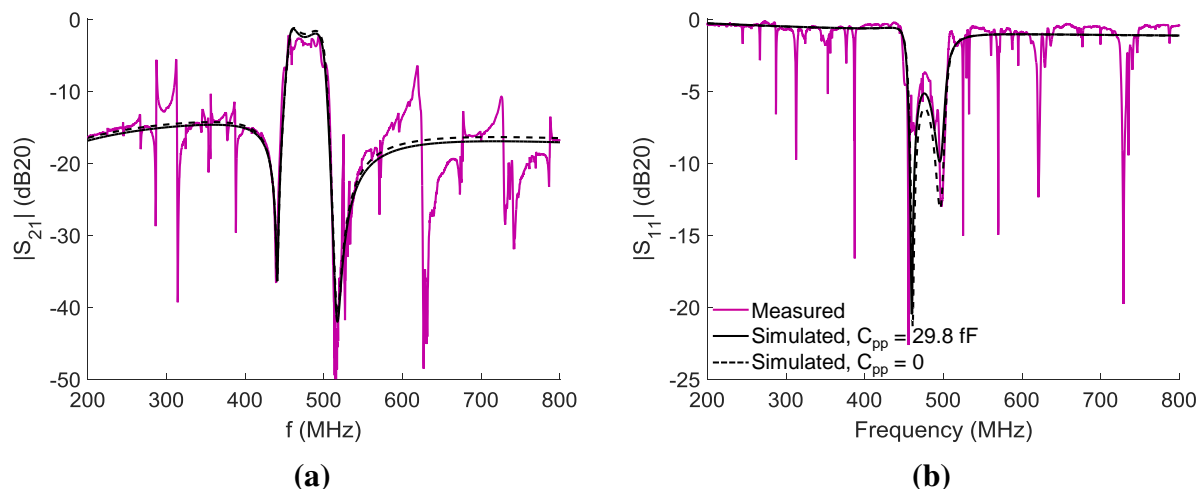


Figure 2.32: Comparison of measured (magenta) and simulated (black) S-parameters with embedding parasitic capacitance added. The simulated response corresponds to the schematic in Figure 2.25 and takes the fitted MBVD parameters (Table 2.2) and the extracted $C_p = 160$ fF, $C_{p1} = 32$ fF, $C_{p2} = 33$ fF, and $C_{12} = 0$. **Black solid:** $C_{pp} = 29.8$ fF as estimated from COMSOL 2D simulations. **Black dashed:** $C_{pp} = 0$, identical to the trace in Figure 2.30. The addition of C_{pp} better models the $|S_{11}|$.

Figure 2.32 shows the simulation of the filter with parasitic capacitances $C_{p1} = 32$ fF, $C_{p2} = 33$ fF, $C_{12} = 0$, and $C_{pp} = 29.8$ fF in the solid black trace. It compares favorably with the measurement (magenta trace), advancing the model from the $C_{pp} = 0$ case from before (dashed trace). With $C_{pp} = 0$ (dashed trace), the difference between simulated and measured $|S_{11}|$ is about 2.5 dB at 475 MHz (the middle of the band), whereas with $C_{pp} = 29.8$ fF (solid black trace), the difference between simulated and measured $|S_{11}|$ becomes 1.4 dB. The discrepancy between measurement and simulation would shrink even further with a more accurate estimate of C_{pp} , for example if fringing in the electric fields or inaccuracy in the simulated dielectric constants for the parasitic capacitance were taken into account.

2. ADAPTING EXISTING RESONATOR FILTERS TO HIGH K_T^2

2.5.3 Filter simulation constructed with measured resonator and capacitor data (not models)

The measurements of the three components (series resonator, shunt resonator, and capacitor) can be inserted into the simulation for the filter and compared to the measured filter response. (This differs from the simulations in the previous section, which had used the MBVD model for the resonator and ideal capacitor for the capacitances). The simulation using the measurements of the standalone devices (dubbed the “constructed” response) is shown in Figure 2.33, where the black trace is the constructed response. Parasitic capacitances are included as ideal capacitances, with $C_{p1} = 32$ fF, $C_{p2} = 33$ fF, $C_{12} = 0$, and $C_{pp} = 29.8$ fF (the same values as in the previous section).

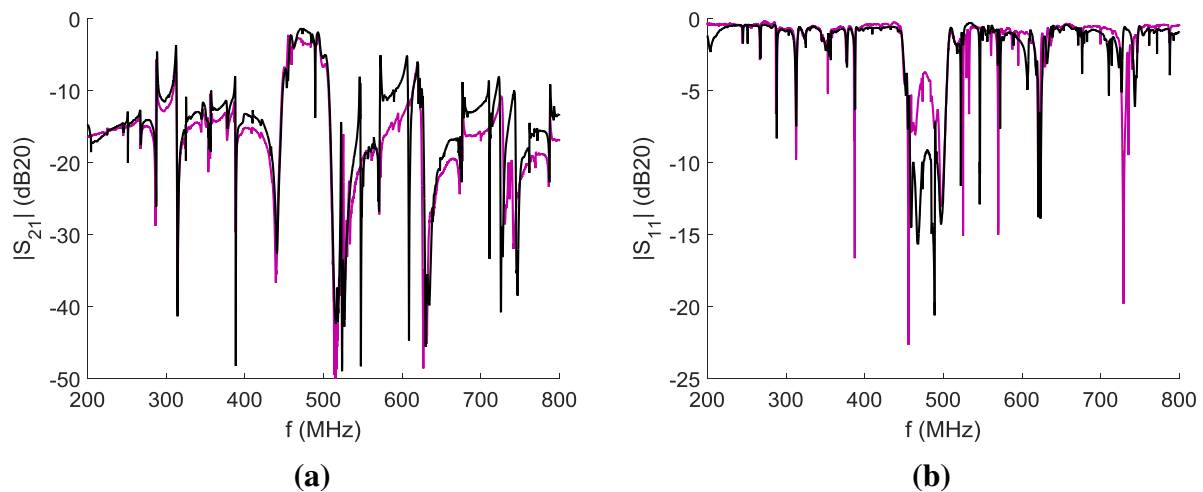


Figure 2.33: Constructing S-parameter response by inserting measurements of standalone resonators and capacitors into circuit simulation. Parasitic capacitances (illustrated in Figure 2.25) are included as ideal capacitors, with $C_{p1} = 32$ fF, $C_{p2} = 33$ fF, $C_{12} = 0$, and $C_{pp} = 29.8$ fF. Black: constructed; magenta: filter measurement.

As shown in Figure 2.33, there is now very close correspondence in the “shape” of the simulated and measured S-parameters. The constructed response captures the spurious passbands and sharp ripples present in the measurement.

These features originate from the spurs in the resonators (and to a far lesser extent, the capacitor C_p). Figure 2.34 compares the simulations using MBVD (and ideal C_p) against measured resonator and capacitor responses. Only the resonators and C_p are different; all else is equal. The sharp ripples appear only in the constructed response. This comparison isolates resonator spurs (which the MBVD model fails to capture; see Figure 2.20) as their cause.

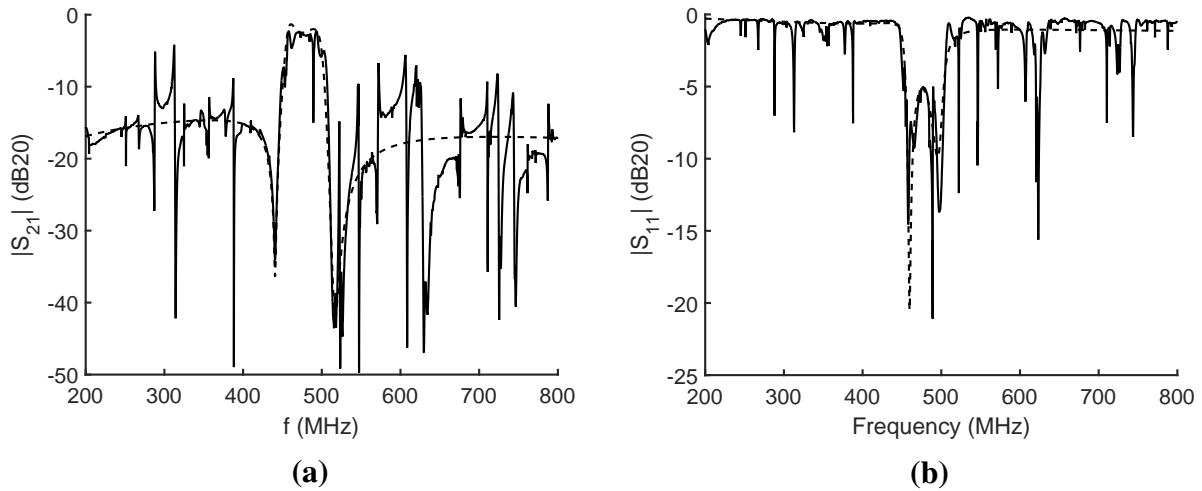


Figure 2.34: Comparison of simulating 1-T full ladder filter using (**dashed**) MBVD and ideal capacitor models vs. using (**solid**) measurements from the standalone devices, both with ideal parasitic capacitances included. Parasitic capacitances (illustrated in Figure 2.25) are included as ideal capacitors, with $C_{p1} = 32$ fF, $C_{p2} = 33$ fF, $C_{12} = 0$, and $C_{pp} = 29.8$ fF.

Also note that there are no “shoulders” in the simulated response using MBVD models, indicating that the topology is not to blame for the small hiccups seen in the rolloff of the measured and constructed responses. These filter fluctuations are due to “spurs” or fluctuations due to modal coupling in the resonators.

2.6 Discussion and conclusions

The initial filter measurements are quite encouraging: they demonstrate a high fractional bandwidth (9.1%) and good insertion loss (about 2.7 dB). To the author’s knowledge, this is the best

2. ADAPTING EXISTING RESONATOR FILTERS TO HIGH K_T^2

fractional bandwidth achieved using S0-mode microresonators to date (though SH0 mode resonator filters have been demonstrated with even higher FBW of over 40% and with peak insertion loss of 0.8 dB [15], also in LN). The results were also consistent across multiple chips; in all four chips of the fabrication run, the IL was within 5 dB at midband and the frequency definition very consistent (within about 2%). The data for the other chips are plotted in Appendix D. This demonstrates that LN microresonators can achieve competent baseline performance.

The results presented in this chapter can be improved in several ways. First, tuning should be demonstrated in a microresonator filter. Tuning is an important requisite for the ultimate vision of a reconfigurable filter bank. Tuning is considered in Chapter 3, with a notch filter as a demonstration platform.

Second, the termination impedance of the filter can be lowered. The filter as measured has a termination impedance of about 2500 Ω . One way is to use through-field excitation devices (where there is a bottom electrode and the electric fields penetrate predominantly in the out-of-plane direction), which have higher capacitance densities. If that is not available (which was the case at the time of this publication) then multiple resonators can be arrayed in parallel to increase their aggregate size (thus lowering the termination impedance in Equation (2.3)). With arrays, it is important to avoid mechanical coupling and mismatch between resonators, which may introduce fluctuations near resonance that increase ripple in the passband. This is addressed in Chapter 4.

Third, the performance of the measured filter response could be improved by reducing the spurious passbands in the stopband of the filter. For example, the measured out-of-band rejection is, strictly speaking, only about 5.5 dB (instead of the designed 10 dB) because of the spurious passbands. These are caused by spurs in the resonators. Chapter 5 studies the causes of the various types of spurs in individual resonators, and endeavors to eliminate the out-of-band spurs while simultaneously increasing the resonator K_T^2 by improving the alignment and etch accuracy.

Chapter 3

Varactor tuning of filters

3.1 Introduction

This chapter is motivated by a desire to maximize the bandwidth and tuning range of the resonator filters. Doing so increases the filter coverage, and thereby reduces the size and complexity of filter banks composed of tunable filters.

The bandwidth and tuning range are limited by the K_t^2 of the resonators [20],[16]. Tuning methods for bandpass filters have employed bandwidth trimming with variable capacitors (varactors), steering a narrow passband within a large envelope passband to achieve frequency tuning [9], where the envelope becomes larger with increasing K_t^2 .

In the main part of this chapter, varactor tuning is applied to a notch filter. A tunable notch filter can provide reconfiguration to filter banks by blocking interfering signals at a particular (tunable) frequency while passing the remaining band with minimal loss. The tunability confers frequency agility against changes in the interferer frequency.

The tuning range turns out to be limited by the K_t^2 as well as the spurs in the resonators. This chapter proposes a way to offload the K_t^2 limit from the resonators to the external circuit. The spurs

3. VARACTOR TUNING OF FILTERS

will be addressed in Chapter 4 and Chapter 5.

The chapter begins with a review of the tuning of single resonators using varactors, along with an overview of how to apply the technique to bandpass filters, with a contribution being an analysis and mitigation of parasitic capacitance due to bondpads. Then, an overview the design of an absorptive notch filter is presented, along with measured results from an example using LN resonators wirebonded to external components. Tuning is added to the notch filter, for which a sample was fabricated and measured. The results demonstrate that impedance mismatch limits tuning range. A method to address the impedance mismatch is proposed, in order to increase the tuning range. Resonator fluctuations or spurs are shown to make the tuning range in the measurement discontinuous.

3.2 Tuning single resonators and bandpass filter example

This section is an overview of how to tune individual resonators using varactors. The scope of this section covers attaching one varactor, though it is certainly possible to use two or more varactors [9]. As an example, varactor tuning of resonators is applied to the full ladder filter presented in the previous chapter.

The MBVD model for the resonator provides a tractable model to perform analysis. (The MBVD model is reviewed in Appendix A.3 and illustrated in Figure 3.1).

The MBVD model alone has a resonance at

$$f_s = \frac{1}{2\pi\sqrt{L_m C_m}} \quad (3.1)$$

3.2 Tuning single resonators and bandpass filter example

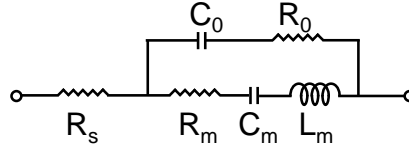


Figure 3.1: Schematic of MBVD model of resonator.

and an antiresonance approximately at

$$f_p = \frac{1}{2\pi\sqrt{L_m\frac{C_m C_0}{C_m + C_0}}}, \quad (3.2)$$

which can be thought of as the effect of resonating L_m with the series combination of C_m and C_0 .

Combining the resonator in series with a varactor (modeled as C_{var} , an ideal capacitor with adjustable capacitance) adjusts the resonance as approximately

$$f_s = \frac{1}{2\pi\sqrt{L_m C_m \frac{C_0 + C_{var}}{C_m + C_0 + C_{var}}}} = f_{s0} \sqrt{1 + \frac{8}{\pi^2} K_t^2 \frac{C_0}{C_0 + C_{var}}} \quad (3.3)$$

where $f_{s0} = \frac{1}{2\pi\sqrt{L_m C_m}}$ is the resonance frequency before adding the varactor. Equation (3.3) is most accurate for high Q resonators¹. As C_{var} decreases in value, f_s increases (thus moving the resonance closer to the antiresonance). The antiresonance stays at the original frequency. This is illustrated in Figure 3.2, which plots the admittance of an MBVD model in series with an ideal varactor.

The magnitude of the resonance decreases as it is tuned toward the antiresonance. This is

¹With low Q , the frequency at which the phase is zero (which is calculated here) starts to differ from the frequency at which the magnitude is maximal.

3. VARACTOR TUNING OF FILTERS

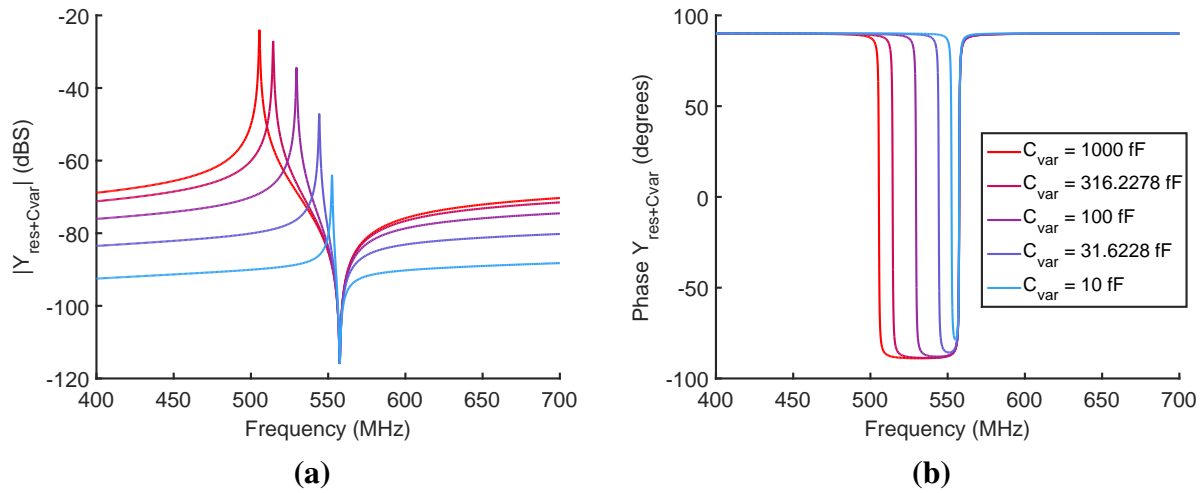


Figure 3.2: Series capacitor tuning of a single resonator, admittance magnitude and phase. The resonator parameters are $f_s = 500$ MHz, $K_t^2 = 0.30$, $C_0 = 100$ fF, $Q = 1000$, and $R_s = R_0 = 0$. The capacitor in series is varied between 10 fF and 1000 fF, or $C_0/10$ to $10C_0$. As the C_{var} decreases, the resonance frequency increases.

because of the series impedance of the varactor, which increases as the capacitance is decreasing (by $\frac{1}{j\omega C_{\text{var}}}$). (Note that this does *not* significantly change the Q of the resonance, assuming an ideal varactor). This admittance amplitude change will turn out to limit tuning range in the notch filter.

A complementary tuning method is to place the varactor in parallel to the resonator; this will move the antiresonance without moving the resonance. The intuition is to consider the varactor as adjusting the effective C_0 without changing the motional branch of the overall network. The antiresonance frequency is approximately

$$f_p = \frac{1}{2\pi\sqrt{L_m C_m \frac{C_0 + C_{\text{var}}}{C_m + C_0 + C_{\text{var}}}}} \quad (3.4)$$

where C_{var} is now the varactor in parallel to the resonator¹. The antiresonance moves toward the resonance as the parallel capacitance is increased. The magnitude of the antiresonance is increasing

¹The keen reader might notice that this is the same formula as Equation (3.3), but should keep in mind that the circuit topology is different; C_{var} is a varactor in *parallel* with the resonator.

3.2 Tuning single resonators and bandpass filter example

because the overall admittance is increasing due to the $j\omega C_{var}$ conducting path in parallel. This is illustrated in Figure 3.3, which plots the admittance of an MBVD model in parallel with an ideal varactor.

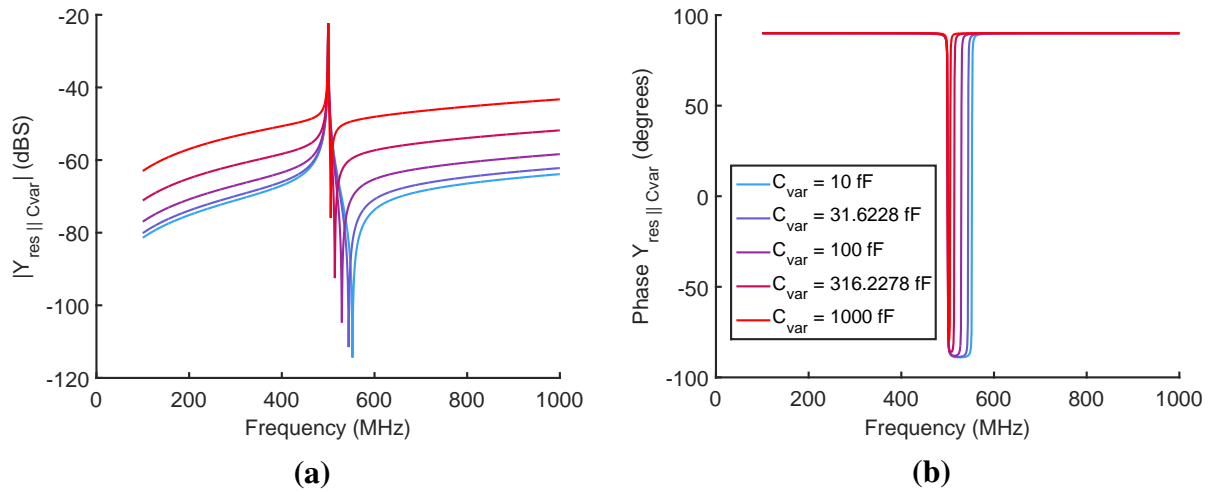


Figure 3.3: Parallel capacitor tuning of a single resonator, admittance magnitude and phase. The resonator parameters are $f_s = 500$ MHz, $K_t^2 = 0.30$, $C_0 = 100$ fF, $Q = 1000$, and $R_s = R_0 = 0$. The capacitor in parallel is varied between 10 fF and 1000 fF, or $C_0/10$ to $10C_0$. As the C_{var} increases, the antiresonance frequency decreases.

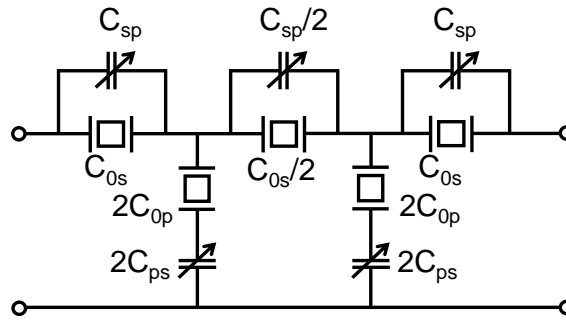


Figure 3.4: Schematic of tunable full ladder filter with varactor tuning. C_{sp} controls the antiresonance of the series resonators, thus controlling the right skirt of the filter. C_{ps} controls the resonance of the shunt resonators, thus controlling the left skirt of the filter.

As an example, the tuning methods can be applied to the ladder filter introduced in Chapter 2.

Figure 3.4 shows a full-ladder bandpass topology similar to Figure 2.8, but with a varactor to

3. VARACTOR TUNING OF FILTERS

tune each resonator. The series resonators have parallel varactors (C_{sp}) to tune their antiresonance (which controls the right skirt of the filter), while the shunt resonators (C_{ps}) to tune their resonance (which controls the left skirt of the filter). The scaling on the middle varactor ($C_{sp}/2$) matches the scaling of the middle resonator. The S-parameters of the filter as the varactors are tuned are shown in Figure 3.5.

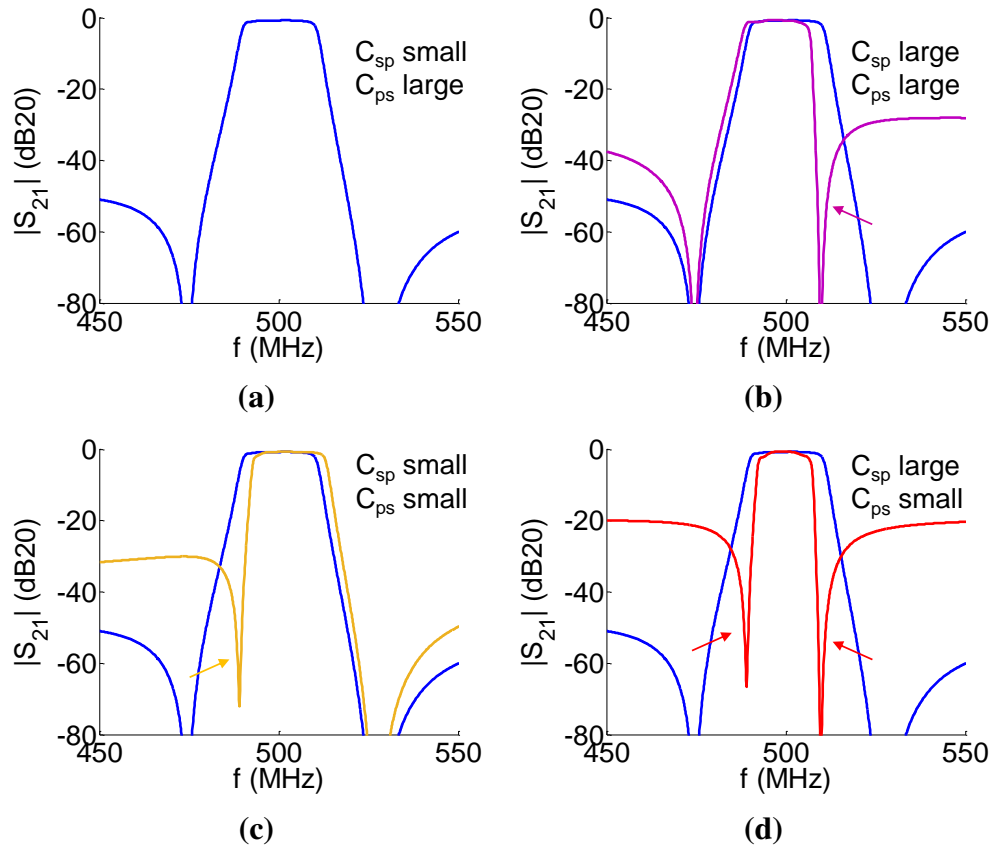


Figure 3.5: Simulated corner configurations for a tunable ladder filter, whose topology is shown in Figure 3.4. (a) Baseline case with small C_{sp} and large C_{ps} , with the skirts as wide as possible; (b) tuning the right skirt by increasing the C_{sp} (C_{ps} remains large); (c) tuning the left skirt by decreasing the C_{ps} (C_{sp} remains small); (d) tuning both skirts by increasing the C_{sp} and decreasing the C_{ps} . The baseline trace is shown in blue in all plots. The K_t^2 used in these simulations is 14.5%.

Figure 3.5 illustrates the tuning via skirt trimming. For the baseline configuration (Figure 3.5a), the smallest C_{sp} should be small relative to C_{0s} , and the largest C_{ps} should be large relative to C_{0p} ,

3.2 Tuning single resonators and bandpass filter example

in order to minimize their impact upon the baseline bandwidth. When C_{sp} increases, the series resonator antiresonance moves, thus moving the right skirt inward (Figure 3.5b). Likewise, when C_{ps} decreases, the shunt resonator resonance moves, thus moving the left skirt inward (Figure 3.5c). Both varactor types can be tuned at the same time to move both the right and left skirts (Figure 3.5d).

Trimming the skirts can tune the bandwidth and the center frequency of the filter. For example, Figure 3.5d shows the bandwidth being tuned while holding the center frequency constant, while Figure 3.5b and Figure 3.5c show the frequency being tuned while holding the bandwidth constant. A way to visualize these and the intermediate cases is a bandwidth-frequency diagram, which illustrates what configurations of filter bandwidth (expressed as fractional bandwidth, FBW) and center frequency (f_c) are possible for a topology. An example is shown in Figure 3.6. The topmost point corresponds to the baseline configuration shown in Figure 3.5a, the leftmost point to the right-skirt-only tuning (Figure 3.5b), the rightmost point to the left-skirt-only tuning (Figure 3.5c), and the bottommost point to tuning both skirts (Figure 3.5d).

The tuning space forms a diamond; the top edges of the diamond are a hard limit defined by the maximum bandwidth baseline (the skirts only move inward), while the bottom edges are limited by the filter specifications (typically out-of-band rejection – note how the OBR decreases as the skirts are tuned in Figure 3.5 because the varactors decrease the frequency selectivity of the system). The upper edges illustrate why K_t^2 is said to limit the tuning range. With increased K_t^2 , the baseline bandwidth (topmost point in the FBW- f_c diagram) increases (compare Figure 2.5 and Figure 2.6, for example). This provides more room for the skirts to be trimmed. The lower edges of the FBW- f_c diagram can be engineered lower by addressing the OBR and IL, which are the typical limiting metrics.

To achieve more coverage of the FBW- f_c space, the filters can be arrayed in a filter bank (as illustrated in the introduction, in Figure 1.1a) providing piecewise coverage. An example is shown

3. VARACTOR TUNING OF FILTERS

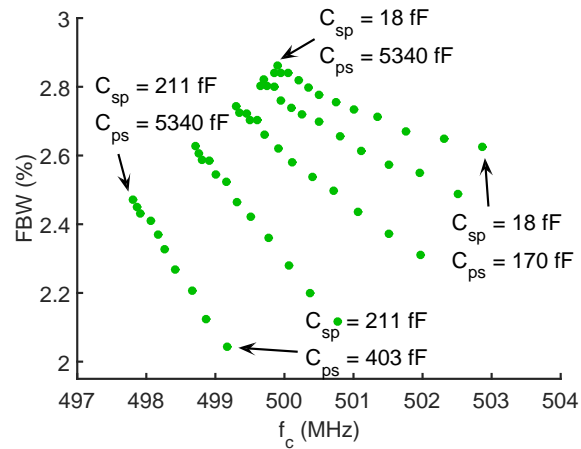


Figure 3.6: Simulated fractional bandwidth (FBW) vs. center frequency (f_c) plot for tunable full ladder filter. The FBW and f_c data are extracted from frequency responses similar to those shown in Figure 3.5. The tuning space forms a diamond; the top edges of the diamond are defined by the nature of the tuning, while the bottom edges are defined by the filter specifications (typically out-of-band rejection). The varactor capacitances are swept in log steps from 18 fF to 1335 fF for C_{sp} and from 72 fF to 5340 fF for C_{ps} . The capacitances are marked for the corners. The size of the series resonator in the filter simulation is $C_{0s} = 100$ fF and the size of the shunt resonator is $C_{0p} = 500$ fF. The K_l^2 used in these simulations is 10.5%.

in Figure 3.7 with two tunable bandpass filters. Here, there are two filters networked in parallel, with one filter centered at 495 MHz and one at 500 MHz. This array forms a piecewise coverage of the tuning space, where switching between filters provides coarse tuning while the varactors provide fine tuning within the diamond-shaped range of each filter. One could extend the concept to more filters for wider coverage.

3.2.1 Parasitic capacitance of varactors

A practical concern for varactor tuning is parasitic capacitance due to the bondpads, which cannot be made arbitrarily small. This imposes a constant capacitance to ground that must exist in all practical resonator-varactor combinations. (The specific value depends on the bondpad size as well as the a chosen varactor technology).

The parasitic capacitance is modeled as a shunt capacitance to ground, C_{pb} , on each terminal

3.2 Tuning single resonators and bandpass filter example

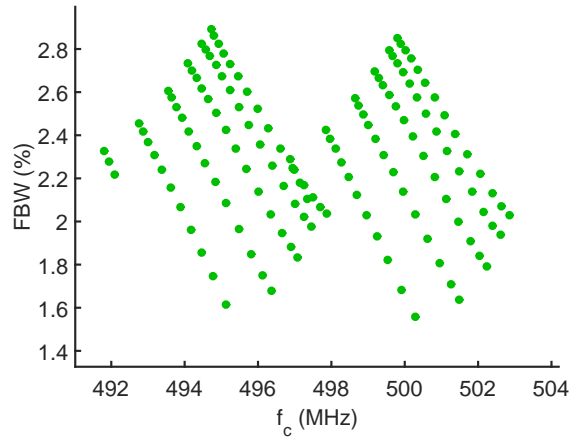


Figure 3.7: Simulated fractional bandwidth (FBW) vs. center frequency (f_c) plot for two tunable full ladder filters, one at 495 MHz and the other at 500 MHz, showing piecewise coverage of the tuning area. The K_t^2 used in these simulations was 10.5%.

of the varactor as shown in Figure 3.8. (The parasitic capacitance due to the resonator chip is neglected because of the use of high-resistivity substrates for the resonator chip substrate [19]). The sensitivity to parasitic capacitance depends on the filter topology. The ladder filter with parasitics is shown in Figure 3.9.

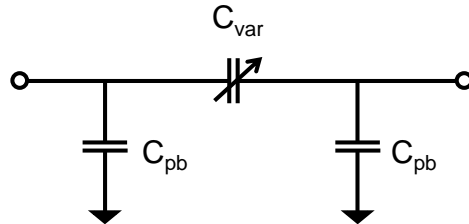


Figure 3.8: Model of parasitic capacitance of varactors.

For intuition about the impact of the parasitics on the bandpass filter, the parasitics can be categorized into three kinds of effects depending on the node location of the capacitance. The parasitic capacitance at the outer nodes will distort the passband by adding a shunt component to the input and output ports; this reduces the efficiency of the impedance match. The parasitic capacitance at the middle node (the two $N_s C_{pb}$) will reduce the effective $K_{t,p}^2$ of the shunt resonator-

3. VARACTOR TUNING OF FILTERS

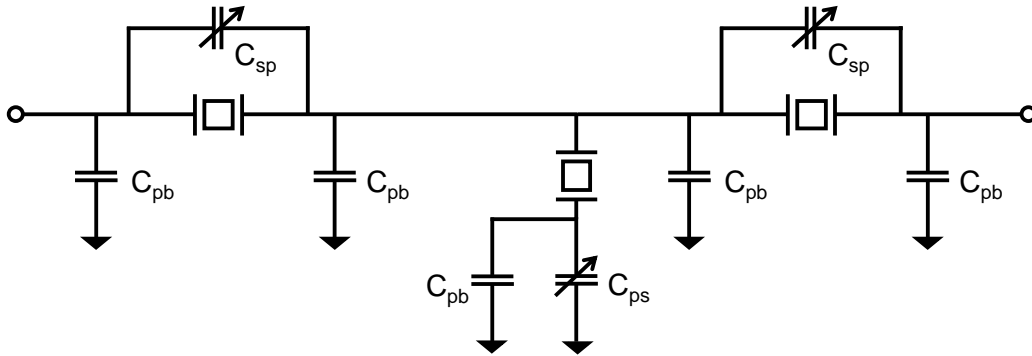


Figure 3.9: Model of a tunable bandpass ladder filter (one T-section) including parasitic capacitance due to bondpads when connecting the resonators to the varactors.

varactor combination by acting as an effective increase to C_{0p} , as with the trimmed-capacitor in Section 2.3. The parasitic capacitance associated with varactor C_{ps} (the varactor in series with the shunt resonator) will add in parallel with C_{ps} , resulting in a reduced the tuning range for that varactor.

Plotting filter frequency response can help visualize this intuition. It is assumed that the shunt capacitance in parallel with the C_{ps} varactor can be absorbed by the varactor (which is nominally large, about $10C_{0p}$ as a guideline), so only the parasitics connected to the series resonators remain. A simulation illustrating the effect of the parasitic capacitance is shown in Figure 3.10 with $C_{sp} = 0$ and $C_{ps} + C_{pb} \approx 10C_{0p}$. The results confirm the intuition above: the outer node parasitics cause impedance mismatch (dotted trace) while inner node parasitics causes a reduction in the effective $K_{t,p}^2$ as shown by the sag in the passband of the solid trace.

To compute the smallest C_0 (resonator size, here calculated as $\sqrt{C_{0s}C_{0p}}$) that can be achieved given bondpad capacitance, the C_0/C_{pb} (size of resonators relative to bondpad capacitance) is swept. The point at which the response will break specification dictates the limit on the smallest

3.2 Tuning single resonators and bandpass filter example

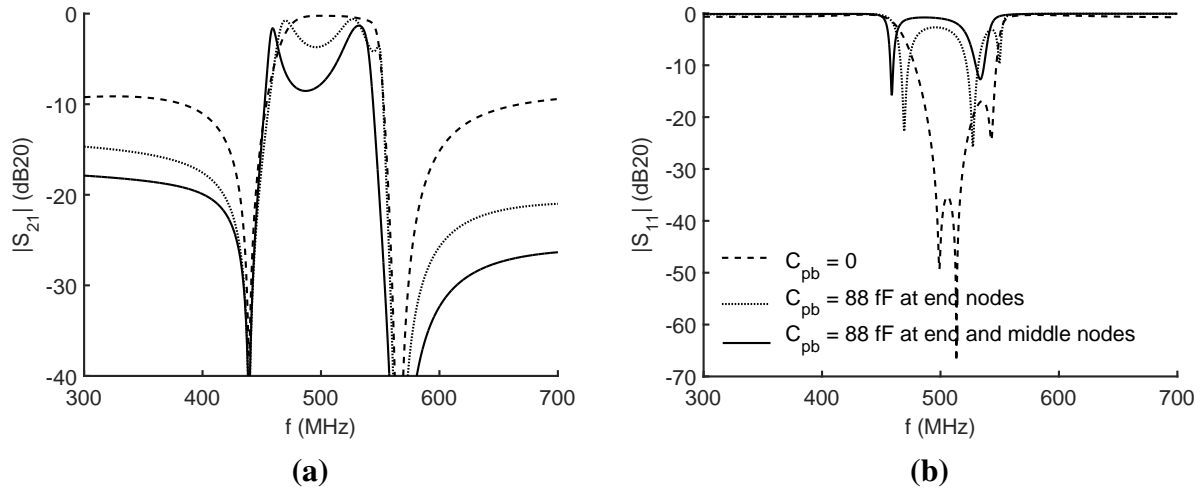


Figure 3.10: Simulation of 1T ladder filter showing the effect of parasitic shunt capacitance. Dashed: no parasitic capacitance; dotted: parasitic capacitance at the outer nodes only; solid: parasitic capacitance at both inner and outer nodes. In this simulation, $C_{pb} = 88$ fF, $C_{0s} = 95$ fF, and $2C_{0p} = 165.2$ fF. The MBVD model parameters are from Table 2.1 except with the f_s of the shunt resonator set to 434 MHz because of the removal of the trimming capacitor from that chapter.

C_0 for a given pad capacitance. This is illustrated in Figure 3.11, showing increasing passband sagging with decreasing resonator size. For a 0.5 dB ripple specification, this occurs when C_0/C_{pb} is approximately 5 to 6.67. As a numerical example, if the bondpad capacitance is 50 fF, then the resonators must have a C_0 of at least 250 fF to 330 fF. This value C_0 is equivalent to about three individual resonators in parallel (at about 100 fF each).

Mitigation of the parasitic capacitance is guided by the observation that the effective $K_{t,p}^2$ is being trimmed by the parasitic capacitance of the middle nodes. The parasitic capacitance can be compensated for by adjusting the frequency of the shunt resonator to align the shunt resonator-varactor-parasitic combination, using Equation (2.8). For example, if the size of the filter needs to be reduced so that there is one resonator (about 100 fF) matched to each bondpad (about 50 fF as an example), then the $K_{t,p}^2$ is scaled by $\frac{100 \text{ fF}}{100 \text{ fF} + 50 \text{ fF}}$. Increasing the shunt resonator frequency accordingly (and also reducing the termination impedance to adjust the impedance match for the

3. VARACTOR TUNING OF FILTERS

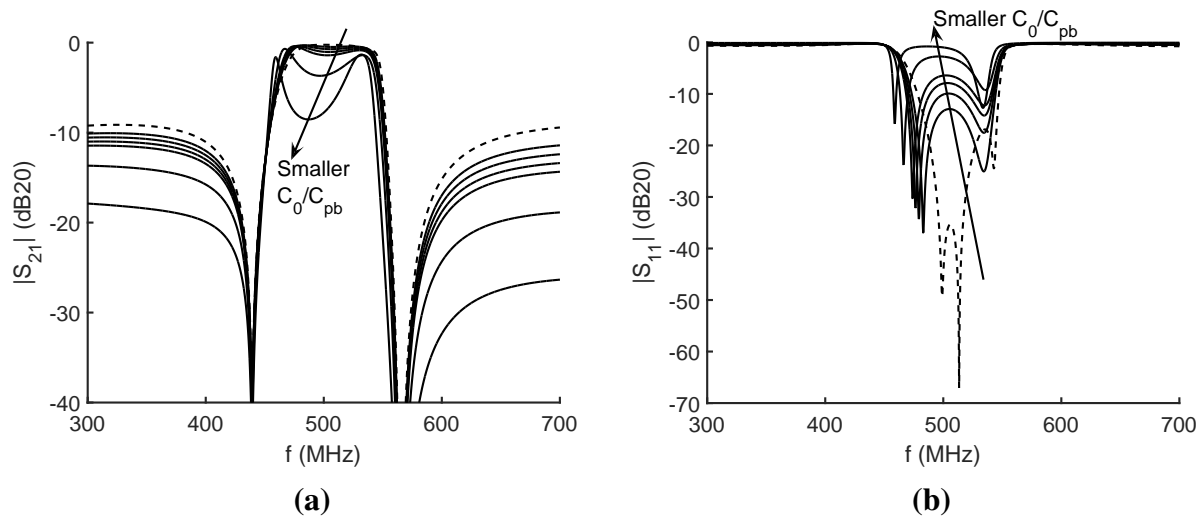


Figure 3.11: Simulation of 1T ladder with parasitic capacitance (at outer and inner nodes). Dashed: No parasitic capacitance, solid: parasitic capacitance $\sqrt{C_0 C_{0p}}/C_{pb} = \{1, 2, 4, 5, 6.67, 10\}$.

parasitic capacitance loading) results in the smoothed plot of Figure 3.12. With the cost of a reduction of fractional bandwidth from 16% to 12.9% (for this numerical example), it is possible to mitigate the ripple due to parasitic capacitance.

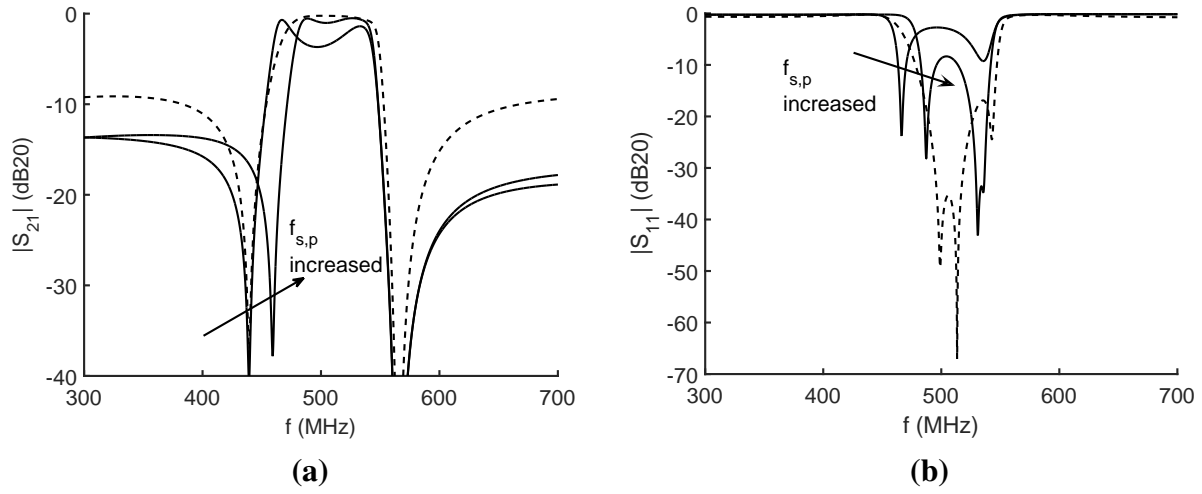


Figure 3.12: Simulation of 1T ladder filter with compensation of parasitic shunt capacitance by frequency-shifting the shunt resonator. Dashed: no parasitics, baseline design; solid, sagging: with parasitic capacitance $C_{pb} = 50$ fF and original $f_{s,p} = 434$ MHz; solid, narrower band: with parasitic capacitance $C_{pb} = 50$ fF and $f_{s,p} = 454$ MHz and termination impedance reduced by about 25% to accommodate the increased total shunt capacitance. In all cases, $C_{0s} = 95$ fF and $2C_{0p} = 165.2$ fF. The fractional bandwidth is about 16% for the no-parasitics case and 12.9% for the compensated case. The ripple is reduced to about 0.5 dB.

3.3 Absorptive notch filter design

The varactor tuning can extend to notch filters as well. Notch filters serve to block out specific channels of interference, a function that can augment the frequency selectivity of a filter bank. With tuning, a notch filter gains agility in selecting the channel to block. An eventual application could be the reconfiguration of the filter bank frequency response to insert notches into bandpass filters similar to the electromagnetic programmable filter array in [21].

This section presents the design of an absorptive notch filter (here without tuning, which will be added in the next section). There are two reasons for selecting an absorptive topology. The primary reason was that the Q of the first fabrication runs was low, leading to poor notch depth (the primary specification for notch filters) in reflective notch filters, whereas absorptive topologies can work around the low Q [22]. The other reason is that absorbing the incoming energy benefits the

3. VARACTOR TUNING OF FILTERS

receiver because it eliminates the energy reflected back to the source.

The topology, introduced by Jachowski [23], consists of two branches in parallel, illustrated in Figure 3.13. There is a transmission line branch and a bandpass filter branch. In the stopband of the bandpass branch, the signal passes only through the transmission line branch, thus forming the passband of the overall notch filter. In the passband of the bandpass branch, the signal is divided between the two branches, but with a 180 degree phase difference, thus cancelling each other out and forming a notch or stopband in the overall notch filter.

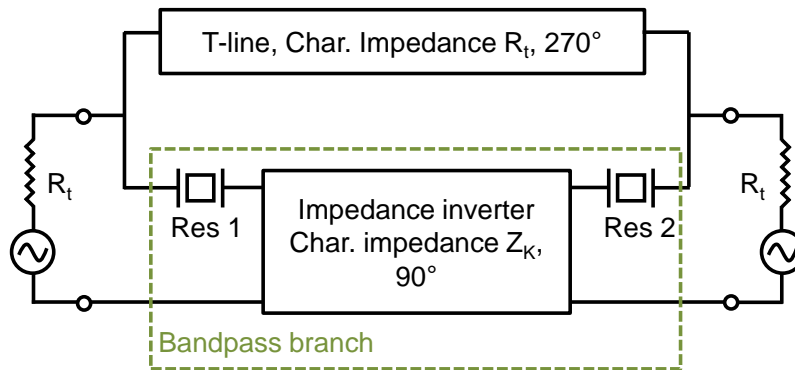


Figure 3.13: Absorptive notch filter topology with generic coupling and transmission line. The main changes from [23] are that the resonators are coupled directly, and they are series resonators.

The transmission line branch is characterized by its phase (270 degrees in its S_{21}) and its characteristic impedance R_t . The bandpass branch, consisting of two resonators coupled by an impedance inverter, is characterized by the resonator impedances or admittances, as well as the characteristic impedance of the inverter, Z_k . (The topology has been modified to use series resonators rather than the original parallel RLC resonances in [23], because for the microresonators, it is the series resonance, not antiresonance, that is directly defined by the lithography. Additionally, the coupling to the resonators has been removed such that the coupling to the resonators is

3.3 Absorptive notch filter design

direct, which is easier to lay out on the printed circuit board when implementing the circuit. This subtracts a 180 degree phase from the original passband branch, leading to the transmission line phase of 270 degrees instead of the original 90 degrees. These two modifications are not strictly necessary, but they make the realization of the filter more practical.)

The design of the filter begins by characterizing the resonators, because the filter (being absorptive) is designed around the resonator losses. In the fabricated LN die, there are resonators routed with bondpads (larger than RF probe pads) from which two are chosen. The microscope images of the resonators are shown in Figure 3.14. Their measurements and their fitted MBVD models are shown in Figure 3.15 and Figure 3.16. The fitted MBVD model parameters for the two resonators are listed in Table 3.1, showing good matching of the resonance frequency.

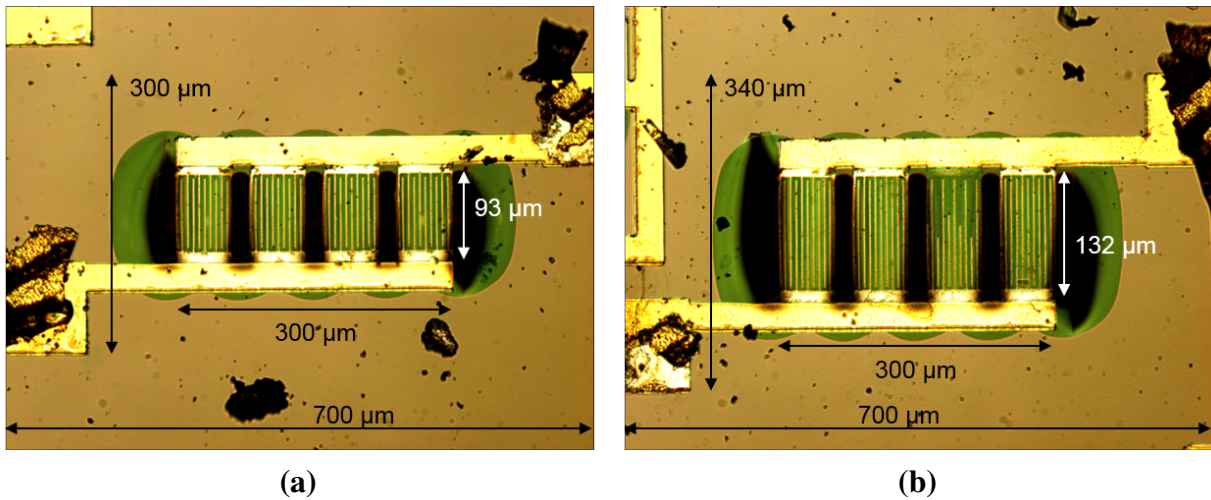


Figure 3.14: Microscope images of the resonators used in the absorptive notch filter; (a) Resonator 1, (b) Resonator 2. The missing fingers from the third sub-resonator in Resonator 2 reduces the total electrical size of Resonator 1. This is why the two resonators have similar frequency responses despite one resonator being physically larger than the other. The total size measured from the lower left pad corner to the upper right pad corner is $700\ \mu\text{m} \times 300\ \mu\text{m}$ for Resonator 1 and $700\ \mu\text{m} \times 340\ \mu\text{m}$ for Resonator 2.

The notch frequency f_n occurs where the net phase of the two resonators is zero. The termination (R_t) and inverter characteristic impedance (Z_K) are determined by $|Y_1|$ and $|Y_2|$, the admittance magnitudes of the resonators at the notch frequency.

3. VARACTOR TUNING OF FILTERS

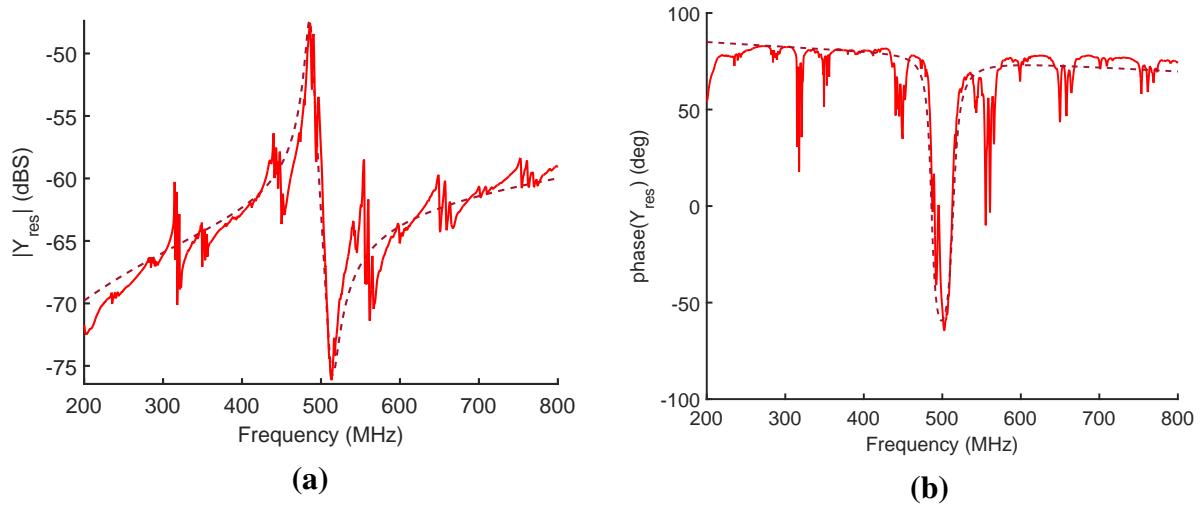


Figure 3.15: Admittance magnitude and phase for the “Resonator 1” used in the tunable absorptive notch filter. Solid: measurement, dashed: fitted MBVD model.

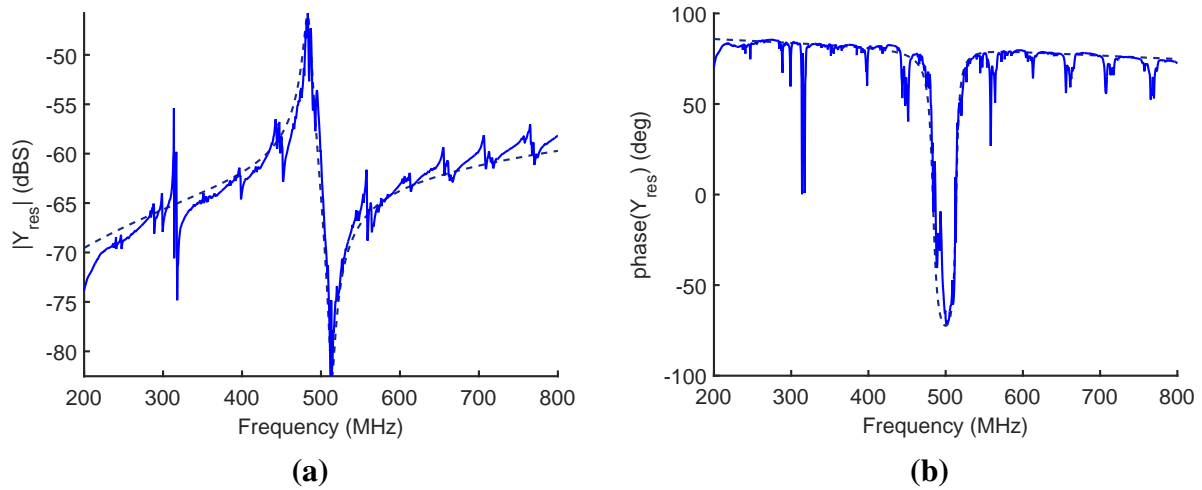


Figure 3.16: Admittance magnitude and phase for the “Resonator 2” used in the tunable absorptive notch filter. Solid: measurement, dashed: fitted MBVD model.

$$R_t = 2Z_K = \frac{2}{\sqrt{|Y_1||Y_2|}_{f=f_n}} \quad (3.5)$$

For matched resonators, the notch occurs at the resonance, and $|Y_1| = |Y_2| \approx (R_m + R_s)^{-1}$. The C_0 has been neglected for the design of the R_t and Z_k , because its impedance is typically greater

Table 3.1: Parameters for MBVD models fitted to measurement of the two resonators used in the tunable absorptive notch filter.

	f_s (MHz)	K_t^2 (%)	Q	C_0 (fF)	R_0 (Ω)	R_s (Ω)	R_m (Ω)	C_m (fF)	L_m (μ H)
Res 1	486	14.5	100	227	200	115	127	25.8	4.16
Res 2	483	16.0	220	230	150	88	50	29.8	3.64

than $10R_m$ at resonance; this is from a high K_t^2 , which increases the $C_m : C_0$ ratio.

One way to implement the transmission line and impedance inverter is with lumped elements arranged in Π -sections with the negative capacitance implemented as an inductor. This is illustrated in Figure 3.17. The choice of Π -sections instead of T-sections in the impedance inverter is because Π -sections use fewer inductors. This is because C_0 can *not* be neglected due to its placement in the MBVD model. Without a C_0 , the resonance would be a pure series RLC resonance, and the inverter could be a T-inverter with negative capacitances being absorbed into C_m in series [13], and there would be no inductors. But because of the C_0 , the negative capacitances cannot be absorbed, and would instead be approximated by inductances in the branches of the T-sections, meaning two inductors for the inverter. To reduce the inductor count to one, the T-inverter is converted to a Π -inverter.

The design equations relating component values to impedances can be derived in a similar manner to the image technique in Section 2.2.3. The equations to satisfy the image impedance and phase are

$$C_{inv} = 2/(2\pi f_n R_t) \quad (3.6)$$

$$L_{inv} = R_t/(4\pi f_n) \quad (3.7)$$

$$C_{line} = 1/(2\pi f_n R_t) \quad (3.8)$$

$$L_{line} = R_t/(2\pi f_n). \quad (3.9)$$

3. VARACTOR TUNING OF FILTERS

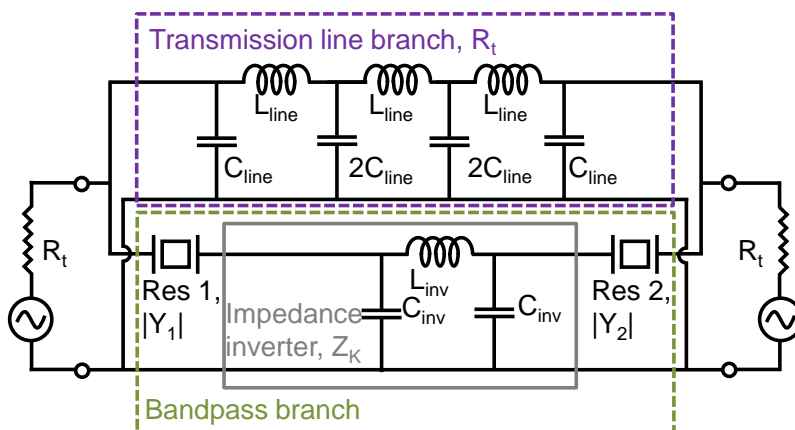


Figure 3.17: Absorptive notch filter topology with lumped-element coupling and transmission line.

This topology will favor integrated circuit implementations (smaller inductors) as the resonator performance ($K_t^2 Q$ figure-of-merit) improves because the inductances required decrease with better resonator $K_t^2 Q$. This is because $|Y_1|$ and $|Y_2|$ at resonance, used in Equation (3.5), are inversely proportional to the $K_t^2 Q$ product. Hence R_t (and therefore L_{inv} and L_{line}) will decrease as the $K_t^2 Q$ increases.

Assuming perfect matching, using the MBVD values for Resonator 1 for both resonators in the filter and Equation (3.5)-(3.9), the filter is designed with $C_{inv} = 1.35$ pF, $L_{inv} = 79.3$ nH, $C_{line} = 676$ fF, and $L_{line} = 159$ nH. S-parameters from an ideal circuit simulation using these design parameters are shown in Figure 3.18.

The simulated notch depth is 64 dB at 486.8 MHz, corresponding to a 40 dB return loss due to absorption. The 3 dB fractional bandwidth is 3.7% and the 10 dB fractional bandwidth is 1.2%. These become narrower with increasing resonator Q [23] (Figure 3.19), which justifies the choice of LN resonators instead of integrated CMOS LC. While the Q of CMOS LC tanks is typically about 50 to 100, corresponding to wide notches (about 2-4% 3 dB fractional bandwidth), the Q of the LN resonators (after refinements in materials and processing) has the potential to reach the

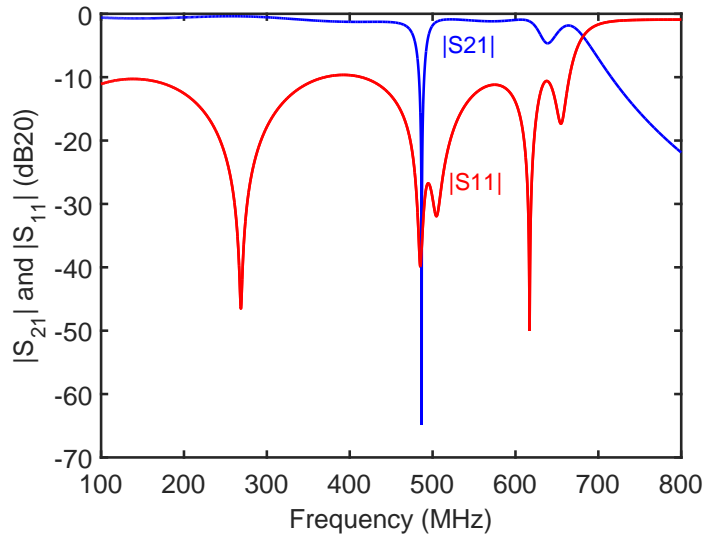


Figure 3.18: Simulated S-parameters of an ideal absorptive notch filter using matched MBVD models. Blue: $|S_{21}|$, red: $|S_{11}|$.

thousands [24], thus providing a path to improve the steepness of the notch (to less than 0.2% 3 dB fractional bandwidth).

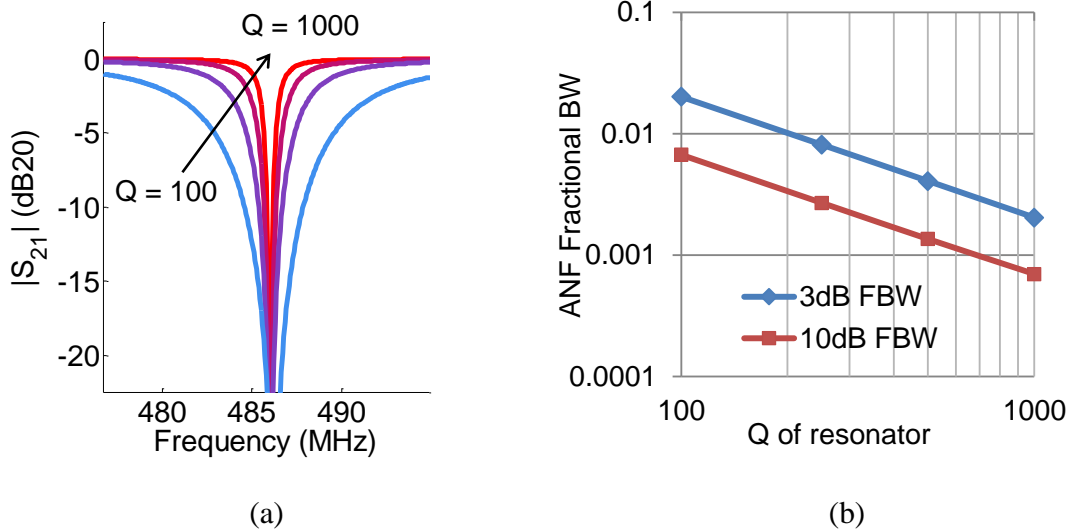


Figure 3.19: Effect of resonator Q upon filter. (a) Close-up plots of notch for Q ranging from 100 to 1000. (b) Filter fractional bandwidth (3 dB and 10 dB) as a function of resonator Q .

3. VARACTOR TUNING OF FILTERS

3.4 Fabrication and measurement of a fixed absorptive notch filter

The circuit was assembled on an FR-4 PCB by wirebonding the resonators to the PCB and soldering discrete inductors and capacitors. The vias (connecting the front and back side of the board) are implemented by tying a thin wire into a knot between the double holes and wicking solder through. To account for mismatch, the termination impedance is calculated using Equation (3.5) with *both* MBVD models in Table 3.1. In addition, the capacitances had to be adjusted to compensate for parasitic capacitances to backside ground, which were estimated using finite element analysis. The values used were $C_{inv} = 1.1$ pF, $2C_{line} = 1$ pF and the outer C_{line} was entirely due to the parasitic capacitance of the traces on the board. An image of the assembled circuit and its corresponding schematic are shown in Figure 3.20. Microscope images of the two resonators used in the filter are shown in Figure 3.14. The resonators are different physical sizes, but, because of missing electrodes in Resonator 1 (Figure 3.14b, due to poor fabrication), the electrical sizing (C_0) are similar for the two resonators, as evidenced in their frequency responses in Figure 3.15 and Figure 3.16.

The measured S-parameters of the constructed filter are shown in Figure 3.21. The notch is 36.4 dB deep at 487.6 MHz, with approximately 3.2% 3 dB bandwidth and 1% 10 dB bandwidth. The close-up view of the notch in Figure 3.21b also shows the designed frequency response (using the mismatched MBVD models).

The discrepancies between design and measurement in the *passband* are caused by inaccuracies in the transmission line branch. The high $|S_{11}|$ around 200-300 MHz and 500-600 MHz arises because of inaccuracy in estimating the parasitic capacitance in C_{line} , causing the transmission line impedance to have poor internal matching. This also explains the insertion losses of approximately 2 dB (below notch) and 3 dB (above notch). The matching can be improved with better control

3.4 Fabrication and measurement of a fixed absorptive notch filter

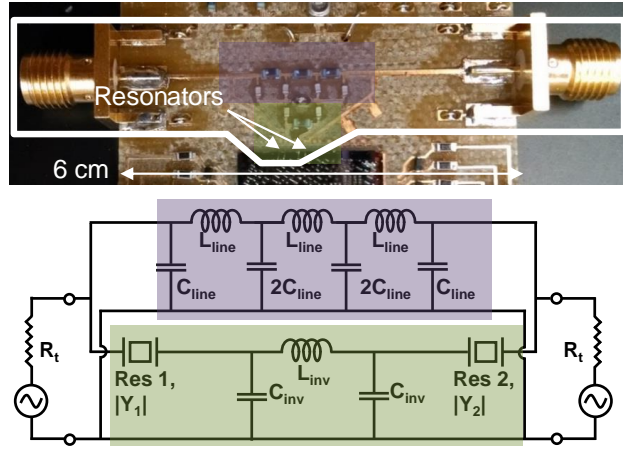


Figure 3.20: Photograph and schematic of assembled absorptive notch filter without tuning. The purple and green highlights show the correspondence between the photograph and the schematic. The resonators occupy two microscopic locations on the bottom of the picture where indicated by arrows.

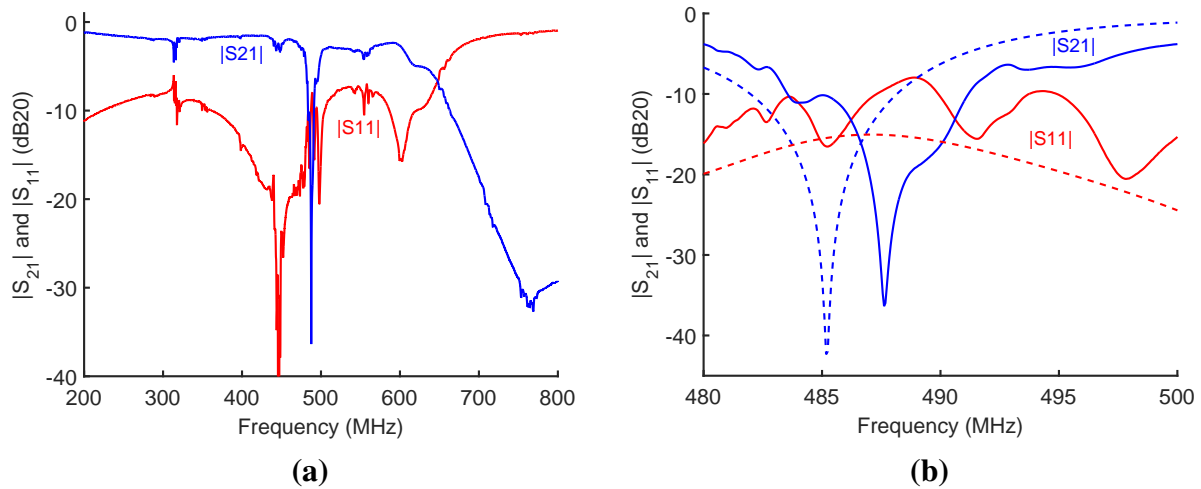


Figure 3.21: Measured S-parameters of an absorptive notch filter. (a) Wide band measurement, (b) zoomed view of notch, overlaid by the designed result (dashed traces) using the mismatched MBVD models whose parameters can be found in Table 3.1. Blue: $|S_{21}|$, red: $|S_{11}|$.

over parasitic capacitance, such as with improved backplane geometry for the PCB or more tightly specified materials.

The *notch* differs from design because of the spurs near the resonance (Figure 3.15 and Fig-

3. VARACTOR TUNING OF FILTERS

ure 3.16), which are not captured by the MBVD model. The notch frequency deviates from design (shown in Figure 3.21b, dashed traces) as the spurs change the notch frequency, the frequency at which the net phase is zero (compounded by the mismatch in spurs between the two resonators). The magnitude difference between MBVD model and measured spur, on the order of 3 dB, causes impedance mismatch which decreases notch depth. For the design to better match measurement, the spurs should be eliminated in future fabrication runs.

3.5 Tuning the absorptive notch filter

In this section, tuning is added to the absorptive notch filter. The simplest way to do so is by using the varactor tuning described in Section 3.2. The schematic for the filter is shown in Figure 3.22, with the varactor-resonator combination marked with a dashed red box.

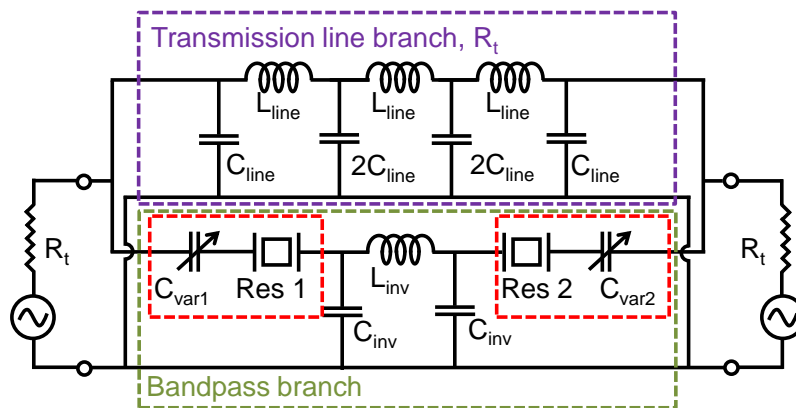


Figure 3.22: Absorptive notch filter topology with tuning, with lumped-element coupling and transmission line. The tuning is implemented by adding varactors to the resonators, as highlighted in the red dashed boxes.

The mechanism of tuning is that the series varactor combination moves series resonance, which is what defines the notch frequency in this topology. The simulated S-parameters are shown in Figure 3.23.

3.5 Tuning the absorptive notch filter

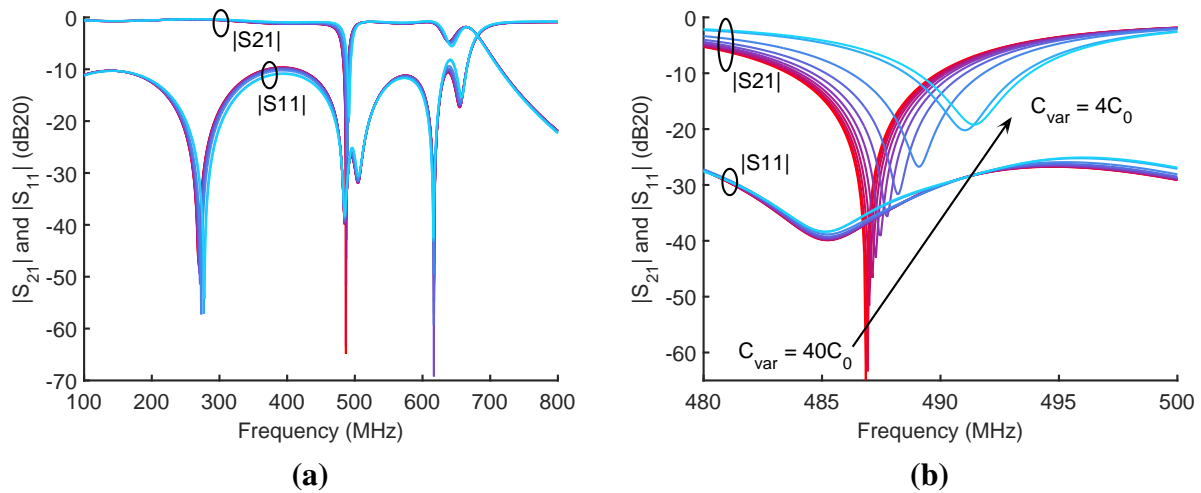


Figure 3.23: Simulated S-parameters of an ideal tunable absorptive notch filter with varactor tuning. (a) Wideband plots, (b) zoomed-in view showing notch tuning as a function of varactor capacitance.

The zoomed-in view of the notch in Figure 3.23b shows the notch to be moving while becoming shallower, until it hits the notch depth specification. This is why K_f^2 is said to determine the tuning range; higher K_f^2 values means a slower change in impedance as the resonator is tuned. Figure 3.24 graphs the relationship between frequency tuning range and K_f^2 for the ANF topology. For the $K_f^2 = 14.5\%$ used here and a 20 dB notch specification, the frequency tuning range is approximately 4.15 MHz, or about 0.85%. The tuning range of the varactor is about 10:1, which is a realistic value, so the limiting factor to the tuning range is the notch depth.

3. VARACTOR TUNING OF FILTERS

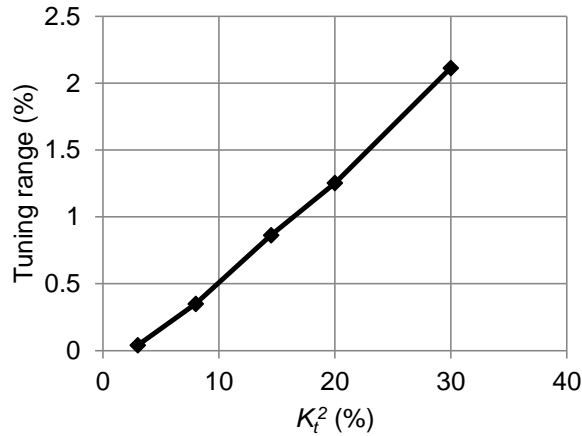


Figure 3.24: Frequency tuning range of absorptive notch filter as a function of resonator K_t^2 at a 20 dB notch depth specification. As the K_t^2 increases, the tuning range grows, assuming that the varactor tuning range (here assumed to be 10:1) is not a limiting factor.

3.6 Fabrication and measurement of a tunable absorptive notch filter

A practical concern when implementing the tuning in the notch filter is the mismatch between resonators and spurs near resonance (Figure 3.15 and Figure 3.16). These cause the impedance to fluctuate dramatically as the notch frequency is tuned. To address this, varactors are added to the surrounding circuit (in C_{line} and C_{inv}); the schematic as implemented is shown in Figure 3.25, and the photograph of the circuit is in Figure 3.26. The varactors tune the impedance of the transmission line and impedance inverter, allowing the circuit to adjust to the variation due to the spurs. In addition, to reduce parasitic capacitance, the backplane is patterned using the double-side feature of the LPKF S63 milling machine, removing most of the metal, and used a Rogers Duroid¹

¹The dielectric constant for Rogers Duroid 5880 is 2.20 ± 0.02 according to the specification sheet. However, the reader looking to replicate these results should be warned that the Duroid turned out to be very difficult to mill in the milling machine! This was because of the soft PTFE-based material, whose bending also threatened to break the wirebonds. It would be easier to use something rigid, such as Rogers TMM3, which resulted in much cleaner milling and yielded encouraging results on the dielectric constant (but the thin traces were damaged by repeated soldering attempts before the full circuit could be built and measured).

3.6 Fabrication and measurement of a tunable absorptive notch filter

5880 substrate which has a lower and better controlled dielectric constant than FR-4.

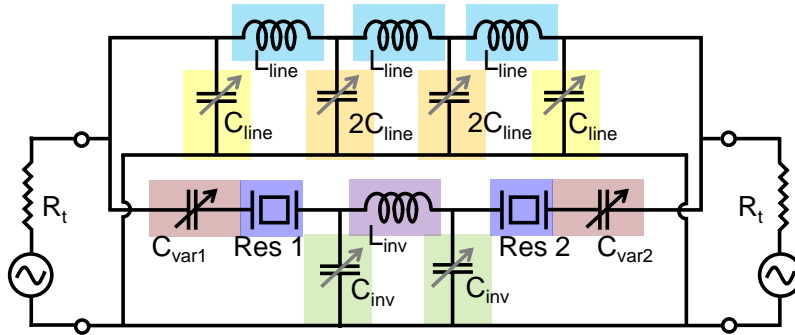


Figure 3.25: Absorptive notch filter topology with tuning, as implemented with fine-tunable shunt capacitors (C_{line} and C_{inv}) in the transmission line and inverter sections.

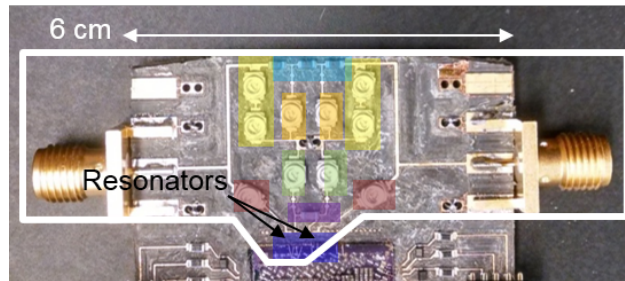


Figure 3.26: Photograph of the tunable absorptive notch filter as implemented. The highlights correspond to the portions of the schematic highlighted in Figure 3.25. The varactors are implemented using screw-top varactors.

Measurements of this circuit demonstrate frequency tuning, as shown in Figure 3.27. The passband varies when the C_{line} capacitance is changed, so the measured worst-case insertion loss ranges from 3 dB to 10 dB (the best-case insertion loss being about 2 dB). The notch tunes from 484.3 MHz to 491.2 MHz as the C_{var} varactor tunes from 10 pF to about 5 pF (about $40C_0$ to $20C_0$). This tuning range exceeds the theoretical tuning range because the spurs add extra notch frequencies (in addition to adding spurious notches within the filter response); the notch criteria (0 phase and impedance match) are nearly met at these frequencies and therefore form extra notches.

3. VARACTOR TUNING OF FILTERS

Likewise, at other frequencies, the spurs cause impedance fluctuations that exceed the matching capability of the circuit, thus preventing appreciable tuning to those frequencies.

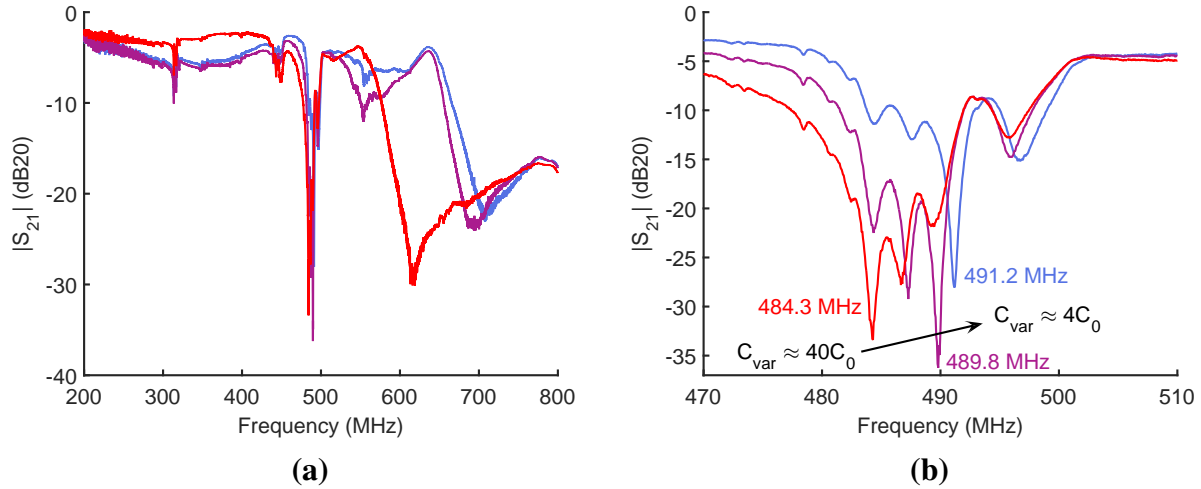


Figure 3.27: Measured S-parameters of tunable absorptive notch filter with varactor tuning. (a) Wideband plots, showing variation in the passband due to changes in C_{line} ; (b) zoomed-in view showing notch tuning as a function of varactor capacitance.

3.7 Discussion on discontinuous tuning range

The operation of the absorptive topology relies on the impedance match. Equation (3.5) prescribes the impedance in order to create optimal passage through the bandpass branch, thus creating the notch.

In addition, the phase of the branches matters as well. The destructive interference creating the notch will only work if the net phase of the two resonators in series, at the notch frequency, is zero; otherwise, the bandpass branch phase will deviate from 90 degrees and fail to completely cancel with the transmission line phase of 270 degrees, even if the impedance magnitudes are perfectly matched.

The nonzero phase (in addition to impedance magnitude mismatch) explains the discontinuous

3.7 Discussion on discontinuous tuning range

tuning (Figure 3.27). When the resonator has fluctuations in its frequency response, the net phase (sum of the admittance phase of the two resonators) jumps away from zero, thus preventing successful destructive interference and preventing the notch from being tuned to those frequencies, thus creating discontinuities in the tuning range.

Filter simulations using resonator measurements free of large fluctuations (Figure 3.28a, measurements taken from devices with just one individual resonator instead of four in parallel) demonstrate that clean resonators can provide continuous tuning range. The result, shown in Figure 3.28b, is that the filter can tune continuously. However, there still are fluctuations in the notch, as seen by the non-monotonic left slope of the simulated notch. This motivates the investigations on fluctuations due to modal coupling in Chapter 4 and on spurs (especially due to transverse modes) in Chapter 5.

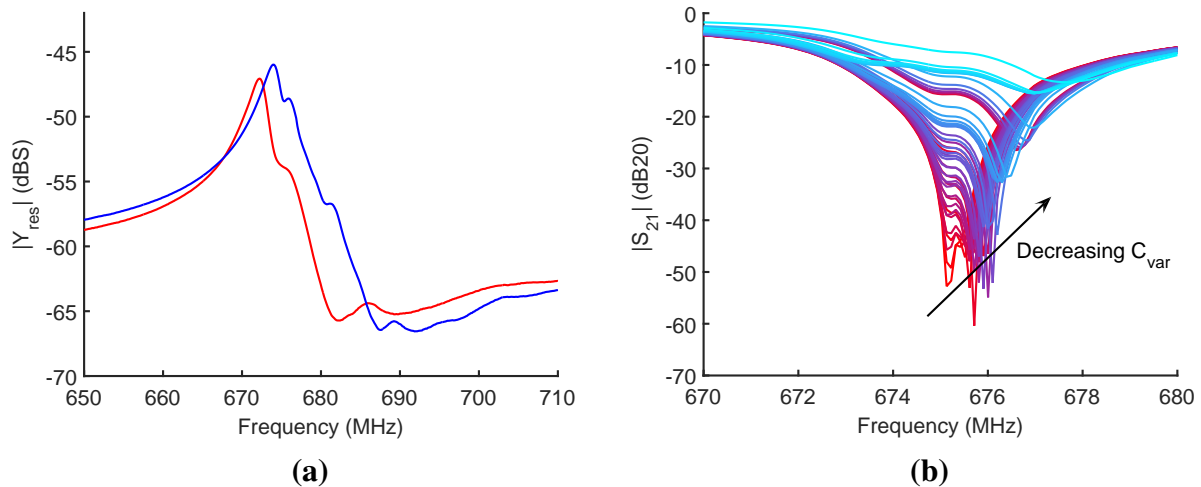


Figure 3.28: (a) Measured admittances of two relatively clean resonators on the same die used for the notch filter; (b) simulated $|S_{21}|$ of an absorptive notch filter inserting the relatively clean resonator measurements into the circuit. The spurs are mild enough that the tuning (within a 20 dB notch specification) is continuous.

3. VARACTOR TUNING OF FILTERS

3.8 Proposed method to extend the tuning range

Even in the ideal simulation, the tuning range is quite low for this absorptive notch filter. In the ideal tunable filter (Figure 3.24), the tuning range-to- K_t^2 ratio of approximately 0.06, which is lower than that of the ladder filter (whose ratio was about 0.1 for the example in the earlier part of this chapter). This can be explained from the perspective of impedance matching. The impedance magnitude of the resonator changes as it is tuned (Figure 3.2), while the impedance of the surrounding circuit remains the same. This creates an impedance mismatch as the resonators are tuned, which causes the notch to become increasingly shallow as the resonance is tuned toward the antiresonance.

One way to address this limitation head-on is to make the circuit adjust to the changing impedance of the resonators. One possible solution is proposed in the schematic shown in Figure 3.29. All the elements in the circuit are now adjustable, so one could imagine switching the impedance once the tuning range at a particular impedance is exhausted. The idea of switching impedance (rather than continuously varying impedance) means that there is no need for continuously tunable inductors; switched inductors are adequate.

Figure 3.30 shows a simulated response of the proposed circuit, using MBVD models for the resonators, where at each new impedance, the circuit elements can be configured according to Equation (3.5)-(3.9) to the new impedance. The leftmost subset of traces (in blue) show the same behavior as in the tuned circuit from before, being limited by the notch specification at around 491.7 MHz. Now, however, the inductors, capacitors, and termination are switched to a new impedance, 621 Ω , which is the impedance of the resonator at 491.7 MHz. The notch deepens as a result of this refreshed impedance match, and the series varactors can push the frequency along some more. In this demonstration, the impedance is reset a third time, at 495 MHz. The overall tuning range for this demonstration is now 2%, more than twice the original 0.85%.

3.8 Proposed method to extend the tuning range

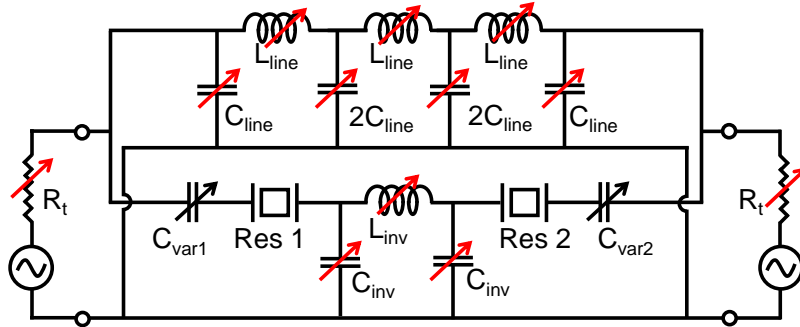


Figure 3.29: Proposed topology to offload impedance match burden to the remainder of the circuit by adding tunability to the operating impedance. The inductors may be switched inductances.

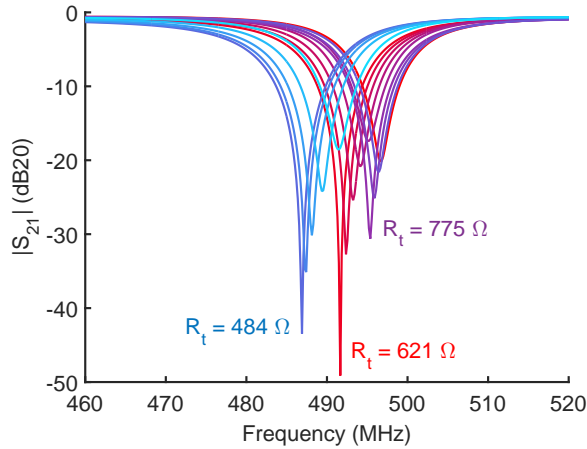


Figure 3.30: Simulated $|S_{21}|$ of tunable absorptive notch filter with proposed stepped impedance tuning. In this demonstration there are three impedances to which the circuit is coarse-tuned (484, 621, and 775 Ω). Within each impedance, the varactors in series with the resonators provides fine tuning.

The limit to this proposed technique is the tuning limits on the varactors, inductors, and/or the termination. In effect, some of the tuning burden from the resonator has been offloaded to the rest of the circuit. Note that a large K_t^2 in the resonators still helps by extending the tuning range at each impedance level.

3.9 Conclusions

This chapter has reviewed the tuning of a bandpass filter using varactors. In this chapter, only one varactor has been used to tune each resonator, but it is possible to attach two (or more) varactors, as done in [9]. A contribution for the bandpass filter is the analysis on the effects of parasitic capacitance to ground from the varactor pads; this was found to cause sagging in the passband (because of the reduction in the effective K_t^2 of the shunt branch resonators) and to increase the passband ripple (because of the loading from the extra capacitance). An increase in the frequency of the shunt branch (per Equation (2.8)) can compensate for the reduced effective shunt K_t^2 due to parasitic capacitance, and a decrease in the termination impedance can compensate for the ripple due to the loading from the extra capacitance.

For an experimental demonstration of tuning, this chapter has presented the design, construction, and measurement of a tunable absorptive notch filter. The measured results have a notch depth exceeding 30 dB, and a worst-case passband insertion loss ranging from 2 dB to 10 dB depending on the quality of the impedance matching of the transmission line branch. The tuning range of the filter is about 1.4% in measurement, compared to 0.85% in theory (for a $K_t^2 = 0.145$). The discrepancy, along with the discontinuous nature of the tuning range, is due to the fluctuations that occur in the resonator frequency response near resonance; at these frequencies, the impedance match fails (both in magnitude and phase) and hence the filter has shallow notch depth at those frequencies, to the extent that tuning to those frequencies violates the notch depth specification. This motivates studies on fluctuations in the resonator response, especially those near the resonance. Because each fabricated resonator for this demonstration consisted of four individual (visibly non-identical) resonators in parallel with shared release pits, it is hypothesized that one possible cause of the fluctuations is mismatch or mechanical coupling between the resonators. This is studied in Chapter 4. Another cause of the fluctuations could be from spurious modes within the individual

resonators themselves; these causes (namely transverse modes) are studied in Chapter 5.

To increase the tuning range of the circuit, a switched-impedance method has been proposed. Using switched inductors, tunable capacitors, and tunable termination impedance, it is possible to increase the tuning range in a piecewise manner. This method distributes the tuning burden to the circuit surrounding the resonators. For example, it is possible to increase the theoretical tuning range from 0.85% to 2% by changing switching the impedance from 484 Ω to 775 Ω in two steps.

This page intentionally left blank

Chapter 4

Fluctuations from modal coupling in arrayed resonators

4.1 Introduction

In Chapter 3, the tunable absorptive notch filter turned out to suffer from a discontinuous tuning range, which was caused by the fluctuations in the resonator response near resonance. These fluctuations, manifesting as large swings in the admittance of the resonator, led to frequencies at which the impedance and phase matching were impossible, leading to forbidden frequencies to which the filter could not be tuned. The conclusion was that these fluctuations would need to be eliminated or strongly mitigated in order to make the tuning range continuous and to smooth out the filter notch.

This chapter considers a possible mechanism that may lead to the undesirable fluctuations, especially in large resonators. The large resonators consist of several smaller resonators in parallel, as shown in Figure 3.14. These large resonator combinations will be called **“arrayed resonators”**. The hypothesis is that the fluctuations could be due to mismatch or mechanical coupling between

4. FLUCTUATIONS FROM MODAL COUPLING IN ARRAYED RESONATORS

the individual resonators within the larger resonators, even if each individual resonator were to be free of fluctuations.

Figure 4.1 illustrates the impact of the fluctuations upon the tuning of the resonator. The schematic of the arrayed resonator with varactor is shown in Figure 4.1a. This models the four individual resonators of “Resonator 1”, whose microscope image is shown in Figure 3.14a. Visual inspection shows that the resonators are not identical. The arrayed resonator behavior is taken from measurement of “Resonator 1” (Figure 3.15), while the varactor behavior is that of an ideal tunable capacitor. Figure 4.1b shows the simulated admittance as C_{var} is tuned. The fluctuations have compromised the ability to tune the resonance peak continuously; as C_{var} is decreased, there is no clear or consistent movement of a resonance peak.

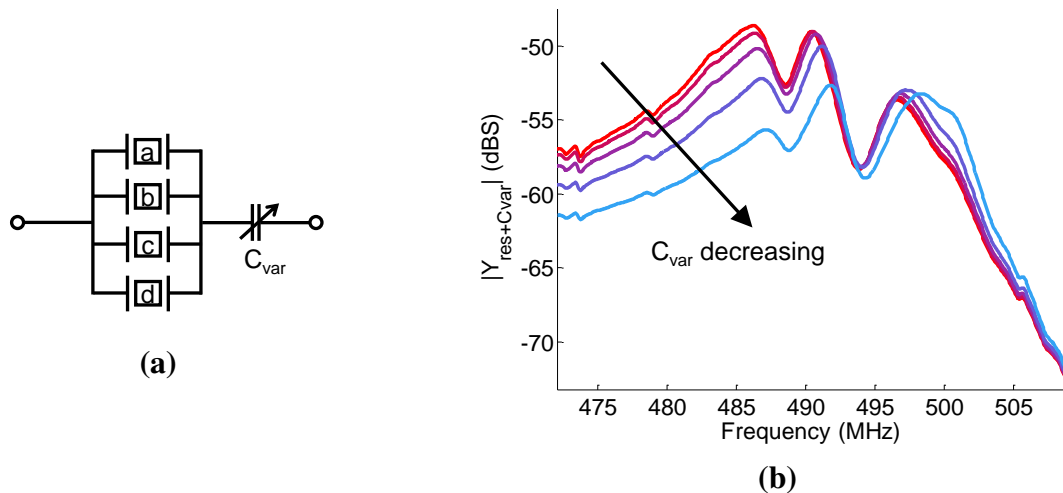


Figure 4.1: Simulated tuning of the resonator response using measured resonator admittance and an ideal varactor, showing how the fluctuations in the arrayed resonator compromise the tuning of the peak (that is, it is unclear that there is any appreciable tuning of the peak).

The challenge of designing *individual* resonators free of fluctuations is addressed in Chapter 5. In the analysis for this chapter, the arrayed resonators consist of individual resonators each modeled by an MBVD model. The chapter is organized as follows. First, the need for arrayed resonators is presented. Then basic analyses of mechanical and electrical coupling between individual res-

onators reveal possible sources of fluctuations in the resonator response. Finally, a solution that can help align the resonator responses is proposed for the case where frequency variation dominates the fluctuations.

4.2 Why arrayed resonators?

Impedance matching (by Equation (2.3)) dictates the need for resonators with large C_0 on the order of picofarads for 50 Ω termination impedances. The C_0 is related to the size of the resonators (number of fingers, length of fingers), so a (naïve) solution is simply to increase the number and length of the fingers. This approach has the disadvantage of requiring large release undercuts, which leave large undercut areas of unused LN material because the undercut is at least half the resonator width, as illustrated in Figure 4.2. Also, if there are excessive residual stresses in the LN film, then large resonators are more susceptible to cracking and therefore yield loss. Another effect is that a resonator with long or many fingers will have long and narrow strips of electrode routing in the fingers or bus, which could lead to non-negligible levels of electrical resistance, leading to losses. Increasing the width or thickness of the fingers and bus to decrease resistance would compromise the resonator performance (K_t^2 and spurs).

Another solution that increases the C_0 is to array several “regular-sized” resonators (C_0 on the order of 100 fF each) in parallel into “arrayed” resonators. If the resonators are identical, and neglecting mechanical coupling, then the resonators in parallel will scale their C_0 only, the remaining parameters (f_s , K_t^2 , Q) remaining constant¹. The release undercut stays the same distance as the individual resonators, while the routing to the individual resonators can be widened to address any sheet resistance concerns. Nominally, this is an elegant way to extend C_0 because of the incremen-

¹The reader can prove this by working out the admittance or impedance for, say, four identical MBVD models in parallel, which turns out to be equivalent to a single MBVD model with 4 times C_0 and C_m and 1/4 times L_m , R_m , R_s , and R_0 .

4. FLUCTUATIONS FROM MODAL COUPLING IN ARRAYED RESONATORS

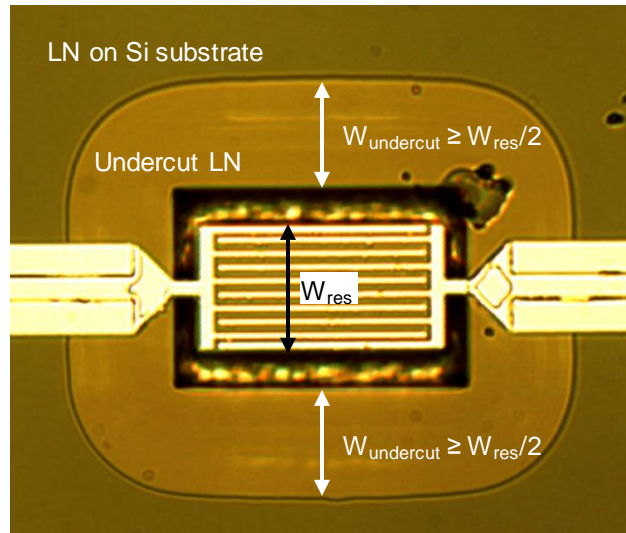


Figure 4.2: Microscope image of a resonator with LN undercut marked. The undercut will be at least half the shorter dimension of the resonator, in this case the width. This means that increasing the size of the resonator will also increase the undercut.

tal area increase (compared to the overhead amount of area consumption for the release pit) for a linear capacitance gain.

However, imperfections in this method of C_0 expansion may lead to fluctuations due to mechanical or electrical coupling of resonances, which are explored in this chapter: Section 4.3 explores what happens when identical resonators are arrayed together while sharing a release pit, while Section 4.4 explores what happens when the individual resonators have no mechanical coupling but are *not* identical.

4.3 Mechanical coupling of parallel identical resonators

This section considers the impact of mechanical coupling between resonators. In general, coupling between resonators (even identical resonators) can spread out the poles (as in the case of the coupled filter in Chapter 2). Mechanical coupling is similar; in fact, mechanical couplers have been used with microresonators to create filters [25]. The concern is that uncontrolled or unin-

4.3 Mechanical coupling of parallel identical resonators

tended mechanical coupling across the undercut LN plate could distort the resonance of arrayed resonator such as those depicted in Figure 3.14, where the etch pit is shared.

Of course, a simple solution to this concern would be to separate the individual resonators such that their etch pits are mechanically isolated. For example, this idea was applied to the filter in Figure 2.17, where the resonators were spaced such that the etch pits were disconnected. An illustration is shown in Figure 4.3. The tradeoff with this etch pit isolation technique is that more area (about twice) is consumed by the sparsely packed resonators than if the resonators were packed close together with shared pits. As such, it is worth the effort to determine whether the impact of sharing the pits is enough to create noticeable fluctuations in the arrayed resonator frequency response.

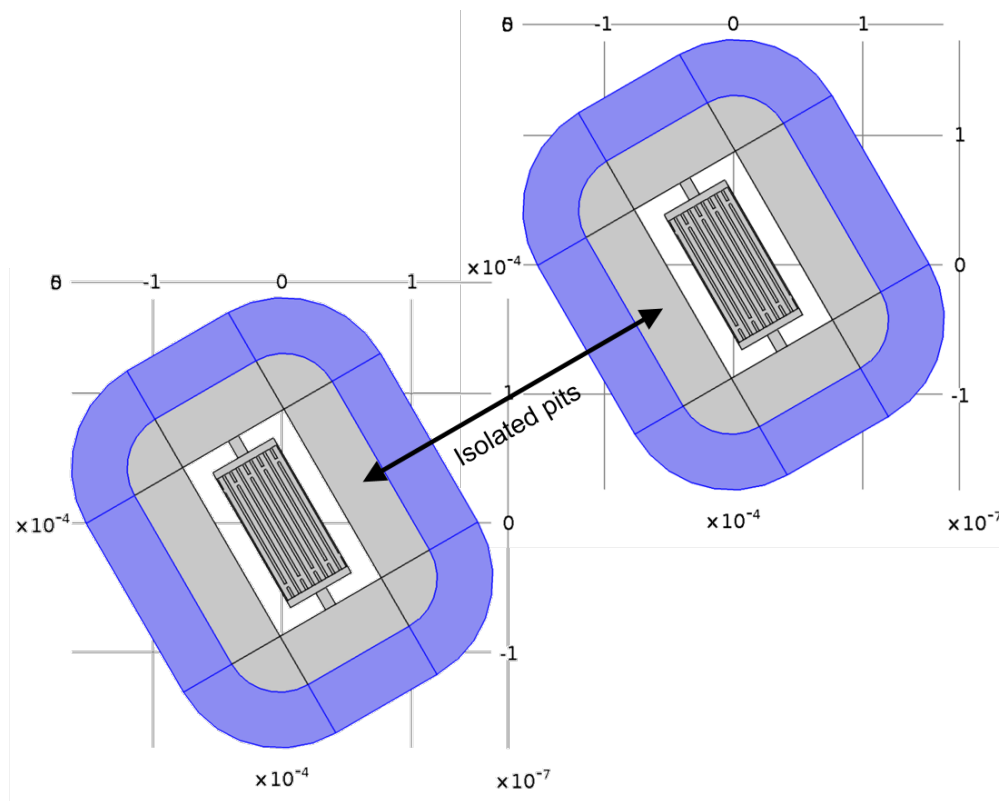


Figure 4.3: COMSOL 3D geometry setup for two resonators with isolated pits. The highlighted rings (purple) indicate the regions of the PML boundary condition; there is a Fixed Constraint applied to the backside to simulated anchoring effects.

4. FLUCTUATIONS FROM MODAL COUPLING IN ARRAYED RESONATORS

4.3.1 COMSOL simulation of mechanical coupling

The effect of mechanical coupling can be understood from a comparison of COMSOL FEA simulations of two devices with isolated pits versus simulations of two devices with a shared pit. In this simulation, a Fixed Constraint boundary condition has been added underneath the LN material where it would be attached to the silicon in the actual device. This, in conjunction with the Perfectly Matched Layer (PML), simulates the anchoring of the silicon, which can cause reflections of the acoustic waves (whereas without the Fixed Constraint, all the energy goes into the PML without reflection). The setup of the geometry are shown in Figure 4.3 and Figure 4.4 where the Fixed Constraint regions are highlighted. Figure 4.3 illustrates a double resonator with isolated release pits, while Figure 4.4 illustrates a double resonator with shared pits, where the spacing between resonator anchor centers is $72\ \mu\text{m}$.

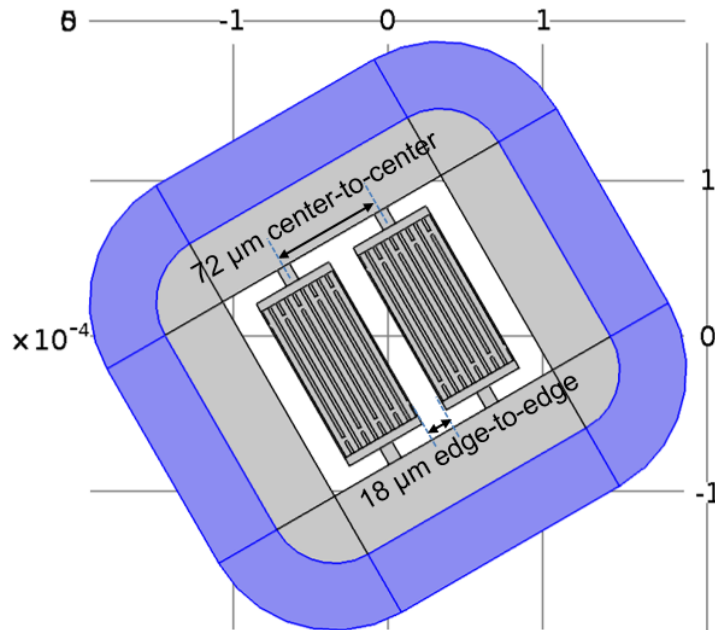


Figure 4.4: COMSOL 3D geometry setup for two resonators with shared pit. The highlighted ring indicates the region of the PML boundary condition; there is a Fixed Constraint applied to the backside to simulated anchoring effects. The spacing between the resonator edges is $18\ \mu\text{m}$, or $72\ \mu\text{m}$ between resonator centers (the resonators are $54\ \mu\text{m}$ wide).

4.3 Mechanical coupling of parallel identical resonators

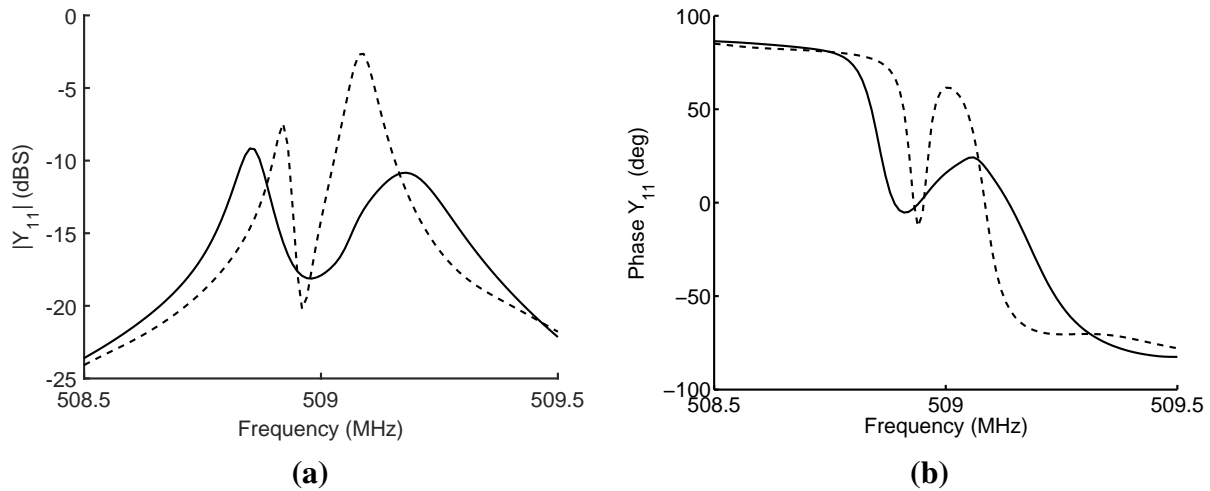


Figure 4.5: COMSOL simulations of mechanical coupling comparing two resonators with isolated pits (dashed, Figure 4.3) to two resonators with a shared etch pit (solid, Figure 4.4). In this simulation, the PML has an additional Fixed Constraint boundary condition on the bottom of the LN material layer to simulate the anchoring scheme. The length of the anchors is $12\ \mu\text{m}$ (Figure 4.6a), as optimized before the Fixed Constraint was added to the simulation. The isolated-pit resonator has a split in the peak, and the shared-pit widens the separation between the two peaks.

The simulation results are shown in Figure 4.5. The dashed trace is the admittance of the isolated pits, while the solid trace is for the shared pit, both with Fixed Constraint for the pit perimeter. The dashed trace has far more splitting of the peak, which suggests that mechanical coupling could play a role. However, the split peak in the baseline (isolated pit), which is introduced as a result of adding the Fixed Constraint (it does not appear without the Fixed Constraint, all else being held equal), causes confusion in understanding the source of the peak splitting. A device needs to be designed so that the isolated pit simulation does not have peak splitting.

In order to suppress the peak-splitting that appears in the *isolated* pit resonators upon introduction of the Fixed Constraint, the anchor length is extended to $L_a = 15\ \mu\text{m}$ (illustrated in Figure 4.6b), which is a quarter wavelength longer than the original design ($12\ \mu\text{m}$, illustrated in Figure 4.6a). The results comparing the two anchor lengths are shown in Figure 4.7. The peaks are brought together (solid trace) with $L_a = 15\ \mu\text{m}$, with a slight penalty to Q due to the different

4. FLUCTUATIONS FROM MODAL COUPLING IN ARRAYED RESONATORS

boundary condition. The $Q \approx 2800$ is adequate for filter designs with insertion loss less than 1 dB (recall that the filter simulations in Chapter 2 use $Q < 1000$).

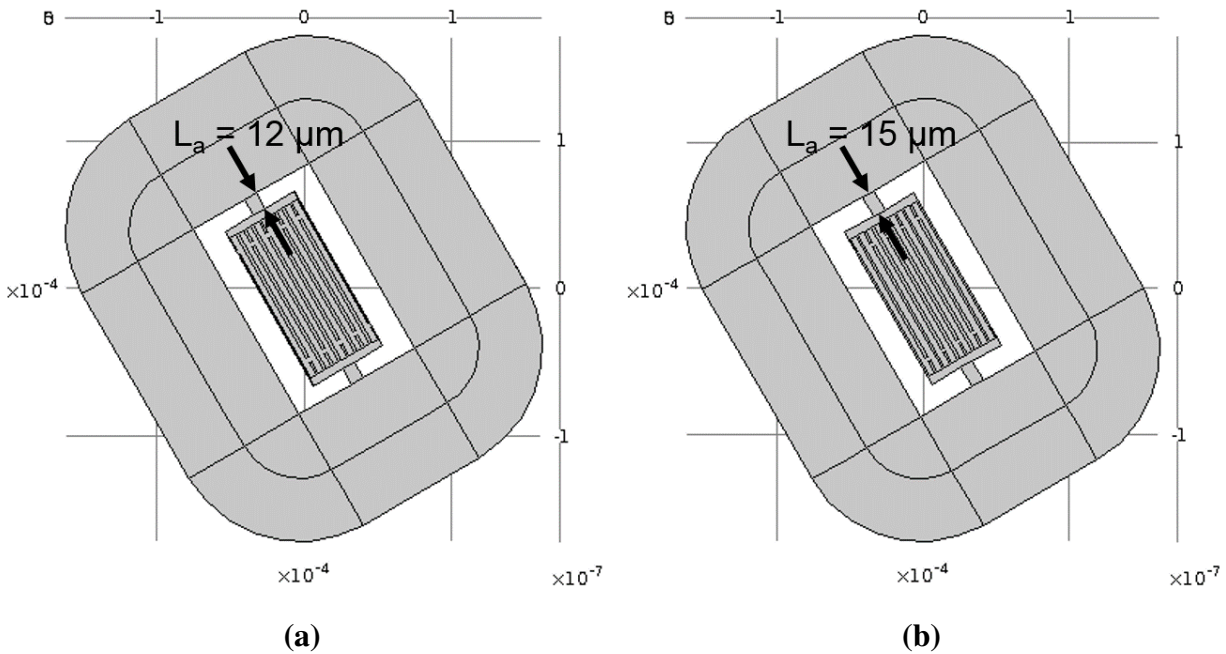


Figure 4.6: COMSOL 3D geometry setup for isolated-pit resonators (just one resonator shown) with (a) $12 \mu\text{m}$ and (b) $15 \mu\text{m}$ long anchors. Only the anchor length (and the corresponding release hole length) is changed.

The results for mechanical coupling with the lengthened anchor are shown in Figure 4.8, with several distances of separation between the resonators in order to see trends in the coupling as a function of distance.

The two resonators with isolated pits corresponds to the dashed black trace, which has a single peak (unlike in Figure 4.5). In terms of sizing for fabrication, the resonators would be separated by about $130 \mu\text{m}$ edge-to-edge in order to provide the mechanical isolation.

When two copies of these resonators are placed adjacent to each other with an $18 \mu\text{m}$ release hole separating the edges ($72 \mu\text{m}$ between resonator anchor centers), the simulation results in the orange trace exhibiting a split peak. This suggests that mechanical coupling may cause fluctuations in the individual resonators.

4.3 Mechanical coupling of parallel identical resonators

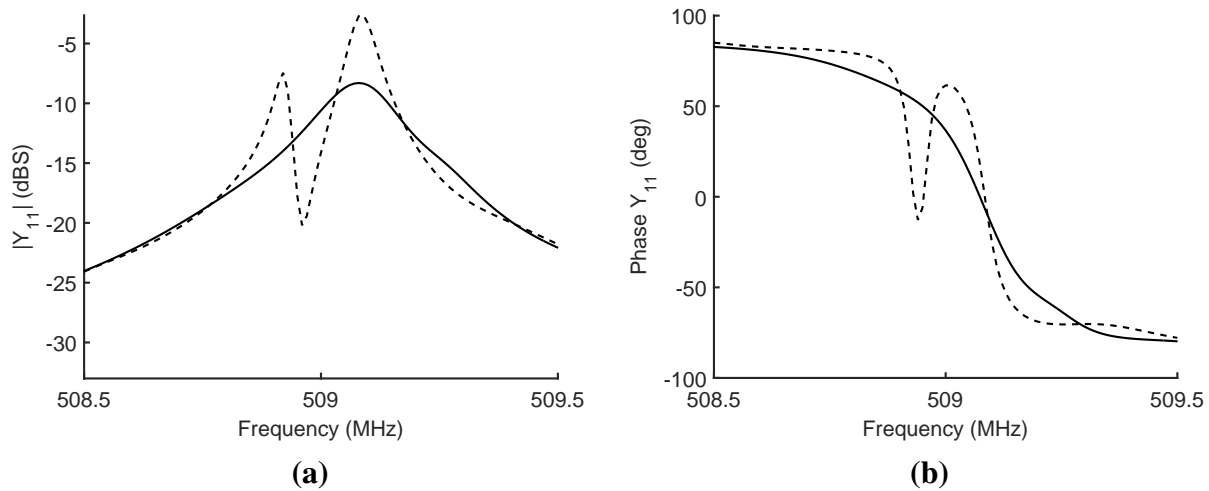


Figure 4.7: COMSOL simulations of isolated pit resonator devices with PML and Fixed Constraint boundary conditions comparing anchor length (dashed) $L_a = 12 \mu\text{m}$ and (solid) $L_a = 15 \mu\text{m}$. The electrical behavior exhibits similar C_0 (at the ends of the frequency range) but different resonance due to the differing mechanical boundary conditions. The $L_a = 15 \mu\text{m}$ has a Q about 2800 and the $L_a = 12 \mu\text{m}$ has a Q around 8000, but with a split peak.

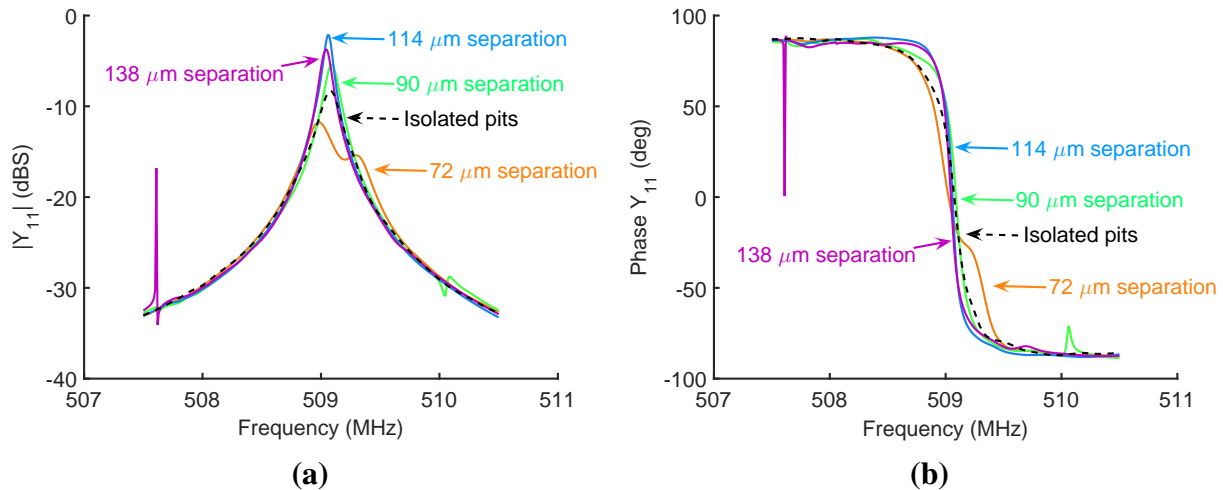


Figure 4.8: COMSOL simulations of mechanical coupling comparing two resonators with isolated pit (dashed black) to shared etch pit (illustrated in Figure 4.4) with $72 \mu\text{m}$ (orange), $90 \mu\text{m}$ (green), $114 \mu\text{m}$ (blue), and $138 \mu\text{m}$ (magenta) separation between resonator centers. In this simulation, the PML has a Fixed Constraint boundary condition on the bottom of the LN material layer to simulate the anchoring scheme. The simulation setups are shown in Figure 4.3 and Figure 4.4 with length of the anchors being $15 \mu\text{m}$.

4. FLUCTUATIONS FROM MODAL COUPLING IN ARRAYED RESONATORS

When the distance between resonator edges (still sharing the release hole) is increased to $36\ \mu\text{m}$ ($90\ \mu\text{m}$ between resonator anchor centers), the peak splitting is mitigated (green trace). This result suggests that it may be possible to avoid the mechanical coupling (previously done with $100\ \mu\text{m}$ spacing) while still sharing an etch pit, by spacing the resonators slightly wider.

When the distance is increased even further to $60\ \mu\text{m}$ ($114\ \mu\text{m}$ between resonator anchor centers) and $84\ \mu\text{m}$ ($138\ \mu\text{m}$ between resonator anchor centers), the peak continues to stay single. The spike near $507.5\ \text{MHz}$ for the $138\ \mu\text{m}$ (magenta) trace is due to energy escaping the resonator body through the anchoring and resonating in the released area; hence it is hypothesized that the sizing of the undercut LN area may add additional constructive or destructive mechanical interference, at least when using the Fixed Constraint to model the anchored LN film. This is a topic appropriate for future investigation.

4.4 Electrical coupling of parallel mismatched resonators

This section presents the analysis of the parallel combination of resonators that are mismatched. The MBVD model is used to model the individual resonators.

The measurement of “Resonator 1” from Chapter 3 provides a basis for comparison. Its admittance near resonance is plotted in Figure 4.9 (the full sweep is plotted in Figure 3.15, and its microscope image in Figure 3.14a).

To match the frequency mismatch theory to the measurement, four MBVD models can be modeled in parallel. The schematic describing the resonator is shown in Figure 4.10 and consists of four parallel MBVD models labeled “a” to “d”.

The “nominal” MBVD values for the individual resonators are extrapolated from the MBVD model of the arrayed resonator, from Table 3.1 (“Resonator 1”). The C_0 is estimated to be a quarter of the total arrayed value for each individual resonator. For the Q , it is assumed that individual

4.4 Electrical coupling of parallel mismatched resonators

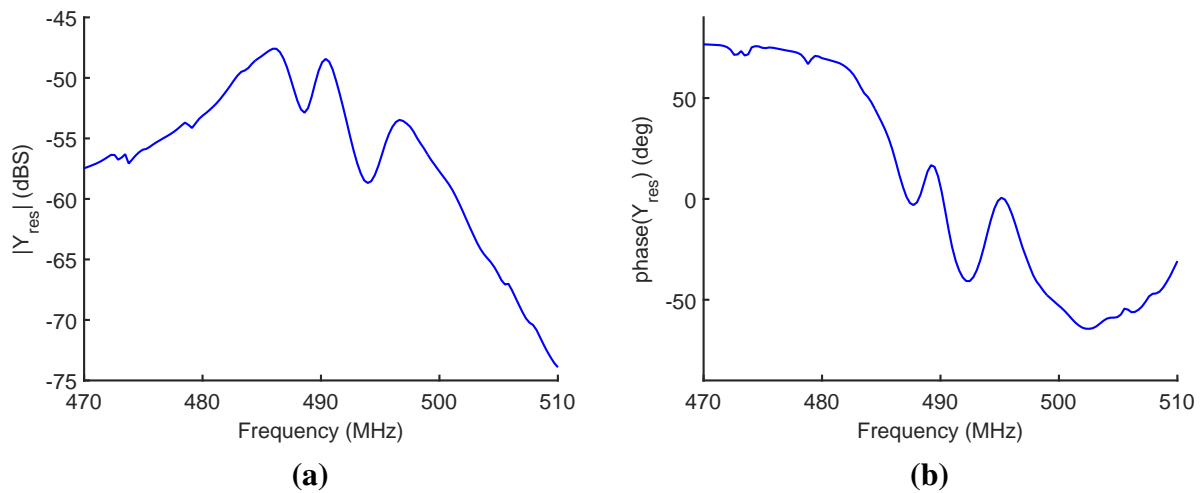


Figure 4.9: Close-up view of the measured admittance near resonance for “Resonator 1” used in the absorptive notch filter in Chapter 3.

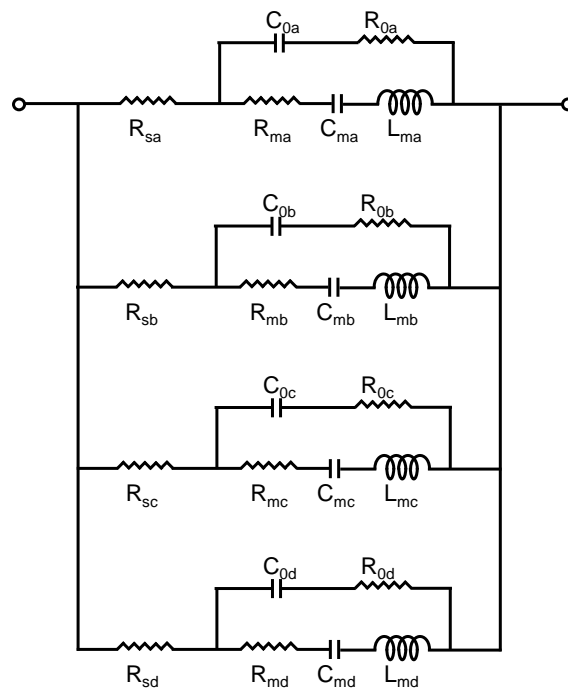


Figure 4.10: Schematic of arrayed resonator with four parallel MBVD models with possibly different frequencies. For the example in this chapter, resonators “a” and “b” are at the nominal frequency (486 MHz), resonator “c” at 0.823% offset (490 MHz), and resonator “d” at a 2% offset (496.6 MHz).

4. FLUCTUATIONS FROM MODAL COUPLING IN ARRAYED RESONATORS

resonator Q is 200 (whereas the Q of the array is only 100 because of the fluctuations). This is approximately in line with the Q measured in the other single resonators in this run.

The frequency ($f_s = \frac{1}{2\pi\sqrt{L_m C_m}}$) of each resonator can be varied to compare the arrayed response to the measurement. Here, this is done manually. Figure 4.11 shows the results of aggregating resonators “a” through “d”, with resonators “a” and “b” at the nominal frequency (486 MHz), resonator “c” at 0.823% offset (490 MHz), and resonator “d” at a 2% offset (496.6 MHz).

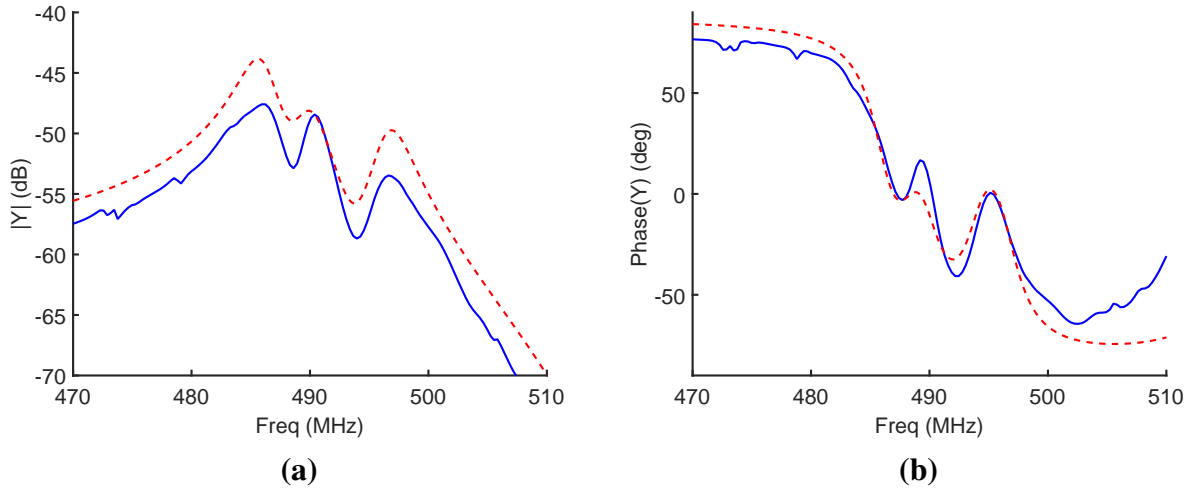


Figure 4.11: Comparison of measurement vs. simulation with four MBVD models with mismatched frequency. The solid blue is the measurement and the dashed red is the model. For the model, resonators “a” and “b” are at the nominal frequency (486 MHz), resonator “c” at 0.823% offset (490 MHz), and resonator “d” at a 2% offset (496.6 MHz).

The frequencies of the fluctuations match quite well, suggesting that frequency mismatch could be a valid origin. The variation in frequency for individual resonators across the die was about 1.2%, so the spur around 497 MHz (due to the 2%-offset resonator) could instead have been a transverse mode spur (which is not modeled by the MBVD model) in individual resonators. Transverse mode spurs will be discussed in Chapter 5.

4.5 Proposed method to align the response of arrayed resonators

If the resonator fluctuations in arrayed resonator combination are dominated by frequency mismatch between individual resonators, then tuning the *individual* resonators can be used to align their peaks, thus smoothing out the arrayed response.

Returning to the example in Section 4.4, tuning of the arrayed resonator is desired. This was implemented with a single varactor in series with the arrayed resonator, as illustrated in Figure 4.1a. This technique had failed to produce continuous tuning of the resonance.

Instead, the resonator-varactor combination can be changed slightly: the varactor can be broken into smaller sub-varactors and wired individually to the individual resonators, as illustrated in Figure 4.12. This allows each individual resonator to be tuned by its own varactor.

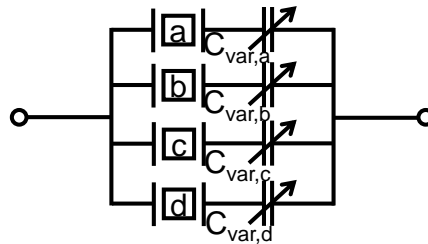


Figure 4.12: Schematic of arrayed resonator with varactor tuning of individual resonators.

Using the arrayed resonator model and values in Figure 4.11, values for $C_{var,a}$, $C_{var,b}$, $C_{var,c}$, and $C_{var,d}$ can be designed to pull the peaks together. The approach is to pick the highest frequency of the four resonators and tune the others toward that frequency. In this example, resonator “d” had the highest frequency at 496.6 MHz. To tune the other resonators to that frequency, the findings in Section 3.2 can be used to guide the sizing of the C_{var} , namely using Equation (3.3).

To tune to approximately 496.6 MHz, it is found that $C_{var,a} = C_{var,b} = 70$ fF, $C_{var,c} = 140$ fF, and $C_{var,d} = 1$ pF produces close alignment of the frequencies of the individual resonator-varactor combinations. In aggregate (Figure 4.12) this results in the response shown in Figure 4.13. The

4. FLUCTUATIONS FROM MODAL COUPLING IN ARRAYED RESONATORS

varactors have pushed the responses into alignment, which smooths the arrayed response.

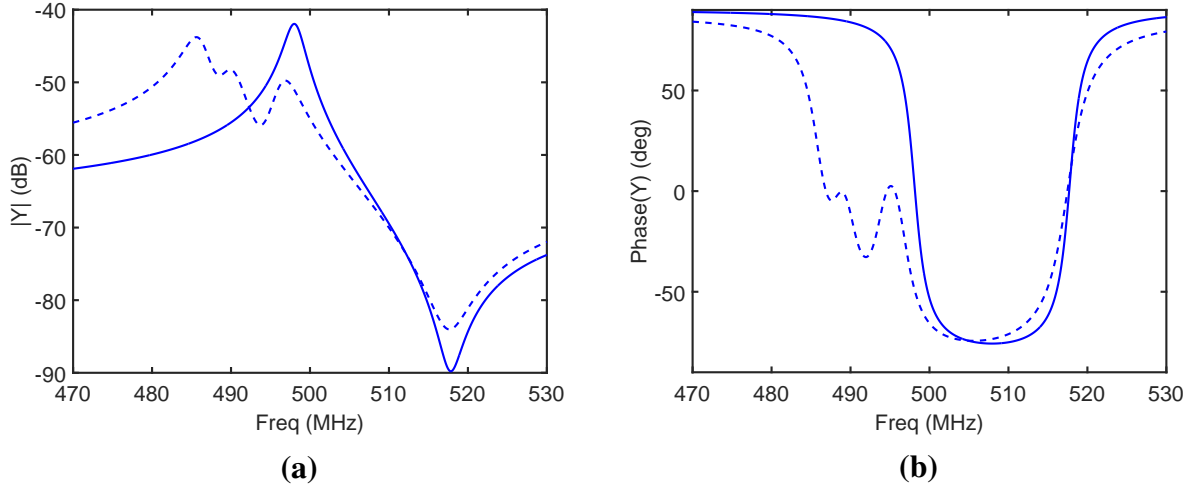


Figure 4.13: Demonstration of frequency alignment using varactors tuning each individual resonator within the arrayed resonator. The dashed line is the model from Figure 4.11, while the solid line corresponds to the circuit in Figure 4.12, using the same resonator values and adding ideal capacitances to align the individual resonators.

4.5.1 Remark on Q and split varactor tuning

This technique holds even if the Q of the resonators is high (in the forgoing simulation, Q had been in the hundreds, whereas the Q of LN resonators can exceed 1000 with adequate process development). Figure 4.14 repeats the simulation, except using $Q = 2000$ and $R_s = R_0 = 0$ per individual resonator. The alignment is still possible (though more sensitive because of the increased Q).

4.5.2 Practical considerations

This subsection identifies and makes estimates about the practical considerations needed to implement the proposed technique of splitting the tuning varactor. The considerations are the varactor size and tuning range, and parasitic capacitance to ground.

4.5 Proposed method to align the response of arrayed resonators

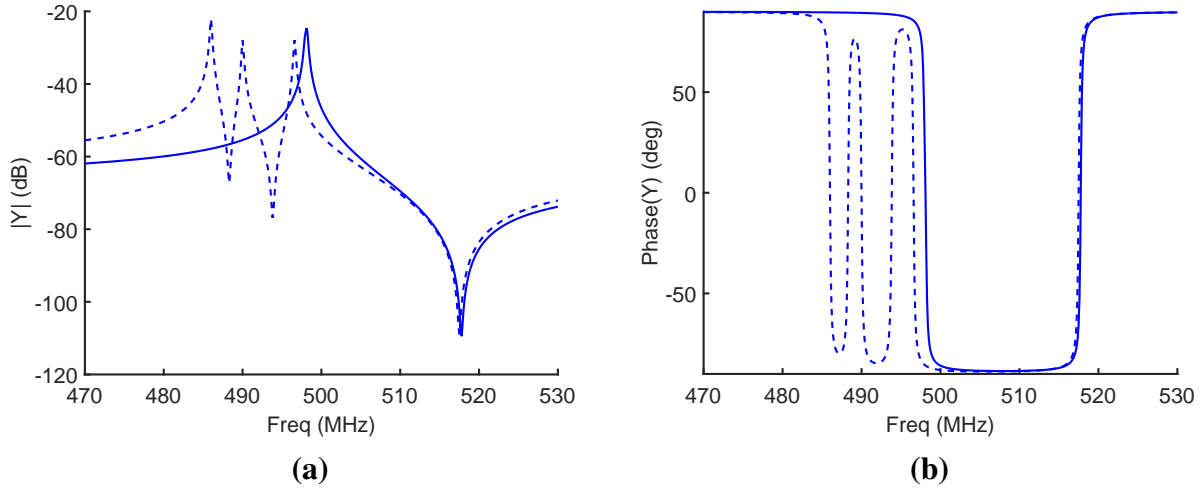


Figure 4.14: High Q demonstration of frequency alignment using varactors tuning each individual resonator within the arrayed resonator. The dashed line is the model from Figure 4.11, while the solid line corresponds to the circuit in Figure 4.12, demonstrating proper alignment. The parameters are the same as for Figure 4.13, except that the Q of each resonator is 2000 instead of 200 and $R_s = R_0 = 0$ for all resonators.

Varactor size is guided by the C_0 of the individual resonators. In the example illustrated in Figure 4.13, the varactor sizing ranged from 70 fF to 1 pF for a $C_0 = 57$ fF (per individual resonator), the maximum size being approximately $C_{var,max}/C_0 = 1 \text{ pF}/57 \text{ fF} = 17.5$ and the minimum size being approximately $C_{var,min}/C_0 = 70 \text{ fF}/57 \text{ fF} = 1.2$. More generally, given a maximum (fractional) frequency deviation Δf , the approximate minimum required varactor capacitance can be estimated using the first-order Taylor expansion of Equation (3.3):

$$C_{var,min} \approx \left(\frac{1}{2} \frac{8}{\pi^2} K_t^2 \frac{1}{\Delta f} - 1 \right) C_0. \quad (4.1)$$

For example, if $\Delta f = \frac{496.6 \text{ MHz} - 486 \text{ MHz}}{486 \text{ MHz}} = 0.022$, $C_0 = 57$ fF, and $K_t^2 = 0.145$, then the above formula predicts $C_{var,min} \approx 1.6C_0$. This is different from the $1.2C_0$ used in the demonstration because, in addition to the Taylor approximation, the formula neglects the tuning of the target frequency (496.6 MHz) by $C_{var,max}$, which in the example was about 498 MHz. Nonetheless,

4. FLUCTUATIONS FROM MODAL COUPLING IN ARRAYED RESONATORS

Equation (4.1) provides a reasonable estimate of $C_{var,min}$ if the designer is given Δf , for example from statistics from fabricated devices.

Varactor tuning range is another practical consideration closely related to the varactor size. In the example, the varactors had a tuning range of $4 \text{ pF} : 70 \text{ fF} = 57 : 1$, which is already a challenge to obtain. This is only to align the response to a baseline value; further tuning range is needed to provide frequency tuning of the aligned response. MEMS-based variable capacitors, such as those integrated in CMOS [26], may meet that challenge with their large tuning ratios, small minimum capacitance, and low parasitic capacitance. Switched varactors may also extend the total capacitance tuning range.

Parasitic capacitance is a practical concern that imposes limits on the minimum size of the individual resonators. As discussed in Chapter 3, a primary source of parasitic capacitance is the bondpads, which cannot be made arbitrarily small; this imposes a constant capacitance to ground that must exist in all practical resonator-varactor combinations. Because each bond comes with a parasitic capacitance, the single varactor in series with the arrayed resonator will have lower parasitic capacitance than the sub-varactors individually bonded to each resonator.

The parasitic capacitance is modeled as a shunt capacitance to ground, C_{pb} , on each terminal of the varactor as shown in Figure 3.8. The resonator-varactor configuration for the notch filter is shown in Figure 4.15 with N being the number of varactors for each arrayed resonator.

Let us assume that the designed value for C_{inv} is large enough to absorb the NC_{pb} parasitic capacitance; this simplifies the number of parasitic elements to only the two parasitics between the two series resonator-varactor combinations. The effect of the parasitic capacitance is two-fold: first, the notch will become shallower because the parasitic capacitance will change the impedance matching, and second, the passband will have more ripple because the parasitic capacitance loads the bandpass filter branch, roughly adding to the outer C_{line} . This is illustrated in Figure 4.16a, where the $|S_{21}|$ ripple at 570 MHz is 0.3 dB without parasitics and about 0.8 dB at the $NC_{pb} \approx$

4.5 Proposed method to align the response of arrayed resonators

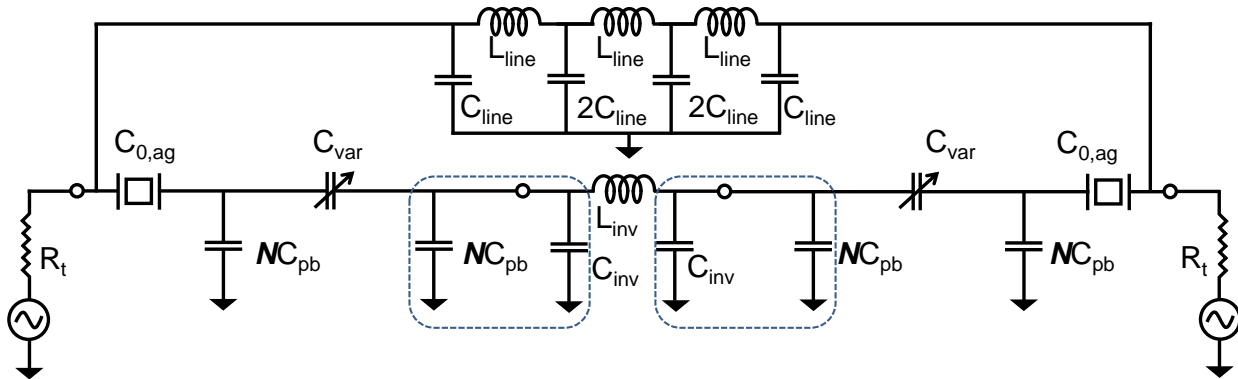


Figure 4.15: Model of an absorptive notch filter including parasitic capacitance due to bond-pads. N is the number of varactors per resonator. The dashed lines indicate where the parasitic capacitance could be absorbed into the design of the filter.

100 fF (and arrayed resonator size $C_{0,ag} = 227$ fF) level of parasitic (to bond one varactor per individual resonator), and the notch depth is about 64 dB without parasitics and about 40 dB at the one varactor per individual resonator.

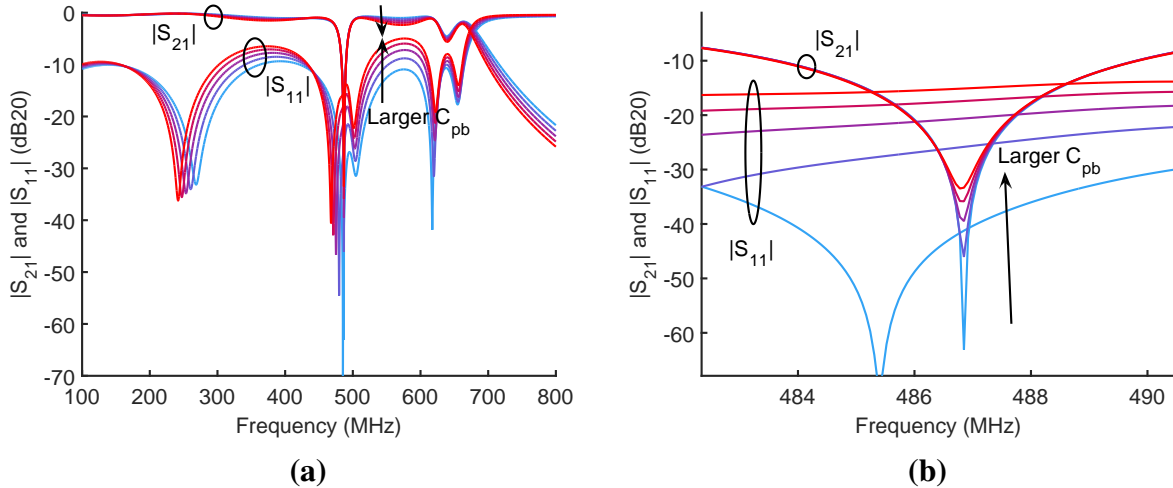


Figure 4.16: Simulated S-parameters for the absorptive notch filter with varying shunt parasitic capacitance C_{pb} . (a) Wide sweep showing increased ripple in the passband, (b) close-up of the notch showing a shallower notch with increased C_{pb} . Filter parameters are the same as in Section 3.3 and the parasitic capacitance is varied from 0 to 227 fF in five linear steps.

To mitigate the parasitic capacitance, the impedance matching can be adjusted to improve the notch depth, and the transmission line capacitors can be adjusted to improve the ripple in

4. FLUCTUATIONS FROM MODAL COUPLING IN ARRAYED RESONATORS

the passband. For the notch, the C_{inv} should be increased slightly to compensate for the current being diverted by the shunt capacitance. This is illustrated in Figure 4.17 (for the $NC_{pb} = 113$ fF, $C_{0,ag} = 227$ fF example), where a notch depth exceeding 50 dB can be achieved.

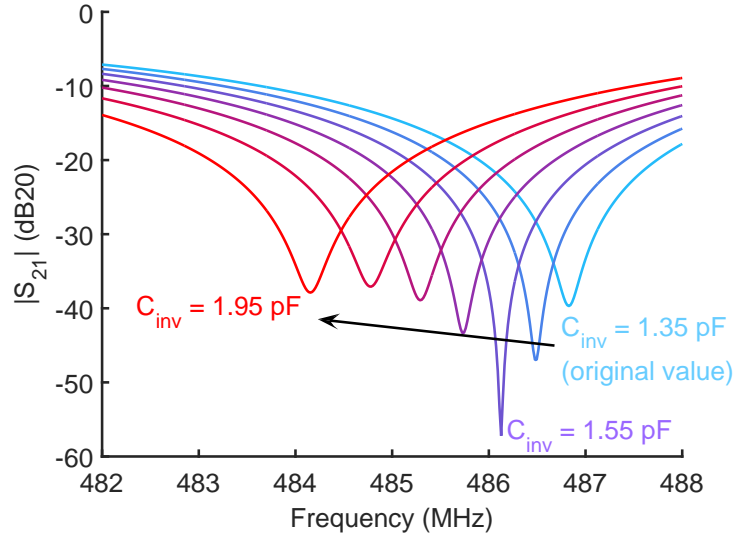


Figure 4.17: Simulated $|S_{21}|$ demonstrating improvement of the notch depth by increasing C_{inv} , which compensates for the parasitic capacitance. The parasitic capacitance is set at $NC_{pb} = 113$ fF (and $C_{0,ag} = 227$ fF) for this example as an estimate of the parasitics expected for one varactor per individual resonator.

To mitigate the ripple in the passband, the outer C_{line} can be adjusted. As shown in Figure 4.18, reducing the outer C_{line} to 476 fF (from 676 fF) smooths the passband to less than 0.2 dB of ripple. Note that the C_{inv} is the 1.55 pF from deepening the notch (Figure 4.17); the reduction of the outer C_{line} does not affect the notch depth.

With these mitigation techniques, it is possible to engineer a deep notch and smooth passband for the estimated $NC_{pb} = 113$ fF and $C_{0,ag} = 227$ fF corresponding to one varactor per individual resonator, thus indicating that the subdivision of arrayed resonators into individually tunable resonators is feasible for the notch filter from the perspective of parasitic capacitance.

4.5 Proposed method to align the response of arrayed resonators

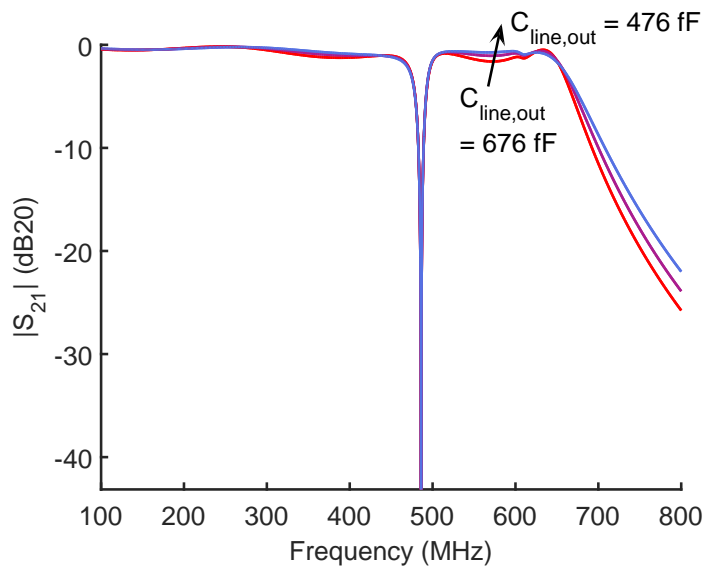


Figure 4.18: Simulated $|S_{21}|$ demonstrating improvement of the passband ripple by decreasing the C_{line} at the outer nodes of the transmission line (shown: 676 fF, 576 fF, and 476 fF), compensating for the parasitic capacitance. The C_{inv} is the 1.55 pF shown to deepen the notch (Figure 4.17); the reduction of the outer C_{line} does not affect the notch depth. The parasitic capacitance is set at $NC_{pb} = 113$ fF (while $C_{0,ag} = 227$ fF) for this example as an estimate of the parasitics expected for one varactor per individual resonator.

This page intentionally left blank

Chapter 5

Resonator spur mitigation

5.1 Introduction

This chapter discusses the origin and mitigation of spurs in single, standalone resonator devices. The filter motivation for spur mitigation, developed in the preceding chapters, is to smooth the passband and to make the tuning range continuous. The chapter starts with methods to quantify the spurs. Then the origins of spurs are surveyed, and scaling laws and tradeoffs are discussed. This chapter ends with a description of the simulations performed to explore the mitigation of spurs due to misalignment and underetch and spurs due to transverse modes.

To quantify the spurs, it is necessary to quantify the frequency of occurrence and some measure of the size of the spurs. One way to do this is to note the difference between magnitude of the spur admittance peak and what the admittance magnitude *would* be if the spur were not there, which can be obtained by interpolating through the spur or by fitting the entire resonator response to a MBVD model (procedure and code to fit to the MBVD model are given in Appendix A.3), which does not contain spurs. An example is shown in Figure 5.1. This method of computing the magnitude difference is the primary method used quantify spurs in this chapter.

5. RESONATOR SPUR MITIGATION

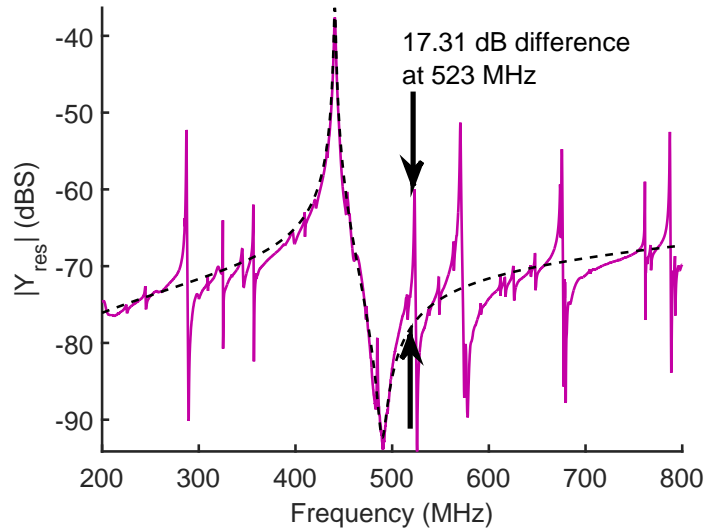


Figure 5.1: Quantifying spurs by their peaks in $|Y|$. The solid trace is the measurement (with spurs). The dashed trace is the fitted MBVD model, which approximates the response if it did not have spurs. Spurs can be quantified by the difference between the measured admittance magnitude at the peak and the MBVD value at that frequency. Appendix A.3 contains the procedure and code used to fit the MBVD model to the measurement.

Another way to quantify the spurs is to consider their impact upon filters. For example, spurs in the passband region will cause ripple in the $|S_{21}|$. In addition, the group delay τ_g will suffer. Outside the passband, spurs might compromise the out-of-band rejection, as in the measured results in Section 2.5, illustrated in Figure 5.2. Therefore, an indirect way to quantify spurs is through comparing the $|S_{21}|$ and τ_g against what they would be without spurs. This can be helpful when deciding on whether a given spur suppression technique is adequate.

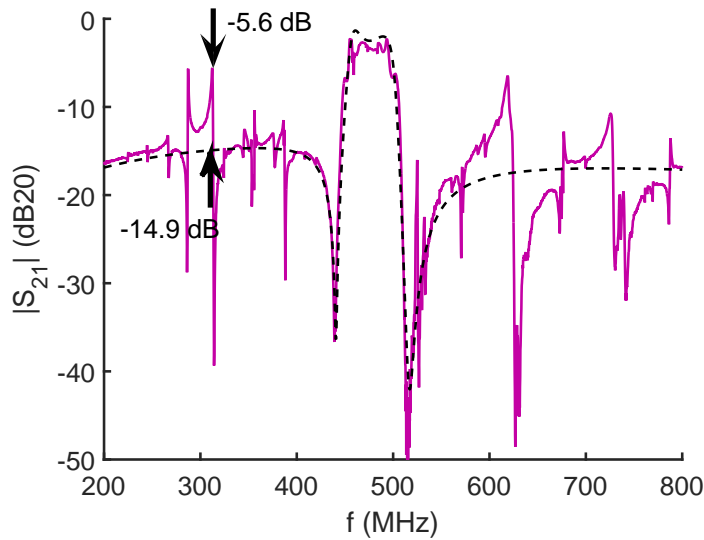


Figure 5.2: Quantifying spurs by their peaks in the filter $|S_{21}|$. The solid trace is the measurement (with spurs). The dashed trace is the filter simulation using a fitted MBVD model, which approximates the response if it did not have spurs. Spurs can be quantified by the difference between the measured admittance magnitude at the spur peak and the simulated value at that frequency. For the spur indicated by arrows, the difference is $-5.6 \text{ dB} + 14.9 \text{ dB} = 9.3 \text{ dB}$.

5.2 Origins of spurs in standalone resonators

This section introduces the equations or techniques to identify the spurs that may appear in measurement of standalone resonators. The spurs appear at all parts of the resonator frequency response, both inside and outside the passband region. Although this makes it difficult at first glance to identify the spurs, the spurs can be divided into those that can be modeled in one, two, and three dimensions.

5.2.1 Misalignment and under/overetch (1D)

Spurs can arise because of the imperfect boundary conditions in the axis of the wave propagation. There are two sources of these spurs: under/overetch and misalignment.

Underetch is defined here as *symmetric* extension W_u of the LN plate in the direction of the

5. RESONATOR SPUR MITIGATION

wave propagation. Overetch is defined using negative W_u . Misalignment is defined as a shift of the electrodes relative to the LN plate. These are illustrated in Figure 5.3.

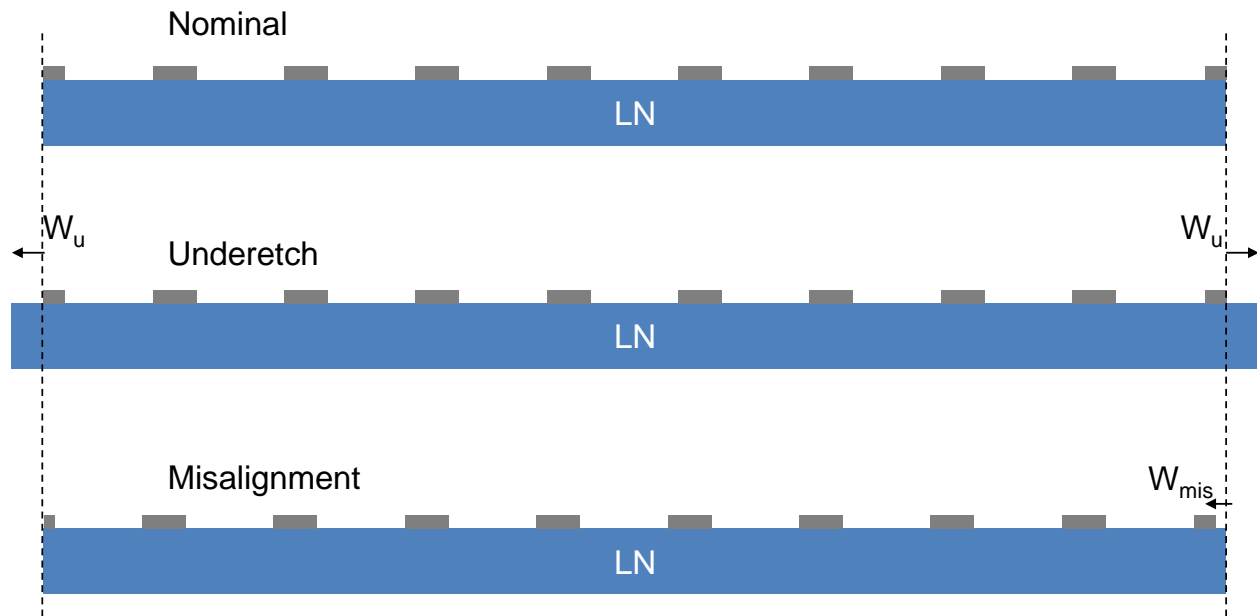


Figure 5.3: Illustration of nominal, underetched, and misaligned resonators. The dashed lines indicate the edge of the nominal device where the edges of the LN and electrodes are aligned.

The number of electrode pairs and the width of the plate dictate the number of nodes in displacement that are transduced. With perfect etching and alignment, and with the electrode fingers located at the mechanical anti-nodes (locations of maximum displacement), the modes fit perfectly into the length of the cavity and only the fundamental frequency is supported; other modes are canceled by the electrodes and cavity length [27].

With under- and overetch, when the cavity length lengthens or shortens relative to the electrode span, two things occur: first, the main mode frequency decreases or increases (respectively), and second, the harmonics start to appear because of the under-enforced boundary conditions on the sides of the resonator. The simulated admittance magnitude is shown in Figure 5.4a; the simulation is performed using COMSOL 2D FEA on a cross section similar to that of Figure 5.3.

With misalignment, the under-enforced boundary condition appears on one side only. The

5.2 Origins of spurs in standalone resonators

simulated admittance magnitude (again using COMSOL 2D FEA) is shown in Figure 5.4b. This thesis will only consider cases where the misalignment is far smaller than the width of the edge fingers, but an extreme case would be a whole half-wavelength shift of the electrodes such that they became located at the nodes (instead of the anti-nodes), which is shown in [27] to suppress the main resonance while exhibiting dominant under- and overtones.

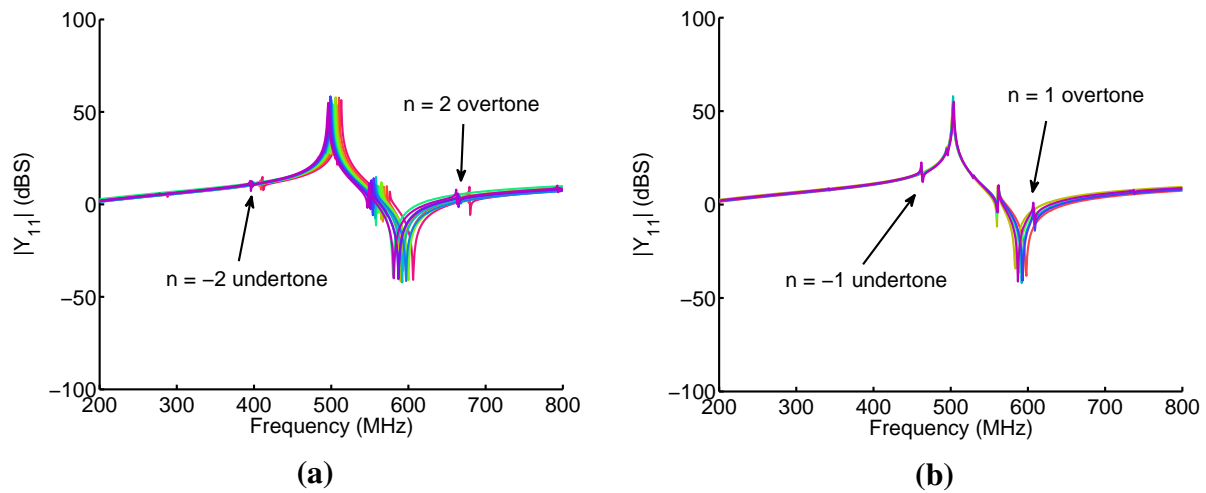


Figure 5.4: 2D COMSOL FEA simulations for (a) under/overetch and (b) misalignment. The underetch is varied from -0.4 to $0.4 \mu\text{m}$, while the misalignment is varied from -0.25 to $0.25 \mu\text{m}$. The pitch of the electrodes is $6 \mu\text{m}$ and there are ten fingers, so the plate width is $54 \mu\text{m}$. The finger width is $2 \mu\text{m}$ for the inner fingers and $1 \mu\text{m}$ for the outermost two fingers. The mode number labels for n correspond to Equation (5.1).

The harmonics appear approximately at frequencies modeled by 1D standing wave theory. Each harmonic corresponds to an integer addition or reduction in the number of displacement nodes in the response. Plots of the displacement across the resonator cross-section are shown for underetch in Figure 5.5 and for misalignment in Figure 5.6. In each plot, the main mode and the closest undertone and overtone are shown. To aid in the development of the model, it can be noted that the number of nodes changes by integer multiples.

Using a 1D model, the modes appear at approximately half-wavelength multiples such that for

5. RESONATOR SPUR MITIGATION

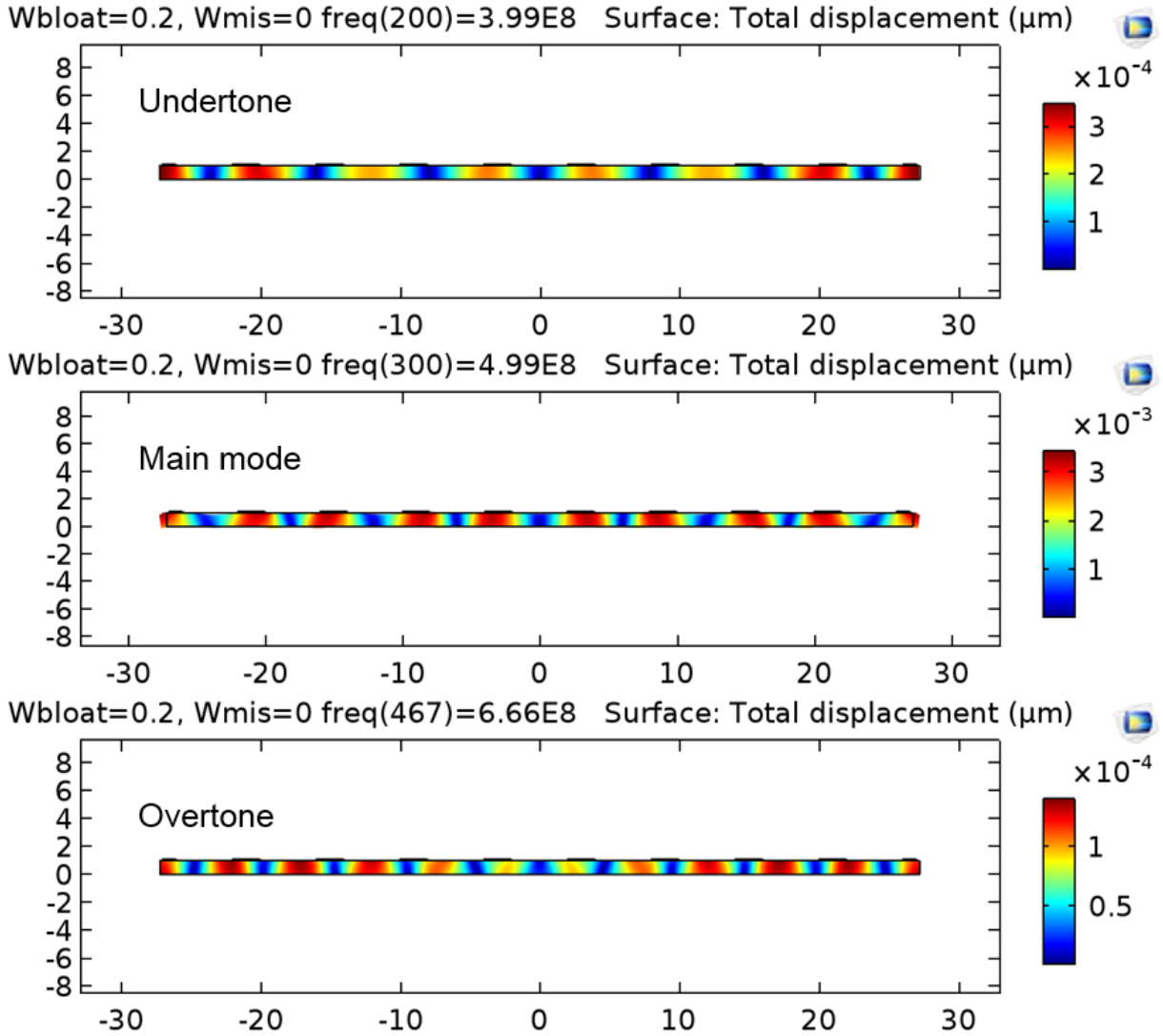


Figure 5.5: Visualization of mode shapes for underetch using 2D COMSOL simulation. Plots of total displacement magnitude are shown for a $0.2 \mu\text{m}$ underetch. The undertone has 7 nodes, the main mode has 9 nodes, and the overtone has 11 nodes. These correspond to $n = -2$, $n = 0$, and $n = 2$ in Equation (5.1). The nominal width of the plate is $54 \mu\text{m}$, or nine half-wavelengths.

overtone number n , the mode frequency appears at approximately

$$f_n = ((N_f - 1) + n) \frac{v_0}{2(W + 2W_u)} = \frac{(N_f - 1) + n}{N_f - 1} f_0 \quad (5.1)$$

where N_f is the number of fingers, n is the mode number (relative to the main mode), v_0 is the

5.2 Origins of spurs in standalone resonators

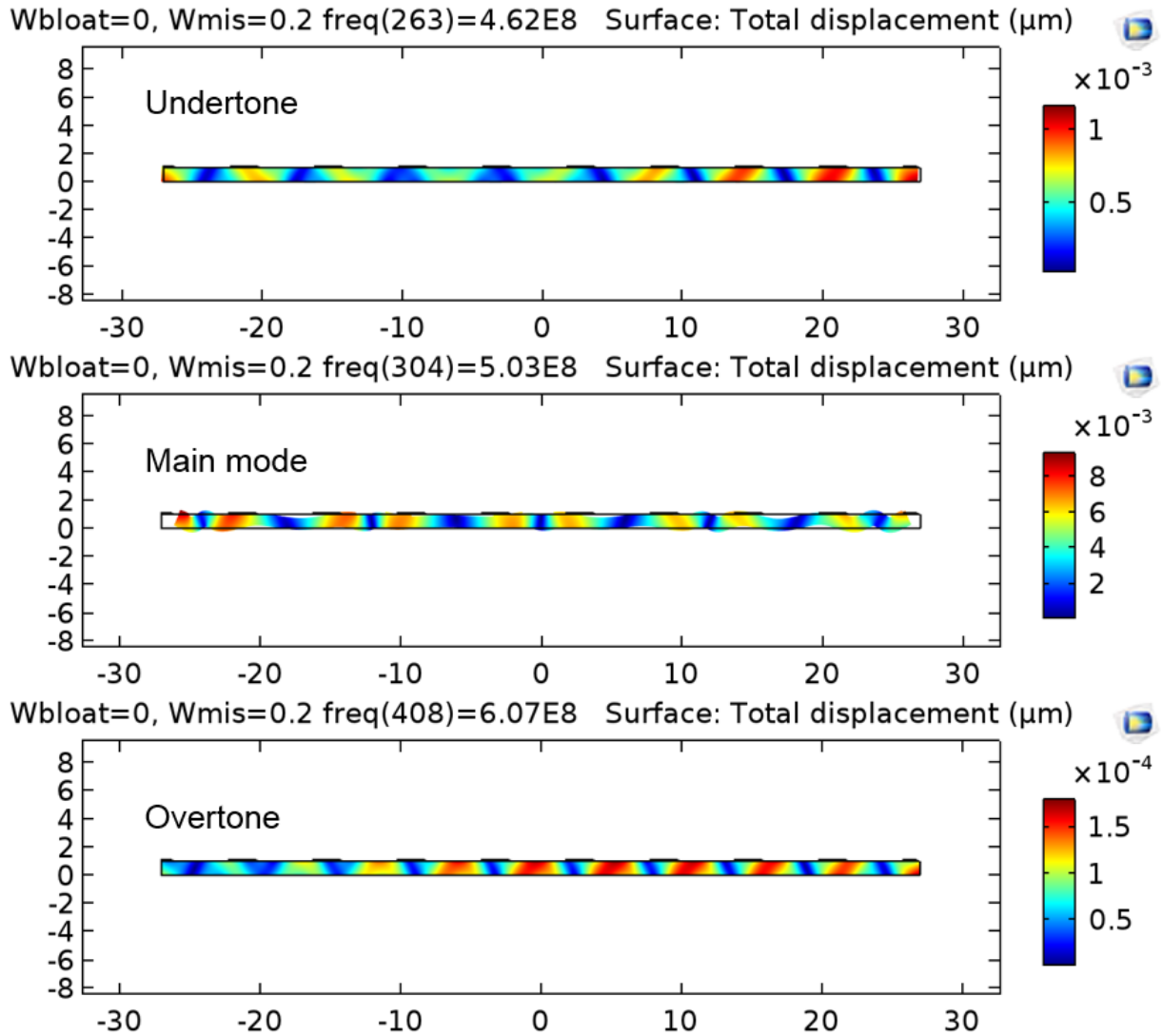


Figure 5.6: Visualization of mode shapes for misalignment using 2D COMSOL simulation. Plots of total displacement magnitude are shown for a $0.2 \mu\text{m}$ misalignment. The undertone has 8 nodes, the main mode has 9 nodes, and the overtone has 10 nodes. These correspond to $n = -1$, $n = 0$, and $n = 1$ in Equation (5.1). The width of the LN plate is $54 \mu\text{m}$, or nine half-wavelengths.

acoustic velocity of the mode, and W is the nominal width of the cavity. f_0 is the main mode with $n = 0$ (including the effect of underetch).

Odd n correspond to the misalignment spurs, where odd multiples of half wavelengths are being added to one side of the cavity. Even n correspond to the spurs due to underetch. $n = 0$

5. RESONATOR SPUR MITIGATION

corresponds to the fundamental mode. The equation indicates that the spurs from misalignment and underetch will superimpose, which can be seen in the measurement later in this chapter.

For ten fingers, the model predicts spurs at $\frac{8}{9}f_0 \approx 0.89f_0$ and $\frac{10}{9}f_0 \approx 1.11f_0$ due to misalignment, and approximately $\frac{7}{9}f_0 \approx 0.78f_0$ and $\frac{11}{9}f_0 \approx 1.22f_0$ due to underetch. The simulations (in COMSOL 2D FEA) result in $0.92f_0$, $1.20f_0$, $0.80f_0$, and $1.33f_0$, respectively. One major contributing factor for the inaccuracy between model and simulation is the antiresonance, which will push out (increase) the frequencies of the upper modes (the ones higher than the main resonance).

The underetch term (W_u) in the equation indicates that there is a change in the frequency even at $n = 0$. This is because of an extension (for $W_u > 0$) or contraction ($W_u < 0$) of the 1D cavity, resulting in longer or shorter vibrational wavelengths, meaning decreased or increased frequencies, respectively. Reframing Equation (5.1), the resonance frequency will be $f_0 = f_{design} \frac{W}{W+W_u}$, where f_{design} is the frequency as designed (no underetch).

5.2.2 Non-S0 modes of vibration (2D)

Spurs can arise because of modes of acoustic vibration that are not the extensional S0 mode being targeted in the resonator design. This effect manifests in 2D analysis of the resonator (with the cross-section slicing along the direction of wave propagation and including the thickness of the film). In terms of design, knowledge about the location of unintended modes of vibration can guide the selection of the device thickness.

The established method to predict the vibrational modes that appear at a given frequency and device thickness is to consult the dispersion diagram for a given material. However, if a dispersion diagram is not available for the particular material stack (as is the case), then simulation of the device in 2D, with visualization of the displacement, can provide information on location of flexural modes that may appear in a given resonator design. In addition, simulating in 3D can capture modes with displacement going out of the page, namely shear modes.

5.2 Origins of spurs in standalone resonators

For example, flexural (asymmetric) modes can be transduced in the resonators in this work because of asymmetry in the material stack [28]. An illustration using COMSOL 2D simulation is shown in Figure 5.7. This A0 mode occurs at 495 MHz, slightly lower in frequency than the main S0 mode (503 MHz), which is consistent with the tendency of the A0 mode to have lower velocity than symmetric modes in a typical dispersion diagram [29] for thin plates.

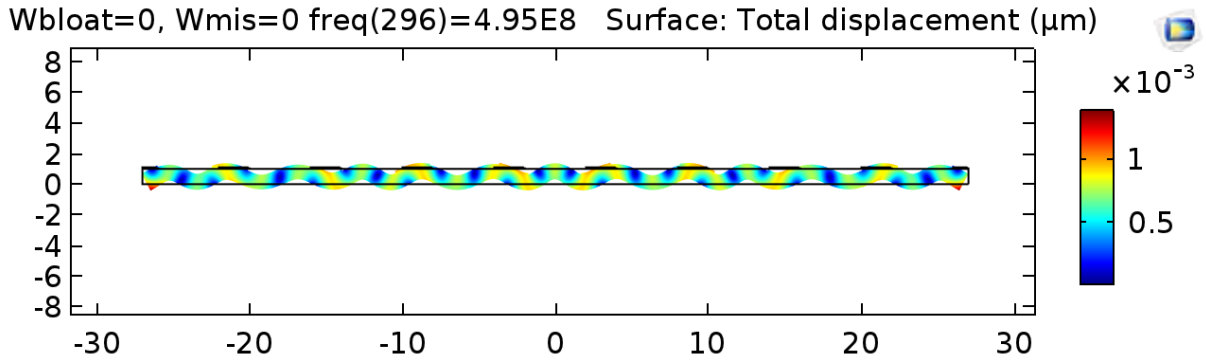


Figure 5.7: Visualization of flexural mode in COMSOL 2D simulation. The total displacement is plotted (with a $500\times$ magnification); the serpentine profile is characteristic of the flexural mode. The frequency is at 495 MHz for a resonator whose S0 mode is at 503 MHz.

5.2.3 Transverse modes (3D)

Going into 3D analysis of the resonator can explain modes that occur close to the resonance of standalone resonators.

In particular, the third-order transverse mode (characterized by the k_{13} wavevector) can occur significantly close to the resonance for typical resonator sizing proportions.

Although the transverse modes are a 3D effect, the model can be compressed into 2D when considering only one type of vibrational mode (e.g., S0). The characteristic equation (adapted from [28]) becomes that of a 2D standing wave, similar to modes in a waveguide:

$$f_{n,m} = v_0 \sqrt{\left(\frac{(N_f - 1) + n}{2W}\right)^2 + \left(\frac{m}{2L}\right)^2}. \quad (5.2)$$

5. RESONATOR SPUR MITIGATION

Similar to before, n is the harmonic number in the direction of wave propagation, v_0 is the acoustic velocity of the mode, and W is the width of the cavity. In the transverse direction, m is the transverse mode number (a positive odd number) and L is the length of the cavity. For example, if the fundamental mode ($N_f = 10$, $n = 0$, $m = 0$) appears at 509.2 MHz, $W = 54 \mu\text{m}$, and $L = 120 \mu\text{m}$, then the third-order ($m = 3$) transverse mode is predicted to appear at 514.9 MHz.

An illustration of the third-order ($m = 3$) transverse mode is shown in Figure 5.8. The x -displacement field (relative to the x of the device) is plotted. This mode appears at 514.9 MHz, in excellent agreement with Equation (5.2).

The approximate x -displacement shape, according to [28], is

$$S(n, m) = A \sin \left(\frac{((N_f - 1) + n)\pi}{W} x \right) \sin \left(\frac{m\pi}{L} \right) \quad (5.3)$$

where A is the amplitude, n and m are the mode numbers (in the case of Figure 5.8, $N_f = 10$, $n = 0$, and $m = 3$), W is the cavity width (x -direction), and L is the cavity length (y -direction). This agrees with the simulation, where in the x direction there is a sinusoidal variation with half-period equal to the finger pitch (the argument of the sine being $\frac{((N_f - 1) + n)\pi}{W} x = \frac{(N_f - 1)\pi}{(N_f - 1)P} x = \frac{\pi}{P} x$), and in the y direction there is a sinusoidal variation with three half-periods fitted in the length of the resonator.

The transverse mode theory also applies to vibrational modes other than S0. For instance, it is possible to encounter third-order transverse modes for the SH0 mode of vibration [30, 31].

These tools enable identification of the spurs by the following steps:

- Measure fabricated dimensions of the resonator as well as possible, including W_u and W_{mis} for the spurs due to underetch and misalignment, and film and electrode thicknesses for spurs due to non-S0 modes of vibration.
- Consult the dispersion diagram or run a simulation to identify the modes of vibration that are possible, and at which frequencies. If an exact film thickness is not available, vary the

5.2 Origins of spurs in standalone resonators

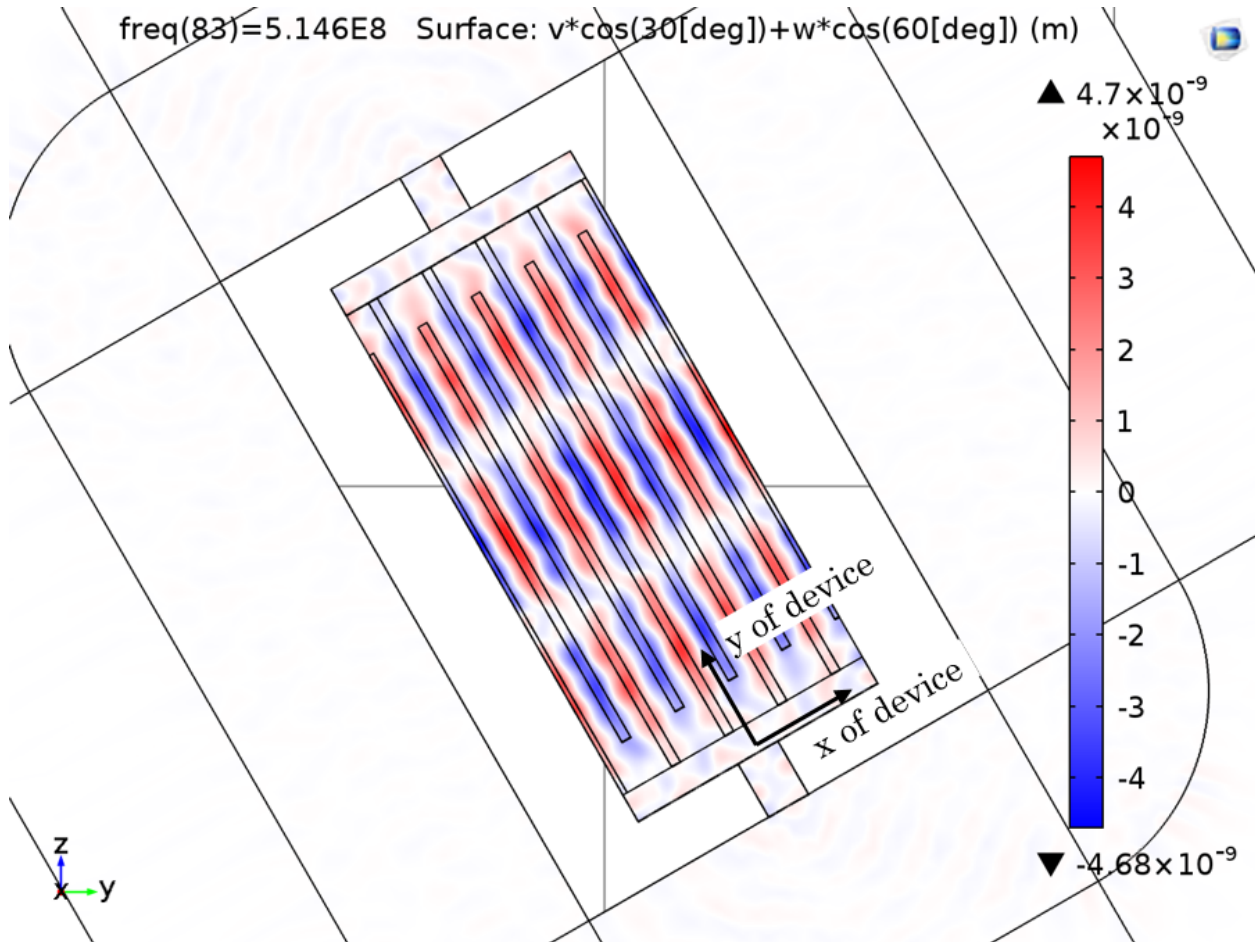


Figure 5.8: Visualization of third-order transverse S0 mode in COMSOL 3D simulation. The color scale represents the x -displacement field. The x and y of the device (the coordinate system of interest) are marked on the resonator. (The rotation relative to the global coordinates is at -60 degrees to the z -axis in x -cut LN to obtain high K_t^2).

thickness (of the piezoelectric film and of the electrode) slightly to see if flexural modes coincide with measured spurs.

- Find ν_0 (or f_0) for each mode of vibration from knowledge about the main mode frequency and 1D cavity size, using Equation (5.1) with $n = 0$ for the main mode.
- Calculate the 1D harmonics due to misalignment and under- or overetch for each mode of vibration using Equation (5.1).

5. RESONATOR SPUR MITIGATION

- Calculate the transverse modes for each mode of vibration using Equation (5.2).

As an example, the measurement of the shunt resonator device of Section 2.5 can be dissected. An annotated image of the device is shown in Figure 5.9. The simulation indicates that the $6.551 \mu\text{m}$ pitch will provide a nominal resonance frequency of 457 MHz. The admittance magnitude is plotted in Figure 5.10, showing an actual resonance frequency of 440.7 MHz.

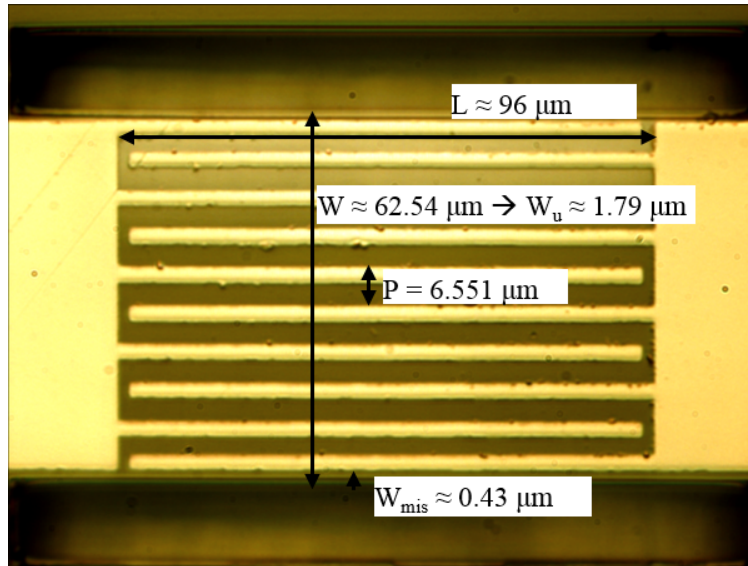


Figure 5.9: Microscope image ($50\times$ magnification) of standalone shunt resonator, with $6.551 \mu\text{m}$ pitch, with measured dimensions labeled.

There are ten fingers, so the nominal width of the cavity is $58.959 \mu\text{m}$. The image has labels of the actual dimensions of the device (as measured from the image using ImageJ software), showing underetch of $W_u = (62.54 \mu\text{m} - 58.959 \mu\text{m})/2 = 1.79 \mu\text{m}$ on each side, and misalignment of $W_{mis} = 0.43 \mu\text{m}$. The fingers were designed to all be $2.265 \mu\text{m}$ wide, but the fabricated widths are $2.348 \mu\text{m}$ for the inner fingers and $2.663 \mu\text{m}$ for the outer fingers. The thickness of the metal is nominally 100 nm , but estimated to be about 50 nm because resistivity measurements (using a meandering line test structure) were about twice the nominal value.

A 2D simulation (runtime: about five minutes) using the measured dimensions explains most of the spurs outside the resonance. To estimate the thickness of the LN film (nominally $1 \mu\text{m}$),

5.2 Origins of spurs in standalone resonators

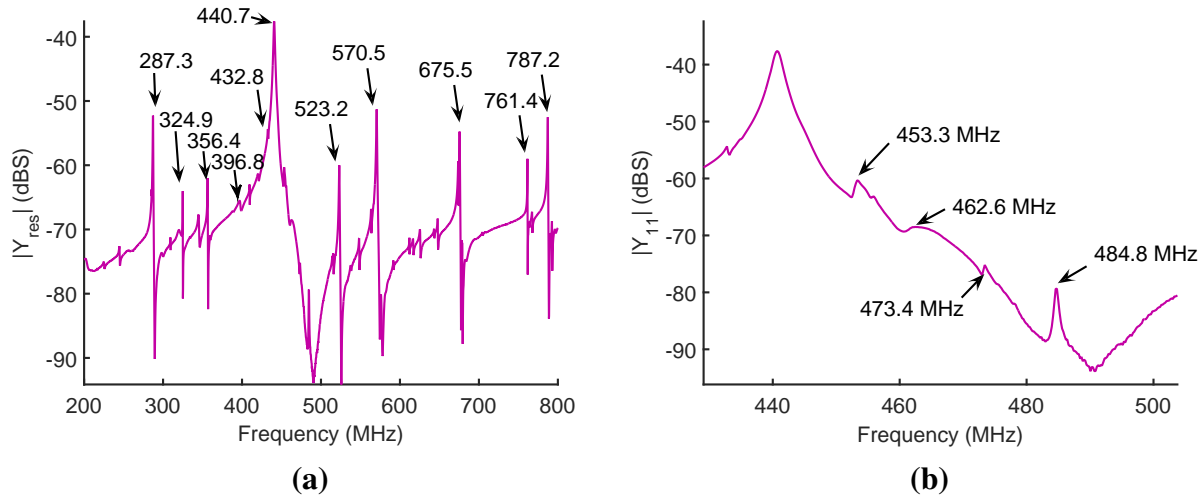


Figure 5.10: Admittance of the standalone shunt resonator, with close-up view of rolloff. Labels indicate the location of spurs.

the thickness is swept in the simulation and the behavior of the flexural modes is compared to the spurs in the measurement. In the 2D simulations shown, the thickness used is $0.9 \mu\text{m}$. Figure 5.11 plots the simulated admittance on the measured response, showing good agreement in between simulation and measurement in terms of the frequency locations. Three major discrepancies between design and measurement are explained by the misalignment and underetch: the K_t^2 reduction (predicted: 40%, measured: 28%), the frequency reduction (predicted: 457 MHz, measured: 440.7 MHz), and spurs outside the resonance. A comparison of measurement, simulation, and 1D theory is summarized in Table 5.1, showing good agreement between simulation and measurement and a consistent underestimation of the theory (by about 6%) for the spurs above resonance.

The transverse modes for the S0 mode are predicted (by Equation (5.2), using measured dimensions) to appear at 450 MHz, 465 MHz, and 488 MHz. This agrees quite well with the measurement (Figure 5.10b), which has spurs at 453.3 MHz, 462.6 MHz, and 484.8 MHz.

The flexural mode frequencies change with the thickness of the LN film (by dispersion), so a simulation thickness is chosen to place flexural modes in locations corresponding to measured

5. RESONATOR SPUR MITIGATION

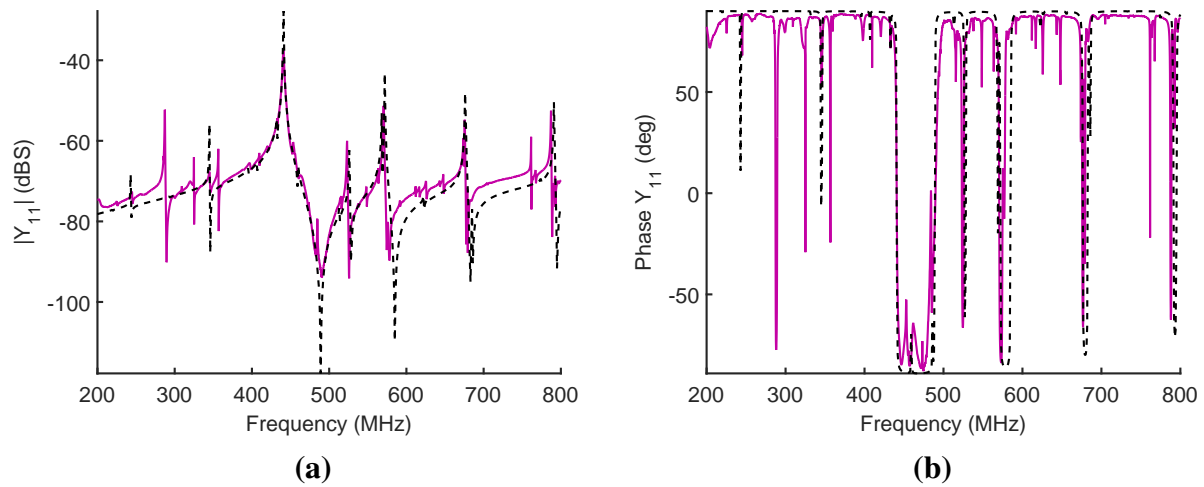


Figure 5.11: 2D COMSOL simulation (dashed) vs. measurement (solid) for resonator, explaining the K_t^2 reduction, the frequency shift, and spurs outside resonance, all due to misalignment and underetch. The dimensions were obtained from the microscope image of the device, shown in Figure 5.9. A close-up showing the location of flexural modes is shown in Figure 5.12.

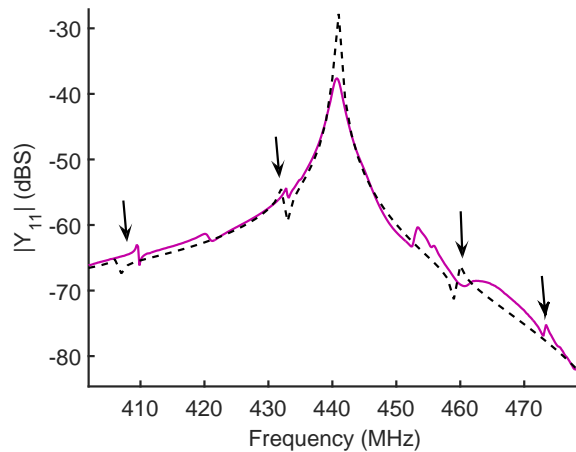


Figure 5.12: Zoomed-in view of 2D COMSOL simulation (dashed) vs. measurement (solid) for the resonator, focusing on flexural modes.

spurs: in this simulation a $0.9 \mu\text{m}$ film ($1 \mu\text{m}$ is the nominal thickness according to the vendor) in the 2D simulation shows flexural modes near 406 MHz (with 28 displacement nodes), 432 MHz (29 nodes), and 460 MHz (30 nodes). The measurement has spurs at 409.4 MHz, and 432.8 MHz. The comparison between measurement and 2D simulation near the resonance is shown in Figure 5.12.

5.2 Origins of spurs in standalone resonators

Table 5.1: Comparison of spur frequencies for measurement, 2D simulation, and theory for misalignment and underetch, using the values marked in Figure 5.9. This table does not provide much information about amplitude, though in general the spurs for odd n were smaller than for even n . The “none” for $n = 5$ is because the spur was too small to measure in both the simulation and measurement. The equation routinely underestimates the spurs above the resonance ($n > 0$) by about 6% because the antiresonance (which is not accounted for by theory) pushes the frequencies higher. The $n = 0$ frequency for the theory is 440.7 MHz as an input taken from the measured value, whereas calculating Equation (5.1) using just the nominal designed velocity and measured underetch would predict 443 MHz.

n	Measurement	2D simulation	Equation (5.1)
-4	244.7 MHz	243 MHz	245 MHz
-3	298.1 MHz	293 MHz	294 MHz
-2	345.0 MHz	345 MHz	342 MHz
-1	396.8 MHz	395 MHz	392 MHz
0	440.7 MHz	441 MHz	440.7 MHz (input)
1	523.2 MHz	526 MHz	490 MHz
2	570.5 MHz	572 MHz	539 MHz
3	625.3 MHz	622 MHz	587.6 MHz
4	675.5 MHz	676 MHz	637 MHz
5	none	none	686 MHz
6	787.2 MHz	791 MHz	734 MHz

It is ambiguous whether the simulated 460 MHz A0 mode (in the 2D simulation) corresponds to the measured 462.8 MHz spur (which was accounted for by transverse mode theory) or the measured 473.4 MHz spur; a 3D simulation (runtime: about 33 hours) can clarify this. A 3D simulation including misalignment, underetch, and guessed thickness is shown in Figure 5.13. The simulation exaggerates the Q (because it only accounts for anchor loss). The order of the spurs is close to those seen in the measurement. It can be seen that the flexural mode most closely relates to the spur measured at 462.8 MHz.

5. RESONATOR SPUR MITIGATION

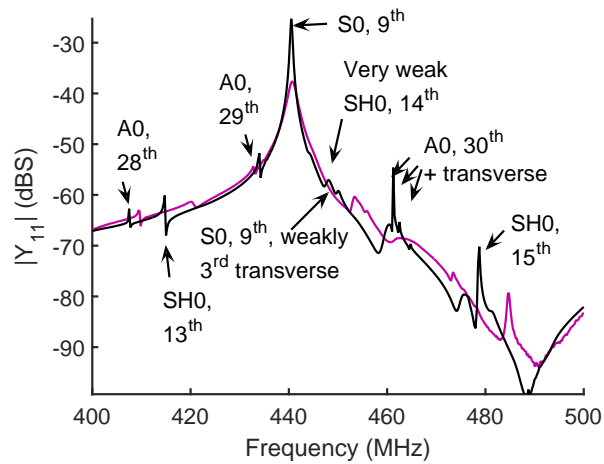


Figure 5.13: Zoomed-in view of 3D COMSOL simulation (dashed) vs. measurement (solid) for the resonator, with modes labeled. The cardinal number by each mode indicates the number of nodes that are in the width direction of the resonator.

5.3 Scaling laws and tradeoffs

The resonator spurs may change their behavior when scaling the size and frequency of the resonators. This section describes these scaling laws and tradeoffs.

- **Misalignment and under/overetch: scaling with frequency.** The absolute value of misalignment and under/overetch are independent of the device frequency. However, their relative value will scale with frequency, because the electrode pitch and width scale inversely with frequency. Therefore, for a given amount of misalignment and underetch, resonators at higher frequencies will experience more severe harmonics outside resonance.
- **Dispersion: scaling with frequency or thickness.** Changing the thickness of the film or the frequency of operation moves along the dispersion curve; therefore, the relative locations of the non-S0 modes will move around unless the ratio of frequency to thickness is held constant. This scaling is dictated by the dispersion relation of the material stack.
- **Transverse modes: scaling with aspect ratios and frequency.** The location of the trans-

5.4 Further details on mitigating spurs due to misalignment and under- and overetch

verse mode scales by the aspect ratio of the resonator width and length. For a fixed frequency (W), this means that (by Equation (5.2)) a longer L will bring the transverse mode closer to the main mode. When changing the frequency while maintaining aspect ratio, the location of the transverse modes will remain the same, relative to the main mode.

5.4 Further details on mitigating spurs due to misalignment and under- and overetch

This section presents a study of the spurs due to misalignment and under- and overetch in more detail. For this study the spurs due to non-S0 modes and transverse modes are neglected; this effort is focused primarily on spurs due to misalignment and under- or overetch.

5.4.1 Simulation of sensitivity to misalignment and underetch

Using 2D COMSOL FEA simulations provide the sensitivity of the resonator spurs to underetch and misalignment, which can provide an idea of how much tolerance to misalignment and underetch can be tolerated. Initial tests with the stepper machine in the CMU NanoFab provided alignment within $\pm 0.25 \mu\text{m}$; the amount of underetch has been about $0.4 - 0.8 \mu\text{m}$ in previous runs but is not well characterized. The spur amplitudes increase as the misalignment and over/underetch deviate farther from 0, as illustrated in the simulated results of Figure 5.14.

The filter is sensitive to the spurs because of the spurious peaks in the stopband. The misalignment and underetch spurs affect the out-of-band rejection, so these spurs can be quantified in the filter domain by the difference between the filter $|S_{21}|$ with and without the spurs. For example, the simulated filter sensitivity to misalignment at the $n = -1$ undertone is plotted in Figure 5.15. The simulation is performed by inserting the results of COMSOL 2D simulations of series and shunt

5. RESONATOR SPUR MITIGATION

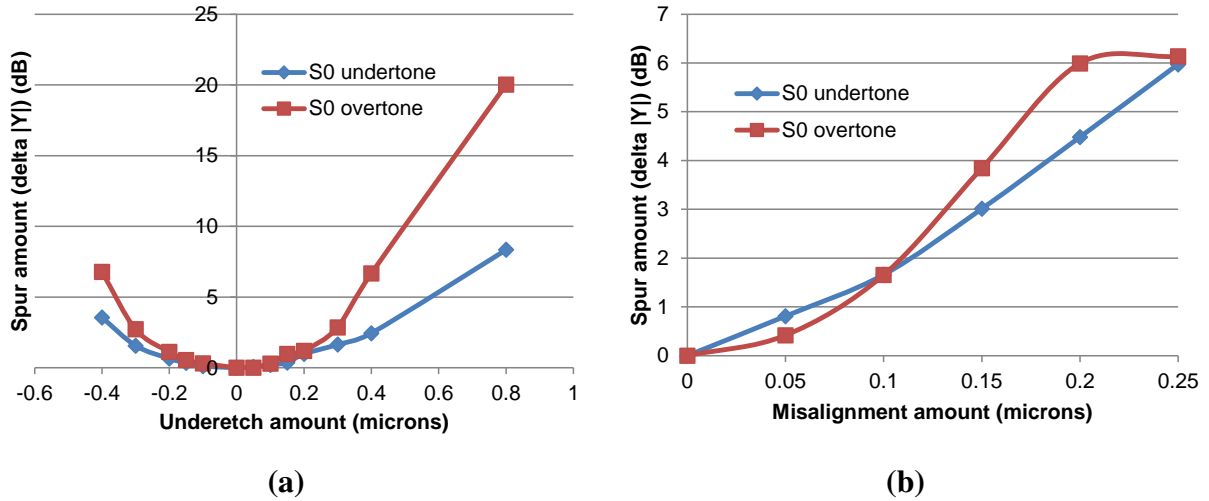


Figure 5.14: Simulated spur magnitude as a function of (a) underetch (W_u) and (b) misalignment (W_{mis}) amounts, for the undertone and overtone spurs, using COMSOL 2D simulation. The frequency responses are plotted in Figure 5.4. In the case of misalignment, the undertone corresponds to $n = -1$ and the overtone corresponds to $n = 1$. In the case of underetch, the undertone corresponds to $n = -2$ and the overtone corresponds to $n = 2$.

resonators (at the varying W_{mis}) into the 1T ladder topology (Figure 2.11).

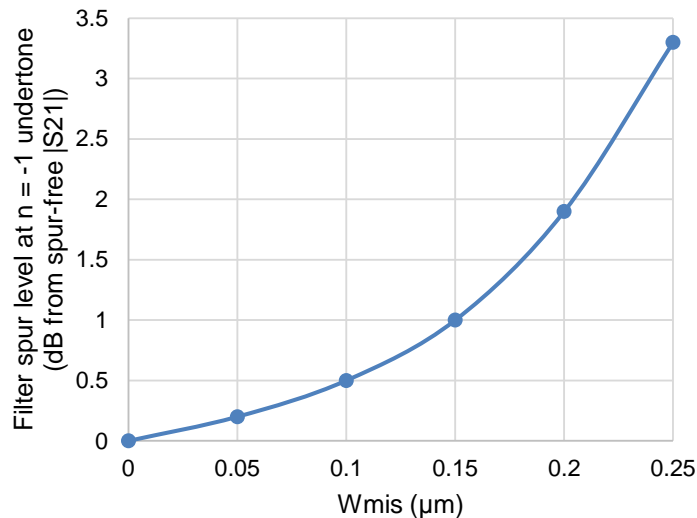


Figure 5.15: Simulated effect of misalignment spurs upon filter out-of-band rejection in the region of the $n = -1$ undertone. The admittance from COMSOL 2D simulation are inserted into an ideal filter simulation to obtain the response with spurs. The method to quantify the spurs is illustrated in Figure 5.2.

5.4 Further details on mitigating spurs due to misalignment and under- and overetch

If this were to be fabricated, a method of control would be to design single resonators with prescribed amounts of overetch compensation and x and y misalignment; a well-chosen range will yield one device that “perfectly” compensates for overetch and misalignment. The misalignment could range from $-0.2\ \mu\text{m}$ to $0.2\ \mu\text{m}$ in steps of $0.2\ \mu\text{m}$, which, according to the simulation, results in fairly small resonator spurs ($< 2\ \text{dBS}$) and small filter spurs ($< 1\ \text{dB}$). The overetch compensation ranges from $0.5\ \mu\text{m}$ to $1.5\ \mu\text{m}$ in steps of $0.5\ \mu\text{m}$, which results in resonator spurs below $3\ \text{dBS}$ and filter spurs below $1\ \text{dB}$. A layout of a full ladder filter is included at each combination of misalignment and underetch in order to study their effects on the filter.

The baseline resonator is designed for future fabrication runs to carry out this misalignment and underetch study. The design target is minimal loss in order to avoid smothering the spurs. The design process starts with the design of the interdigitated electrodes to have optimal reflector electrode coverage ($W_r = W_f/2$, where W_r is the width of the fingers at the edges of the resonator and W_f is the width of the main electrode fingers in the middle of the resonator). This reflector electrode coverage uniformly distributes the electric field across the cavity, so that a perfectly fabricated device would have no overtones or undertones [27]. (This is different from the “active reflectors” in [10], where the reflector electrode coverage was intentionally increased to compensate for overetch at the expense of spurs outside the passband, even with perfect alignment and etching, due to the unevenly distributed electric field). Then, to design the ends of the resonators, sweeps of anchor dimensions and gap-to-bus spacing are employed, using COMSOL Multiphysics FEA with a Perfectly Matched Layer, similar to in [19]. An excellent Q comes with anchor width $W_a = 9\ \mu\text{m}$, anchor length $L_a = 12\ \mu\text{m}$, and finger-to-bus spacing $G = 9\ \mu\text{m}$. This configuration yields an anchor-loss-only Q exceeding 53,000. The frequency response as simulated using COMSOL 3D FEA is shown in Figure 5.16. The spur around 515 MHz is caused by the third-order transverse mode, which is to be addressed in a separate study.

5. RESONATOR SPUR MITIGATION

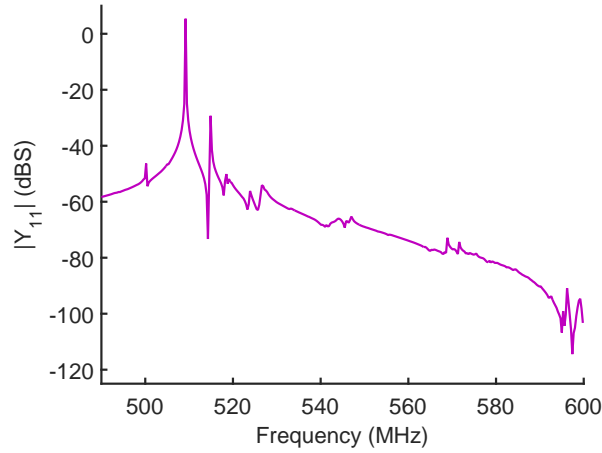


Figure 5.16: Admittance of resonator with high Q simulated in COMSOL 3D FEA with a Perfectly Matched Layer boundary condition, to be used for the study of misalignment and underetch. The gap between the finger and bus is $G = 9 \mu\text{m}$ and the anchor dimensions are $W_a = 9 \mu\text{m}$ and $L_a = 12 \mu\text{m}$.

5.5 Transverse mode suppression techniques

In addition to the study on the misalignment and underetch, several devices to validate a technique to suppress the third order transverse mode spur were also designed. This technique involves the use of stubs [28, 32] in order to cancel the third order transverse mode while minimally affecting the main mode.

5.5.1 Simulation setup

A layout labeled with the dimensions of interest is shown in Figure 5.17.

The optimum electrode overlap, L_{ov} , should be two-thirds the total length of the resonator, L_{res} [28]. Therefore, for a 500 MHz ($\lambda = 12 \mu\text{m}$) resonator length of $L_{res} = 120 \mu\text{m} = 10\lambda$, the nearest half-wave multiple of $\frac{2}{3}L_{res}$ is chosen, so $L_{ov} = 84 \mu\text{m}$. Leaving the bus width at $\lambda/2 = 6 \mu\text{m}$ [19], this leaves a $12 \mu\text{m}$ gap between the end of the resonator and the bus. Therefore, the parameter being swept is L_{stub} , the stub length.

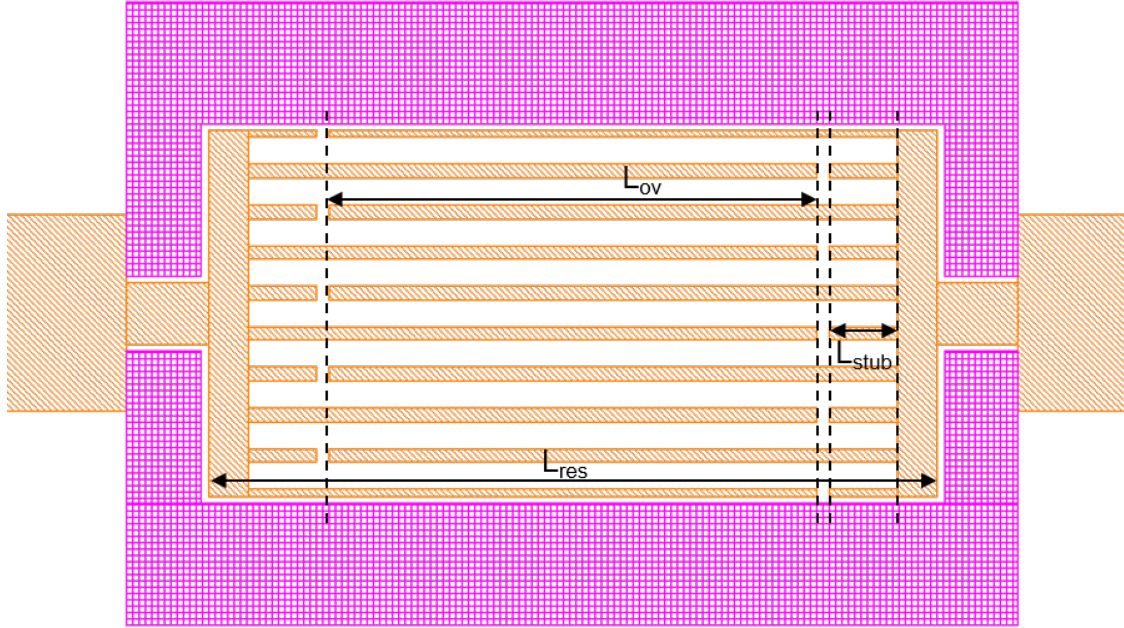


Figure 5.17: Labeled layout of resonator with stubs for transverse spur suppression. The orange hatch is the electrode layer, the white is LN, and the pink grid-hatch is the etch pit layer.

The hypothesis is that the stub length will control the amount of spur suppression, with the longest stub lengths maximally canceling out the third-order transverse mode. However, if the stub is long enough such that the gap to the end of the opposing electrode is “small” (smaller than the spacing between adjacent electrodes, for instance), then the hypothesis is that the gap will promote electric fields in the perpendicular direction to wave transduction, thus impacting $K_t^2 Q$.

Initial simulations performed using COMSOL 3D FEA indicate successful spur suppression as a result of adequately long stubs. Figure 5.18 shows a comparison of $L_{stub} = 0 \mu\text{m}$ (no stub) swept in $3 \mu\text{m}$ (quarter-wavelength) increments to $L_{stub} = 9 \mu\text{m}$ in 3D simulation. In the case of the no-stub design, there is a third-order transverse mode around 516 MHz. Lengthening the stub to $9 \mu\text{m}$ largely attenuates that mode. The Q (counting anchor losses only, for this simulation with

5. RESONATOR SPUR MITIGATION

PML boundary conditions) is reduced from over 7,000 ($L_{stub} = 0 \mu\text{m}$) to 2,100 ($L_{stub} = 9 \mu\text{m}$). This is an acceptable trade-off, as filter design would be adequate with $Q = 1000$ (as in the simulations in Chapter 2).

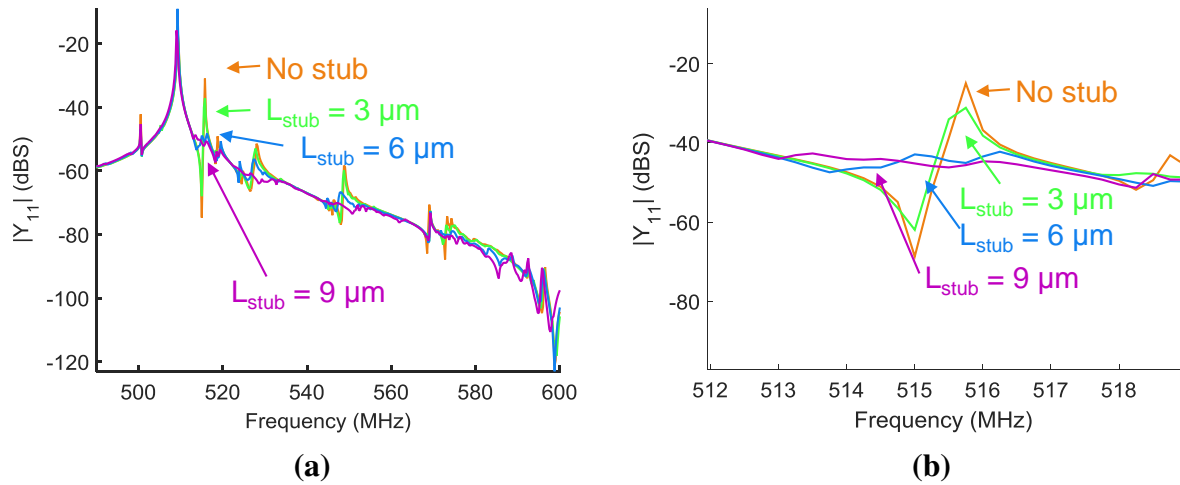


Figure 5.18: COMSOL 3D simulation showing suppression of the third order transverse mode with increased stub coverage. (a) Wide frequency sweep, (b) close-up of the third-order transverse mode, which is suppressed as the stub length is increased.

Chapter 6

Conclusion

This thesis has presented groundwork that can lead to compact reconfigurable filter banks. It has addressed key challenges to advancing the state-of-the-art using filters implemented in lithium niobate.

The first challenge is to demonstrate a fixed filter in LN with good performance (low insertion loss, wide bandwidth, and a smooth and accurate frequency response). To that end a ladder filter has been designed as a testbed for baseline filter performance. The design includes image impedance design principles to smooth the passband and rolloff as compared to the direct adaptation of filter topologies designed with low- K_f^2 approximations. The measured results from an initial fabrication run showed good frequency precision (within 1% tolerance) and comparable insertion loss (< 3 dB) to that of the state-of-the-art, but had spurious modes and poor frequency accuracy. These shortcomings prompted the investigation of spurs in the latter half of this thesis.

The second challenge, that of tuning the filters, is addressed in theory for the ladder bandpass filters and in measurement for an absorptive notch filter. For the bandpass filter, an outline is presented overviewing the varactor configurations that can steer a narrow passband within the envelope defined by the maximum filter bandwidth. The effect of parasitic capacitance from bonding

6. CONCLUSION

the resonators to the varactors is also analyzed, and a way to compensate for the parasitic capacitance by increasing the frequency of the shunt resonators is proposed, thus sacrificing a small amount of tuning range (in the example presented, about a 20% reduction in tuning range) for a smooth passband. A tunable notch filter has demonstrated in experiment the viability of using external varactors in series with the resonators to tune the frequency with a tuning range of about 6% of the K_t^2 . Whereas the state-of-the-art bulk acoustic wave filter bank lacks tuning of the individual filters, this demonstration has finally brought tuning (in a prototype form on a PCB) to the realm of filters created with miniaturized resonators, and could be extended to using chipscale components such as CMOS or CMOS-MEMS inductors and tunable capacitors. Discontinuities in the tuning range are due to fluctuations in the resonator near resonance, further motivating the investigation into fluctuations due to coupling and spurs in individual resonators.

Because of their impact on filter performance and tuning range, fluctuations or spurs are a major challenge impacting the filters. Fluctuations are considered from the perspective of arrayed resonators (resonators in parallel), and spurs are considered from the perspective of individual resonators.

For arrayed resonators, Chapter 4 has presented studies on the effect of mechanical coupling (through the released plate) between identical resonators and the effect of electrical coupling between non-identical, mechanically-isolated resonators. For the latter, a way to align the frequency response using varactor tuning of the individual resonators has been proposed, including an analysis and proposed method to mitigate the effects of parasitic capacitance (from the bond pads) upon the tunable notch filter.

For spurs in individual resonators, the impact of misalignment and underetch has been studied. The misalignment and underetch not only introduce spurs at intervals modeled by a 1D cavity, but also reduce the K_t^2 . In addition, the underetch lowers the resonance frequency because of the extension in the acoustic cavity width.

In addition to the study of spurs due to misalignment and underetch, the technique of mitigating spurs due to transverse modes by using stubs in the electrodes was simulated for extensional-mode LN microresonators. An investigation was carried out in simulation to study the effect of stub length upon the mitigation of the third-order transverse spur (for a fixed resonator and interdigitated electrode overlap amount). The results suggest that a stub at least half the gap is needed to suppress the third order transverse mode.

6.1 Future prospects

Several research and development directions have been identified to increase the usability of the LN microresonator reconfigurable filter banks.

6.1.1 Increasing resonator f_s, C_0, K_t^2 , and Q

The reader might wonder: out of the four main parameters in the MBVD model (f_s, C_0, K_t^2 , and Q), which parameters would be the best to improve? This section explains the benefits of improving each parameter.

It is critically important to increase the resonator frequency f_s in order for LN filter banks to become reality. This thesis has provided demonstrations using 500 MHz resonators for the practical reason of clean lift-off during fabrication, but there is no fundamental barrier to applying the design principles here to resonators at frequencies in the GHz range where the radio spectrum is most crowded [1]. The designer should choose a thin LN substrate to cut off higher order vibrational modes (from dispersion).

The C_0 was found to impact the termination impedance, and 50Ω requires about 6 pF of C_0 at around 500 MHz. This work has examined the effects of modal coupling when extending the C_0 by using arrayed resonators (Chapter 4). The C_0 required for 50Ω scales inversely with the frequency,

6. CONCLUSION

and the resonator has higher capacitance density for higher frequencies (because the interdigitated electrodes are closer), so the size requirements relax as frequency is increased. As an example, a 2.4 GHz resonator would need to be just $70 \mu\text{m} \times 120 \mu\text{m}$ in size to satisfy the approximately 1.2 pF C_0 for 50Ω termination impedance. Therefore, pushing for higher f_s should relax the sizing requirements (C_0) for termination impedance.

The K_t^2 has been found to directly dictate the tuning range of the filters. As such, increasing the K_t^2 would mean increasing the tuning range, which would decrease the number of filters needed to cover a given tuning range application. This relaxes the requirements on the reconfiguration (switching) network. In addition, higher K_t^2 means more margin for using the techniques to compensate for parasitic capacitance (Chapter 3 and Chapter 4).

At first glance, increasing Q seems to be a development with steeply diminishing returns; the insertion loss of the bandpass filter was demonstrated to be low despite some losses due to $Q < 1000$ (Chapter 2 used $Q = 500$ for the simulations using the COMSOL model). However, high Q has a second-order effect on tuning range. From the design sections in Chapter 2, it can be seen that the IL and out-of-band rejection trade off when cascading filter sections – the more filter sections, the higher (worse) the IL and the higher (better) the OBR. Therefore, an increased Q would increase the IL-OBR design space. In the f_c -FBW tuning range diagram of Chapter 3, the OBR turned out to be the limiting factor for the bottom edge of the tuning range. Therefore, increasing Q can indirectly increase tuning range by allowing more OBR for the same IL.

It is therefore beneficial to increase all four MBVD parameters. However, the f_s and K_t^2 each bring multiple benefits for filter bank applications, and thus may be prioritized.

6.1.2 More resonator routing layers

In this thesis, the microresonators used were built with just one routing layer for the electrodes. This means that the devices were lateral field excitation (LFE) devices, with a low C_0 density thanks

to the wide spacing of the electrodes (relative to their pitch). This low C_0 can lead to large arrays of devices in order to satisfy impedance matching (the notch filter had a termination impedance of almost 500Ω and already had arrays of four resonators), which motivates the work in Chapter 4 on handling the multiple resonators.

In contrast, a device with two routing layers (driven by through field excitation, TFE) would have high C_0 density because the finger designs are wider for maximizing through field excitation and because the capacitance would be dominated by the thickness of the LN film. The capacitance density increases by approximately an order of magnitude according to parallel-plate capacitance estimates (C_0 of individual devices would be on the order of 1 pF for the TFE devices as compared to the approximately 100 fF for the LFE devices for the same resonator width and length), so reaching 50Ω termination (C_0 on the order of 10 pF) would require fewer than ten TFE devices in parallel. This C_0 benefit has the most benefit at lower frequencies because C_0 scales inversely with frequency for a given termination impedance.

An additional benefit of two routing layers is the suppression of asymmetric wave modes [28]. The development of a LN microresonator with two routing layers could have adequate geometry parameters to address the spurs due to dispersion in Chapter 5; future work would focus on optimizing the electrodes of the bottom routing layer to suppress the unwanted vibrational modes.

Combined with the frequency scaling (increasing the f_s), one potential challenge for the development of a two routing layer resonator is the electrode thickness. As the LN layer becomes thinner when the frequency increases, the mass loading due to the electrodes will increase. The designer could exploit the mass loading to suppress spurious modes due to acoustic energy leakage out of the resonator body [33].

6. CONCLUSION

6.1.3 Investigation of undercut LN film effects

In addition to simulations in Section 4.3 with double resonators with shared pits, several additional simulations were performed keeping the etch pit the same size but using only one resonator. This is illustrated in Figure 6.1 with the key parameter (pit opening width) labeled.

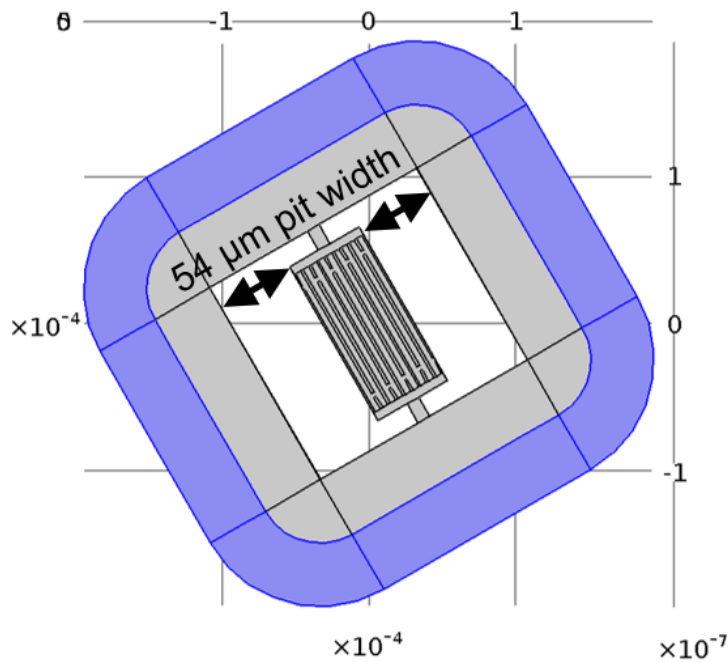


Figure 6.1: COMSOL geometry for single resonator placed in widened pit. In this case, the pit width (marked) corresponds to a pit the same size as the one used in the 72 μm spaced resonators in Figure 4.4.

The results of the simulation are shown in Figure 6.2 for the “default” pit width (18 μm), the pit width corresponding to the overall etch opening for the double resonators with 72 μm center-to-center spacing (54 μm pit width), and the pit width corresponding to the overall etch opening for the double resonators with 90 μm center-to-center spacing (63 μm pit width). The key observation is that the peak of the resonance changes with the width of the pit, with varying Q and shape.

It is hypothesized that the geometry of the undercut LN film can be optimized to sharpen the peak of the resonator as well as to reduce the spurs in the frequency response, at least to the

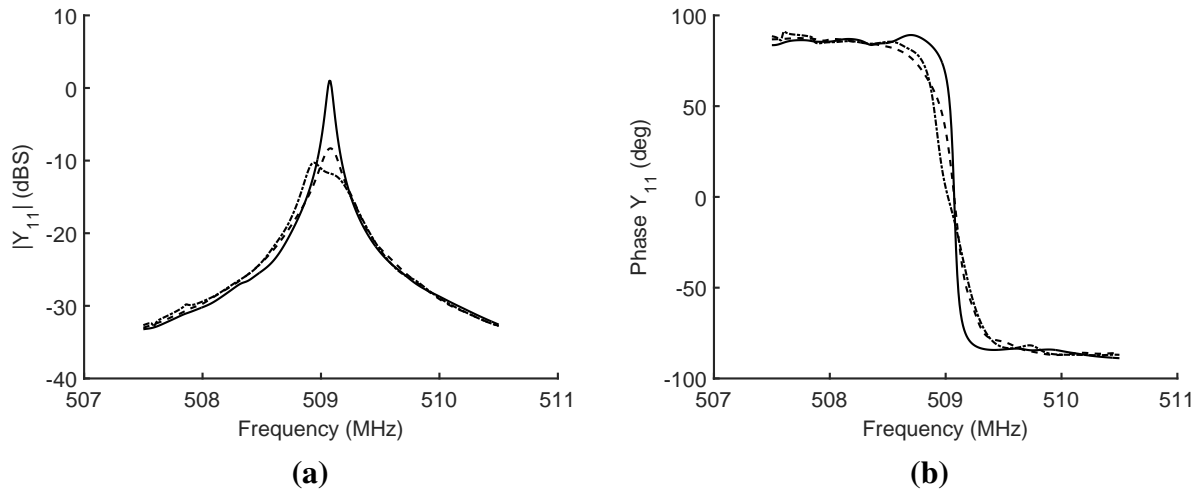


Figure 6.2: COMSOL 3D simulations of a single resonator with varying pit widths. Dash: “default” pit width of 18 μm , solid: pit width 54 μm (corresponding to the overall etch opening for the double resonators with 72 μm center-to-center spacing), dot-dash: pit width 63 μm (corresponding to the overall etch opening for the double resonators with 90 μm center-to-center spacing). The ring around the resonator is subject to PML and Fixed Constraint boundary conditions as done in Section 4.3.

extent that the Fixed Constraint approximates the anchoring of the LN by the silicon underneath. A study on this effect would augment the transmission line model in [34]. A similar study has been performed in aluminum nitride [32], where the release area was pre-patterned in an attempt to reduce the interaction between resonator and silicon. A future study could better characterize the effect of anchor distance (undercut radius) and etch pit width upon the quality factor and spurs in LN microresonators.

6.1.4 Switching networks

To build a bridge between individual filters and filter banks, an efficient network is desired to connect and select the filters. This can be achieved using a switching network or manifold.

A switching network was illustrated in the introduction chapter (Figure 1.1a), using a single-pole- N -throw switch to connect N parallel filters. A potential limitation for this idea is the parasitic

6. CONCLUSION

capacitance to ground at the ports of each switch; for large N , the sum of the parasitic capacitance could load the input and output of the filter bank and compromise its insertion loss by introducing ripple (similar to the effect of the outer parasitic capacitance for tuning the bandpass filter in Chapter 3).

A more elegant solution might be found in the form of switchless filter banks, introduced as “intrinsically switched” filter banks by Guyette [7, 8, 21]. The idea is to move the switching mechanism to within the individual filters, thus reducing the loading on the input of the filter bank. The filter topologies in the intrinsically switched filter banks have controlled coupling between the resonators (unlike in Chapter 2, they are not directly coupled). Controlling the coupling (magnitude and phase of the connection between the resonators) allows control over the configuration of the filter bank without using switches, including selecting the filter band, bandwidth, and even inserting notches into bandpass filters. The existing work uses electromagnetic resonators with microstrip routing, where the coupling is controlled by tuning the electric field distribution. As noted in the Introduction, electromagnetic resonators are large for the GHz frequencies of interest, so being able to use LN resonators would confer a size benefit.

To adapt these intrinsic switching techniques to LN microresonator filters, methods of controllable coupling would need to be developed. Whereas in microstrip resonators, the coupling is readily tunable by using varactors to control the electric field distribution, the coupling to the microresonators of this thesis is less obvious. Indeed, in Chapter 3, the coupling between resonators in the notch filter was an external Π network – not an elegant integrated solution.

A potential path to explore is the idea of toggling the drive on the resonator electrodes. For example, a network of switches as shown in Figure 6.3a can control a resonator with four terminal electrodes. Toggling switches S13/S24 and S14/S23 can turn the resonance on and off, effectively switching the motional (R_m , L_m , and C_m) branch of the MBVD model on and off (leaving just C_0 in the “off” state at the frequency of interest). The admittance is simulated using the Mason model

[35] of a normalized resonator and the results are shown in Figure 6.3b. This multiport switching idea, along with other ways to exploit driving multiple terminals, could enable control of the coupling to resonance at the resonator level, with the potential to reduce the parasitic capacitance at the filter bank input and output. This research direction would also need to address how to handle the “off”-state capacitance (C_0) of the resonators.

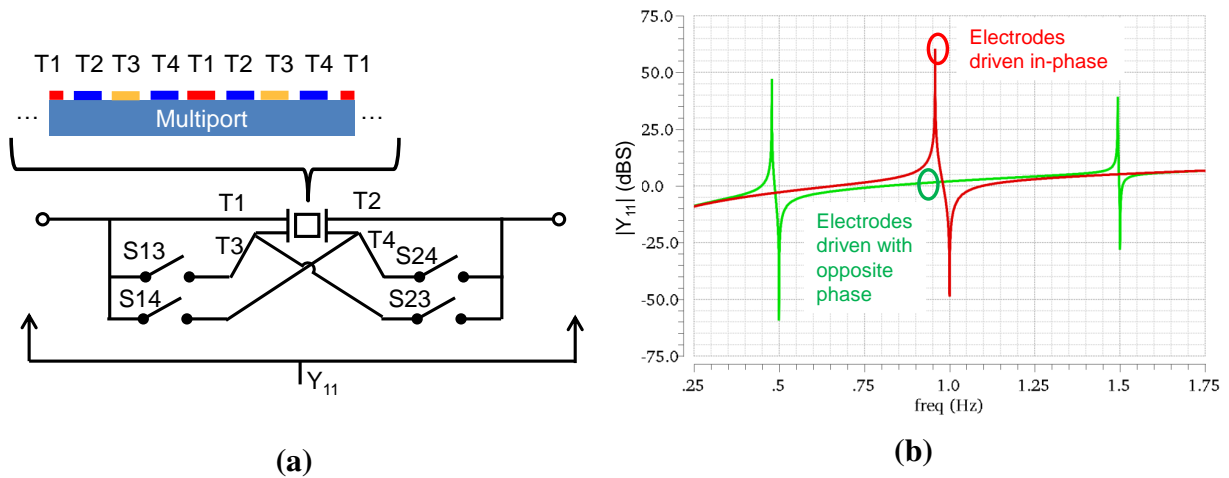


Figure 6.3: Potential “intrinsic” switching topology to turn resonance on and off. (a) topology and illustration of electrode allocation, (b) simulated admittance with the electrodes driven in phase (S13 and S24 on, S14 and S23 off) and out-of-phase (S13 and S24 off, S14 and S23 on), showing switching of the resonance (motional branch of the MBVD model) on and off in the frequency of interest.

6.1.5 Integration with CMOS

At the time of publication of this thesis, the LN devices are prepared on one chip and the electronics (switches, non-resonator filter components) on a separate sample; the two are then wirebonded together. This level integration is appropriate for the demonstrations in this thesis work, but might not be compact or robust enough for the final application in handheld devices.

A development that would advance integration is to engineer flip-chip bonding of the LN and CMOS samples. This effort would involve developing an encapsulation structure to protect the

6. CONCLUSION

resonators [36, 37]. The parasitic capacitance of the bump pads would need careful consideration, similar to the analysis in Chapter 3 and Chapter 4. The reward of successful flip-chip bonding is access to CMOS and CMOS-MEMS components for networks that might be too intricate for wirebonding, such as large switch networks.

Further integration could be pursued to monolithically combine both the filters and the CMOS on a single chip, reducing the parasitics and size of the system. Initial efforts using aluminum nitride have successfully integrated four coupled ladder filters with a single-pole-four-throw CMOS switch network monolithically [38]. A fundamental challenge of integrating the LN material would be the method to deposit or attach crystalline LN at the desired orientation upon the CMOS.

6.1.6 Optimization for reconfiguration control

A reconfigurable filter bank is most useful if it can be reprogrammed automatically and spontaneously in order to quickly shield against interference. In the envisioned radio application, the filter bank would be used in an RF receiver front-end along with variable amplifiers, resulting in many variables that can be controlled. Efficient optimization (against power and noise specifications) of the variables is an ongoing effort [39] that is critical for the use of the filter banks in varying spectral environments.

References

- [1] “United States Frequency Allocations – The Radio Spectrum,” https://www.ntia.doc.gov/files/ntia/publications/spectrum_wall_chart_aug2011.pdf, August 2011, accessed June 2016. 1, 123
- [2] W. Chappell, E. Naglich, C. Maxey, and A. Guyette, “Putting the Radio in ‘Software-Defined Radio’: Hardware Developments for Adaptable RF Systems,” *Proc. of the IEEE*, vol. 102, no. 3, pp. 307–320, March 2014. 1, 4
- [3] “iPhone 6s Teardown - iFixit,” <https://www.ifixit.com/Teardown/iPhone+6s+Teardown/48170>, September 2015, accessed May 2016. 3
- [4] “Ettus Research USRP B200mini Series datasheet,” <https://www.ettus.com/product/category/USRP-Bus-Series>, accessed April 2016. 3, 4
- [5] “K & L Microwave Switched Filter Bank Products,” http://www.klmicrowave.com/category/switched-filter-bank_8.html, accessed May 2016. 5, 6
- [6] S. Mahon, J. Zepess, and M. Andrews, “BAW Flip-Chip Switched Filter Bank Delivers Dramatic Form Factor Reduction,” TriQuint Semiconductor, Tech. Rep., 2008, <http://www.triquint.com/products/d/baw-flip-chip-switched-filter-bank-aug2008>. 5, 6
- [7] A. C. Guyette, “Intrinsically Switched Varactor-Tuned Filters and Filter Banks,” *IEEE Trans-*

REFERENCES

- actions on Microwave Theory and Techniques*, vol. 60, no. 4, pp. 1044–1056, April 2012. 5, 6, 128
- [8] E. J. Naglich, A. C. Guyette, and D. Peroulis, “High-Q intrinsically-switched quasi-absorptive tunable bandstop filter with electrically-short resonators,” in *2014 IEEE MTT-S International Microwave Symposium (IMS2014)*, June 2014, pp. 1–4. 5, 6, 128
- [9] T. Komatsu, K. Hashimoto, T. Omori, and M. Yamaguchi, “Tunable Radio-Frequency Filters Using Acoustic Wave Resonators and Variable Capacitors,” *Japanese Journal of Applied Physics*, vol. 49, no. 7, 2010. 5, 16, 47, 48, 76
- [10] L. Shi and G. Piazza, “Active Reflectors for High Performance Lithium Niobate on Silicon Dioxide Resonators,” in *Micro Electro Mechanical Systems (MEMS), 2015 IEEE 28th International Conference on*, 2015, pp. 992–995. 7, 8, 117
- [11] C. Zuo, N. Sinha, M. Pisani, C. Perez, R. Mahameed, and G. Piazza, “Channel-Select RF MEMS Filters Based On Self-Coupled AlN Contour-Mode Piezoelectric Resonators,” in *IEEE Ultrasonics Symposium, 2007. Proceedings., IEEE 2007*, 2007, pp. 1156–1159. 15, 25
- [12] K. M. Lakin, G. R. Kline, and K. T. McCarron, “Thin film bulk acoustic wave filters for GPS,” in *Ultrasonics Symposium, 1992. Proceedings., IEEE 1992*, vol. 1, 1992, pp. 471–476. 15, 18, 145
- [13] G. Matthaei, L. Young, and E. Jones, *Microwave Filters, Impedance-Matching Networks, and Coupling Structures*. Norwood, MA: Artech House, 1980, pp. 49–60, 355–519. 16, 22, 63
- [14] O. Ikata, T. Miyashita, T. Nishihara, and Y. Satoh, “Development of low-loss band-pass filters using SAW resonators for portable telephones,” in *Ultrasonics Symposium, 1992. Proceedings., IEEE 1992*, vol. 1, 1992, pp. 111–115. 16

REFERENCES

- [15] M. Kadota and S. Tanaka, “Wideband ladder filters fully covering digital TV band based on shear horizontal plate wave,” in *Frequency Control Symposium the European Frequency and Time Forum (FCS), 2015 Joint Conference of the IEEE International*, April 2015, pp. 412–415. 16, 46
- [16] T.-C. Lee, A. Guyette, E. Naglich, and D. Peroulis, “Coupling-matrix-based SAW filter design,” in *Microwave Symposium (IMS), 2014 IEEE MTT-S International*, 2014. 18, 47
- [17] G. Piazza, P. J. Stephanou, and A. P. Pisano, “Single-Chip Multiple-Frequency ALN MEMS Filters Based on Contour-Mode Piezoelectric Resonators,” *Journal of Microelectromechanical Systems*, vol. 16, no. 2, pp. 319–328, April 2007. 18
- [18] A. I. Zverev, *Handbook of Filter Synthesis*. New York, NY: John Wiley and Sons, Inc., 1967, pp. 428–430. 22
- [19] L. Shi, “Lithium Niobate-based High-Electromechanical-Coupling RF-MicroElectroMechanical Resonators for Wideband Filtering,” Ph.D. dissertation, Carnegie Mellon University, Pittsburgh, PA, February 2016. 31, 55, 117, 118, 162
- [20] S. Gong and G. Piazza, “An 880 MHz ladder filter formed by arrays of laterally vibrating thin film Lithium Niobate resonators,” in *Micro Electro Mechanical Systems (MEMS), 2014 IEEE 27th International Conference on*, 2014, pp. 1241–1244. 47
- [21] R. Gómez-García and A. C. Guyette, “Reconfigurable Multi-Band Microwave Filters,” *IEEE Transactions on Microwave Theory and Techniques*, vol. 63, no. 4, pp. 1294–1307, April 2015. 59, 128
- [22] T. Snow, J. Lee, and W. J. Chappell, “Tunable high quality-factor absorptive bandstop filter design,” in *Microwave Symposium Digest (MTT), 2012 IEEE MTT-S International*, June 2012, pp. 1–3. 59

REFERENCES

- [23] D. Jachowski, "Compact, frequency-agile, absorptive bandstop filters," in *Microwave Symposium (IMS), 2005 IEEE MTT-S International*, 2005. 60, 64
- [24] R. Wang, S. Bhave, and K. Bhattacharjee, "High k_t^2Q , multi-frequency lithium niobate resonators," in *Micro Electro Mechanical Systems (MEMS), 2013 IEEE 26th International Conference on*, January 2013, pp. 165–168. 65
- [25] P. J. Stephanou, G. Piazza, C. D. White, M. B. J. Wijesundara, and A. P. Pisano, "Mechanically Coupled Contour Mode Piezoelectric Aluminum Nitride MEMS Filters," in *19th IEEE International Conference on Micro Electro Mechanical Systems*, 2006, pp. 906–909. 82
- [26] J. Reinke, G. K. Fedder, and T. Mukherjee, "CMOS-MEMS 3-bit Digital Capacitors With Tuning Ratios Greater Than 60:1," *IEEE Transactions on Microwave Theory and Techniques*, vol. 59, no. 5, pp. 1238–1248, May 2011. 94
- [27] R. Wang, S. A. Bhave, and K. Bhattacharjee, "Modeling of inter-digitated transducer for high-order contour mode resonators," in *2013 IEEE International Ultrasonics Symposium (IUS)*, July 2013, pp. 1926–1929. 102, 103, 117
- [28] H. Zhang, J. Liang, X. Zhou, H. Zhang, D. Zhang, and W. Pang, "Transverse Mode Spurious Resonance Suppression in Lamb Wave MEMS Resonators: Theory, Modeling, and Experiment," *IEEE Transactions on Electron Devices*, vol. 62, no. 9, pp. 3034–3041, Sept 2015. 107, 108, 118, 125
- [29] D. W. Branch, K. E. Wojciechowski, and R. H. Olsson, "Elucidating the origin of spurious modes in aluminum nitride microresonators using a 2-D finite-element model," *IEEE Transactions on Ultrasonics, Ferroelectrics, and Frequency Control*, vol. 61, no. 5, pp. 729–738, May 2014. 107

-
- [30] Y. H. Song and S. Gong, "Arraying SH0 Lithium Niobate laterally vibrating resonators for mitigation of higher order spurious modes," in *2016 IEEE 29th International Conference on Micro Electro Mechanical Systems (MEMS)*, Jan 2016, pp. 111–114. 108
- [31] —, "Elimination of Spurious Modes in SH0 Lithium Niobate Laterally Vibrating Resonators," *IEEE Electron Device Letters*, vol. 36, no. 11, pp. 1198–1201, Nov 2015. 108
- [32] R. H. Olsson, K. E. Wojciechowski, and D. W. Branch, "Origins and mitigation of spurious modes in aluminum nitride microresonators," in *2010 IEEE International Ultrasonics Symposium*, Oct 2010, pp. 1272–1276. 118, 127
- [33] D. W. Branch and R. H. Olsson, "Suppressing fine-frequency modes in aluminum nitride microresonators," in *2014 IEEE International Ultrasonics Symposium*, Sept 2014, pp. 572–577. 125
- [34] C. Cassella, "Techniques for Phase Noise Evasion in Very High Frequency AlN Contour-Mode Oscillators," Ph.D. dissertation, Carnegie Mellon University, Pittsburgh, PA, May 2014. 127
- [35] S. Gong and G. Piazza, "Large frequency tuning of Lithium Niobate laterally vibrating MEMS resonators via electric boundary reconfiguration," in *2013 Transducers Eurosensors XXVII: The 17th International Conference on Solid-State Sensors, Actuators and Microsystems (TRANSDUCERS EUROSENSORS XXVII)*, June 2013, pp. 2465–2468. 129
- [36] M. D. Henry, T. Young, A. E. Hollowell, M. Eichenfield, and R. H. Olsson, "Wafer-level packaging of aluminum nitride RF MEMS filters," in *2015 IEEE 65th Electronic Components and Technology Conference (ECTC)*, May 2015, pp. 1331–1337. 130
- [37] J. Sharma, J. W. Lee, S. Merugu, and N. Singh, "A Robust Bilayer Cap in Thin Film Encap-

REFERENCES

- sulation for MEMS Device Application,” *IEEE Transactions on Components, Packaging and Manufacturing Technology*, vol. 5, no. 7, pp. 930–937, July 2015. 130
- [38] E. R. Crespin, R. H. Olsson, K. E. Wojciechowski, D. W. Branch, P. Clews, R. Hurley, and J. Gutierrez, “Fully integrated switchable filter banks,” in *Microwave Symposium Digest (MTT), 2012 IEEE MTT-S International*, June 2012, pp. 1–3. 130
- [39] M. Jun, R. Negi, J. Tao, Y. C. Wang, S. Yin, T. Mukherjee, X. Li, and L. Pileggi, “Environment-Adaptable Efficient Optimization for Programming of Reconfigurable Radio Frequency (RF) Receivers,” in *2014 IEEE Military Communications Conference*, Oct 2014, pp. 1459–1465. 130

Appendix A

Definitions and models

A.1 Acronyms and abbreviations

LN: Lithium niobate, or LiNbO_3 , the piezoelectric material used for resonators in this work.

IL: Insertion loss (of a filter), defined as the $|S_{21}|$ of the passband. Lower IL is better.

OBR: Out-of-band rejection (of a passband filter), defined as the highest $|S_{21}|$ in the stopband.

For single-sideband filters, this can be divided into upper- and lower-sideband OBRs.

FBW: Fractional (3 dB) bandwidth of a bandpass filter, defined as $\frac{f_h - f_l}{\sqrt{f_h f_l}}$, where f_h is the upper 3 dB cutoff frequency and f_l is the lower 3 dB cutoff frequency.

FEA: Finite-element analysis.

S0: Lowest-order symmetric mode of acoustic vibration on a plate, with an extensional displacement profile.

A0: Lowest-order asymmetric mode of acoustic vibration on a plate, with a flexural displacement profile.

SH0: Lowest-order shear mode of acoustic vibration on a plate, with a displacement profile that shears periodically in the length axis of the resonator.

A.2 Resonator geometry parameters

An image of a canonical resonator is annotated with geometry parameters in Figure A.1. The edges of the image (marked by diagonal lines) are undercut LN film. The width of the resonator body is $L_{LN} = 2L_b + G + L_f$ and the width of the body is $W_{LN} = (N_f - 1)P$, where N_f is the total number of fingers.

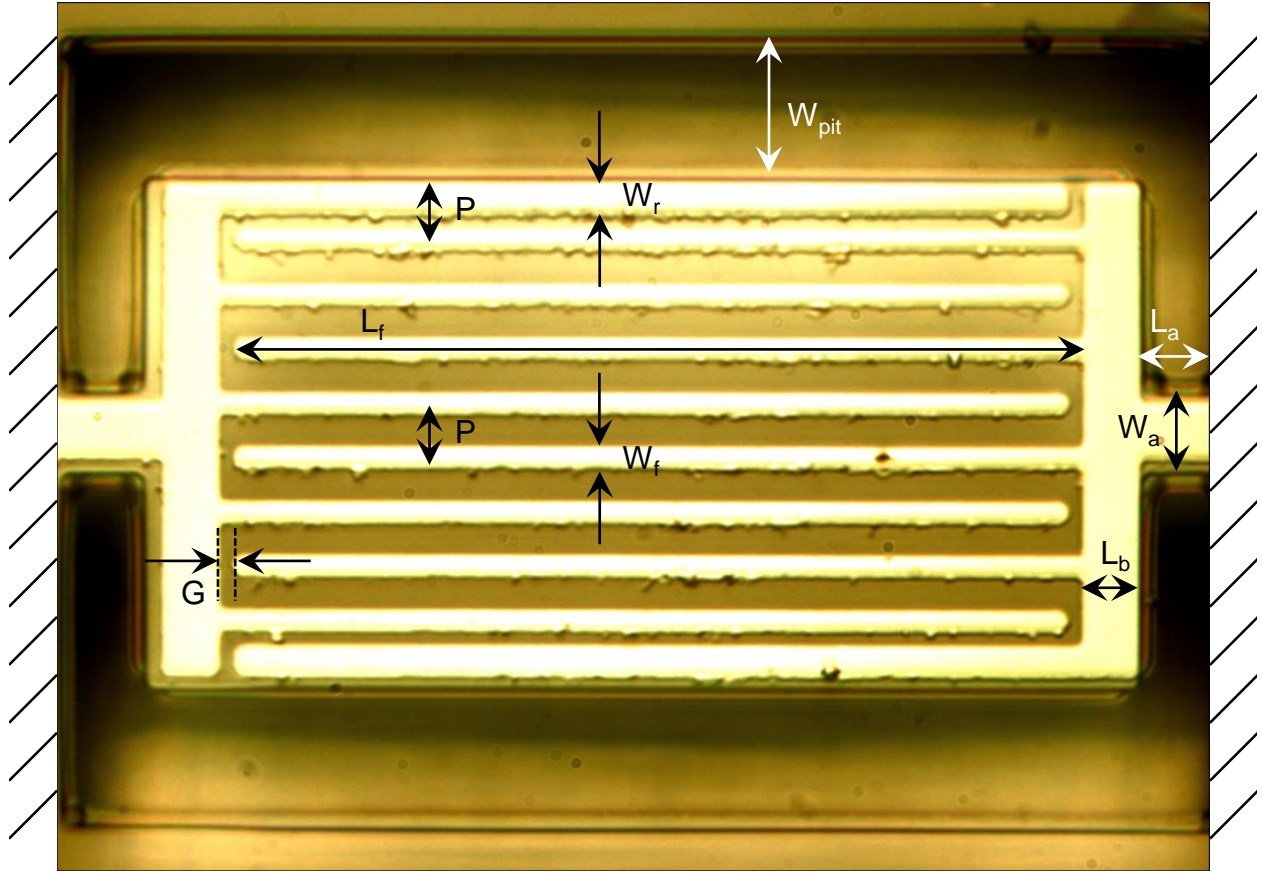


Figure A.1: Image of resonator annotated with geometry parameters. The edges of the image (marked by diagonal lines) are undercut LN film.

A.3 Modified Butterworth-Van-Dyke (MBVD) model

The Modified Butterworth-Van-Dyke (MBVD) model describes a spur-free resonator with one series resonance and one antiresonance, with parameters to describe the resonator size, electromechanical coupling, and losses.

The MBVD circuit schematic is shown in Figure A.2a and the frequency response of its admittance is shown in Figure A.2b. Note that the MBVD model does *not* capture the behavior of spurs.

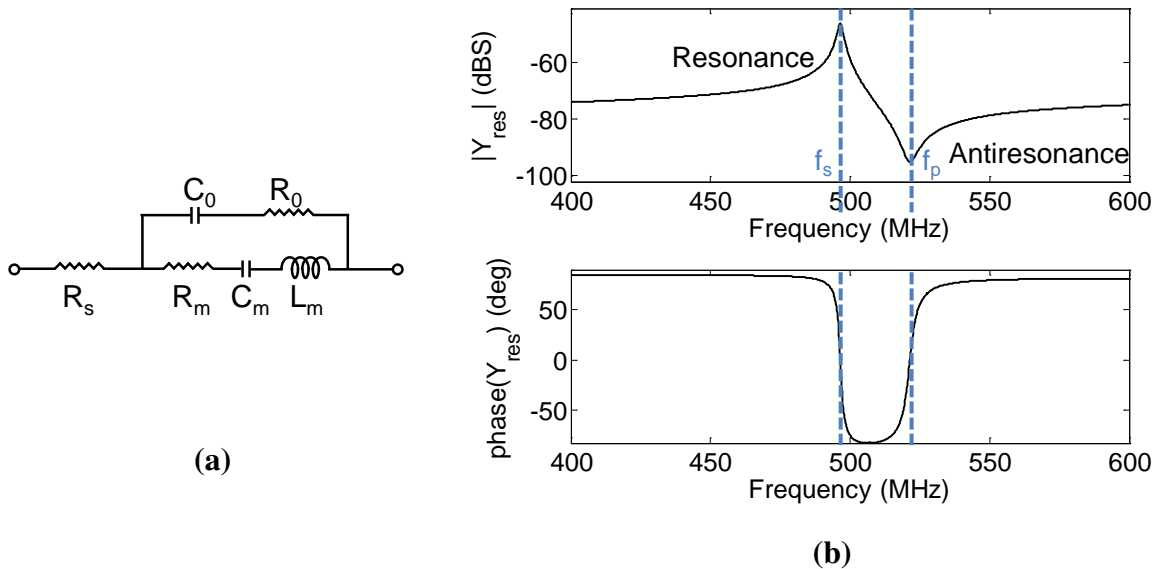


Figure A.2: Modified Butterworth-Van-Dyke model (a) schematic and (b) frequency response of the admittance magnitude and phase.

The equations relating the K_t^2 , Q , C_0 , and f_s set of parameters to the C_m , R_m , C_0 , and L_m set of parameters are

A. DEFINITIONS AND MODELS

$$C_m = \frac{8}{\pi^2} C_0 K_t^2 \quad (\text{A.1})$$

$$R_m = \frac{\pi^2}{8} \frac{1}{2\pi f_s C_0} \frac{1}{K_t^2 Q} = \frac{1}{2\pi f_s C_m Q} = \frac{2\pi f_s L_m}{Q} \quad (\text{A.2})$$

$$L_m = \frac{\pi^2}{8} \frac{1}{(2\pi f_s)^2 C_0 K_t^2} = \frac{1}{(2\pi f_s)^2 C_m}. \quad (\text{A.3})$$

Typically one uses the K_t^2 , Q , C_0 , and f_s set when analyzing measurements and discussing resonator performance, and the C_m , R_m , C_0 , and L_m set when conducting circuit design. In both cases, the R_s and R_0 are typically extracted from measurement.

A least-squares fitting is employed to obtain fit MBVD model parameters to the measurement. Priority weighting is given to the regions of resonance and antiresonance. The algorithm can be described as:

1. Calculate f_s by finding the frequency at which the $|Y|$ is maximum. Calculate f_p by finding the frequency at which the $|Y|$ is minimum, or from manual override.
2. Considering only the regions immediately around the resonance and antiresonance (in code, flolo to flohi and fhilo to fhihi), use least-squares fit to get K_t^2 and an initial Q .
3. Smooth the area outside resonance (here, the area $1 \times$ the frequency spacing between the resonance and antiresonance is smoothed, from $f_s - (f_p - f_s)$ to $f_p + (f_p - f_s)$). Combine this with the measured data inside the resonance region (forming y_{comb}).
4. Perform least-squares fit on the combined (smoothed outside resonance) curve to get C_0 , R_s , R_0 (denoted in the code as R_p)
5. Re-fit for Q using the regions immediately around the resonance and antiresonance.

Several heuristics are used:

A.3 Modified Butterworth-Van-Dyke (MBVD) model

- Unit sizes are scaled to powers that keep the values in the range of 10-1000 to avoid error due to too much numerical dynamic range. Within the calculations, admittance is in dBS and degrees, frequency in MHz, capacitance in fF, and K_t^2 in percent. (These are converted back to complex siemens, Hz, F, and decimal, respectively, for the output). This scaling should be reviewed when adapting this code to resonators of very different frequency or size.
- The regions immediately near the resonance are assumed to be about 1/10 the distance between f_s and f_p ; this has provided a sufficient number of data points while excluding spurs.
- There is an option in the code to manually enter the antiresonance frequency in Hz. This is because some measurements have spurs that are deeper than the antiresonance.
- The Q may be over-estimated; it is recommended that the user check carefully to make sure the Q is acceptable (that the peak amplitudes match and peak phase slopes match).
- The R_s may be too high in the fitting, which optimizes to the measured frequency response without regard to the actual electrical resistance of the electrodes.

The last point (about R_s being too high) introduces the question of whether there is a way to force the R_s to be a physical value (corresponding to the measured resistance of the series routing, for instance) without impacting the fit of the model. Because the MBVD model resembles R_s and R_m in series at resonance (neglecting C_0 because the high $K_t^2 Q$ means its admittance will be lower than that of R_m), R_s and Q may be traded off as long as

$$R_s + R_m = \text{Constant.} \quad (\text{A.4})$$

R_m is inversely related to Q by (A.2), so R_s can inversely trade off with Q . As an example, the MBVD fitting for the resonator in Figure 2.21b (parameters listed in Table 2.2) have $R_s = 55.6 \Omega$. This is an unphysical value, as sheet resistance measurements ($0.587 \Omega/\text{square}$) suggest that $R_s =$

A. DEFINITIONS AND MODELS

2.3 Ω . Figure A.3 shows that using Equation (A.4) does not significantly change the MBVD trace, while allowing for a more physical R_s than from fitting to just the frequency response measurement. Therefore, the user of the fitting code is advised to check the R_s and make adjustments to Q , using Equation (A.4), accordingly.

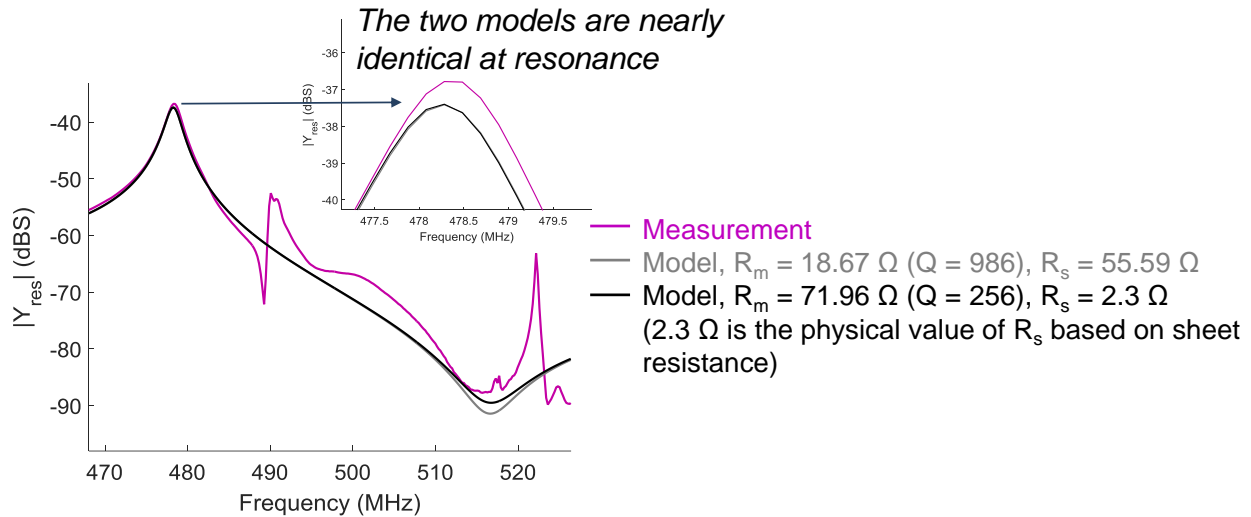


Figure A.3: Example of trading off Q and R_s in the MBVD model, where the model is not very sensitive to the tradeoff. The gray trace is the model as fitted by the fitting code, while the black trace is the model when forced to an $R_s = 2.3 \Omega$ as calculated from sheet resistance measurements. Equation (A.4) can be used to manually override R_s if the fitted model exaggerates its value.

The least-squares fitting code is included as follows:

```

1 function [fs, kt2, C0, Q, Rs, Rp, ycomb] = fitBVDv5(freq, yres, fpHz)
2 % Least-squares fit to Modified Butterworth-Van-Dyke model
3 % Sean Yen
4 %
5 % Inputs:
6 % freq: array of frequencies
7 % yres: resonator admittance (real+imaginary) evaluated at frequencies in
8 %       freq
9 % fpHz: manual override of antiresonance frequency in Hz
10 %
11 % Outputs:
12 % fs: series-resonance frequency of the resonator (Hz)
13 % kt2: kt2 of the resonator (decimal)

```

A.3 Modified Butterworth-Van-Dyke (MBVD) model

```
15 % C0: C0 of the resonator (F)
% Q: Series unloaded Q of the resonator (unitless)
% Rs: resistance in series with resonator impedance
17 % Rp (AKA R0): resistance in series with C0 in the C0 branch
% ycomb: admittance response used for fitting -- smoothed outside resonance
19
20 yres=squeeze(yres);
21
22 % Find the resonance
23 [~,fsi] = max(abs(yres));
[~,fpi] = min(abs(yres(fsi:end)));
25 fpi = fpi+fsi-1;
fs = freq(fsi);
27 fp = freq(fpi);

29 if nargin == 3 % Manual override of fp
    fpitemp = freq>fpHz;
31    fpitemp = diff(fpitemp);
    fpi = find(fpitemp);
33    fp = freq(fpi);
end
35

% frequency band 2*(fs-fp) away from series and anti resonances
37 flowi = fsi-round(1*(fpi-fsi));
fhii = fpi+round(1*(fpi-fsi));
39

% frequency band for resonance and antiresonance
41 flolo = fsi-round(0.1*(fpi-fsi));
flohi = fsi+round(0.1*(fpi-fsi));
43 fhilo = fpi-round(0.1*(fpi-fsi));
fhihi = fpi+round(0.1*(fpi-fsi));
45 freqbandi= [flolo:flohi fhilo:fhihi];
freqband=freq(freqbandi);
47

% Smooth data outside of band to get reduce spurs
49 ysmooth = smooth(yres,round(length(freq)/10),'rloess');

51 % Combine the smoothed out-of-band data with in-band raw data
ycomb = [ysmooth(1:flowi-1); yres(flowi:fhii-1); ysmooth(fhii:end)];
53

% Calculate initial parameters
55 fsMHz=fs/10^6;
kt2 = (1- (fs/fp)^2)*100; % approximate initial kt2
57 C0fF = imag(ysmooth(1))/(2*pi*freq(1))*10^15; % approximate initial C0fF
Rm = 1/real(yres(fsi))
59 Q = 1/(2*pi*fs* C0fF*10^-15 * 8/pi^2 * kt2 * Rm);
Rs = 0;
61 Rp = 0;

63 bvdffitted = [fsMHz, kt2, C0fF, Q,Rs,Rp];
```

A. DEFINITIONS AND MODELS

```
65 fs=fs/10^6;
   bvdffitted=bvdffitted(2:end);
67
   % Fit to both resonances (in range of "freqbandi") ONLY
69 % kt2 = bvdffitted(1);
   % C0fF = bvdffitted(2);
71 % Q = bvdffitted(3);
   % Rs = bvdffitted(4);
73 % Rp = bvdffitted(5);

75 Yresfs = @(bvdffitted,f) [20*log10(abs( 1./(bvdffitted(4) + 1 ./ ( 1./(1./(1i*2*
   pi*f*bvdffitted(2)*10^-15) + bvdffitted(5)) + 1./( 1/( (2*pi*fs*10^6)^2 * 8/
   pi^2*bvdffitted(2)*10^-15*bvdffitted(1)/100 ) * 2*pi*fs*10^6/bvdffitted(3) + 1i
   * 2*pi*f*1/( (2*pi*fs*10^6)^2 * 8/pi^2*bvdffitted(2)*10^-15*bvdffitted(1)/100
   ) + 1./(1i*2*pi*f*8/pi^2*bvdffitted(2)*10^-15*bvdffitted(1)/100) ) ) ) )
   180/pi*unwrap(angle(1./(bvdffitted(4) + 1 ./ ( 1./(1./(1i*2*pi*f*bvdffitted
   (2)*10^-15) + bvdffitted(5)) + 1./( 1/( (2*pi*fs*10^6)^2 * 8/pi^2*bvdffitted
   (2)*10^-15*bvdffitted(1)/100 ) * 2*pi*fs*10^6/bvdffitted(3) + 1i*2*pi*f*1/( (2
   *pi*fs*10^6)^2 * 8/pi^2*bvdffitted(2)*10^-15*bvdffitted(1)/100 ) + 1./(1i*2*
   pi*f*8/pi^2*bvdffitted(2)*10^-15*bvdffitted(1)/100) ) ) ) ) ];
   Ydata = [20*log10(abs(ycomb(freqbandi))) 180/pi*unwrap(angle(ycomb(freqbandi)
   ))];
77 [bvdffitted,resnorm] = lsqcurvefit(Yresfs,bvdffitted,freqband,Ydata,zeros(size(
   bvdffitted)),1e10*ones(size(bvdffitted)));

79 % Keep kt2, and Q; then fit to whole curve
   kt2=bvdffitted(1);
81 Q=bvdffitted(3);
   bvdffitted=[bvdffitted(2) bvdffitted(4:end)];
83
   % Fitting to whole curve (smoothed outside resonance)
85 Zresfskt2Q = @(bvdffitted,f) [20*log10(abs(bvdffitted(2) + 1 ./ ( 1./(1./(1i*2*
   pi*f*bvdffitted(1)*10^-15) + bvdffitted(3)) + 1./( 1/( (2*pi*fs*10^6)^2 * 8/
   pi^2*bvdffitted(1)*10^-15*kt2/100 ) * 2*pi*fs*10^6/Q + 1i*2*pi*f*1/( (2*pi*fs
   *10^6)^2 * 8/pi^2*bvdffitted(1)*10^-15*kt2/100 ) + 1./(1i*2*pi*f*8/pi^2*
   bvdffitted(1)*10^-15*kt2/100) ) ) ) ) 180/pi*unwrap(angle(bvdffitted(2) + 1 ./
   ( 1./(1./(1i*2*pi*f*bvdffitted(1)*10^-15) + bvdffitted(3)) + 1./( 1/( (2*pi
   *fs*10^6)^2 * 8/pi^2*bvdffitted(1)*10^-15*kt2/100 ) * 2*pi*fs*10^6/Q + 1i*2*
   pi*f*1/( (2*pi*fs*10^6)^2 * 8/pi^2*bvdffitted(1)*10^-15*kt2/100 ) + 1./(1i*
   2*pi*f*8/pi^2*bvdffitted(1)*10^-15*kt2/100) ) ) ) ) ];
   Zdata = [20*log10(abs(1./ycomb)) 180/pi*unwrap(angle(1./ycomb))];
87 [bvdffitted,resnorm] = lsqcurvefit(Zresfskt2Q,bvdffitted,freq,Zdata,zeros(size(
   bvdffitted)),1e10*ones(size(bvdffitted)));

89 C0fF = bvdffitted(1);
   Rs = bvdffitted(2);
91 Rp = bvdffitted(3);

93 % Re-fit the Q given the Rs and Rp
   bvdffitted = Q;
95 Yresfskt2QC0RsRp = @(bvdffitted,f) [20*log10(abs(1./(Rs + 1 ./ ( 1./(1./(1i*2*
```

```

pi*f*C0fF*10^-15) + Rp) + 1./ ( 1./ ( (2*pi*fs*10^6)^2 * 8/pi^2*C0fF*10^-15*
kt2/100 ) * 2*pi*fs*10^6/bvdfitted(1) + 1i*2*pi*f*1./ ( (2*pi*fs*10^6)^2 * 8/
pi^2*C0fF*10^-15*kt2/100 ) + 1./ (1i*2*pi*f*8/pi^2*C0fF*10^-15*kt2/100) ) )
))) 180/pi*unwrap(angle(1./(Rs + 1 ./ ( 1./ (1./ (1i*2*pi*f*C0fF*10^-15) +
Rp) + 1./ ( 1./ ( (2*pi*fs*10^6)^2 * 8/pi^2*C0fF*10^-15*kt2/100 ) * 2*pi*fs*
10^6/bvdfitted(1) + 1i*2*pi*f*1./ ( (2*pi*fs*10^6)^2 * 8/pi^2*C0fF*10^-15*
kt2/100 ) + 1./ (1i*2*pi*f*8/pi^2*C0fF*10^-15*kt2/100) ) ) ) ) ) );
Ydata = [20*log10(abs(ycomb(freqbandi))) 180/pi*unwrap(angle(ycomb(freqbandi)
))] ;
97 [bvdfitted, resnorm] = lsqcurvefit(Yresfskt2QC0RsRp, bvdfitted, freqband, Ydata,
zeros(size(bvdfitted)), 1e10*ones(size(bvdfitted)));
Q = bvdfitted(1);
99
fs=fs*10^6;
101 kt2=kt2/100;
C0 = C0fF*10^-15;

```

A.4 K_t^2 vs. k_t^2

In order to make fair comparisons, one must distinguish between upper-case K_t^2 and lower-case k_t^2 , both expressing electromechanical coupling. The literature can be unclear or use the definitions interchangeably, so use caution when reading! The following definitions are used in this thesis:

Upper-case K_t^2 is the definition used by the acoustic community [12]. It is defined as

$$K_t^2 = \frac{\pi^2 C_m}{8 C_0} = \frac{\pi^2}{8} \left[\left(\frac{f_p}{f_s} \right)^2 - 1 \right]. \quad (\text{A.5})$$

The capacitances C_0 and C_m represent the static and motional capacitances, respectively, in the MBVD model, while f_s and f_p are the resonance and antiresonance frequencies, respectively.

Lower-case k_t^2 , defined by IEEE Standard 176-1987, is given by

$$k_t^2 = \frac{\pi f_s}{2 f_p} \tan \left(\frac{\pi f_p - f_s}{2 f_p} \right). \quad (\text{A.6})$$

The two definitions are approximately related as

A. DEFINITIONS AND MODELS

$$K_t^2 \approx \frac{k_t^2}{1 - k_t^2}. \quad (\text{A.7})$$

Appendix B

RF measurement

B.1 RF Probe Station setup

The RF measurements for the resonators and bandpass filters are performed using an RF network analyzer with a probe station (for the resonators and bandpass filters) or SMA connectors (for the notch filter). The probes used are PicoProbe Model 40A GSG 150 RF probes (PicoProbe by GGB Industries, Naples, Florida, USA) with 150 μm pitch.

B.2 Network analyzer setup

A vector network analyzer (VNA) is used to take the RF measurements. The Agilent (now Keysight Technologies, Santa Rosa, California, USA) N5230A VNA is used for the resonator and bandpass filter measurements, and the Agilent E8358A VNA is used for the notch filter measurements.

Calibration is performed using short-open-load-thru (SOLT) calibration with calibration substrates from the probe manufacturer for the probed setups (for resonators and bandpass filters) and using the LCAL06A SMA SOLT calibration kit (LiConn, Inc., Arden Hills, Minnesota, USA) for

B. RF MEASUREMENT

connectorized measurements (for the notch filter).

The settings for all measurements in this work are at least 6401 frequency points linearly spaced, IF bandwidth at most 100 Hz (lower IF bandwidth reduces noise in the measurement), power at most -10 dBm, and no averaging or smoothing.

Files are stored as S-parameters in real/imaginary TouchStone format (.s2p file extension) and can be processed using Matlab.

B.3 Deembedding procedures

In this work, open deembedding is used to remove parasitic capacitance due to test structures that would be minimized in a final application, such as probe pads.

The model for the parasitic elements is a Π network as shown in Figure B.1. These elements can be isolated in measurement by creating an “open” structure corresponding to Figure B.2. This usually means leaving the routing and release holes to the DUT intact, but removing the electrodes from where the DUT usually would be located. It is important to leave the etch release holes intact in order to estimate the parasitic admittance correctly.

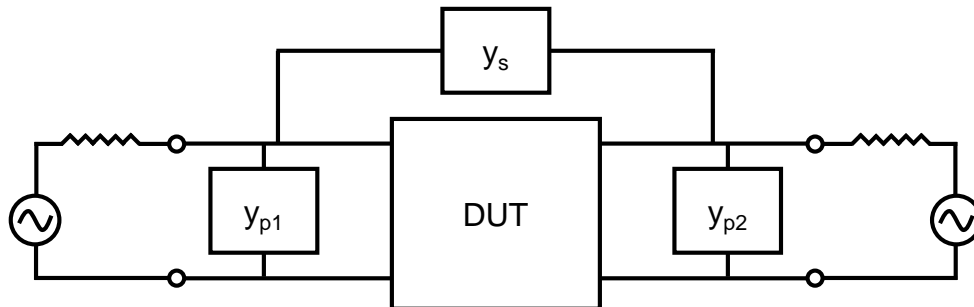


Figure B.1: Model of embedding network assumed during open deembedding. The “DUT” is the device under test, whose network parameters are desired.

The embedding parameters can be obtained by applying the definition of Y-parameters upon

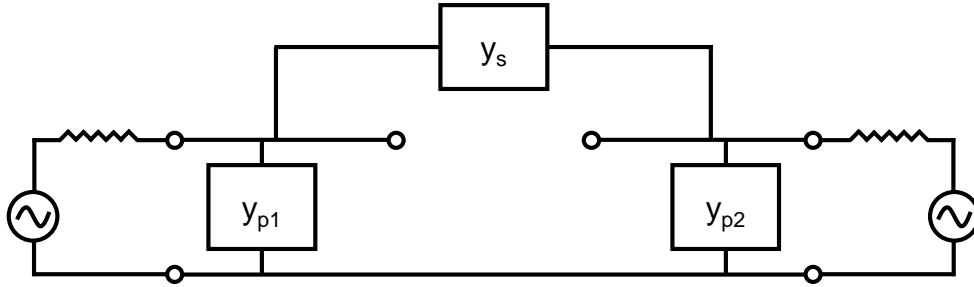


Figure B.2: Schematic of “open” structure to isolate embedding network assumed during open deembedding.

the measurement. The embedding parameters are

$$y_s = -Y_{21,open} \quad (\text{B.1})$$

$$y_{p1} = Y_{11,open} - y_s \quad (\text{B.2})$$

$$y_{p2} = Y_{22,open} - y_s \quad (\text{B.3})$$

where $y_{11,open}$, $y_{22,open}$, and $y_{12,open}$ are the measured Y-parameters of the deembedding structure (modeled by Figure B.2). Measured Y-parameters can be obtained from measured S-parameters using the conversion `s2y` in Matlab.

The deembedding step refers to subtracting the embedding parameters (y_s , y_{p1} , and y_{p2}) from the measurement (y_{meas}) to obtain the network parameters for only the device under test (DUT).

The equations to do this are

$$Y_{11,DUT} = Y_{11,meas} - y_{p1} - y_s \quad (\text{B.4})$$

$$Y_{22,DUT} = Y_{22,meas} - y_{p2} - y_s \quad (\text{B.5})$$

$$Y_{21,DUT} = Y_{21,meas} + y_s \quad (\text{B.6})$$

$$Y_{12,DUT} = Y_{12,meas} + y_s \quad (\text{B.7})$$

B. RF MEASUREMENT

The Y_{DUT} parameters can be converted back to S-parameters using $s2y$.

Appendix C

COMSOL FEA simulation setups

This appendix contains the COMSOL model files in .m format, showing the setup of key simulations.

C.1 2D simulation

This simulation gives information to estimate the behavior of K_t^2 and spurs due to 1D cavity modes. Wbloat is equivalent to W_u in this work.

```
function out = model
2 %
3 % resonator2dLNx60_even_electrode_share.m
4 %
5 % Model exported on May 26 2016, 17:43 by COMSOL 5.1.0.145.
6
7 import com.comsol.model.*
8 import com.comsol.model.util.*
9
10 model = ModelUtil.create('Model');
11
12 model.modelPath('/afs/ece.cmu.edu/usr/syen/Private/FP2 system simulations/
    gratings');
13
14 model.label('resonator2dLNx60-even-electrode-share.mph');
```

C. COMSOL FEA SIMULATION SETUPS

```
16 model.comments(['LNSiO3X-cutw2s2-weighted500M-tapeout-N21extend-DCbiasExpt\n\n
    ']);
18 model.param.set('Wf', '2', 'Width of inner fingers');
model.param.set('P', '6', 'Pitch of electrodes');
20 model.param.set('Wfout', '1', 'Width of outer fingers');
model.param.set('TLN', '1', 'Thickness of LN');
22 model.param.set('Nmid', '8', 'Number of middle fingers');
model.param.set('WLN', 'P*(Nmid+1)', 'Width of LN body');
24 model.param.set('WPTX', '0.75', 'Width of bottom Pt ledge');
model.param.set('WPT', 'WLN+2*WPTX', 'Width of bottom Pt');
26 model.param.set('Xleft', '-WLN/2+(P-Wf)/2+P/2', 'X-location of leftmost middle
    finger');
model.param.set('TPT', '0.09', 'Thickness of Pt bottom electrode');
28 model.param.set('TAL', '0.1', 'Thickness of Al electrode');
model.param.set('TALOX', '0.04', 'Thickness of Al2O3 coating');
30 model.param.set('Wmis', '0', 'Misalignment amount (Wmis>0, Wmis - Wbloat <
    Wfout)');
model.param.set('Wbloat', '0', 'LN bloat amount (symmetric, can be negative,
    but Wmis - Wbloat < Wfout)');
32
model.modelNode.create('mod1');
34 model.modelNode('mod1').label('Model 1');
model.modelNode('mod1').defineLocalCoord(false);
36
model.file.clear;
38
model.geom.create('geom1', 2);
40
model.mesh.create('mesh1', 'geom1');
42
model.geom('geom1').lengthUnit([native2unicode(hex2dec({'00' 'b5'}), 'unicode'
    ) 'm']);
44 model.geom('geom1').create('r1', 'Rectangle');
model.geom('geom1').feature('r1').label('LN body');
46 model.geom('geom1').feature('r1').set('size', {'WLN+Wbloat*2' 'TLN'});
model.geom('geom1').feature('r1').set('pos', {'-WLN/2-Wbloat' '0'});
48 model.geom('geom1').create('r2', 'Rectangle');
model.geom('geom1').feature('r2').active(false);
50 model.geom('geom1').feature('r2').label('Pt bottom electrode');
model.geom('geom1').feature('r2').set('size', {'WPT' 'TPT'});
52 model.geom('geom1').feature('r2').set('pos', {'-WPT/2' '-TPT'});
model.geom('geom1').create('r3', 'Rectangle');
54 model.geom('geom1').feature('r3').label('Leftmost middle finger Al');
model.geom('geom1').feature('r3').set('size', {'Wf' 'TAL'});
56 model.geom('geom1').feature('r3').set('pos', {'Xleft-Wmis' 'TLN'});
model.geom('geom1').create('r4', 'Rectangle');
58 model.geom('geom1').feature('r4').active(false);
model.geom('geom1').feature('r4').label('Al2O3 top of finger');
60 model.geom('geom1').feature('r4').set('size', {'Wf' 'TALOX'});
```

```

model.geom('geom1').feature('r4').set('pos', {'Xleft' 'TLN+TAL'});
62 model.geom('geom1').create('r5', 'Rectangle');
model.geom('geom1').feature('r5').active(false);
64 model.geom('geom1').feature('r5').label('Al203 left of finger');
model.geom('geom1').feature('r5').set('size', {'(P-Wf)/2' 'TALOX'});
66 model.geom('geom1').feature('r5').set('pos', {'Xleft-(P-Wf)/2' 'TLN'});
model.geom('geom1').create('r6', 'Rectangle');
68 model.geom('geom1').feature('r6').active(false);
model.geom('geom1').feature('r6').label('Al203 right of finger');
70 model.geom('geom1').feature('r6').set('size', {'(P-Wf)/2' 'TALOX'});
model.geom('geom1').feature('r6').set('pos', {'Xleft+Wf' 'TLN'});
72 model.geom('geom1').create('r7', 'Rectangle');
model.geom('geom1').feature('r7').active(false);
74 model.geom('geom1').feature('r7').label('Al203 left of finger conformal ledge'
);
model.geom('geom1').feature('r7').set('size', {'TALOX' 'TAL'});
76 model.geom('geom1').feature('r7').set('pos', {'Xleft-TALOX' 'TLN+TALOX'});
model.geom('geom1').create('r8', 'Rectangle');
78 model.geom('geom1').feature('r8').active(false);
model.geom('geom1').feature('r8').label('Al203 right of finger conformal ledge
');
80 model.geom('geom1').feature('r8').set('size', {'TALOX' 'TAL'});
model.geom('geom1').feature('r8').set('pos', {'Xleft+Wf' 'TLN+TALOX'});
82 model.geom('geom1').create('unil', 'Union');
model.geom('geom1').feature('unil').active(false);
84 model.geom('geom1').feature('unil').label('Al203 union over left middle finger
');
model.geom('geom1').feature('unil').set('intbnd', false);
86 model.geom('geom1').feature('unil').selection('input').set({});
model.geom('geom1').create('arr1', 'Array');
88 model.geom('geom1').feature('arr1').label('Middle finger array');
model.geom('geom1').feature('arr1').set('displ', {'P' '0'});
90 model.geom('geom1').feature('arr1').set('size', {'Nmid' '1'});
model.geom('geom1').feature('arr1').selection('input').set({'r3'});
92 model.geom('geom1').create('r9', 'Rectangle');
model.geom('geom1').feature('r9').label('Left reflector finger');
94 model.geom('geom1').feature('r9').set('size', {'Wfout+min(-Wmis,Wbloat,0)' '
TAL'});
model.geom('geom1').feature('r9').set('pos', {'-WLN/2-min(Wmis,Wbloat)' 'TLN'
});
96 model.geom('geom1').create('r10', 'Rectangle');
model.geom('geom1').feature('r10').active(false);
98 model.geom('geom1').feature('r10').label('Al203 right of left reflector finger
');
model.geom('geom1').feature('r10').set('size', {'P/2-Wfout' 'TALOX'});
100 model.geom('geom1').feature('r10').set('pos', {'-WLN/2+Wfout' 'TLN'});
model.geom('geom1').create('r11', 'Rectangle');
102 model.geom('geom1').feature('r11').active(false);
model.geom('geom1').feature('r11').label('Al203 right of left reflector finger
conformal ledge');
104 model.geom('geom1').feature('r11').set('size', {'TALOX' 'TAL'});

```

C. COMSOL FEA SIMULATION SETUPS

```
model.geom('geom1').feature('r11').set('pos', {'-WLN/2+Wfout' 'TLN+TALOX'});
106 model.geom('geom1').create('r12', 'Rectangle');
model.geom('geom1').feature('r12').active(false);
108 model.geom('geom1').feature('r12').label('Al203 top of left reflector finger')
    ;
model.geom('geom1').feature('r12').set('size', {'Wfout' 'TALOX'});
110 model.geom('geom1').feature('r12').set('pos', {'-WLN/2' 'TLN+TAL'});
model.geom('geom1').create('uni2', 'Union');
112 model.geom('geom1').feature('uni2').active(false);
model.geom('geom1').feature('uni2').label('Al203 union over Left reflector');
114 model.geom('geom1').feature('uni2').set('intbnd', false);
model.geom('geom1').feature('uni2').selection('input').set({});
116 model.geom('geom1').create('r13', 'Rectangle');
model.geom('geom1').feature('r13').label('right reflector finger');
118 model.geom('geom1').feature('r13').set('size', {'Wfout+min(0,Wmis+Wbloat)' '
    TAL'});
model.geom('geom1').feature('r13').set('pos', {'WLN/2-Wfout-Wmis' 'TLN'});
120 model.geom('geom1').create('mir1', 'Mirror');
model.geom('geom1').feature('mir1').active(false);
122 model.geom('geom1').feature('mir1').set('keep', true);
model.geom('geom1').feature('mir1').selection('input').set({'r9'});
124 model.geom('geom1').create('uni3', 'Union');
model.geom('geom1').feature('uni3').active(false);
126 model.geom('geom1').feature('uni3').label('Union of all Al203');
model.geom('geom1').feature('uni3').set('intbnd', false);
128 model.geom('geom1').feature('uni3').selection('input').set({});
model.geom('geom1').run;
130 model.geom('geom1').run('fin');

132 model.variable.create('var1');
model.variable('var1').model('mod1');
134 model.variable('var1').set('I_piezo', 'intop1(-es.Dx*nx-es.Dy*ny)*2*pi*freq*j*
    intop1(es.d)/intop1(1)');
model.variable('var1').set('Y11_piezo', 'I_piezo/lindev(es.V0_1)', 'admittance
    Y11');
136
model.view.create('view2', 2);
138
model.material.create('mat2', 'Common', 'mod1');
140 model.material.create('mat10', 'Common', 'mod1');
model.material.create('mat9', 'Common', 'mod1');
142 model.material.create('mat7', 'Common', 'mod1');
model.material.create('mat8', 'Common', 'mod1');
144 model.material('mat2').selection.set([]);
model.material('mat2').propertyGroup.create('Enu', 'Young''s modulus and
    Poisson''s ratio');
146 model.material('mat2').propertyGroup.create('StressCharge', 'Stress-charge
    form');
model.material('mat10').propertyGroup.create('Enu', 'Young''s modulus and
    Poisson''s ratio');
148 model.material('mat9').selection.set([2 3 4 5 6 7 8 9 10 11]);
```

```

model.material('mat9').propertyGroup.create('Enu', 'Young''s modulus and
    Poisson''s ratio');
150 model.material('mat7').selection.set([1]);
model.material('mat7').propertyGroup.create('StressCharge', 'Stress-charge
    form');
152 model.material('mat8').propertyGroup.create('Enu', 'Young''s modulus and
    Poisson''s ratio');

154 model.cpl.create('intop1', 'Integration', 'geom1');
model.cpl('intop1').selection.geom('geom1', 1);
156
model.coordSystem.create('mod1_xy_sys', 'geom1', 'VectorBase');
158 model.coordSystem.create('mod1_yz_sys', 'geom1', 'VectorBase');
model.coordSystem.create('mod1_zx_sys', 'geom1', 'VectorBase');
160 model.coordSystem.create('mod1_yx_sys', 'geom1', 'VectorBase');
model.coordSystem.create('mod1_xz_sys', 'geom1', 'VectorBase');
162 model.coordSystem.create('mod1_zy_sys', 'geom1', 'VectorBase');
model.coordSystem.create('pml1', 'geom1', 'PML');
164 model.coordSystem.create('pml2', 'geom1', 'PML');
model.coordSystem('mod1_xy_sys').set('orthonormal', true);
166 model.coordSystem('mod1_yz_sys').set('orthonormal', true);
model.coordSystem('mod1_zx_sys').set('orthonormal', true);
168 model.coordSystem('mod1_yx_sys').set('orthonormal', true);
model.coordSystem('mod1_xz_sys').set('orthonormal', true);
170 model.coordSystem('mod1_zy_sys').set('orthonormal', true);

172 model.physics.create('solid', 'SolidMechanics', 'geom1');
model.physics('solid').field('displacement').field('u2');
174 model.physics('solid').field('displacement').component({'u2' 'v2' 'w2'});
model.physics('solid').create('pzml', 'PiezoelectricMaterialModel', 2);
176 model.physics('solid').feature('pzml').selection.set([1]);
model.physics('solid').feature('pzml').create('dmp1', 'Damping', 2);
178 model.physics.create('es', 'Electrostatics', 'geom1');
model.physics('es').field('electricpotential').field('V2');
180 model.physics('es').create('ccnpl', 'ChargeConservationPiezo', 2);
model.physics('es').feature('ccnpl').selection.set([1]);
182 model.physics('es').create('gnd1', 'Ground', 1);
model.physics('es').feature('gnd1').selection.set([4 14 24 34 44]);
184 model.physics('es').create('term1', 'Terminal', 1);
model.physics('es').feature('term1').selection.set([9 19 29 39 49]);
186 model.physics('es').feature('term1').create('hp1', 'HarmonicPerturbation', 1);
model.physics('es').create('pot1', 'ElectricPotential', 1);
188 model.physics('es').feature('pot1').create('hp1', 'HarmonicPerturbation', 1);
model.physics('es').feature('pot1').feature('hp1').selection.set([]);
190 model.physics('es').create('term2', 'Terminal', 1);
model.physics('es').feature('term2').create('hp1', 'HarmonicPerturbation', 1);
192 model.physics('es').create('fp1', 'FloatingPotential', 1);
model.physics('es').feature('fp1').selection.set([2]);
194
model.multiphysics.create('pzel', 'PiezoelectricEffect', 'geom1', 2);
196

```

C. COMSOL FEA SIMULATION SETUPS

```
model.mesh('mesh1').autoMeshSize(4);
198
model.result.table.create('tbl1', 'Table');
200 model.result.table.create('evl2', 'Table');

202 model.probe.create('var1', 'GlobalVariable');
model.probe('var1').model('mod1');
204

model.view('view1').axis.set('abstractviewxscale', '0.0029729728121310472');
206 model.view('view1').axis.set('ymin', '-12.147374153137207');
model.view('view1').axis.set('xmax', '29.700000762939453');
208 model.view('view1').axis.set('abstractviewyscale', '0.0029729728121310472');
model.view('view1').axis.set('abstractviewbratio', '-11.04306697845459');
210 model.view('view1').axis.set('abstractviewratio', '11.04306697845459');
model.view('view1').axis.set('abstractviewrratio', '0.050000015646219254');
212 model.view('view1').axis.set('xmin', '-29.700000762939453');
model.view('view1').axis.set('abstractviewlratio', '-0.050000015646219254');
214 model.view('view1').axis.set('ymax', '13.247374534606934');
model.view('view2').axis.set('viewscaletype', 'automatic');
216

model.material('mat2').active(false);
218 model.material('mat2').label('SiO2');
model.material('mat2').propertyGroup('def').set('electricconductivity', {'0[S/
m]' '0' '0' '0' '0[S/m]' '0' '0' '0' '0[S/m]'});
220 model.material('mat2').propertyGroup('def').set('thermalexpansioncoefficient',
{'0.5e-6[1/K]' '0' '0' '0' '0.5e-6[1/K]' '0' '0' '0' '0.5e-6[1/K]'});
model.material('mat2').propertyGroup('def').set('heatcapacity', '730[J/(kg*K)]
');
222 model.material('mat2').propertyGroup('def').set('relpermittivity', {'4.2' '0'
'0' '0' '4.2' '0' '0' '0' '4.2'});
model.material('mat2').propertyGroup('def').set('density', '2200[kg/m^3]');
224 model.material('mat2').propertyGroup('def').set('thermalconductivity', {'1.4[W
/(m*K)]' '0' '0' '0' '1.4[W/(m*K)]' '0' '0' '0' '1.4[W/(m*K)]'});
model.material('mat2').propertyGroup('Enu').set('youngsmodulus', '70e9[Pa]');
226 model.material('mat2').propertyGroup('Enu').set('poissonsration', '0.17');
model.material('mat2').propertyGroup('StressCharge').set('cE', '');
228 model.material('mat2').propertyGroup('StressCharge').set('eES', '');
model.material('mat2').propertyGroup('StressCharge').set('epsilonSr', '');
230 model.material('mat2').propertyGroup('StressCharge').set('eta_cE', '');
model.material('mat2').propertyGroup('StressCharge').set('eta_eES', '');
232 model.material('mat2').propertyGroup('StressCharge').set('eta_epsilonS', '');
model.material('mat2').propertyGroup('StressCharge').set('cE', {'1.27205e11' '
8.02122e10' '0' '1.27205e11' '0' '2.29886e10' '8.02122e10' '8.46702e10' '0
' '8.46702e10' ...
234 '1.17436e11' '0' '0' '0' '0' '0' '0' '0' '1.27205e11' '8.46702e10' ...
'0' '0' '0' '2.29886e10' '0' '1.17436e11' '0' '0' '0' '0' ...
236 '2.29886e10' '0' '0' '2.29886e10' '0' '2.34742e10'});
model.material('mat2').propertyGroup('StressCharge').set('eES', {'0' '0' '0' '
0' '0' '0' '0' '0' ...
238 '0' '0' '0' '0' '0' '0' '0' '0'});
model.material('mat2').propertyGroup('StressCharge').set('epsilonSr', {'
```


C. COMSOL FEA SIMULATION SETUPS

```
model.material('mat7').propertyGroup('StressCharge').set('eta_eES', '');
276 model.material('mat7').propertyGroup('StressCharge').set('eta_epsilonS', '');
model.material('mat7').propertyGroup('StressCharge').set('cE', {'1.8671e11' '
    0.8218e11' '0.6478e11' '-0.0000' '-0.0000' '-0.0141e11' '0.8218e11' '
278     2.1794e11' '0.5788e11' '-0.0000' ...
'0.0000' '-0.0997e11' '0.6478e11' '0.5788e11' '1.9886e11' '0.0000' '0.0000' '
    -0.0968e11' '-0.0000' '-0.0000' ...
'0.0000' '0.5613e11' '0.0139e11' '0.0000' '-0.0000' '0.0000' '0.0000' '0.0139
280     e11' '0.7581e11' '0.0000' ...
'-0.0141e11' '-0.0997e11' '-0.0968e11' '0.0000' '0.0000' '0.7405e11'});
model.material('mat7').propertyGroup('StressCharge').set('eES', {'4.7231' '
    2.0081' '0' '-1.6556' '-2.5811' '0' '-1.9375' '-1.3842' '0' '-0.0000' ...
282 '0.0000' '-4.5019' '0.0000' '0.0000' '-0.1375' '-1.1096' '0.1444' '0.0000'});
model.material('mat7').propertyGroup('StressCharge').set('epsilonrS', {'
    41.0000' '6.9282' '0.0000' '6.9282' '33.0000' '-0.0000' '0.0000' '-0.0000'
284     '45.0000'});
model.material('mat7').propertyGroup('StressCharge').set('eta_cE', {'0' '0' '0
    ' '0' '0' '0' '0' '0' '0' '0' '0' '0' '0' '0' '0' '0' '0' '0' '0' '0' '0'
286     '0' '0' '0' '0' '0' '0' '0' '0' '0' '0' '0' '0' '0' '0' '0' '0' '0' '0' '0' '0'
'0' '0' '0' '0' '0' '0'});
288 model.material('mat7').propertyGroup('StressCharge').set('eta_eES', {'0' '0' '0
    ' '0' '0' '0' '0' '0' '0' '0' '0' '0' '0' '0' '0' '0' '0' '0' '0' '0' '0'
'0' '0' '0' '0' '0' '0'});
290 model.material('mat7').propertyGroup('StressCharge').set('eta_epsilonS', {'0'
    '0' '0' '0' '0' '0' '0' '0' '0'});
model.material('mat8').active(false);
292 model.material('mat8').label('Pt - Platinum');
model.material('mat8').set('diffuse', 'custom');
294 model.material('mat8').set('noise', 'on');
model.material('mat8').set('family', 'custom');
296 model.material('mat8').set('specular', 'custom');
model.material('mat8').set('customambient', {'0.7843137254901961' '
    0.7843137254901961' '0.7843137254901961'});
298 model.material('mat8').set('noisefreq', '1');
model.material('mat8').set('customspecular', {'0.7843137254901961' '1' '1'});
300 model.material('mat8').set('lighting', 'cooktorrance');
model.material('mat8').set('ambient', 'custom');
302 model.material('mat8').set('fresnel', '0.9');
model.material('mat8').set('customdiffuse', {'0.7843137254901961' '
    0.7843137254901961' '0.7843137254901961'});
304 model.material('mat8').propertyGroup('def').set('electricconductivity', {'8.9
    e6[S/m]' '0' '0' '0' '8.9e6[S/m]' '0' '0' '0' '8.9e6[S/m]});
model.material('mat8').propertyGroup('def').set('thermalexpansioncoefficient',
    {'8.80e-6[1/K]' '0' '0' '0' '8.80e-6[1/K]' '0' '0' '0' '8.80e-6[1/K]});
306 model.material('mat8').propertyGroup('def').set('heatcapacity', '133[J/(kg*K)
    ');
model.material('mat8').propertyGroup('def').set('density', '21450[kg/m^3]');
308 model.material('mat8').propertyGroup('def').set('thermalconductivity', {'71.6[
    W/(m*K)]' '0' '0' '0' '71.6[W/(m*K)]' '0' '0' '0' '71.6[W/(m*K)]'});
model.material('mat8').propertyGroup('def').set('relpermittivity', {'1e11' '0'
```

```

    '0' '0' '1e11' '0' '0' '0' '1e11'});
310 model.material('mat8').propertyGroup('Enu').set('youngsmodulus', '168e9[Pa]');
model.material('mat8').propertyGroup('Enu').set('poissonsratio', '0.38');
312
model.coordSystem('mod1_xy_sys').label('Material XY-Plane System');
314 model.coordSystem('mod1_yz_sys').label('Material YZ-Plane System');
model.coordSystem('mod1_yz_sys').set('outofplane', '0');
316 model.coordSystem('mod1_yz_sys').set('base', {'0' '0' '1'; '1' '0' '0'; '0' '1'
' '0'});
model.coordSystem('mod1_zx_sys').label('Material ZX-Plane System');
318 model.coordSystem('mod1_zx_sys').set('outofplane', '1');
model.coordSystem('mod1_zx_sys').set('base', {'0' '1' '0'; '0' '0' '1'; '1' '0'
' '0'});
320 model.coordSystem('mod1_yx_sys').label('Material YX-Plane System');
model.coordSystem('mod1_yx_sys').set('base', {'0' '1' '0'; '1' '0' '0'; '0' '0'
' '1'});
322 model.coordSystem('mod1_xz_sys').label('Material XZ-Plane System');
model.coordSystem('mod1_xz_sys').set('outofplane', '1');
324 model.coordSystem('mod1_xz_sys').set('base', {'1' '0' '0'; '0' '0' '1'; '0' '1'
' '0'});
model.coordSystem('mod1_zy_sys').label('Material ZY-Plane System');
326 model.coordSystem('mod1_zy_sys').set('outofplane', '0');
model.coordSystem('mod1_zy_sys').set('base', {'0' '0' '1'; '0' '1' '0'; '1' '0'
' '0'});
328
model.physics('solid').feature('lem1').set('coordinateSystem', 'mod1_xz_sys')
;
330 model.physics('solid').feature('pz1').feature('dmp1').set('DampingType', '
IsotropicLossFactor');
model.physics('solid').feature('pz1').feature('dmp1').set('eta_s_mat', '
userdef');
332 model.physics('solid').feature('pz1').feature('dmp1').set('eta_s', '0.001');
model.physics('es').feature('ccn1').set('coordinateSystem', 'mod1_xz_sys');
334 model.physics('es').feature('term1').set('TerminalType', 'Voltage');
model.physics('es').feature('term1').set('V0', '0');
336 model.physics('es').feature('pot1').active(false);
model.physics('es').feature('term2').active(false);
338 model.physics('es').feature('fp1').active(false);

340 model.multiphysics('pz1').set('InitializePiezoCoupling', '1');

342 model.mesh('mesh1').run;

344 model.result.table('tbl1').active(false);
model.result.table('tbl1').label('Probe Table 1');
346 model.result.table('evl2').label('Evaluation 2D');
model.result.table('evl2').comments('Interactive 2D values');
348
model.probe('var1').active(false);
350 model.probe('var1').set('window', 'window1');
model.probe('var1').set('expr', 'pzd.V0_2');

```

C. COMSOL FEA SIMULATION SETUPS

```
352 model.probe('var1').set('unit', 'V');
model.probe('var1').set('descr', 'Terminal voltage');
354 model.probe('var1').set('table', 'tbl1');

356 model.study.create('std1');
model.study('std1').create('param', 'Parametric');
358 model.study('std1').create('stat', 'Stationary');
model.study('std1').create('frlin', 'Frequencylinearized');
360

model.result.dataset.create('dset1', 'Solution');
362 model.result.dataset.create('dset3', 'Solution');
model.result.dataset.create('dset4', 'Solution');
364 model.result.dataset.create('dset5', 'Solution');
model.result.dataset('dset3').set('probetag', 'var1');
366 model.result.numerical.create('gev1', 'EvalGlobal');
model.result.numerical('gev1').set('data', 'dset3');
368 model.result.numerical('gev1').set('probetag', 'var1');
model.result.create('pg5', 'PlotGroup2D');
370 model.result.create('pg6', 'PlotGroup2D');
model.result.create('pg7', 'PlotGroup2D');
372 model.result.create('pg8', 'PlotGroup1D');
model.result.create('pg10', 'PlotGroup2D');
374 model.result.create('pg11', 'PlotGroup2D');
model.result.create('pg12', 'PlotGroup2D');
376 model.result('pg5').create('surf1', 'Surface');
model.result('pg6').create('surf1', 'Surface');
378 model.result('pg6').feature('surf1').create('def', 'Deform');
model.result('pg7').set('data', 'dset5');
380 model.result('pg7').create('surf1', 'Surface');
model.result('pg7').feature('surf1').create('def1', 'Deform');
382 model.result('pg8').create('glob1', 'Global');
model.result('pg10').create('arws1', 'ArrowSurface');
384 model.result('pg11').set('data', 'dset5');
model.result('pg11').create('surf1', 'Surface');
386 model.result('pg11').feature('surf1').create('def', 'Deform');
model.result('pg12').set('data', 'dset5');
388 model.result('pg12').create('surf1', 'Surface');
model.result.export.create('data1', 'Data');
390

model.study('std1').feature('param').active(false);
392 model.study('std1').feature('param').set('pname', {'Wbloat' 'Wmis'});
model.study('std1').feature('param').set('plistarr', {'-0.4,-0.4,-0.4,
    0,0,0,0,0,0.4,0.4,0.4,0.8,0.8,0.8' '0.3,0.1,0,0.9,0.7, 0.6, 0.4, 0.25,
    0,0.9,0.4,0,0.9,0.4,0'});
394 model.study('std1').feature('param').set('punit', {'' ''});
model.study('std1').feature('param').set('plotgroup', 'pg8');
396 model.study('std1').feature('param').set('plot', 'on');
model.study('std1').feature('stat').set('geometricNonlinearity', true);
398 model.study('std1').feature('frlin').set('plist', 'range(200,1,800)');
model.study('std1').feature('frlin').set('geometricNonlinearity', true);
400 model.study('std1').feature('frlin').set('punit', 'MHz');
```

```

402 model.result.dataset('dset3').label('Probe Solution 3');
model.result.numerical('gev1').active(false);
404 model.result.numerical('gev1').label('Global Variable Probe 1');
model.result.numerical('gev1').set('expr', 'pzd.V0_2');
406 model.result.numerical('gev1').set('descr', 'pzd.V0_2');
model.result.numerical('gev1').set('table', 'tbl1');
408 model.result('pg5').label('Electric Potential (es)');
model.result('pg5').set('frametype', 'spatial');
410 model.result('pg5').feature('surfl').set('expr', 'V2');
model.result('pg5').feature('surfl').set('unit', 'V');
412 model.result('pg5').feature('surfl').set('descr', 'Electric potential');
model.result('pg6').label('Stress (solid)');
414 model.result('pg6').feature('surfl').set('expr', 'solid.mises');
model.result('pg6').feature('surfl').set('unit', 'N/m^2');
416 model.result('pg6').feature('surfl').set('descr', 'von Mises stress');
model.result('pg6').feature('surfl').feature('def').set('scale', '0');
418 model.result('pg6').feature('surfl').feature('def').set('scaleactive', false);
model.result('pg7').feature('surfl').feature('def1').set('scaleactive', true);
420 model.result('pg7').feature('surfl').feature('def1').set('scale', '150');
model.result('pg8').label('admittance from I-V');
422 model.result('pg8').set('ylabel', 'admittance dBS');
model.result('pg8').set('xlabel', 'freq');
424 model.result('pg8').set('xlabelactive', false);
model.result('pg8').set('ylabelactive', false);
426 model.result('pg8').feature('glob1').set('unit', {'});
model.result('pg8').feature('glob1').set('descr', {'admittance dBS'});
428 model.result('pg8').feature('glob1').set('expr', {'20*log10(abs(es.IO_1/es.
    V0_1))'});
model.result('pg10').label('2D Plot Efield');
430 model.result('pg10').feature('arws1').set('scale', '3.026164385948591E-7');
model.result('pg10').feature('arws1').set('expr', {'es.EX' 'es.EY'});
432 model.result('pg10').feature('arws1').set('ynumber', '5');
model.result('pg10').feature('arws1').set('descr', 'Electric field (Material)');
434 model.result('pg10').feature('arws1').set('xnumber', '100');
model.result('pg10').feature('arws1').set('scaleactive', false);
436 model.result('pg11').label('Stress (solid) 1');
model.result('pg11').feature('surfl').set('expr', 'solid.mises');
438 model.result('pg11').feature('surfl').set('unit', 'N/m^2');
model.result('pg11').feature('surfl').set('descr', 'von Mises stress');
440 model.result('pg11').feature('surfl').feature('def').set('scale', '0');
model.result('pg11').feature('surfl').feature('def').set('scaleactive', false);
442 model.result('pg12').label('Electric Potential (es) 1');
model.result('pg12').set('frametype', 'spatial');
444 model.result('pg12').feature('surfl').set('expr', 'V2');
model.result('pg12').feature('surfl').set('unit', 'V');
446 model.result('pg12').feature('surfl').set('descr', 'Electric potential');
model.result.export('data1').set('data', 'dset5');
448 model.result.export('data1').set('descr', {'Admittance'});

```

C. COMSOL FEA SIMULATION SETUPS

```
450 model.result.export('data1').set('expr', {'es.I0_1/es.V0_1'});
    model.result.export('data1').set('filename', '/afs/ece.cmu.edu/usr/syen/
        Private/FP2_system_simulations/gratings/Y11-1portLN60x-500M-Nmid8-AlElec-
        Wf2p265AR2p265um-Wbloat1p5Wmis1.csv');
452 model.result.export('data1').set('sdim', 'global');
    model.result.export('data1').set('unit', {''});
454 out = model;
```

C.2 3D simulation with misalignment and underetch

This simulation includes a Perfectly Matched Layer (PML) boundary condition on the undercut LN plate to model anchor loss and spurs. For the resonator simulations of Chapter 2, there was only the rectangular undercut segment immediately attached to the anchor (as depicted in Figure 1.5b), and a Fixed Constraint boundary condition was used at the vertical edge of that segment (no PML). For the resonator simulations in Chapter 4, there was no Linear Elastic Model condition (LinearElasticModel) on the electrodes.

This model is inherited from [19]. Changes from the inherited simulation are:

- Rotated the orientation of the corner PML elements (the cylinders) to match the x -cut 60 degree orientation of the geometry
- Finer meshing, such that COMSOL gave no warnings regarding element size
- Calculation of x and y displacements (in the resonator frame of reference) added using a rotation upon v and w from the global coordinate system
- Addition of Linear Elastic Material Model (LinearElasticModel) to the electrodes to model their mechanical loading (but not for the simulations in Chapter 4)

C.2 3D simulation with misalignment and underetch

```
function out = model
2 %
3 % Anchor_losses_3D_substrate_PML_even_manualmeshfine_Ey197GPaNu1_...
4 % rotatePMLcyls_misalignbloat_P6p551xmis0p43bloat1p69_TLN0p875TA10p05.m
5 %
6 % Model exported on May 26 2016, 17:55 by COMSOL 5.1.0.145.
7
8 import com.comsol.model.*
9 import com.comsol.model.util.*
10
11 model = ModelUtil.create('Model');
12
13 model.modelPath('/afs/ece.cmu.edu/usr/syen/Private/FP2 system simulations/
14 gratings');
15
16 model.label('Anchor_losses_3D_substrate_PML_even_manualmeshfine-Ey197GPaNu1-
17 rotatePMLcyls-misalignbloat-P6p551xmis0p43bloat1p69-TLN0p875TA10p05-
18 RESULTS.mph');
19
20 model.comments(['500MHz anchor losses 3D substrate PML\n\n']);
21
22 model.param.set('Wa', '4.5*13.102[um]', 'anchor width');
23 model.param.set('La', '13.102[um]', 'anchor length');
24 model.param.set('L', '111.367[um]', 'resonator length');
25 model.param.set('Rs', '43[um]', 'substrate radius');
26 model.param.set('PML', '43[um]', 'PML radius');
27 model.param.set('lambda', '13.102[um]', 'PML wavelength');
28 model.param.set('scale', '1', 'PML scaling factor');
29 model.param.set('order', '1', 'PML order');
30 model.param.set('TAL', '0.05[um]', 'thickness of metal');
31 model.param.set('sp', '2[um]', 'gap between bus and finger end');
32 model.param.set('bus', '6.551[um]', 'bus width');
33 model.param.set('TLN', '0.875[um]', 'thickness of LN');
34 model.param.set('oe', '0[um]', 'overetch');
35 model.param.set('pitwidth', '18[um]', 'width of etch pit');
36 model.param.set('Wf', '2.348[um]', 'Width of fingers');
37 model.param.set('Wr', '2.663[um]', 'Width of reflector finger');
38 model.param.set('pitrectwidth', '2*pitwidth+9/2*lambda', 'width of overall
39 etch pit (both etch pits plus resonator)');
40 model.param.set('angle', '-60[deg]', 'angle of rotation of x-cut LN relative
41 to +z axis');
42 model.param.set('ypml', 'cos(angle)*(L+La)-sin(angle)*(pitrectwidth/2)', '
43 rotated y-coord of cylinder radius for PML, for 1st quadrant before
44 rotation');
45 model.param.set('zpml', 'sin(angle)*(L+La)+cos(angle)*(pitrectwidth/2)', '
46 rotated z-coord of cylinder radius for PML, for 1st quadrant before
47 rotation');
48 model.param.set('xmis', '0.43[um]', 'amount of misalignment in x (direction of
49 wave propagation)');
50 model.param.set('bloat', '1.69[um]', 'amount of underetch');
```

C. COMSOL FEA SIMULATION SETUPS

```
42 model.modelNode.create('mod1');
model.modelNode('mod1').label('Model 1');
44 model.modelNode('mod1').defineLocalCoord(false);

46 model.file.clear;

48 model.geom.create('geom1', 3);

50 model.mesh.create('mesh1', 'geom1');

52 model.geom('geom1').geomRep('comsol');
model.geom('geom1').repairTol(1.0E-7);
54 model.geom('geom1').create('blk2', 'Block');
model.geom('geom1').feature('blk2').label('anchor');
56 model.geom('geom1').feature('blk2').set('axis', {'0' '0' '1'});
model.geom('geom1').feature('blk2').set('size', {'Wa-2*oe+2*bloat' 'La' 'TLN'
});
58 model.geom('geom1').feature('blk2').set('pos', {'0' 'L/2+La/2' '0'});
model.geom('geom1').feature('blk2').set('base', 'center');
60 model.geom('geom1').create('mir1', 'Mirror');
model.geom('geom1').feature('mir1').set('keep', true);
62 model.geom('geom1').feature('mir1').set('axis', {'0' '-1' '0'});
model.geom('geom1').feature('mir1').set('pos', {'0' '0' '0'});
64 model.geom('geom1').feature('mir1').selection('input').set({'blk2'});
model.geom('geom1').create('unil', 'Union');
66 model.geom('geom1').feature('unil').set('repairtol', '1.0E-6');
model.geom('geom1').feature('unil').selection('input').set({'blk2' 'mir1'});
68 model.geom('geom1').create('blk5', 'Block');
model.geom('geom1').feature('blk5').label('undercut area before anchor');
70 model.geom('geom1').feature('blk5').set('size', {'pitrectwidth' 'Rs' 'TLN'});
model.geom('geom1').feature('blk5').set('pos', {'0' 'L/2+La+Rs/2' '0'});
72 model.geom('geom1').feature('blk5').set('base', 'center');
model.geom('geom1').create('int1', 'Intersection');
74 model.geom('geom1').feature('int1').active(false);
model.geom('geom1').feature('int1').set('intbnd', false);
76 model.geom('geom1').feature('int1').set('repairtol', '1.0E-6');
model.geom('geom1').feature('int1').selection('input').set({});
78 model.geom('geom1').create('blk6', 'Block');
model.geom('geom1').feature('blk6').label('undercut area next to etch pit
parallel to resonator length');
80 model.geom('geom1').feature('blk6').set('size', {'Rs' 'L+2*La' 'TLN'});
model.geom('geom1').feature('blk6').set('pos', {'-Rs/2-pitrectwidth/2' '0' '0'
});
82 model.geom('geom1').feature('blk6').set('base', 'center');
model.geom('geom1').create('mir5', 'Mirror');
84 model.geom('geom1').feature('mir5').set('keep', true);
model.geom('geom1').feature('mir5').set('axis', {'1' '0' '0'});
86 model.geom('geom1').feature('mir5').selection('input').set({'blk6'});
model.geom('geom1').create('cyl2', 'Cylinder');
88 model.geom('geom1').feature('cyl2').set('r', 'Rs');
```

C.2 3D simulation with misalignment and underetch

```
model.geom('geom1').feature('cyl2').set('axis', {'0' '0' '1'});
90 model.geom('geom1').feature('cyl2').set('pos', {'-pitrectwidth/2' 'L/2+La' '-
    TLN/2'});
model.geom('geom1').feature('cyl2').set('h', 'TLN');
92 model.geom('geom1').create('mir6', 'Mirror');
model.geom('geom1').feature('mir6').set('keep', true);
94 model.geom('geom1').feature('mir6').set('axis', {'1' '0' '0'});
model.geom('geom1').feature('mir6').selection('input').set({'cyl2'});
96 model.geom('geom1').create('blk7', 'Block');
model.geom('geom1').feature('blk7').label('block for subtracting cylinder');
98 model.geom('geom1').feature('blk7').set('size', {'pitrectwidth + 2*Rs' 'Rs' '
    TLN'});
model.geom('geom1').feature('blk7').set('pos', {'0' 'La+L/2-Rs/2' '0'});
100 model.geom('geom1').feature('blk7').set('base', 'center');
model.geom('geom1').create('dif1', 'Difference');
102 model.geom('geom1').feature('dif1').set('repairtol', '1.0E-6');
model.geom('geom1').feature('dif1').set('intbnd', false);
104 model.geom('geom1').feature('dif1').selection('input').set({'cyl2' 'mir6'});
model.geom('geom1').feature('dif1').selection('input2').set({'blk5' 'blk7'});
106 model.geom('geom1').create('copy1', 'Copy');
model.geom('geom1').feature('copy1').selection('input').set({'dif1'});
108 model.geom('geom1').create('blk8', 'Block');
model.geom('geom1').feature('blk8').label('undercut area before anchor 2');
110 model.geom('geom1').feature('blk8').set('size', {'pitrectwidth' 'Rs' 'TLN'});
model.geom('geom1').feature('blk8').set('pos', {'0' 'L/2+La+Rs/2' '0'});
112 model.geom('geom1').feature('blk8').set('base', 'center');
model.geom('geom1').create('mir7', 'Mirror');
114 model.geom('geom1').feature('mir7').set('keep', true);
model.geom('geom1').feature('mir7').set('axis', {'0' '-1' '0'});
116 model.geom('geom1').feature('mir7').selection('input').set({'blk8' 'dif1'});
model.geom('geom1').create('uni3', 'Union');
118 model.geom('geom1').feature('uni3').set('repairtol', '1.0E-6');
model.geom('geom1').feature('uni3').selection('input').set({'blk6' 'blk8' '
    dif1' 'mir5' 'mir7(1)'});
120 model.geom('geom1').create('blk9', 'Block');
model.geom('geom1').feature('blk9').set('size', {'pitrectwidth+Rs' 'Rs+PML' '
    TLN'});
122 model.geom('geom1').feature('blk9').set('pos', {'Rs/2' 'L/2+La+(Rs+PML)/2' '0'
    });
model.geom('geom1').feature('blk9').set('base', 'center');
124 model.geom('geom1').create('blk10', 'Block');
model.geom('geom1').feature('blk10').set('size', {'PML' 'L+2*La' 'TLN'});
126 model.geom('geom1').feature('blk10').set('pos', {'-Rs-pitrectwidth/2-PML/2' '0'
    '0'});
model.geom('geom1').feature('blk10').set('base', 'center');
128 model.geom('geom1').create('mir8', 'Mirror');
model.geom('geom1').feature('mir8').set('keep', true);
130 model.geom('geom1').feature('mir8').set('axis', {'1' '0' '0'});
model.geom('geom1').feature('mir8').set('pos', {'0' '0' '0'});
132 model.geom('geom1').feature('mir8').selection('input').set({'blk10'});
model.geom('geom1').create('cyl3', 'Cylinder');
```

C. COMSOL FEA SIMULATION SETUPS

```
134 model.geom('geom1').feature('cyl3').set('r', 'Rs+PML');
model.geom('geom1').feature('cyl3').set('pos', {'-pitrectwidth/2' 'L/2+La' '-
    TLN/2'});
136 model.geom('geom1').feature('cyl3').set('h', 'TLN');
model.geom('geom1').create('mir9', 'Mirror');
138 model.geom('geom1').feature('mir9').active(false);
model.geom('geom1').feature('mir9').set('keep', true);
140 model.geom('geom1').feature('mir9').set('axis', {'1' '0' '0'});
model.geom('geom1').feature('mir9').selection('input').set({'cyl3'});
142 model.geom('geom1').create('blk11', 'Block');
model.geom('geom1').feature('blk11').set('size', {'100e-6+2*Rs+2*PML' 'Rs+PML'
    'TLN'});
144 model.geom('geom1').feature('blk11').set('pos', {'0' 'La+L/2-PML/2-Rs/2' '0'})
    ;
model.geom('geom1').feature('blk11').set('base', 'center');
146 model.geom('geom1').create('dif2', 'Difference');
model.geom('geom1').feature('dif2').set('repairtol', '1.0E-6');
148 model.geom('geom1').feature('dif2').set('intbnd', false);
model.geom('geom1').feature('dif2').selection('input').set({'cyl3'});
150 model.geom('geom1').feature('dif2').selection('input2').set({'blk11' 'blk9'
    'copy1'});
model.geom('geom1').create('blk12', 'Block');
152 model.geom('geom1').feature('blk12').set('size', {'pitrectwidth' 'PML' 'TLN'})
    ;
model.geom('geom1').feature('blk12').set('pos', {'0' 'L/2+La+Rs+PML/2' '0'});
154 model.geom('geom1').feature('blk12').set('base', 'center');
model.geom('geom1').create('mir10', 'Mirror');
156 model.geom('geom1').feature('mir10').set('keep', true);
model.geom('geom1').feature('mir10').set('axis', {'0' '-1' '0'});
158 model.geom('geom1').feature('mir10').selection('input').set({'blk12' 'dif2'});
model.geom('geom1').create('mir11', 'Mirror');
160 model.geom('geom1').feature('mir11').set('keep', true);
model.geom('geom1').feature('mir11').set('axis', {'1' '0' '0'});
162 model.geom('geom1').feature('mir11').selection('input').set({'blk10' 'dif2'
    'mir10(2)'});
model.geom('geom1').create('blk17', 'Block');
164 model.geom('geom1').feature('blk17').label('LN plate');
model.geom('geom1').feature('blk17').set('axis', {'0' '0' '1'});
166 model.geom('geom1').feature('blk17').set('size', {'9/2*lambda - oe*2+2*bloat'
    'L' 'TLN'});
model.geom('geom1').feature('blk17').set('pos', {'-9/4*lambda+oe-bloat' '-L/2'
    '-TLN/2'});
168 model.geom('geom1').create('blk13', 'Block');
model.geom('geom1').feature('blk13').label('reflector finger');
170 model.geom('geom1').feature('blk13').set('size', {'Wr - oe' 'L-bus*2-sp' 'TAL'
    });
model.geom('geom1').feature('blk13').set('pos', {'-9/4*lambda + Wr/2 +oe/2 +
    xmis' '-sp/2' 'TLN/2+TAL/2'});
172 model.geom('geom1').feature('blk13').set('base', 'center');
model.geom('geom1').create('rot3', 'Rotate');
174 model.geom('geom1').feature('rot3').label('Rotate reflector finger');
```

C.2 3D simulation with misalignment and underetch

```
model.geom('geom1').feature('rot3').set('keep', true);
176 model.geom('geom1').feature('rot3').set('rot', '180');
model.geom('geom1').feature('rot3').selection('input').set({'blk13'});
178 model.geom('geom1').create('mov2', 'Move');
model.geom('geom1').feature('mov2').label('Move rotated reflector finger for
    misalignment');
180 model.geom('geom1').feature('mov2').set('displx', '2*xmis');
model.geom('geom1').feature('mov2').selection('input').set({'rot3'});
182 model.geom('geom1').create('blk15', 'Block');
model.geom('geom1').feature('blk15').label('lower bus');
184 model.geom('geom1').feature('blk15').set('size', {'9/2*lambda-oe*2' 'bus' 'TAL
    '});
model.geom('geom1').feature('blk15').set('pos', {'-9/4*lambda+oe+xmis' '-L/2'
    'TLN/2'});
186 model.geom('geom1').create('blk16', 'Block');
model.geom('geom1').feature('blk16').label('upper bus');
188 model.geom('geom1').feature('blk16').set('size', {'9/2*lambda-oe*2' 'bus' 'TAL
    '});
model.geom('geom1').feature('blk16').set('pos', {'-9/4*lambda+oe+xmis' 'L/2-
    bus' 'TLN/2'});
190 model.geom('geom1').create('blk14', 'Block');
model.geom('geom1').feature('blk14').label('middle finger');
192 model.geom('geom1').feature('blk14').set('size', {'Wf' 'L-bus*2-sp' 'TAL'});
model.geom('geom1').feature('blk14').set('pos', {'-3*lambda/2-lambda/4+xmis' '
    sp/2' 'TLN/2+TAL/2'});
194 model.geom('geom1').feature('blk14').set('base', 'center');
model.geom('geom1').create('arr1', 'Array');
196 model.geom('geom1').feature('arr1').set('size', {'4' '1' '1'});
model.geom('geom1').feature('arr1').set('displ', {'lambda' '0' '0'});
198 model.geom('geom1').feature('arr1').selection('input').set({'blk14'});
model.geom('geom1').create('mov1', 'Move');
200 model.geom('geom1').feature('mov1').label('move to create alternating middle
    fingers');
model.geom('geom1').feature('mov1').set('keep', true);
202 model.geom('geom1').feature('mov1').set('displx', 'lambda/2');
model.geom('geom1').feature('mov1').set('disply', '-sp');
204 model.geom('geom1').feature('mov1').selection('input').set({'arr1(1,1,1)' '
    arr1(2,1,1)' 'arr1(3,1,1)' 'arr1(4,1,1)'});
model.geom('geom1').create('blk18', 'Block');
206 model.geom('geom1').feature('blk18').label('anchor electrode');
model.geom('geom1').feature('blk18').set('axis', {'0' '0' '1'});
208 model.geom('geom1').feature('blk18').set('size', {'Wa-2*oe' 'La' 'TAL'});
model.geom('geom1').feature('blk18').set('pos', {'xmis' 'L/2+La/2' 'TLN/2+TAL
    /2'});
210 model.geom('geom1').feature('blk18').set('base', 'center');
model.geom('geom1').create('mir12', 'Mirror');
212 model.geom('geom1').feature('mir12').set('keep', true);
model.geom('geom1').feature('mir12').set('axis', {'0' '-1' '0'});
214 model.geom('geom1').feature('mir12').set('pos', {'0' '0' '0'});
model.geom('geom1').feature('mir12').selection('input').set({'blk18'});
216 model.geom('geom1').create('arr2', 'Array');
```

C. COMSOL FEA SIMULATION SETUPS

```
model.geom('geom1').feature('arr2').active(false);
218 model.geom('geom1').feature('arr2').set('size', {'60' '1' '1'});
model.geom('geom1').feature('arr2').set('displ', {'1e-6' '0' '0'});
220 model.geom('geom1').feature('arr2').selection('input').set({'blk17'});
model.geom('geom1').create('ext1', 'Extrude');
222 model.geom('geom1').feature('ext1').active(false);
model.geom('geom1').feature('ext1').set('unite', false);
224 model.geom('geom1').feature('ext1').setIndex('distance', 'Lm', 0);
model.geom('geom1').feature('ext1').selection('inputface').set('uni1(1)', [4
    9]);
226 model.geom('geom1').create('uni4', 'Union');
model.geom('geom1').feature('uni4').active(false);
228 model.geom('geom1').feature('uni4').set('keep', true);
model.geom('geom1').feature('uni4').set('repairtol', '1.0E-6');
230 model.geom('geom1').feature('uni4').selection('input').set({'arr1' 'blk10' '
    blk12' 'blk13' 'blk15' 'blk16' 'dif2' 'mir10' 'mir11' 'mir8' ...
    'mov1' 'uni1' 'uni3'});
232 model.geom('geom1').create('rot1', 'Rotate');
model.geom('geom1').feature('rot1').set('rot', '90');
234 model.geom('geom1').feature('rot1').set('axis', {'0' '1' '0'});
model.geom('geom1').feature('rot1').selection('input').set({'arr1' 'blk10' '
    blk12' 'blk13' 'blk15' 'blk16' 'blk17' 'blk18' 'dif2' 'mir10' ...
236 'mir11' 'mir12' 'mir7(2)' 'mir8' 'mov1' 'mov2' 'uni1' 'uni3'});
model.geom('geom1').create('rot2', 'Rotate');
238 model.geom('geom1').feature('rot2').set('rot', 'angle');
model.geom('geom1').feature('rot2').set('axis', {'1' '0' '0'});
240 model.geom('geom1').feature('rot2').selection('input').set({'rot1'});
model.geom('geom1').run;
242 model.geom('geom1').run('fin');

244 model.selection.create('sell1', 'Explicit');
model.selection('sell1').geom('geom1', 1);
246 model.selection.create('box1', 'Box');
model.selection('box1').set('entitydim', '2');
248 model.selection('box1').set('condition', 'inside');
model.selection('box1').set('xmin', '-60e-6');
250 model.selection('box1').set('zmax', '0.3e-6');
model.selection('box1').set('zmin', '-0.2e-6');
252 model.selection('box1').set('ymax', '(Rs+L/2+La+1e-6)');
model.selection('box1').set('ymin', '-(Rs+L/2+La+1e-6)');
254 model.selection('box1').set('xmax', '60e-6');
model.selection('box1').label('top');
256
258 model.view.create('view2', 2);
model.view.create('view3', 2);
model.view.create('view4', 3);
260
262 model.material.create('mat1', 'Common', 'mod1');
model.material.create('mat2', 'Common', 'mod1');
model.material.create('mat3', 'Common', 'mod1');
264 model.material.create('mat4', 'Common', 'mod1');
```

C.2 3D simulation with misalignment and underetch

```
model.material.create('mat5', 'Common', 'mod1');
266 model.material.create('mat6', 'Common', 'mod1');
model.material('mat1').propertyGroup.create('StrainCharge', 'Strain-charge
    form');
268 model.material('mat1').propertyGroup.create('StressCharge', 'Stress-charge
    form');
model.material('mat2').propertyGroup('def').func.create('dL', 'Piecewise');
270 model.material('mat2').propertyGroup('def').func.create('k', 'Piecewise');
model.material('mat2').propertyGroup('def').func.create('res', 'Piecewise');
272 model.material('mat2').propertyGroup('def').func.create('epsilon', 'Piecewise'
    );
model.material('mat2').propertyGroup('def').func.create('alpha', 'Piecewise');
274 model.material('mat2').propertyGroup('def').func.create('C_solid_1', '
    Piecewise');
model.material('mat2').propertyGroup('def').func.create('HC_solid_1', '
    Piecewise');
276 model.material('mat2').propertyGroup('def').func.create('mu', 'Piecewise');
model.material('mat2').propertyGroup('def').func.create('sigma', 'Piecewise');
278 model.material('mat2').propertyGroup('def').func.create('rho', 'Piecewise');
model.material('mat2').propertyGroup('def').func.create('VP_solid_1', '
    Piecewise');
280 model.material('mat2').propertyGroup('def').func.create('kappa', 'Piecewise');
model.material('mat2').propertyGroup.create('Enu', 'Young''s modulus and
    Poisson''s ratio');
282 model.material('mat2').propertyGroup('Enu').func.create('E', 'Piecewise');
model.material('mat2').propertyGroup('Enu').func.create('nu', 'Piecewise');
284 model.material('mat3').selection.set([1 2 3 4 5 6 7 8 9 10 11 12 13 14 15 16
    17 18 19 21 22 27 28 29 30 31 32]);
model.material('mat3').propertyGroup.create('StressCharge', 'Stress-charge
    form');
286 model.material('mat4').selection.set([20 21 22 23 24 25 26 27 28 29 30 31 32
    33]);
model.material('mat4').propertyGroup.create('Enu', 'Young''s modulus and
    Poisson''s ratio');
288 model.material('mat5').selection.set([1 2 3 4 5 6 7 8 9 10 11 12 13 14 15 16
    17 18 19]);
model.material('mat5').propertyGroup.create('StressCharge', 'Stress-charge
    form');
290 model.material('mat6').selection.set([1 2 3 4 5 6 7 8 9 10 11 12 13 14 15 16
    17 18 19]);
model.material('mat6').propertyGroup.create('StrainCharge', 'Strain-charge
    form');
292 model.material('mat6').propertyGroup.create('StressCharge', 'Stress-charge
    form');

294 model.physics.create('pzd', 'PiezoelectricDevices', 'geom1');
model.physics('pzd').create('gnd1', 'Ground', 2);
296 model.physics('pzd').feature('gnd1').selection.set([167 169 171 173 175 177
    178]);
model.physics('pzd').create('fix1', 'Fixed', 2);
298 model.physics('pzd').create('term1', 'Terminal', 2);
```

C. COMSOL FEA SIMULATION SETUPS

```
model.physics('pzd').feature('term1').selection.set([165 166 168 170 172 174
176]);
300 model.physics('pzd').create('pml1', 'PML', 3);
model.physics('pzd').feature('pml1').selection.set([16]);
302 model.physics('pzd').create('pml6', 'PML', 3);
model.physics('pzd').feature('pml6').selection.set([2]);
304 model.physics('pzd').create('pml7', 'PML', 3);
model.physics('pzd').feature('pml7').selection.set([3]);
306 model.physics('pzd').create('pml8', 'PML', 3);
model.physics('pzd').feature('pml8').selection.set([17]);
308 model.physics('pzd').create('pml2', 'PML', 3);
model.physics('pzd').feature('pml2').selection.set([11]);
310 model.physics('pzd').create('pml3', 'PML', 3);
model.physics('pzd').feature('pml3').selection.set([1]);
312 model.physics('pzd').create('pml4', 'PML', 3);
model.physics('pzd').feature('pml4').selection.set([7]);
314 model.physics('pzd').create('pml5', 'PML', 3);
model.physics('pzd').feature('pml5').selection.set([19]);
316 model.physics('pzd').create('eqm1', 'ElectricalQuasistaticModel', 3);
model.physics('pzd').feature('eqm1').selection.set([20 21 22 23 24 25 26 27 28
29 30 31 32 33]);
318 model.physics('pzd').create('lemm1', 'LinearElasticModel', 3);
model.physics('pzd').feature('lemm1').selection.set([20 21 22 23 24 25 26 27
28 29 30 31 32 33]);
320
model.mesh('mesh1').create('ftri2', 'FreeTri');
322 model.mesh('mesh1').create('sizel', 'Size');
model.mesh('mesh1').create('ftet1', 'FreeTet');
324 model.mesh('mesh1').create('size2', 'Size');
model.mesh('mesh1').create('ftril', 'FreeTri');
326 model.mesh('mesh1').create('swe3', 'Sweep');
model.mesh('mesh1').create('ftri3', 'FreeTri');
328 model.mesh('mesh1').create('swel', 'Sweep');
model.mesh('mesh1').create('fq2', 'FreeQuad');
330 model.mesh('mesh1').create('swe4', 'Sweep');
model.mesh('mesh1').create('fq1', 'FreeQuad');
332 model.mesh('mesh1').create('swe2', 'Sweep');
model.mesh('mesh1').create('swe5', 'Sweep');
334 model.mesh('mesh1').feature('ftri2').selection.set([75 76 79 80 84 88 94 99
104 108 113 118 123 126 131 134 138 140 161]);
model.mesh('mesh1').feature('ftri2').create('sizel', 'Size');
336 model.mesh('mesh1').feature('ftet1').selection.geom('geom1', 3);
model.mesh('mesh1').feature('ftet1').selection.set([20 21 22 23 24 25 26 27 28
29 30 31 32 33]);
338 model.mesh('mesh1').feature('ftril').selection.set([73 125]);
model.mesh('mesh1').feature('swe3').selection.geom('geom1', 3);
340 model.mesh('mesh1').feature('swe3').selection.set([6 8 9 13 14]);
model.mesh('mesh1').feature('ftri3').selection.set([71 72 91 116 144 163]);
342 model.mesh('mesh1').feature('swel').selection.geom('geom1', 3);
model.mesh('mesh1').feature('swel').selection.set([4 5 10 12 15 18]);
344 model.mesh('mesh1').feature('fq2').create('sizel', 'Size');
```

C.2 3D simulation with misalignment and underetch

```
model.mesh('mesh1').feature('fq2').feature('size1').selection.geom('geom1', 2)
;
346 model.mesh('mesh1').feature('swe4').selection.geom('geom1', 3);
model.mesh('mesh1').feature('swe4').selection.set([6 8 13 14 20 33]);
348 model.mesh('mesh1').feature('fq1').selection.set([71 72 91 116 144 163]);
model.mesh('mesh1').feature('fq1').create('dis1', 'Distribution');
350 model.mesh('mesh1').feature('fq1').create('size1', 'Size');
model.mesh('mesh1').feature('fq1').feature('dis1').selection.set([82 112 144
237]);
352 model.mesh('mesh1').feature('swe2').selection.geom('geom1', 3);
model.mesh('mesh1').feature('swe2').selection.set([1 2 3 7 11 16 17 19]);
354 model.mesh('mesh1').feature('swe2').create('dis1', 'Distribution');
model.mesh('mesh1').feature('swe2').feature('dis1').selection.set([1 7 11 19])
;
356 model.mesh('mesh1').feature('swe5').create('dis1', 'Distribution');

358 model.result.table.create('tbl5', 'Table');
model.result.table.create('tbl6', 'Table');
360 model.result.table.create('tbl7', 'Table');
model.result.table.create('tbl8', 'Table');
362 model.result.table.create('tbl9', 'Table');
model.result.table.create('evl3', 'Table');
364

model.view('view1').set('scenelight', 'off');
366 model.view('view2').axis.set('ymin', '-0.6345691680908203');
model.view('view2').axis.set('xmax', '1.5411033630371094');
368 model.view('view2').axis.set('xmin', '-0.5411035418510437');
model.view('view2').axis.set('ymax', '1.6345691680908203');
370 model.view('view3').axis.set('ymin', '-0.6345691680908203');
model.view('view3').axis.set('xmax', '2.5399553775787354');
372 model.view('view3').axis.set('xmin', '-1.5399553775787354');
model.view('view3').axis.set('ymax', '1.6345691680908203');
374

model.material('mat1').active(false);
376 model.material('mat1').label('Aluminum Nitride');
model.material('mat1').set('diffuse', 'custom');
378 model.material('mat1').set('noise', 'on');
model.material('mat1').set('family', 'custom');
380 model.material('mat1').set('specular', 'custom');
model.material('mat1').set('customambient', {'0.7843137254901961' '
0.7843137254901961' '0.7843137254901961'});
382 model.material('mat1').set('noisefreq', '1');
model.material('mat1').set('customspecular', {'0.7843137254901961' '1' '1'});
384 model.material('mat1').set('lighting', 'cooktorrance');
model.material('mat1').set('ambient', 'custom');
386 model.material('mat1').set('fresnel', '0.9');
model.material('mat1').set('customdiffuse', {'0.7843137254901961' '
0.7843137254901961' '0.7843137254901961'});
388 model.material('mat1').propertyGroup('def').func.label('Functions');
model.material('mat1').propertyGroup('def').set('density', '5080[kg/m^3]');
390 model.material('mat1').propertyGroup('def').set('youngsmodulus', '385e9');
```


C.2 3D simulation with misalignment and underetch

```
    0[C/m^2]' '1.55[C/m^2]' '0[C/m^2]' ...
    '-0.48[C/m^2]' '0[C/m^2]' '-0.48[C/m^2]' '0[C/m^2]' '0[C/m^2]' '0[C/m^2]' '0[C
426 model.material('mat1').propertyGroup('StressCharge').set('epsilonRS', {'9' '0'
    '0' '0' '9' '0' '0' '0' '9'});
model.material('mat1').propertyGroup('StressCharge').set('eta_cE', {'0' '0' '0
    ' '0' '0' '0' '0' '0' '0' '0' ...
428 '0' '0' '0' '0' '0' '0' '0' '0' '0' '0' '0' ...
    '0' '0' '0' '0' '0' '0' '0' '0' '0' ...
430 '0' '0' '0' '0' '0' '0'});
model.material('mat1').propertyGroup('StressCharge').set('eta_eES', {'0' '0' '
    0' '0' '0' '0' '0' '0' '0' '0' ...
432 '0' '0' '0' '0' '0' '0' '0' '0'});
model.material('mat1').propertyGroup('StressCharge').set('eta_epsilonS', {'0'
    '0' '0' '0' '0' '0' '0' '0' '0'});
434 model.material('mat2').active(false);
model.material('mat2').label('Platinum [solid]');
436 model.material('mat2').set('diffuse', 'custom');
model.material('mat2').set('noise', 'on');
438 model.material('mat2').set('family', 'custom');
model.material('mat2').set('specular', 'custom');
440 model.material('mat2').set('customambient', {'0.7843137254901961' '
    0.7843137254901961' '0.7843137254901961'});
model.material('mat2').set('noisefreq', '1');
442 model.material('mat2').set('customspecular', {'0.7843137254901961' '1' '1'});
model.material('mat2').set('lighting', 'cooktorrance');
444 model.material('mat2').set('ambient', 'custom');
model.material('mat2').set('fresnel', '0.9');
446 model.material('mat2').set('customdiffuse', {'0.7843137254901961' '
    0.7843137254901961' '0.7843137254901961'});
model.material('mat2').propertyGroup('def').func.label('Functions');
448 model.material('mat2').propertyGroup('def').func('dL').set('pieces', {'10.0' '
    70.0' '-0.00192855+1.134373E-6*T^1-9.005848E-8*T^2+3.271584E-9*T
    ^3-3.362442E-11*T^4+1.238208E-13*T^5'; '70.0' '280.0' '
    -0.001895358-2.225109E-6*T^1+7.277336E-8*T^2-2.321766E-10*T^3+2.913888E-13
    *T^4'; '280.0' '1973.0' '-0.002617286+8.777313E-6*T^1+3.786334E-10*T
    ^2+5.373731E-13*T^3-6.636722E-17*T^4'});
model.material('mat2').propertyGroup('def').func('dL').set('arg', 'T');
450 model.material('mat2').propertyGroup('def').func('k').set('pieces', {'0.0' '
    13.0' '209.6991*T^1+18.16709*T^2-4.678988*T^3+0.2278691*T^4-0.002748296*T
    ^5'; '13.0' '50.0' '2978.797-201.1759*T^1+3.362113*T^2+0.0713319*T
    ^3-0.002761393*T^4+2.280531E-5*T^5'; '50.0' '100.0' '1212.843-69.25658*T
    ^1+1.763533*T^2-0.0228956*T^3+1.494028E-4*T^4-3.889706E-7*T^5'; '100.0' '
    285.0' '123.3886-1.066855*T^1+0.009646914*T^2-4.536814E-5*T^3+1.072687E-7*
    T^4-1.004522E-10*T^5'; '285.0' '2045.0' '73.99627-0.01557887*T^1+2.646931E
    -5*T^2-6.133801E-9*T^3'});
model.material('mat2').propertyGroup('def').func('k').set('arg', 'T');
452 model.material('mat2').propertyGroup('def').func('res').set('pieces', {'14.0'
    '47.0' '-5.497611E-10+1.415797E-10*T^1-1.305787E-11*T^2+5.545444E-13*T
    ^3-7.41428E-15*T^4+3.513902E-17*T^5'; '47.0' '160.0' '1.845544E-9-3.44008E
    -10*T^1+1.431636E-11*T^2-1.250757E-13*T^3+5.330375E-16*T^4-8.95938E-19*T^5
```

C. COMSOL FEA SIMULATION SETUPS

```
    '160.0' '600.0' '-1.927892E-8+5.233699E-10*T^1-4.107885E-13*T
    ^2+6.694129E-16*T^3-4.447775E-19*T^4'; '600.0' '2000.0' '-4.843579E
    -8+5.552497E-10*T^1-1.600249E-13*T^2+2.814022E-17*T^3'});
model.material('mat2').propertyGroup('def').func('res').set('arg', 'T');
454 model.material('mat2').propertyGroup('def').func('epsilon').set('pieces', {'
    1000.0' '2000.0' '0.1248438+6.688811E-5*T^1+5.827506E-10*T^2'});
model.material('mat2').propertyGroup('def').func('epsilon').set('arg', 'T');
456 model.material('mat2').propertyGroup('def').func('alpha').set('pieces', {'10.0
    ' '70.0' '6.594988E-6+1.839984E-8*T^1+3.921862E-10*T^2-1.081641E-11*T
    ^3+1.007161E-13*T^4-3.398394E-16*T^5'; '70.0' '230.0' '6.867919E
    -6+1.945355E-8*T^1-6.698432E-11*T^2+1.199734E-13*T^3-1.069967E-16*T^4'; '
    230.0' '1973.0' '8.801519E-6+4.097477E-10*T^1+1.248065E-12*T^2-7.133932E
    -16*T^3+1.689741E-19*T^4'});
model.material('mat2').propertyGroup('def').func('alpha').set('arg', 'T');
458 model.material('mat2').propertyGroup('def').func('C_solid_1').set('pieces', {'
    0.0' '19.0' '0.03281349*T^1+0.001129466*T^2+3.449445E-4*T^3+5.174165E-5*T
    ^4-1.325633E-6*T^5'; '19.0' '119.0' '10.30393-1.986516*T^1+0.1283953*T
    ^2-0.002010741*T^3+1.359791E-5*T^4-3.445457E-8*T^5'; '119.0' '290.0' '
    0.4467027+1.721765*T^1-0.009418853*T^2+2.453936E-5*T^3-2.455881E-8*T^4'; '
    290.0' '2000.0' '122.2187+0.03986346*T^1-1.836174E-5*T^2+7.556773E-9*T^3
    '});
model.material('mat2').propertyGroup('def').func('C_solid_1').set('arg', 'T');
460 model.material('mat2').propertyGroup('def').func('HC_solid_1').set('pieces', {
    '0.0' '19.0' '0.006401583*T^1+2.203475E-4*T^2+6.72952E-5*T^3+1.009428E-5*T
    ^4-2.586177E-7*T^5'; '19.0' '119.0' '2.018562-0.3875494*T^1+0.02504865*T
    ^2-3.922754E-4*T^3+2.652817E-6*T^4-6.721742E-9*T^5'; '119.0' '290.0' '
    0.08714724+0.3358992*T^1-0.001837525*T^2+4.787383E-6*T^3-4.791178E-9*T^4';
    '290.0' '2000.0' '23.84364+0.007776964*T^1-3.582192E-6*T^2+1.47425E-9*T^3
    '});
model.material('mat2').propertyGroup('def').func('HC_solid_1').set('arg', 'T')
;
462 model.material('mat2').propertyGroup('def').func('mu').set('pieces', {'293.0'
    '1480.0' '6.55395E10-1.15E7*T^1+3.035766E-9*T^2'});
model.material('mat2').propertyGroup('def').func('mu').set('arg', 'T');
464 model.material('mat2').propertyGroup('def').func('sigma').set('pieces', {'14.0
    ' '47.0' '1/(3.513902E-17*T^5-7.414280E-15*T^4+5.545444E-13*T^3-1.305787E
    -11*T^2+1.415797E-10*T-5.497611E-10)'; '47.0' '160.0' '1/(-8.959380E-19*T
    ^5+5.330375E-16*T^4-1.250757E-13*T^3+1.431636E-11*T^2-3.440080E-10*T
    +1.845544E-09)'; '160.0' '600.0' '1/(-4.447775E-19*T^4+6.694129E-16*T
    ^3-4.107885E-13*T^2+5.233699E-10*T-1.927892E-08)'; '600.0' '2000.0' '
    1/(2.814022E-17*T^3-1.600249E-13*T^2+5.552497E-10*T-4.843579E-08)'});
model.material('mat2').propertyGroup('def').func('sigma').set('arg', 'T');
466 model.material('mat2').propertyGroup('def').func('rho').set('pieces', {'10.0'
    '70.0' '21512.45-0.07336997*T^1+0.005824972*T^2-2.116082E-4*T^3+2.17523E-6
    *T^4-8.010422E-9*T^5'; '70.0' '280.0' '21510.32+0.1433013*T^1-0.00470128*T
    ^2+1.502256E-5*T^3-1.883994E-8*T^4'; '280.0' '1973.0' '21557.19-0.5675783*
    T^1-1.7525E-5*T^2-3.171806E-8*T^3+4.698968E-12*T^4'});
model.material('mat2').propertyGroup('def').func('rho').set('arg', 'T');
468 model.material('mat2').propertyGroup('def').func('VP_solid_1').set('pieces', {
    '293.0' '2041.0' '(exp((-2.938700e+004/T+1.103900e+000*log10(T)+7.762810e
    +000-4.527000e-001/T^3)*log(10.0)))*1.333200e+002'});
```

C.2 3D simulation with misalignment and underetch

```
model.material('mat2').propertyGroup('def').func('VP_solid_1').set('arg', 'T')
;
470 model.material('mat2').propertyGroup('def').func('kappa').set('pieces', {'
    293.0' '1480.0' '1.99731E11-6.619246E7*T^1+4690.398*T^2'});
model.material('mat2').propertyGroup('def').func('kappa').set('arg', 'T');
472 model.material('mat2').propertyGroup('def').set('dL', 'dL(T[1/K])-dL(Tempref
    [1/K])');
model.material('mat2').propertyGroup('def').set('thermalconductivity', {'k(T
    [1/K])[W/(m*K)]' '0' '0' '0' 'k(T[1/K])[W/(m*K)]' '0' '0' '0' 'k(T[1/K])[W
    /
    (m*K)]'});
474 model.material('mat2').propertyGroup('def').set('resistivity', {'res(T[1/K])[
    ohm*m]' '0' '0' '0' 'res(T[1/K])[ohm*m]' '0' '0' '0' 'res(T[1/K])[ohm*m]'
    });
model.material('mat2').propertyGroup('def').set('emissivity', 'epsilon(T[1/K])
    ');
476 model.material('mat2').propertyGroup('def').set('thermalexpansioncoefficient',
    {'alpha(T[1/K])[1/K]+(Tempref-293[K])/(T-Tempref)*(alpha(T[1/K])[1/K]-
    alpha(Tempref[1/K])[1/K])' '0' '0' '0' 'alpha(T[1/K])[1/K]+(Tempref-293[K]
    )/(T-Tempref)*(alpha(T[1/K])[1/K]-alpha(Tempref[1/K])[1/K])' '0' '0' '0'
    'alpha(T[1/K])[1/K]+(Tempref-293[K])/(T-Tempref)*(alpha(T[1/K])[1/K]-alpha
    (Tempref[1/K])[1/K])'});
model.material('mat2').propertyGroup('def').set('heatcapacity', 'C_solid_1(T
    [1/K])[J/(kg*K)]');
478 model.material('mat2').propertyGroup('def').set('HC', 'HC_solid_1(T[1/K])[J/(
    mol*K)]');
model.material('mat2').propertyGroup('def').set('mu', 'mu(T[1/K])[Pa]');
480 model.material('mat2').propertyGroup('def').set('electricconductivity', {'
    sigma(T[1/K])[S/m]' '0' '0' '0' 'sigma(T[1/K])[S/m]' '0' '0' '0' 'sigma(T
    [1/K])[S/m]'});
model.material('mat2').propertyGroup('def').set('density', 'rho(T[1/K])[kg/m
    ^3]');
482 model.material('mat2').propertyGroup('def').set('VP', 'VP_solid_1(T[1/K])[Pa]
    ');
model.material('mat2').propertyGroup('def').set('kappa', 'kappa(T[1/K])[Pa]');
484 model.material('mat2').propertyGroup('def').addInput('temperature');
model.material('mat2').propertyGroup('def').addInput('
    strainreferencetemperature');
486 model.material('mat2').propertyGroup('Enu').info('category').body('
    Solid_mechanics/Linear_elastic_material_model');
model.material('mat2').propertyGroup('Enu').func.label('Functions');
488 model.material('mat2').propertyGroup('Enu').func('E').set('pieces', {'93.0' '
    293.0' '1.667479E11-4.099535E7*T^1+54115.62*T^2-51.62897*T^3'; '293.0' '
    1480.0' '1.68E11-3.38E7*T^1'});
model.material('mat2').propertyGroup('Enu').func('E').set('arg', 'T');
490 model.material('mat2').propertyGroup('Enu').func('nu').set('pieces', {'293.0'
    '1480.0' '0.3516936-1.897311E-5*T^1-5.685048E-9*T^2'});
model.material('mat2').propertyGroup('Enu').func('nu').set('arg', 'T');
492 model.material('mat2').propertyGroup('Enu').set('youngsmodulus', 'E(T[1/K])[Pa
    ]');
model.material('mat2').propertyGroup('Enu').set('poissonsratio', 'nu(T[1/K])'
    );
;
```


C.2 3D simulation with misalignment and underetch

```
    0' '0' '0' '0' '0' '0' '0' '0' '0' ...
    '0' '0' '0' '0' '0' '0' '0' '0' '0'});
606 model.material('mat6').propertyGroup('StrainCharge').set('eta_epsilonT', {'0'
    '0' '0' '0' '0' '0' '0' '0' '0'});
model.material('mat6').propertyGroup('StressCharge').set('cE', '');
608 model.material('mat6').propertyGroup('StressCharge').set('eES', '');
model.material('mat6').propertyGroup('StressCharge').set('epsilonrS', '');
610 model.material('mat6').propertyGroup('StressCharge').set('eta_cE', '');
model.material('mat6').propertyGroup('StressCharge').set('eta_eES', '');
612 model.material('mat6').propertyGroup('StressCharge').set('eta_epsilonS', '');
model.material('mat6').propertyGroup('StressCharge').set('cE', {'2.02897e+011[
    Pa]' '5.29177e+010[Pa]' '7.49098e+010[Pa]' '8.99874e+009[Pa]' '0[Pa]' '0[
    Pa]' '5.29177e+010[Pa]' '2.02897e+011[Pa]' '7.49098e+010[Pa]' '-8.99874e
    +009[Pa]' ...
614 '0[Pa]' '0[Pa]' '7.49098e+010[Pa]' '7.49098e+010[Pa]' '2.43075e+011[Pa]' '0[Pa
    ]' '0[Pa]' '0[Pa]' '8.99874e+009[Pa]' '-8.99874e+009[Pa]' ...
    '0[Pa]' '5.99034e+010[Pa]' '0[Pa]' '0[Pa]' '0[Pa]' '0[Pa]' '0[Pa]' '0[Pa]' '
    5.99018e+010[Pa]' '8.98526e+009[Pa]' ...
616 '0[Pa]' '0[Pa]' '0[Pa]' '0[Pa]' '8.98526e+009[Pa]' '7.48772e+010[Pa]'});
model.material('mat6').propertyGroup('StressCharge').set('eES', {'0[C/m^2]' '
    -2.53764[C/m^2]' '0.193644[C/m^2]' '0[C/m^2]' '2.53764[C/m^2]' '0.193644[C
    /m^2]' '0[C/m^2]' '0[C/m^2]' '1.30863[C/m^2]' '0[C/m^2]' ...
618 '3.69548[C/m^2]' '0[C/m^2]' '3.69594[C/m^2]' '0[C/m^2]' '0[C/m^2]' '-2.53384[C
    /m^2]' '0[C/m^2]' '0[C/m^2]'});
model.material('mat6').propertyGroup('StressCharge').set('epsilonrS', {'43.6'
    '0' '0' '0' '43.6' '0' '0' '0' '29.16'});
620 model.material('mat6').propertyGroup('StressCharge').set('eta_cE', {'0' '0' '0'
    '0' '0' '0' '0' '0' '0' ...
    '0' '0' '0' '0' '0' '0' '0' '0' '0' '0' ...
622 '0' '0' '0' '0' '0' '0' '0' '0' '0' '0' ...
    '0' '0' '0' '0' '0' '0'});
624 model.material('mat6').propertyGroup('StressCharge').set('eta_eES', {'0' '0' '
    0' '0' '0' '0' '0' '0' '0' ...
    '0' '0' '0' '0' '0' '0' '0' '0'});
626 model.material('mat6').propertyGroup('StressCharge').set('eta_epsilonS', {'0'
    '0' '0' '0' '0' '0' '0' '0' '0'});

628 model.coordSystem('sys1').set('frametype', 'material');
model.coordSystem('sys1').set('mastercoordsystcomp', 'manual');
630
model.physics('pzd').feature('pzm1').set('cE', {'1.34868e11[Pa]'; '6.78883e10[
    Pa]'; '6.80876e10[Pa]'; '0[Pa]'; '0[Pa]'; '0[Pa]'; '6.78883e10[Pa]'; '
    1.34868e11[Pa]'; '6.80876e10[Pa]'; '0[Pa]'; ...
632 '0[Pa]'; '0[Pa]'; '6.80876e10[Pa]'; '6.80876e10[Pa]'; '1.13297e11[Pa]'; '0[Pa]
    '; '0[Pa]'; '0[Pa]'; '0[Pa]'; '0[Pa]'; ...
    '0[Pa]'; '2.22222e10[Pa]'; '0[Pa]'; '0[Pa]'; '0[Pa]'; '0[Pa]'; '0[Pa]'; '0[Pa]
    '; '2.22222e10[Pa]'; '0[Pa]'; ...
634 '0[Pa]'; '0[Pa]'; '0[Pa]'; '0[Pa]'; '0[Pa]'; '3.34448e10[Pa]'});
model.physics('pzd').feature('pzm1').set('eES', {'0[C/m^2]'; '0[C/m^2]'; '
    -1.81603[C/m^2]'; '0[C/m^2]'; '0[C/m^2]'; '-1.81603[C/m^2]'; '0[C/m^2]'; '
    0[C/m^2]'; '9.05058[C/m^2]'; '0[C/m^2]'; ...
```

C. COMSOL FEA SIMULATION SETUPS

```
636 '9.77778[C/m^2]'; '0[C/m^2]'; '9.77778[C/m^2]'; '0[C/m^2]'; '0[C/m^2]'; '0[C/m
    ^2]'; '0[C/m^2]'; '0[C/m^2]'});
model.physics('pzd').feature('pzml').set('epsilonRS', {'504.1'; '0'; '0'; '0';
    '504.1'; '0'; '0'; '0'; '270'});
638 model.physics('pzd').feature('pzml').set('sE', {'1.16e-11[1/Pa]'; '0[1/Pa]'; '
    0[1/Pa]'; '0[1/Pa]'; '0[1/Pa]'; '0[1/Pa]'; '-3.33e-12[1/Pa]'; '1.16e-11[1/
    Pa]'; '0[1/Pa]'; '0[1/Pa]'; ...
    '0[1/Pa]'; '0[1/Pa]'; '-4.97e-12[1/Pa]'; '-4.97e-12[1/Pa]'; '1.48e-11[1/Pa]';
    '0[1/Pa]'; '0[1/Pa]'; '0[1/Pa]'; '0[1/Pa]'; '0[1/Pa]'; ...
640 '0[1/Pa]'; '4.5e-11[1/Pa]'; '0[1/Pa]'; '0[1/Pa]'; '0[1/Pa]'; '0[1/Pa]'; '0[1/
    Pa]'; '0[1/Pa]'; '4.5e-11[1/Pa]'; '0[1/Pa]'; ...
    '0[1/Pa]'; '0[1/Pa]'; '0[1/Pa]'; '0[1/Pa]'; '0[1/Pa]'; '2.99E-11[1/Pa]'});
642 model.physics('pzd').feature('pzml').set('dET', {'0[C/N]'; '0[C/N]'; '-6E-11[C
    /N]'; '0[C/N]'; '0[C/N]'; '-6E-11[C/N]'; '0[C/N]'; '0[C/N]'; '1.52E-10[C/N
    ]'; '0[C/N]'; ...
    '4.4E-10[C/N]'; '0[C/N]'; '4.4E-10[C/N]'; '0[C/N]'; '0[C/N]'; '0[C/N]'; '0[C/N
    ]'; '0[C/N]'});
644 model.physics('pzd').feature('pzml').set('epsilonRT', {'990'; '0'; '0'; '0'; '
    990'; '0'; '0'; '0'; '450'});
model.physics('pzd').feature('pzml').set('mininput_electricfield_src', 'root.
    mod1.pzd.EX');
646 model.physics('pzd').feature('pzml').set('mininput_strainreferencetemperature',
    '0');
model.physics('pzd').feature('pzml').label('Piezoelectric Material Model 1');
648 model.physics('pzd').feature('fix1').active(false);
model.physics('pzd').feature('term1').set('TerminalType', 'Voltage');
650 model.physics('pzd').feature('pml1').set('PMLfactor', 'scale');
model.physics('pzd').feature('pml1').set('PMLorder', 'order');
652 model.physics('pzd').feature('pml1').set('lambdaPML', 'lambda');
model.physics('pzd').feature('pml1').feature('lemm1').set('AdvMatRes', '1');
654 model.physics('pzd').feature('pml1').feature('lemm1').set('
    mininput_electricfield_src', 'root.mod1.pzd.EX');
model.physics('pzd').feature('pml1').feature('lemm1').set('
    mininput_strainreferencetemperature', '0');
656 model.physics('pzd').feature('pml1').feature('lemm1').label('Linear Elastic
    Material Model 1');
model.physics('pzd').feature('pml1').featureInfo('warning').set('$message', {'
    This_feature_is_obsolete_and_will_be_removed_in_future_versions'});
658 model.physics('pzd').feature('pml6').set('PMLfactor', 'scale');
model.physics('pzd').feature('pml6').set('PMLorder', 'order');
660 model.physics('pzd').feature('pml6').set('lambdaPML', 'lambda');
model.physics('pzd').feature('pml6').feature('lemm1').set('
    mininput_electricfield_src', 'root.mod1.pzd.EX');
662 model.physics('pzd').feature('pml6').feature('lemm1').set('
    mininput_strainreferencetemperature', '0');
model.physics('pzd').feature('pml6').feature('lemm1').label('Linear Elastic
    Material Model 1');
664 model.physics('pzd').feature('pml6').featureInfo('warning').set('$message', {'
    This_feature_is_obsolete_and_will_be_removed_in_future_versions'});
model.physics('pzd').feature('pml7').set('PMLfactor', 'scale');
666 model.physics('pzd').feature('pml7').set('PMLorder', 'order');
```

C.2 3D simulation with misalignment and underetch

```
model.physics('pzd').feature('pml7').set('lambdaPML', 'lambda');
668 model.physics('pzd').feature('pml7').feature('lemml').set('
    minput_electricfield_src', 'root.mod1.pzd.EX');
model.physics('pzd').feature('pml7').feature('lemml').set('
    minput_strainreferencetemperature', '0');
670 model.physics('pzd').feature('pml7').feature('lemml').label('Linear Elastic
    Material Model 1');
model.physics('pzd').feature('pml7').featureInfo('warning').set('$message', {'
    This_feature_is_obsolete_and_will_be_removed_in_future_versions'});
672 model.physics('pzd').feature('pml8').set('PMLfactor', 'scale');
model.physics('pzd').feature('pml8').set('PMLorder', 'order');
674 model.physics('pzd').feature('pml8').set('lambdaPML', 'lambda');
model.physics('pzd').feature('pml8').feature('lemml').set('
    minput_electricfield_src', 'root.mod1.pzd.EX');
676 model.physics('pzd').feature('pml8').feature('lemml').set('
    minput_strainreferencetemperature', '0');
model.physics('pzd').feature('pml8').feature('lemml').label('Linear Elastic
    Material Model 1');
678 model.physics('pzd').feature('pml8').featureInfo('warning').set('$message', {'
    This_feature_is_obsolete_and_will_be_removed_in_future_versions'});
model.physics('pzd').feature('pml2').set('ScalingType', 'Cylindrical');
680 model.physics('pzd').feature('pml2').set('r0', {'0'; '-ypml'; 'zpml'});
model.physics('pzd').feature('pml2').set('raxis', {'1'; '0'; '0'});
682 model.physics('pzd').feature('pml2').set('PMLfactor', 'scale');
model.physics('pzd').feature('pml2').set('PMLorder', 'order');
684 model.physics('pzd').feature('pml2').set('lambdaPML', 'lambda');
model.physics('pzd').feature('pml2').feature('lemml').set('
    minput_electricfield_src', 'root.mod1.pzd.EX');
686 model.physics('pzd').feature('pml2').feature('lemml').set('
    minput_strainreferencetemperature', '0');
model.physics('pzd').feature('pml2').feature('lemml').label('Linear Elastic
    Material Model 1');
688 model.physics('pzd').feature('pml2').featureInfo('warning').set('$message', {'
    This_feature_is_obsolete_and_will_be_removed_in_future_versions'});
model.physics('pzd').feature('pml3').set('ScalingType', 'Cylindrical');
690 model.physics('pzd').feature('pml3').set('r0', {'0'; '-ypml'; '-zpml'});
model.physics('pzd').feature('pml3').set('raxis', {'1'; '0'; '0'});
692 model.physics('pzd').feature('pml3').set('PMLfactor', 'scale');
model.physics('pzd').feature('pml3').set('PMLorder', 'order');
694 model.physics('pzd').feature('pml3').set('lambdaPML', 'lambda');
model.physics('pzd').feature('pml3').feature('lemml').set('
    minput_electricfield_src', 'root.mod1.pzd.EX');
696 model.physics('pzd').feature('pml3').feature('lemml').set('
    minput_strainreferencetemperature', '0');
model.physics('pzd').feature('pml3').feature('lemml').label('Linear Elastic
    Material Model 1');
698 model.physics('pzd').feature('pml3').featureInfo('warning').set('$message', {'
    This_feature_is_obsolete_and_will_be_removed_in_future_versions'});
model.physics('pzd').feature('pml4').set('ScalingType', 'Cylindrical');
700 model.physics('pzd').feature('pml4').set('r0', {'0'; 'ypml'; '-zpml'});
model.physics('pzd').feature('pml4').set('raxis', {'1'; '0'; '0'});
```

C. COMSOL FEA SIMULATION SETUPS

```
702 model.physics('pzd').feature('pml4').set('PMLfactor', 'scale');
model.physics('pzd').feature('pml4').set('PMLorder', 'order');
704 model.physics('pzd').feature('pml4').set('lambdaPML', 'lambda');
model.physics('pzd').feature('pml4').feature('lemml').set('
    minput_electricfield_src', 'root.mod1.pzd.EX');
706 model.physics('pzd').feature('pml4').feature('lemml').set('
    minput_strainreferencetemperature', '0');
model.physics('pzd').feature('pml4').feature('lemml').label('Linear Elastic
    Material Model 1');
708 model.physics('pzd').feature('pml4').featureInfo('warning').set('$message', {'
    This_feature_is_obsolete_and_will_be_removed_in_future_versions'});
model.physics('pzd').feature('pml5').set('ScalingType', 'Cylindrical');
710 model.physics('pzd').feature('pml5').set('r0', {'0'; 'ypml'; 'zpml'});
model.physics('pzd').feature('pml5').set('raxis', {'1'; '0'; '0'});
712 model.physics('pzd').feature('pml5').set('PMLfactor', 'scale');
model.physics('pzd').feature('pml5').set('PMLorder', 'order');
714 model.physics('pzd').feature('pml5').set('lambdaPML', 'lambda');
model.physics('pzd').feature('pml5').feature('lemml').set('
    minput_electricfield_src', 'root.mod1.pzd.EX');
716 model.physics('pzd').feature('pml5').feature('lemml').set('
    minput_strainreferencetemperature', '0');
model.physics('pzd').feature('pml5').feature('lemml').label('Linear Elastic
    Material Model 1');
718 model.physics('pzd').feature('pml5').featureInfo('warning').set('$message', {'
    This_feature_is_obsolete_and_will_be_removed_in_future_versions'});
model.physics('pzd').feature('eqm1').set('materialType', 'solid');
720
model.mesh('mesh1').feature('size').set('custom', 'on');
722 model.mesh('mesh1').feature('size').set('hmax', '1e-6');
model.mesh('mesh1').feature('size').set('hmin', '0.05e-6');
724 model.mesh('mesh1').feature('ftri2').feature('size1').active(false);
model.mesh('mesh1').feature('ftri2').feature('size1').set('custom', 'on');
726 model.mesh('mesh1').feature('ftri2').feature('size1').set('hmaxactive', true);
model.mesh('mesh1').feature('ftri2').feature('size1').set('hmin', '6.41E-6');
728 model.mesh('mesh1').feature('ftri2').feature('size1').set('hmax', '6e-6');
model.mesh('mesh1').feature('ftri2').feature('size1').set('hminactive', false)
    ;
730 model.mesh('mesh1').feature('size1').set('hauto', 3);
model.mesh('mesh1').feature('size1').set('custom', 'on');
732 model.mesh('mesh1').feature('size1').set('hminactive', true);
model.mesh('mesh1').feature('size1').set('hmin', '0.49E-6');
734 model.mesh('mesh1').feature('size1').set('hmax', '2.23E-5');
model.mesh('mesh1').feature('size1').set('hmaxactive', false);
736 model.mesh('mesh1').feature('size2').set('custom', 'on');
model.mesh('mesh1').feature('size2').set('hminactive', true);
738 model.mesh('mesh1').feature('size2').set('hmaxactive', true);
model.mesh('mesh1').feature('size2').set('hmin', '0.95E-6');
740 model.mesh('mesh1').feature('size2').set('hmax', '3E-6');
model.mesh('mesh1').feature('fq2').active(false);
742 model.mesh('mesh1').feature('fq2').feature('size1').set('hauto', 1);
model.mesh('mesh1').feature('swe4').active(false);
```

C.2 3D simulation with misalignment and underetch

```
744 model.mesh('mesh1').feature('fq1').active(false);
model.mesh('mesh1').feature('fq1').feature('dis1').set('numelem', '26');
746 model.mesh('mesh1').feature('fq1').feature('size1').set('hauto', 3);
model.mesh('mesh1').feature('fq1').feature('size1').set('custom', 'on');
748 model.mesh('mesh1').feature('fq1').feature('size1').set('hmaxactive', true);
model.mesh('mesh1').feature('fq1').feature('size1').set('hmin', '1.42E-6');
750 model.mesh('mesh1').feature('fq1').feature('size1').set('hmax', '6e-6');
model.mesh('mesh1').feature('fq1').feature('size1').set('hmininactive', false);
752 model.mesh('mesh1').feature('swe2').active(false);
model.mesh('mesh1').feature('swe2').feature('dis1').set('elemcount', 'PML/8e-6
');
754 model.mesh('mesh1').feature('swe2').feature('dis1').set('type', 'predefined');
model.mesh('mesh1').run;
756
model.result.table('tbl5').comments('Global Evaluation 1 (arg(pzd.Y11))');
758 model.result.table('tbl6').comments('Global Evaluation 1 (arg(pzd.Y11))');
model.result.table('tbl7').comments('Global Evaluation 1 ( )');
760 model.result.table('tbl8').comments('Global Evaluation 1 (arg(pzd.Y11))');
model.result.table('tbl9').comments('Global Evaluation 1 (pzd.Q_freq)');
762 model.result.table('evl3').label('Evaluation 3D');
model.result.table('evl3').comments('Interactive 3D values');
764
model.study.create('std1');
766 model.study('std1').create('freq', 'Frequency');
768
model.sol.create('soll');
model.sol('soll').study('std1');
770 model.sol('soll').attach('std1');
model.sol('soll').create('st1', 'StudyStep');
772 model.sol('soll').create('v1', 'Variables');
model.sol('soll').create('s1', 'Stationary');
774 model.sol('soll').feature('s1').create('p1', 'Parametric');
model.sol('soll').feature('s1').create('fc1', 'FullyCoupled');
776 model.sol('soll').feature('s1').create('d1', 'Direct');
model.sol('soll').feature('s1').feature.remove('fcDef');
778
model.result.dataset.create('dset8', 'Solution');
780 model.result.dataset.create('dset9', 'Solution');
model.result.dataset.create('dset10', 'Solution');
782 model.result.dataset.create('dset11', 'Solution');
model.result.dataset.create('dset12', 'Solution');
784 model.result.dataset('dset8').set('solution', 'none');
model.result.dataset('dset9').set('solution', 'none');
786 model.result.dataset('dset10').set('solution', 'none');
model.result.dataset('dset11').set('solution', 'none');
788 model.result.dataset.remove('dset1');
model.result.numerical.create('gev1', 'EvalGlobal');
790 model.result.numerical('gev1').set('data', 'dset9');
model.result.numerical('gev1').set('probetag', 'none');
792 model.result.create('pg12', 'PlotGroup3D');
model.result.create('pg16', 'PlotGroup1D');
```

C. COMSOL FEA SIMULATION SETUPS

```
794 model.result.create('pg17', 'PlotGroup3D');
model.result.create('pg19', 'PlotGroup3D');
796 model.result.create('pg20', 'PlotGroup3D');
model.result.create('pg18', 'PlotGroup3D');
798 model.result('pg12').create('surf1', 'Surface');
model.result('pg12').feature('surf1').create('def', 'Deform');
800 model.result('pg16').create('glob1', 'Global');
model.result('pg17').create('surf1', 'Surface');
802 model.result('pg17').feature('surf1').create('def', 'Deform');
model.result('pg19').create('surf1', 'Surface');
804 model.result('pg19').feature('surf1').create('def', 'Deform');
model.result('pg20').create('surf1', 'Surface');
806 model.result('pg20').feature('surf1').create('def', 'Deform');
model.result('pg18').create('surf1', 'Surface');
808 model.result.export.create('anim1', 'Animation');
model.result.export.create('data1', 'Data');
810
model.study('std1').feature('freq').set('preusesol', 'yes');
812 model.study('std1').feature('freq').set('plist', 'range(400,0.25,500)');
model.study('std1').feature('freq').set('punit', 'MHz');
814
model.sol('soll').attach('std1');
816 model.sol('soll').feature('s1').set('probesel', 'none');
model.sol('soll').feature('s1').feature('p1').set('punit', {'MHz'});
818 model.sol('soll').feature('s1').feature('p1').set('plistarr', {'range
(400,0.25,500)'});
model.sol('soll').feature('s1').feature('p1').set('pname', {'freq'});
820 model.sol('soll').feature('s1').feature('p1').set('preusesol', 'yes');
model.sol('soll').feature('s1').feature('p1').set('pcontinuationmode', 'no');
822 model.sol('soll').feature('s1').feature('d1').set('linsolver', 'pardiso');

824 model.result.dataset('dset8').label('Solution 8');
model.result.dataset('dset9').label('Solution 9');
826 model.result.numerical('gev1').set('expr', 'arg(pzd.Y11)');
model.result.numerical('gev1').set('descr', 'arg(pzd.Y11)');
828 model.result.numerical('gev1').set('table', 'tbl9');
model.result.numerical('gev1').set('unit', 'rad');
830 model.result.numerical('gev1').setResult;
model.result('pg12').label('Displacement (pzd)');
832 model.result('pg12').set('showlegendsmaxmin', true);
model.result('pg12').feature('surf1').set('const', {'pzd.refpntx' '0' '
Reference point for moment computation, x component'; 'pzd.refpnty' '0' '
Reference point for moment computation, y component'; 'pzd.refpntz' '0' '
Reference point for moment computation, z component'});
834 model.result('pg12').feature('surf1').feature('def').set('scaleactive', true);
model.result('pg12').feature('surf1').feature('def').set('scale', '150');
836 model.result('pg16').label('admittance mag');
model.result('pg16').set('xlabel', 'Frequency (Hz)');
838 model.result('pg16').set('xlabelactive', false);
model.result('pg16').feature('glob1').set('unit', {''});
840 model.result('pg16').feature('glob1').set('descr', {''});
```

C.2 3D simulation with misalignment and underetch

```
model.result('pg16').feature('glob1').set('xdatadescr', 'Frequency');
842 model.result('pg16').feature('glob1').set('xdataexpr', 'pzd.freq');
model.result('pg16').feature('glob1').set('xdataunit', 'Hz');
844 model.result('pg16').feature('glob1').set('solrepresentation', 'solnum');
model.result('pg16').feature('glob1').set('xdata', 'expr');
846 model.result('pg16').feature('glob1').set('expr', {'20*log10(abs(pzd.Y11))'});
model.result('pg17').label('Displacement x');
848 model.result('pg17').set('showlegendsmaxmin', true);
model.result('pg17').feature('surfl1').set('const', {'pzd.refpntx' '0' '
    Reference point for moment computation, x component'; 'pzd.refpnty' '0' '
    Reference point for moment computation, y component'; 'pzd.refpntz' '0' '
    Reference point for moment computation, z component'});
850 model.result('pg17').feature('surfl1').set('descr', 'v*cos(30[deg])+w*cos(60[
    deg]');
model.result('pg17').feature('surfl1').set('colortable', 'WaveLight');
852 model.result('pg17').feature('surfl1').set('colortablesym', true);
model.result('pg17').feature('surfl1').set('expr', 'v*cos(30[deg])+w*cos(60[deg
    ])');
854 model.result('pg17').feature('surfl1').feature('def').set('scaleactive', true);
model.result('pg17').feature('surfl1').feature('def').set('scale', '150');
856 model.result('pg19').label('Displacement y');
model.result('pg19').set('showlegendsmaxmin', true);
858 model.result('pg19').feature('surfl1').set('const', {'pzd.refpntx' '0' '
    Reference point for moment computation, x component'; 'pzd.refpnty' '0' '
    Reference point for moment computation, y component'; 'pzd.refpntz' '0' '
    Reference point for moment computation, z component'});
model.result('pg19').feature('surfl1').set('descr', 'v*cos(-60[deg])-w*cos(30[
    deg]');
860 model.result('pg19').feature('surfl1').set('colortable', 'WaveLight');
model.result('pg19').feature('surfl1').set('colortablesym', true);
862 model.result('pg19').feature('surfl1').set('expr', 'v*cos(-60[deg])-w*cos(30[
    deg]');
model.result('pg19').feature('surfl1').feature('def').set('scaleactive', true);
864 model.result('pg19').feature('surfl1').feature('def').set('scale', '150');
model.result('pg20').label('Displacement z');
866 model.result('pg20').set('showlegendsmaxmin', true);
model.result('pg20').feature('surfl1').set('const', {'pzd.refpntx' '0' '
    Reference point for moment computation, x component'; 'pzd.refpnty' '0' '
    Reference point for moment computation, y component'; 'pzd.refpntz' '0' '
    Reference point for moment computation, z component'});
868 model.result('pg20').feature('surfl1').set('descr', 'Displacement field, X
    component');
model.result('pg20').feature('surfl1').set('colortable', 'WaveLight');
870 model.result('pg20').feature('surfl1').set('colortablesym', true);
model.result('pg20').feature('surfl1').set('expr', 'u');
872 model.result('pg20').feature('surfl1').feature('def').set('scaleactive', true);
model.result('pg18').label('potential');
874 model.result('pg18').feature('surfl1').set('descr', 'Electric potential');
model.result('pg18').feature('surfl1').set('unit', 'V');
876 model.result('pg18').feature('surfl1').set('expr', 'V');
model.result.export('anim1').set('plotgroup', 'pg20');
```

C. COMSOL FEA SIMULATION SETUPS

```
878 model.result.export('anim1').set('height', '640');
model.result.export('anim1').set('fps', '2');
880 model.result.export('anim1').set('framesel', 'all');
model.result.export('anim1').set('synchronize', false);
882 model.result.export('anim1').set('giffilename', 'C:\Users\syen\Desktop\Exempt
    from backup\RshCb_3Dmisbloat_TLN0p875TA10p05_uz.gif');
model.result.export('anim1').set('axisorientation', false);
884 model.result.export('anim1').set('title', 'on');
model.result.export('anim1').set('legend', 'on');
886 model.result.export('anim1').set('logo', 'off');
model.result.export('anim1').set('options', 'on');
888 model.result.export('anim1').set('fontsize', '9');
model.result.export('anim1').set('customcolor', [1 1 1]);
890 model.result.export('anim1').set('background', 'color');
model.result.export('anim1').set('axisorientation', 'off');
892 model.result.export('anim1').set('grid', 'on');
model.result.export('anim1').set('axes', 'on');
894 model.result.export('data1').set('descr', {'Admittance'});
model.result.export('data1').set('expr', {'pzd.Y11'});
896 model.result.export('data1').set('filename', '/afs/ece.cmu.edu/usr/syen/
    Private/FP2_system_simulations/gratings/Y11-1portLNAl-xR60-PML-EVEN-
    LLN111p367Lb6p551-Wa58p959La13p102G2-TLN0p875TA10p05-manualmeshfine-
    Ey197GPaNu1-rotatePMLcyls-Wbloat1p78Wmis0p43-fullsweep.csv');
model.result.export('data1').set('sdim', 'global');
898 model.result.export('data1').set('unit', {'S'});
900 out = model;
```

Appendix D

Additional measurements

D.1 Ladder filter measurements

This section presents the measurements of the ladder filters from the same fabrication run as the one that produced the measured results in Chapter 2. There were four chips on that run. Figure D.1 and Figure D.2 show the measured S-parameters (wide sweep and zoomed in views).

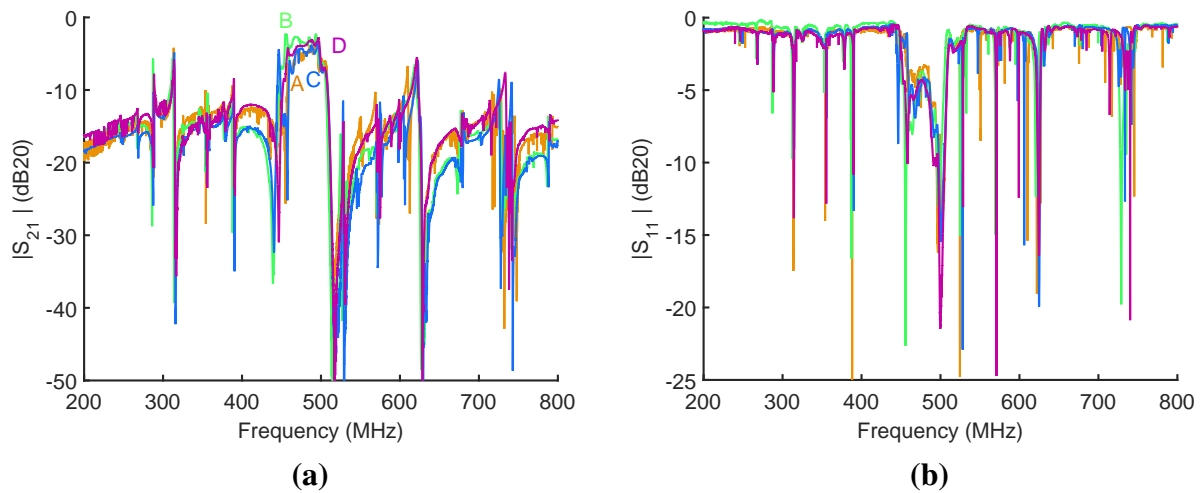


Figure D.1: Measurements of ladder filter S-parameters from the four samples in the 2015 LN fabrication run. The one used in Chapter 2 is “B”.

D. ADDITIONAL MEASUREMENTS

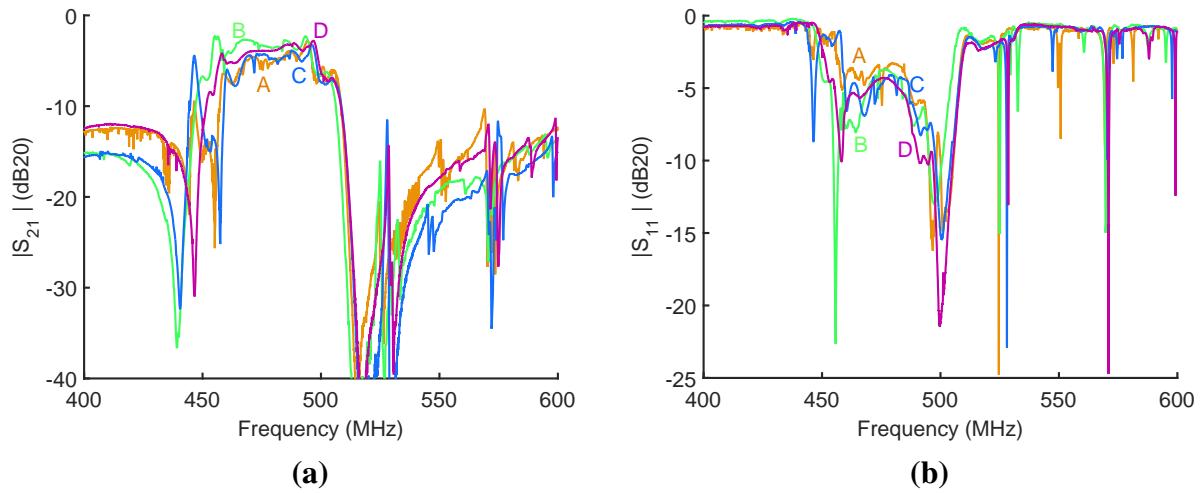


Figure D.2: Measurements of ladder filter S-parameters (zoomed in to passband region) from the four samples in the 2015 LN fabrication run. The one used in Chapter 2 is “B”.

D.2 Resonator measurements

Three chips had measurable resonators corresponding to those used in the shunt branch of the ladder filters above, with very close frequency responses as shown in Figure D.3.

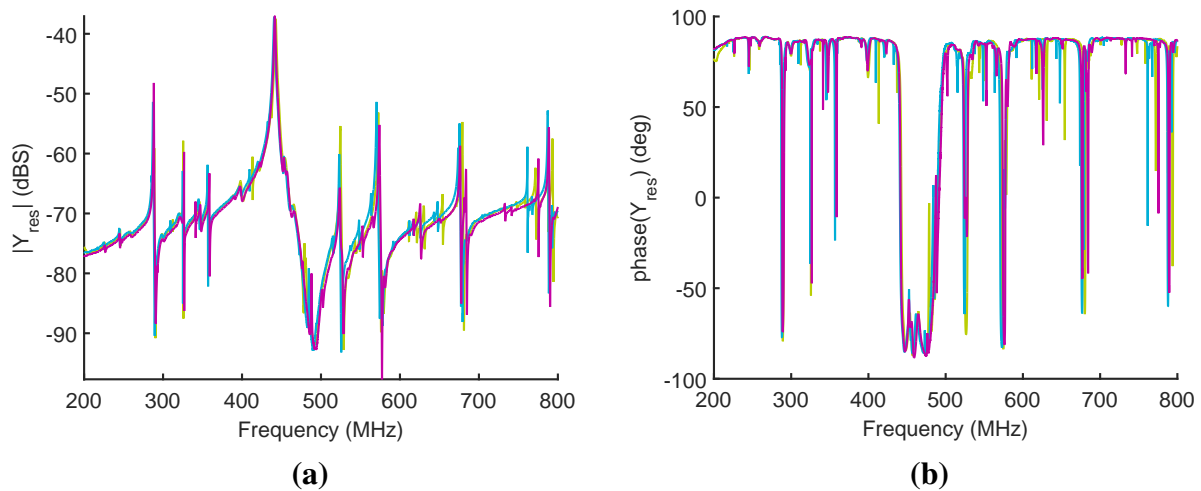


Figure D.3: Measurements of shunt resonator admittance, no deembedding, from three of the samples in the 2015 LN fabrication run, showing very close frequency responses despite being from different chips.

Appendix E

Layout directory

There were two fabrication runs in lithium niobate for this thesis. This appendix lists the materials and layout location for each fabrication run, in chronological order.

E.1 LN/SiO₂ run, 2014

The material stack for this run was 0.5 μm *x*-cut LN on 0.8 μm SiO₂ on a Si handle wafer. The Si is etched to release the mechanical structure, which consists of both the LN and oxide layers. The electrodes are nominally 100 nm Al, with 100 nm Au for the pads. This is the run on which the absorptive notch filter in Chapter 3 was built.

The layout is located in library LN_darpa_Feb_2014 (note that this is using the cmuAlN_cds launch script). The top layout is V5finaltweaks_2014_LN_Feptuneout_Sept_FLATTENED.

E.2 LN run, 2015

The material stack for this run was 1 μm *x*-cut LN on a Si handle wafer. The Si is etched to release the mechanical structure, which consists of the LN layer. This is the run on which the

E. LAYOUT DIRECTORY

bandpass filter in Chapter 2 and misaligned resonator at the beginning of Chapter 5 were built.

The layout is located in library `RF_FPGA_2015` (using the `cmuLN_cds` launch script). The top layout is `top_both_update2`.